ARO 12049.7-EL

Electromagnetics Laboratory Report No. 76-6

A METHOD FOR COMBINING INTEGRAL EQUATION AND ASYMPTOTIC TECHNIQUES FOR SOLVING ELECTROMAGNETIC SCATTERING PROBLEMS

Technical Report

W. L. Ko
R. Mittra

May 1976

DDC

JUN 14 1976

C

Electromagnetics Laboratory
Department of Electrical Engineering
Engineering Experiment Station
University of Illinois at Urbana-Champaign
Urbana, Illinois 61801

THE FINDINGS IN THIS REPORT ARE NOT TO BE
CONSTRUED AS AN OFFICIAL DEPARTMENT OF
THE ARMY POSITION, UNLESS SO DESIGNATED
BY OTHER AUTHORIZED DOCUMENTS.

DOCUMENT CONTROL DATA - R & D

(Security classification of title, body of abstract and indexing annotation must be entered when the overall report is classified)

1. ORIGINATING ACTIVITY (Corporate author)	2a. REPORT SECURITY CLASSIFICATION
Electromagnetics Laboratory	Unclassified
Department of Electrical Engineering	2b. GROUP
University of Illinois, Urbana, Illinois	NA

3. REPORT TITLE

A METHOD FOR COMBINING INTEGRAL EQUATION AND ASYMPTOTIC TECHNIQUES FOR SOLVING ELECTROMAGNETIC SCATTERING PROBLEMS.

4. DESCRIPTIVE NOTES (Type of report and inclusive dates)

Technical report

5. AUTHOR(S) (First name, middle initial, last name)

Wai Lee Ko
Raj Mittra

6. REPORT DATE	7a. TOTAL NO. OF PAGES	7b. NO. OF REFS
May 1976	214	32

8a. CONTRACT OR GRANT NO.	9a. ORIGINATOR'S REPORT NUMBER(S)
DAHC04-74-G-0113 N00014-75-C-0293	Electromagnetics Laboratory Report No. 76-6
8b. PROJECT NO. P12049-E	
ARO	9b. OTHER REPORT NO(S) (Any other numbers that may be assigned this report) UILU-ENG-76-2549

10. DISTRIBUTION STATEMENT

Approved for public release; distribution unlimited.

11. SUPPLEMENTARY NOTES	12. SPONSORING MILITARY ACTIVITY
ARO 12049.7-EL	U. S. Army Research Office ; ONR Box CM, Duke Station Durham, North Carolina 27706

13. ABSTRACT

This paper introduces a new approach for combining the integral equation and high frequency asymptotic techniques, e.g., the geometrical theory of diffraction. The method takes advantage of the fact that the Fourier transform of the unknown surface current distribution is proportional to the scattered far field. A number of asymptotic methods are currently available that provide good approximation to this far field in a convenient analytic form which is useful for deriving an initial estimate of the Fourier transform of the current distribution.

An iterative scheme is developed for systematically improving the initial form of the high frequency asymptotic solution by manipulating the integral equation in the Fourier transform domain.

A synthetic-aperture-distribution scheme is also developed in which the approximate scattered far-field pattern obtained by asymptotic techniques is improved by systematically correcting the scattered field distribution on an aperture erected in juxtaposition with the obstacle. The introduction of such a planar aperture not only provides an additional degree of freedom in performing improving operations, but also renders the scheme to handle n-dimensional geometries by (n - 1)-dimensional fast Fourier transform (FFT), where n = 2, 3, and circumvents the unwieldy three-dimensional FFT, making it a conceptually simple and computationally efficient method.

A salient feature of the method is that it provides convenient validity checks of the solutions for the surface current distribution and the scattered far-field pattern by verifying that the scattered field obtained indeed satisfies the boundary conditions at the surface of the scatterer. Another important feature of the method is that it yields both the induced surface current density and the far field. (continued)

DD FORM 1473, 1 NOV 65 REPLACES DD FORM 1473, 1 JAN 64, WHICH IS OBSOLETE FOR ARMY USE.

408102

14. KEY WORDS	LINK A		LINK B		LINK C	
	ROLE	WT	ROLE	WT	ROLE	WT
Radar Scattering						
Fourier Transform Technique						
Asymptotic Methods						
Integral Equations						
Numerical Solution						

(continued)

13.

Diffractions by a strip, a thin plate, a rectangular cylinder, and a circular cylinder are presented as illustrative examples that demonstrate the usefulness of the approach for handling a variety of electromagnetic scattering problems in the resonance region and above. Some concluding remarks and comparison with other methods are also included.

A METHOD FOR COMBINING INTEGRAL EQUATION AND ASYMPTOTIC TECHNIQUES FOR SOLVING ELECTROMAGNETIC SCATTERING PROBLEMS

Technical Report

W. L. Ko
R. Mittra

May 1976

Electromagnetics Laboratory
Department of Electrical Engineering
Engineering Experiment Station
University of Illinois at Urbana-Champaign
Urbana, Illinois 61801

ACKNOWLEDGMENT

PREFACE

A little over a century ago, Maxwell put together the fundamental laws that govern all the electromagnetic phenomen. in an amazingly elegant form, i.e., the set of equations named after him. Ever since then, the major contributions in the field of electromagnetics have been solving boundary value problems, or seeking solutions which satisfy the Maxwell's equations and match the boundary conditions (including radiating conditions as special cases)in specific environments under consideration.

The dyadic Green's functions technique, an elegant and powerful method for solving boundary-value problems, was first formulated by Schwinger in the early 1940's. However, solutions obtained by that technique are extremely complicated and are not always best suited for numerical computations.

In the late 1950's, Keller conceived the concept of a diffraction-coefficient approach to the high-frequency scattering, and was able to obtain approximate solutions for far-field patterns in a very simple and straightforward manner. Although his method fails at certain aspect angles in space, it has been applied to solve many practical problems.

In the 1960's, the moment method became popular due to the availability of the large scale computer systems. However, for electrically large scatterers, the moment method is limited by the storage of a computer.

In the early 1970's, a trend of combining the Keller's geometrical theory of diffraction with the moment method to solve high-frequency scattering problems was initiated. However, a general approach for combining the two techniques has yet to be developed.

It is the purpose of this study to introduce a method of combining the integral equation and asymptotic techniques for solving electromagnetic scattering problems. The method is conceptually simple and computationally efficient. Comparisons with contemporary combinational approaches show that the method, when fully developed, appears to be highly promising in solving practical problems. Of course, this thesis is merely a start, and there is much left to be studied and investigated. It is the author's hope that future research activities along the same lines as described herein will result in not only a feasible but also a practical way of handling real-world high-frequency scattering problems.

ABSTRACT

This paper introduces a new approach for combining the integral equation and high frequency asymptotic techniques, e.g., the geometrical theory of diffraction. The method takes advantage of the fact that the Fourier transform of the unknown surface current distribution is proportional to the scattered far field. A number of asymptotic methods are currently available that provide good approximation to this far field in a convenient analytic form which is useful for deriving an initial estimate of the Fourier transform of the current distribution.

An iterative scheme is developed for systematically improving the initial form of the high frequency asymptotic solution by manipulating the integral equation in the Fourier transform domain.

A synthetic-aperture-distribution scheme is also developed in which the approximate scattered far-field pattern obtained by asymptotic techniques is improved by systematically correcting the scattered field distribution on an aperture erected in juxtaposition with the obstacle. The introduction of such a planar aperture not only provides an additional degree of freedom in performing improving operations, but also renders the scheme to handle n-dimensional geometries by (n - 1)-dimensional fast Fourier transform (FFT), where n = 2,3, and circumvents the unwieldy three-dimensional FFT, making it a conceptually simple and computationally efficient method.

A salient feature of the method is that it provides convenient validity checks of the solutions for the surface current distribution and the scattered far-field pattern by verifying that the scattered field obtained indeed satisfies the boundary conditions at the surface of the scatterer. Another important feature of the method is that it yields both the induced surface current density *and* the far field.

Diffractions by a strip, a thin plate, a rectangular cylinder, and a circular cylinder are presented as illustrative examples that demonstrate the usefulness of the approach for handling a variety of electromagnetic scattering problems in the resonance region *and* above. Some concluding remarks and comparison with other methods are also included.

TABLE OF CONTENTS

LIST OF FIGURES

LIST OF TABLES

1. INTRODUCTION

It is well-known that the integral equation methods are limited in application to scatterers whose characteristic dimensions are of the order of one wavelength or less. On the other hand, the high-frequency asymptotic techniques can be reliably used only when the scatterer is large compared to the wavelength, and neither of the above two methods is suitable in the resonance region.

This thesis introduces a new hybrid technique,[1] based on a combination of the integral equation and asymptotic methods, that is useful in the entire frequency range encompassing the resonance region and above. Another important feature of the method is that it can be used to check and improve the accuracy of high-frequency asymptotic solutions. Such an accuracy test and systematic improvement of the asymptotic solution are often needed, but no reliable methods for performing these are available at the present time.

In contrast to the ray optics methods, which are based on the diffraction of ray fields as determined by the local properties of the surface of the scatterer, the present method starts with the integral equation formulation incorporating the boundary conditions on the entire surface of the scatterer. Conventionally, the solution of the integral equation for the induced surface current is carried out by matrix methods [1], [2]. The size of the matrix becomes prohibitively large and its solution extremely time-consuming when the characteristic dimension of the scatterer approaches the wavelength of the illuminating field.

---

[1] The original concepts on which this thesis is based were described at the 1975 URSI Symposium in a paper entitled, "A new method for improving the GTD solution via the integral equation formulation," by R. Mittra and W. L. Ko.

The approach developed in this thesis circumvents this difficulty while still preserving the self-consistent nature of the integral equation formulation by constructing the solution in the Fourier transform or spectral domain rather than in the space domain. We take advantage of the facts that the Fourier transform of the surface current distribution *is* directly proportional to the far scattered field and that the asymptotic methods often provide a very good initial estimate of the latter quantity. We next construct an iterative[2] solution of the integral equation in the transform domain with the GTD[3] or other high-frequency solution as the zero-order approximation.

As shown in the thesis, this procedure not only allows us to improve on the GTD or similar solutions but also provides a convenient means for testing the satisfaction of the boundary conditions on the surface of the scatterer. Furthermore, the method yields not only the far field but also the induced surface-current distribution, a feature not readily available in some other high-frequency techniques.

A detailed derivation of the iterative method is presented in Chapter 2. A step-by-step recipe for applying the iterative scheme to construct the solution of the induced surface current can also be found in Chapter 2.

The application of the general procedure outlined in Chapter 2 is illustrated by two examples: the two-dimensional problem of a plane

---

[2]A moment method solution in the spectral domain has also been developed (see [3]).

[3]For a comprehensive discussion of the Geometrical Theory of Diffraction (GTD) and its application, see R. G. Kouyoumjian, Chapter 7 of Numerical and Asymptotic Techniques in Electromagnetics, R. Mittra (Ed.), Springer Verlag, 1975.

wave diffraction by a strip and a three-dimensional problem of a plane wave diffraction by a thin plate.

In Chapter 3, the iteration procedure is applied to solve the strip problem. This problem was chosen for the following reasons: It is shown that when the angle of incidence is normal or near normal, the GTD solution accurately satisfies the boundary condition $\bar{E}_{tan} = 0$ on the strip even when the multiple interaction between the two edges of the strip is neglected. However, it is found that when the angle of incidence is near grazing, the GTD solution is quite unsatisfactory, while the iterated solution generated by the hybrid technique does display the correct behavior.

In Chapter 4, the iteration procedure is applied to solve the plate problem. This problem was chosen for the following reasons: In the plate problem, the difficulty in applying GTD to this geometry stems from the fact that the diffraction coefficient for the corners of the plate is not known and neglecting the corner effects can cause substantial errors in the resonance frequency region where the plate size is of the order of one wavelength squared. However, the present technique, based on a combination of the integral equation and asymptotic methods, does allow the successful computation of the induced surface currents on the plate.

In Chapter 5, diffraction by planar surface solid scatterers with multiple edges, e.g., a rectangular cylinder, is considered. A technique which is based on a representation of the scattered fields in terms of the spectrum of the induced surface current on the scatterer rather than the rays emanating from it is discussed. The scattered far-field

obtained by this technique compares extremely well with that obtained
from the moment method solution for thirty-two unknowns. Comparisons
with results obtained by other approaches in the literature [4] can
also be found in Chapter 5.

In Chapter 6, the method for combining integral equation and asymp-
totic techniques for solving electromagnetic scattering problems of a
convexly curved surface scatterer, e.g., a circular cylinder, is devel-
oped. Detailed descriptions of the synthetic-aperture-distribution
approach are documented, and comparisons with other methods [4], [5],
that have been developed recently for solving problems of a similar
nature are also included in Chapter 6. The idea is to transfer informa-
tion characterizing the curved surface onto a planar aperture where
operations for improving the high-frequency asymptotic solution are
carried out. A salient feature of the method is that the far field is
obtained by Fourier transforming the aperture-field distribution; hence,
it can handle problems of an n-dimensional obstacle by an $(n - 1)$-
dimensional fast Fourier transform (FFT), where $n = 2,3$. Therefore, the
unwieldy three-dimensional FFT is circumvented; hence, the method is
numerically efficient. Moreover, the method is conceptually simpler
than other conventional methods because operations for improvement are
carried out on a plane rather than on a curved surface.

In Chapter 7, concluding remarks are made and future research
activities along similar lines based on the present approach are recom-
mended.

In this method, the fast Fourier transform [6] is a necessary
tool; hence, a brief discussion on FFT is presented in Appendix A.

2. FORMULATION OF AN ITERATION METHOD

2.1 Derivation of the Method

We begin our analysis with the electric-field integral equation
[7] for a perfectly conducting scatterer. The equation may be sym-
bolically written as

$$(\bar{\bar{G}} * \bar{J})_t = -\bar{E}^i_t , \quad \bar{r} \in S \tag{2.1}$$

where $\bar{J}(\bar{r}')$ is the induced surface current density we are attempting
to determine, and the subscript t signifies tangential to the surface S;
$\bar{E}^i_t$ is the tangential component of the incident electric field $\bar{E}^i$ on the
surface S of the scatterer; and $\bar{\bar{G}}$ is the free space Green's Dyadic, which
yields the scattered electric field when operating on $\bar{J}$. In anticipation of
Fourier transforming (2.1), we extend it over all space by first defining
a truncation-projection operator θ as follows:

For any vector $\bar{A}(\bar{r})$, which is a vector function of position $\bar{r}$,

$$\theta(\bar{A}) = \int \bar{A}_t \delta(\bar{r} - \bar{r}_s) dr , \quad \bar{r}_s \in S \tag{2.2a}$$

where $\delta(\bar{r} - \bar{r}_s)$ is the Dirac delta function and the subscript t sig-
nifies tangential to the surface S. Also its complementary operator
$\hat{\theta}$ is defined as

$$\hat{\theta}(\bar{A}) = \bar{A} - \theta(\bar{A}) . \tag{2.2b}$$

We can then rewrite (2.1) as

$$\bar{\bar{G}} * \bar{J} = \theta(-\bar{E}^i) + \hat{\theta}(\bar{\bar{G}} * (\theta\bar{J})) , \quad \text{for all space} . \tag{2.3}$$

As indicated above, (2.3) is valid at all observation points whether on or off the surface S. Note that the integral equation (2.1) is embedded in (2.3) and that we have made use of the obvious identity $\theta \bar{J} = \bar{J}$.

Next we Fourier transform (2.3) by introducing the transform relationships

$$\tilde{F}(\bar{k}) = \int_{-\infty}^{\infty} F(\bar{r}) \, e^{-i\bar{k}\cdot\bar{r}} \, d\bar{r} = F[F(\bar{r})] \qquad (2.4a)$$

and

$$F(\bar{r}) = (\frac{1}{2\pi})^3 \int_{-\infty}^{\infty} \tilde{F}(\bar{k}) \, e^{i\bar{k}\cdot\bar{r}} \, d\bar{k} = F^{-1}[\tilde{F}(\bar{k})] \qquad (2.4b)$$

with ~ on top denoting the transformed quantities.

The transformed version of (2.3) reads

$$\tilde{\bar{\bar{G}}}\tilde{\bar{J}} = -\tilde{\bar{E}}_I + \tilde{\bar{F}} \qquad (2.5)$$

where $\tilde{\bar{F}} = F[\hat{\theta}(\bar{\bar{G}} * (\theta J))]$ and $\tilde{\bar{E}}_I$ is the transform of the tangential component of the incident field truncated on S. Note that the convolution operation in (2.3) is transformed into an algebraic product upon Fourier transformation.

A formal solution to (2.5) can now be written

$$\tilde{\bar{J}} = \tilde{\bar{\bar{G}}}^{-1}(-\tilde{\bar{E}}_I + \tilde{\bar{F}}) \quad . \qquad (2.6)$$

Equation (2.6) says that if we had available the Fourier transform of the scattered electric field, we could construct the solution for the induced surface current density in the transform domain by adding it

to $-\tilde{\bar{E}}_I$, which is known, and by performing an algebraic division represented by $\tilde{\bar{G}}^{-1}$. In practice, of course, $\tilde{\bar{F}}$ is not known and must be solved for along with $\tilde{\bar{J}}$ if (2.6) is to be used in the form as shown. However, instead of using this form, we proceed to derive an iterated form of the equation as shown below:

$$\tilde{\bar{J}}^{(n+1)} = \tilde{\bar{G}}^{-1}(-\tilde{\bar{E}}_I + \tilde{\bar{F}}^{(n)}) \tag{2.7}$$

which indicates the $(n + 1)$th approximation of $\tilde{\bar{J}}$ from the nth approximation for $\tilde{\bar{F}}$. We next show how $\tilde{\bar{F}}^{(n)}$ itself can be derived from $\tilde{\bar{J}}^{(n)}$. To this end, we use the identity

$$\tilde{\bar{F}} = F[F^{-1}[\tilde{\bar{G}}\tilde{\bar{J}}] - \theta(F^{-1}[\tilde{\bar{G}}\tilde{\bar{J}}])] \tag{2.8}$$

which may be verified by writing (2.8) as

$$\tilde{\bar{F}} = F[\bar{\bar{G}} \star \bar{J} - \theta(-\bar{E}^1)] \tag{2.9}$$

and using (2.3) to get

$$\tilde{\bar{F}} = F[\hat{\theta}(\bar{\bar{G}} \star (\theta\bar{J}))] \tag{2.10}$$

which, of course, is the definition of $\tilde{\bar{F}}$. We can now use (2.8) to derive the nth approximation $\tilde{\bar{F}}^{(n)}$ of $\tilde{\bar{F}}$ from the nth approximation of $\bar{J}$, i.e., $\bar{J}^{(n)}$. The relationship is written as

$$\tilde{\bar{F}}^{(n)} = F[F^{-1}[\tilde{\bar{G}}\tilde{\bar{J}}^{(n)}] - \theta(F^{-1}[\tilde{\bar{G}}\tilde{\bar{J}}^{(n)}])] \quad . \tag{2.11}$$

The desired iteration relating $\tilde{\bar{J}}^{(n+1)}$ and $\tilde{\bar{J}}^{(n)}$ may now be written. Using (2.7) and (2.11)

$$\tilde{\bar{J}}^{(n+1)} = \tilde{\bar{G}}^{-1}[-\tilde{\bar{E}}_I + F[F^{-1}[\tilde{\bar{G}}\tilde{\bar{J}}^{(n)}] - \theta(F^{-1}[\tilde{\bar{G}}\tilde{\bar{J}}^{(n)}])]] \quad . \tag{2.12}$$

2.2 Recipe for Applying the Method

The step-by-step procedure for constructing the solution of the transformed surface current $\tilde{\bar{J}}$ will now be given:

1. Begin with an estimate of $\tilde{\bar{J}}^{(0)}$, which is the Fourier transform of the induced surface current, or equivalently, the scattered *far field* within a known multiplicative constant. Typically, the initial approximation for $\tilde{\bar{J}}$, viz., $\tilde{\bar{J}}^{(0)}$, can be obtained as follows:

   (a) Estimate $\tilde{\bar{F}}$, the Fourier transform of the scattered field, $\bar{F}$, outside the scatterer, using GTD or other asymptotic solutions.[4]

   (b) Subtract $\tilde{\bar{E}}_I$, the Fourier transform of the tangential component of the incident electric field truncated to the surface of the scatterer.

   (c) Multiply the result of Step (b) by $\tilde{\bar{\bar{G}}}^{-1}$. Note that $\tilde{\bar{\bar{G}}}^{-1}$ is known and the operation is algebraic.

   (d) Take the inverse Fourier transform of the result of Step (c) and truncate it to the surface of the scatterer to obtain $\tilde{\bar{J}}^{(0)}$, the initial approximation for $\tilde{\bar{J}}$.

2. Multiply $\tilde{\bar{J}}^{(0)}$ by $\tilde{\bar{\bar{G}}}$, the known transform of the Green's Dyadic. Note this involves algebraic multiplication and not the usual time-consuming convolution operation.

---

[4] Note that GTD (Keller's) solutions may either have singularities or may be in error near shadow and reflection boundaries or at caustics, and the Uniform Theory of Diffraction (UTD) [8] and the Uniform Asymptotic Theory (UAT) [9] break down at caustics. The Spectral Theory of Diffraction (STD) [10], on the other hand, is uniform for all observation angles. The criterion for choosing any of these asymptotic forms of solution is convenience of computation for desired accuracy. For a comparative evaluation of the accuracy of the GTD, UTD, UAT and STD, the reader is referred to [11].

3. Take the inverse Fourier transform of the product $\tilde{\bar{\bar{G}}}\tilde{\bar{J}}^{(0)}$ using both *visible and invisible ranges*.

4. Apply the truncation-projection operator θ to $F^{-1}[\tilde{\bar{\bar{G}}}\tilde{\bar{J}}^{(0)}]$, which gives the approximation to the tangential component of the scattered electric field $\bar{E}_t^s$ on the surface S. The accuracy of the solution can be conveniently checked at this point by verifying the satisfaction of the boundary condition by the tangential component of $\bar{E}^s$, viz., $\{\bar{E}_t^s = -\bar{E}_t^i\}$ on S. As mentioned in Chapter 1, this is an important feature of the method.

5. Subtract $\theta(F^{-1}[\tilde{\bar{\bar{G}}}\tilde{\bar{J}}^{(0)}])$ from the total $F^{-1}[\tilde{\bar{\bar{G}}}\tilde{\bar{J}}^{(0)}]$ already evaluated.

6. Take the Fourier transform of the difference obtained in Step 5.

7. Subtract $\tilde{\bar{E}}_I$, the Fourier transform of the tangential component of the incident electric field truncated on the surface, from the result in Step 6.

8. Multiply the result obtained in Step 7 by $\tilde{\bar{\bar{G}}}^{-1}$. Note that $\tilde{\bar{\bar{G}}}^{-1}$ is also known and the operation is again algebraic as in Step 2. The result thus obtained is $\tilde{\bar{J}}^{(1)}$, which is the first iteration of the scattered far field.

9. Take the inverse Fourier transform of $\tilde{\bar{J}}^{(1)}$ obtained in Step 8 and evaluate it on S to get the desired induced surface current on the scatterer. In other words, perform the operation $\theta(F^{-1}[\tilde{\bar{J}}^{(1)}])$. For an exact solution, this operation is redundant, since $\bar{J} = \theta\bar{J}$, and hence, $\theta(F^{-1}[F[\theta\bar{J}]]) = \theta\theta\bar{J} = \bar{J}$. However, the Fourier inversion of an nth approximate solution $\tilde{\bar{J}}^{(n)}$ will not give rise to a current distribution that is nonzero except on S. This step provides a test for the accuracy and for the

convergence of the approximate solution by comparing the approx-imate $\tilde{\tilde{J}}^{(0)}$ with $F[\theta(F^{-1}[\tilde{\tilde{J}}^{(1)}])]$.

10. Take $F[\theta(F^{-1}[\tilde{\tilde{J}}^{(1)}])]$ to derive an *improved* approximation for $\tilde{\tilde{J}}^{(1)}$.

11. Repeat as necessary using, for instance, the *improved* $\tilde{\tilde{J}}^{(1)}$ from Step 10 in the iteration Equation (2.12) to generate the next higher-order approximation $\tilde{\tilde{J}}^{(2)}$.

Before closing this chapter we should point out that Galerkin's method applied in the transformed domain also provides an alternate, and in some cases the more desirable, approach for deriving the solution to the transformed integral equation. $\tilde{\tilde{J}}^{(0)}, \tilde{\tilde{J}}^{(1)}$, etc., as well as other suit-able functions may be employed as a basis set for this purpose.

In the following two chapters, we show, in some detail, the appli-cation of the procedure just described to a two-dimensional and a three-dimensional scattering problem.

3. DIFFRACTION BY AN INFINITE STRIP

3.1 Introduction

In the last chapter, we presented a general iteration method for obtaining solution of the integral equation in the transform domain with the GTD or other high-frequency solution as the zero-order approximation. This iteration method not only allows us to improve on the GTD or similar solutions but also provides a convenient means for testing the satisfaction of the boundary conditions on the surface of the scatterer. Furthermore, the method yields not only the far-field but also the induced surface-current distribution, a feature not readily available in some other high-frequency techniques.

The application of the general procedure outlined in Chapter 2 is illustrated in this chapter by using it to solve the two-dimensional problem of a plane wave diffraction by a strip. This problem was chosen for the following reasons: It is shown that when the angle of incidence is normal or near normal, the GTD solution accurately satisfies the boundary condition $\bar{E}_{tan} = 0$ on the strip even when the multiple interaction between the two edges of the strip is neglected. However, it is found that when the angle of incidence is near grazing, the GTD solution is quite unsatisfactory, while the iterated solution generated by the hybrid technique does display the correct behavior.

3.2 Geometry of the Strip Problem

The geometry of the electromagnetic scattering problem involving a perfectly conducting infinite strip of zero thickness illuminated by a uniform plane wave, whose electric intensity vector is oriented

parallel to the edges of the strip, is depicted in Figure 3.1. For convenience of analysis, an arbitrary incident wave can always be decomposed into two components with respect to the z-axis, namely, TM_z (E-wave) and TE_z (H-wave). In the following discussion we consider the E-wave case only; the H-wave case can be solved in a similar manner by considering $\bar{H}^i = \hat{z} H_0^i$.

The incident field is given by

$$E_z^i(\rho,\phi) = e^{-ik(x\cos\phi_0 + y\sin\phi_0)} \tag{3.1}$$

where the $e^{-i\omega t}$ time dependence is understood.

3.3 Iteration Method Applied to the Strip Problem

The integral equation formulation [12] for the problem at hand takes the form

$$-E_z^i(x) = \int_{-a}^{a} J_z(x')G(x - x') \, dx' \, , \quad x \in [-a,a] \tag{3.2}$$

where $J_z(x')$ is the algebraic sum of the induced surface current densities on the top and the bottom surfaces of the thin strip. The kernel G is the two-dimensional free-space Green's function given by

$$G(x - x') = \frac{1}{4} H_0^{(1)}(k_0|x - x'|) \tag{3.3}$$

where $H_0^{(1)}$ is the Hankel's function of the first kind of order zero. $k_0 = 2\pi/\lambda$ is the free-space propagation constant. Note that (3.2) is the conventional integral equation which equates the integral representation of the tangential component of the scattered E-field radiated
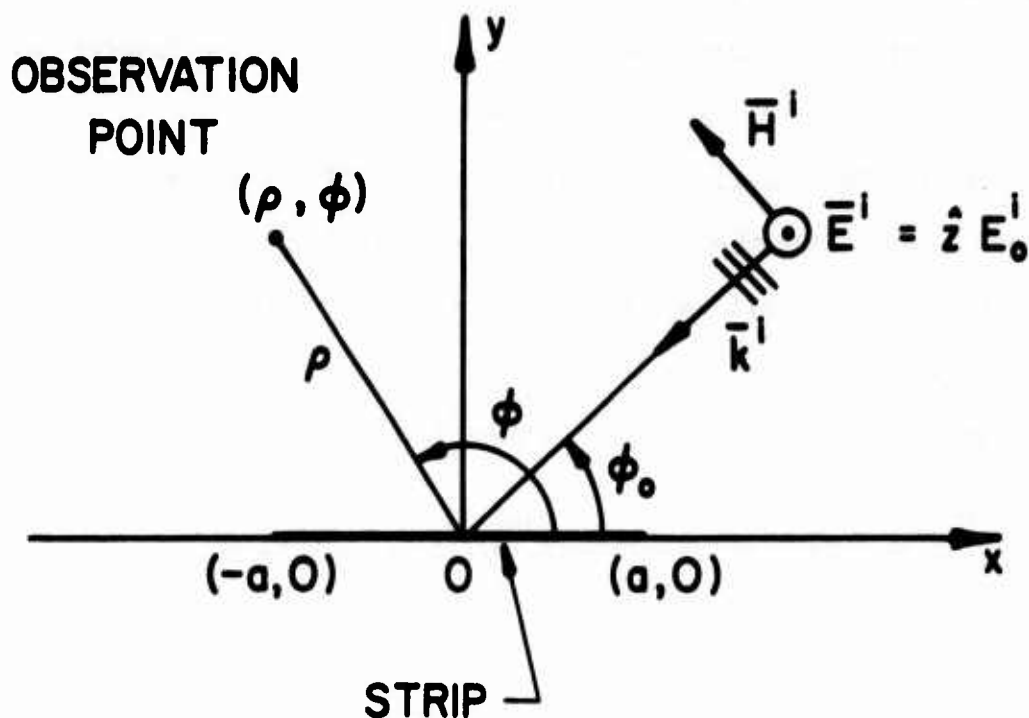
Figure 3.1. Diffraction by a strip illuminated by an E-wave.

(a)   (b)
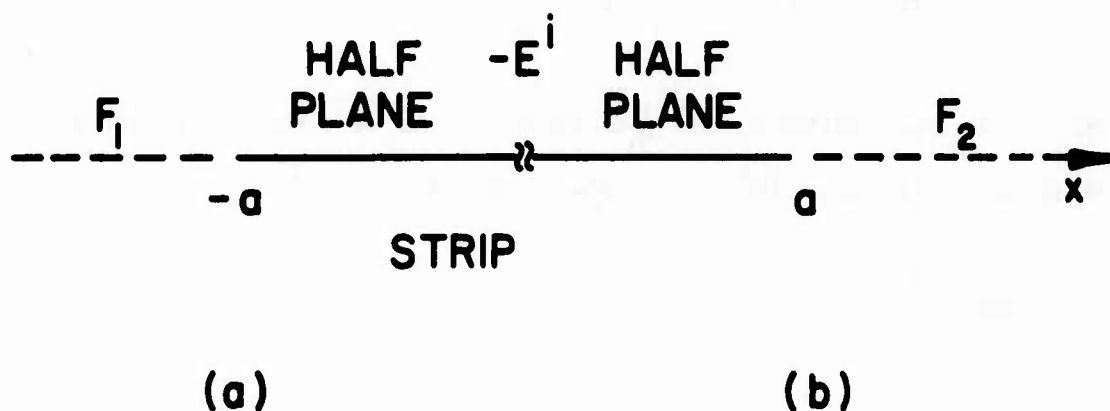
Figure 3.2. $F_1(x)$ can be approximated by the GTD solution to the half-plane problem (a) shown on the left-hand side; $F_2(x)$ can be approximated by the GTD solution to the half-plane problem (b) shown on the right-hand side.

by the induced surface current density to the negative of the tangential component of the incident E-field on the surface of the perfectly conducting scatterer as required by the satisfaction of the boundary condition. Hence, (3.2) is valid on the strip only.

An extended integral equation that is valid for all x can be obtained by including the scattered fields outside the strip as well. If the scattered field on the interval $(-\infty,-a)$ is designated by $F_1(x)$ and the scattered field on the interval (a,∞) is designated by $F_2(x)$, then the extended form of (3.2) becomes [13]

$$\int_{-a}^{a} J_z(x')G(x - x') \, dx' = \theta(-E_z^1(x)) + F_1(x) + F_2(x) \qquad (3.4)$$

where θ is defined in (2.2a).

Since the Fourier transform of the induced surface current density can be related to the far field, (3.4) is Fourier transformed to give

$$\tilde{J}_z(\alpha)\tilde{G}(\alpha) = \widetilde{\theta(-E_z^1)}(\alpha) + \tilde{F}_1(\alpha) + \tilde{F}_2(\alpha) \qquad (3.5)$$

where ~ on top indicates the Fourier transform pair defined in (2.4) which simplifies in the present one-dimensional problem to

$$\tilde{F}(\alpha) = \int_{-\infty}^{\infty} F(x) \, e^{-i\alpha x} \, dx \qquad (3.6a)$$

and

$$F(x) = \frac{1}{2\pi} \int_{-\infty}^{\infty} \tilde{F}(\alpha) \, e^{i\alpha x} \, d\alpha \qquad (3.6b)$$

The Fourier transform of the two-dimensional Green's function in (3.5) takes the form

$$\tilde{G}(\alpha) = \frac{1}{2\sqrt{k_0^2 - \alpha^2}} \quad . \tag{3.7}$$

Note that (3.5) is an algebraic equation in the spectral domain in contrast to the convolution form of the integral equation (3.4) in the spatial domain. The reason for working in the spectral domain will become clear when the method of solution for (3.5) is developed. Following the procedure discussed in Chapter 2 and in terms of the notations introduced in the present problem, we proceed as follows:

1. Obtain $\tilde{J}_z^{(0)}(\alpha)$, the initial approximation of the Fourier transform of the induced surface current density, or equivalently, the scattered *far field* within a known multiplicative constant, as follows:

   1.1. Find the expressions for the first estimate of $\tilde{F}_1^{(0)}(\alpha) + \tilde{F}_2^{(0)}(\alpha)$. Note that GTD may be used to get closed-form expressions for $\tilde{F}_1^{(0)}(\alpha)$ and $\tilde{F}_2^{(0)}(\alpha)$ since $F_1(x)$ and $F_2(x)$ can be approximated by the GTD solutions to the two half-plane problems as shown in Figure 3.2 (page 13). The expressions for $\tilde{F}_1^{(0)}$ and $\tilde{F}_2^{(0)}$ as obtained from GTD read

$$\tilde{F}_1^{(0)}(\alpha) = \frac{1}{2}\left[e^{ikacos\phi_0} \sqrt{8k} \sin\frac{\phi_0}{2}\right] \frac{e^{ia\alpha}}{(\alpha + k \cos\phi_0)\sqrt{\alpha + k}}$$

$$- \frac{ie^{ia(\alpha + k\cos\phi_0)}}{(\alpha + k \cos\phi_0)} \tag{3.8a}$$

and

$$\tilde{F}_2^{(0)}(\alpha) = -\frac{i}{2}\left[e^{-ikacos\phi_0}\sqrt{8k}\cos\frac{\phi_0}{2}\right]\frac{e^{-i\alpha a}}{(\alpha + k\cos\phi_0)\sqrt{k-\alpha}}$$

$$+\frac{ie^{-ia(\alpha+kcos\phi_0)}}{(\alpha + k\cos\phi_0)} \qquad . \qquad (3.8b)$$

Note that these expressions are free of singularities for all α.

    1.2. Solve for the initial approximation of $\tilde{J}_z(\alpha), \tilde{J}_z^{(0)}(\alpha)$, by carrying out the operations shown below:

$$\tilde{J}_z^{(0)}(\alpha) = F\left[\theta\left(F^{-1}\left[\frac{\widetilde{\theta(-E^i)}(\alpha) + \tilde{F}_1^{(0)}(\alpha) + \tilde{F}_2^{(0)}(\alpha)}{\tilde{G}(\alpha)}\right]\right)\right] .$$

  2. Use (2.12) to further improve the solution as necessary.

The check for satisfaction of the integral equation can be applied very simply by computing $\tilde{J}(\alpha)\tilde{G}(\alpha)$, taking its inverse Fourier transform, and verifying how well it approaches $-E^i$ on the surface of the scatterer.

3.4 Numerical Results and Discussions

3.4.1 Normal incidence

Figure 3.3 shows the calculated induced surface current density distribution on the strip with ka = 4 (1.3λ wide) for normal incidence. Note that the current density becomes large at the edges, as it should for E-wave incidence, although no specific condition was enforced at the edges, nor any special care exercised. Note also that the approximate current is confined essentially on the surface of the strip and extends very little outside of this surface. Thus, the solution in this case is very close to the true solution and this is easily verified by truncating the current density, computing the scattered field it radiates on the strip, and verifying that the scattered field is indeed very nearly equal to $-E^i$.
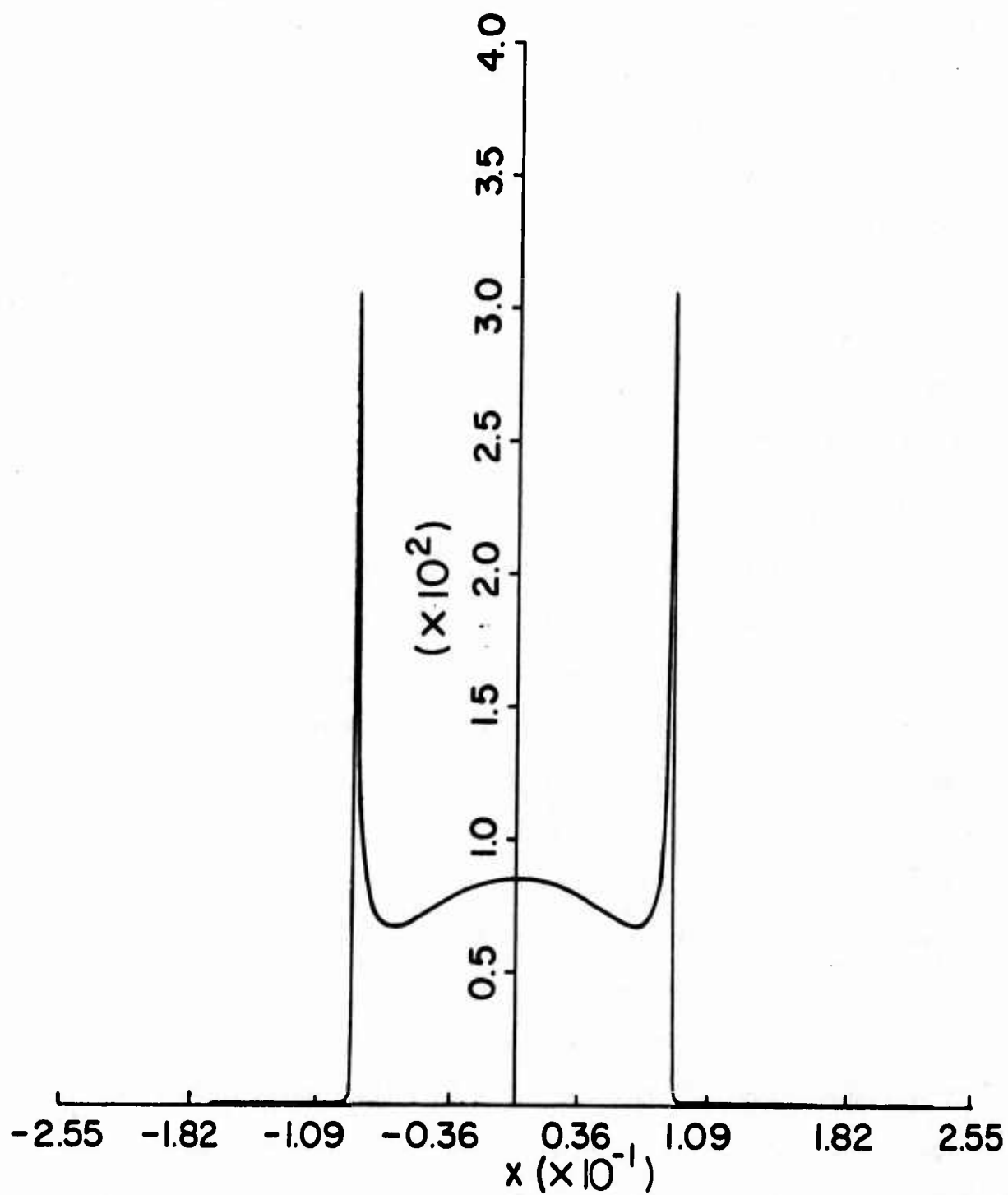
Figure 3.3. Magnitude of the induced surface current density distribution normalized to $(ik_0 Z_0)^{-1}$ on the strip of $ka = 4.$ (1.273λ wide), $\phi_0 = 90^\circ$.

Figure 3.4 depicts the result for ka = 40, i.e., a 13λ strip.
Note that the peak in the center is no longer present and the current
there approaches that given by the physical optics approximation. There
are now more oscillations, however, and the current density has a sharp
dip before rising to infinity at the edges.

Figure 3.5 displays the moment method applied in the spectral do-
main solution [3] and the comparison with the one obtained here is
quite favorable.

Figure 3.6 exhibits the satisfaction of the boundary condition
after one iteration. As mentioned before, such a test is not available
in the conventional GTD approach.

3.4.2 Near grazing incidence

Let us next turn to the interesting case of a near grazing inci-
dence where the zero-order current density has a long tail extending
beyond the edge of the strip (see Figure 3.7). This result is to be
expected since the two half-plane GTD solutions used in the zero-order
approximation represent a poor approximation for the induced current
for shallow incidence angles. If this tail is truncated, the remain-
ing portion of the current density on the strip produces a scattered
field on the surface of the strip which is significantly different from
$-E^1$, as may be seen from Figure 3.8.

Figure 3.9 shows the effect of one iteration on the zero-order
GTD solution shown in Figure 3.7. Note that the current density is
significantly altered in the neighborhood of the shadowed edge demonstra-
ting the fact that even with a relatively poor initial guess, the con-
vergence is quite rapid in this case.
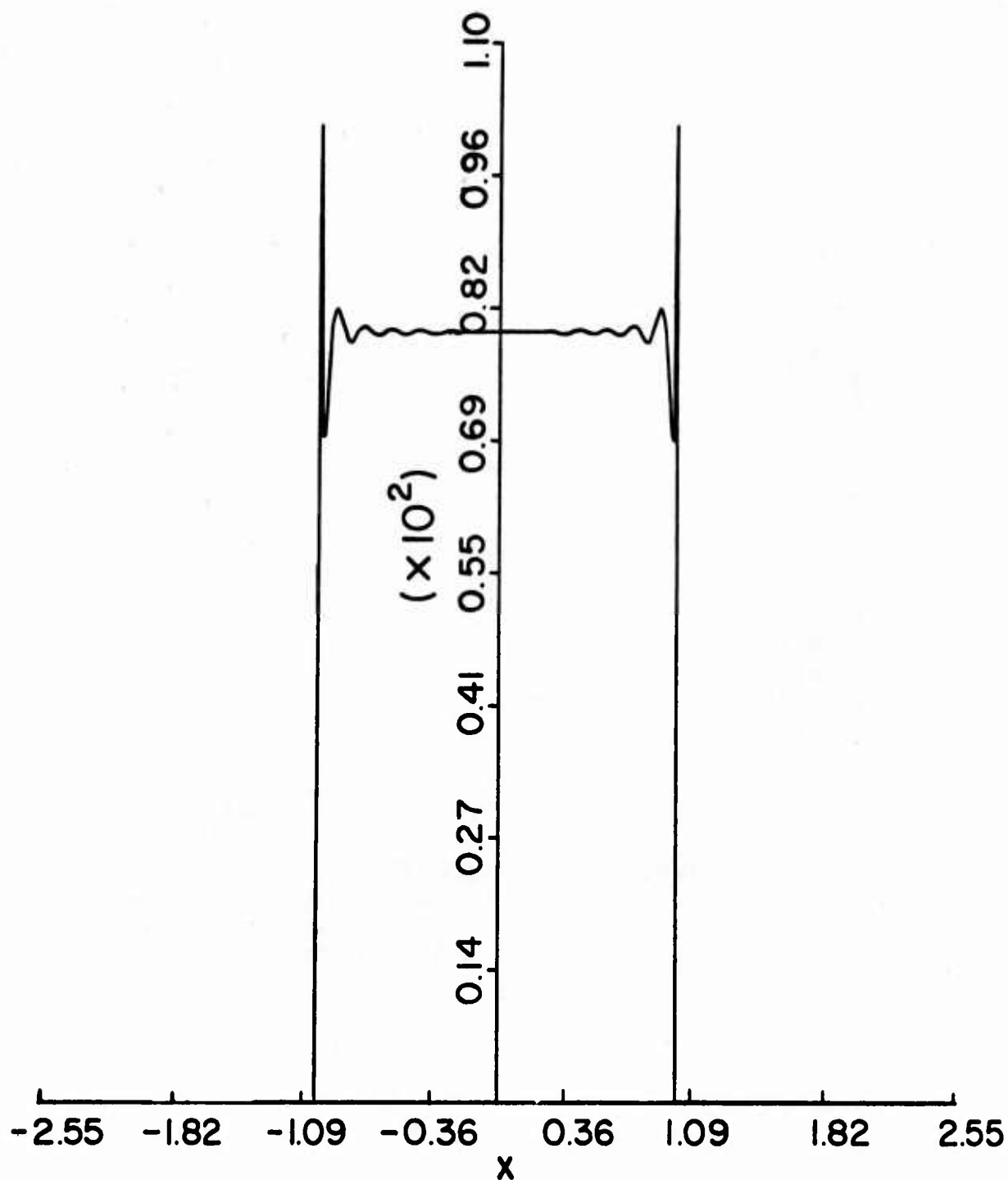
Figure 3.4. Magnitude of the induced surface current density distribution normalized to $(ik_0 Z_0)^{-1}$ on the strip of $ka = 40.$ (12.73λ wide), $\phi_0 = 90^o$.
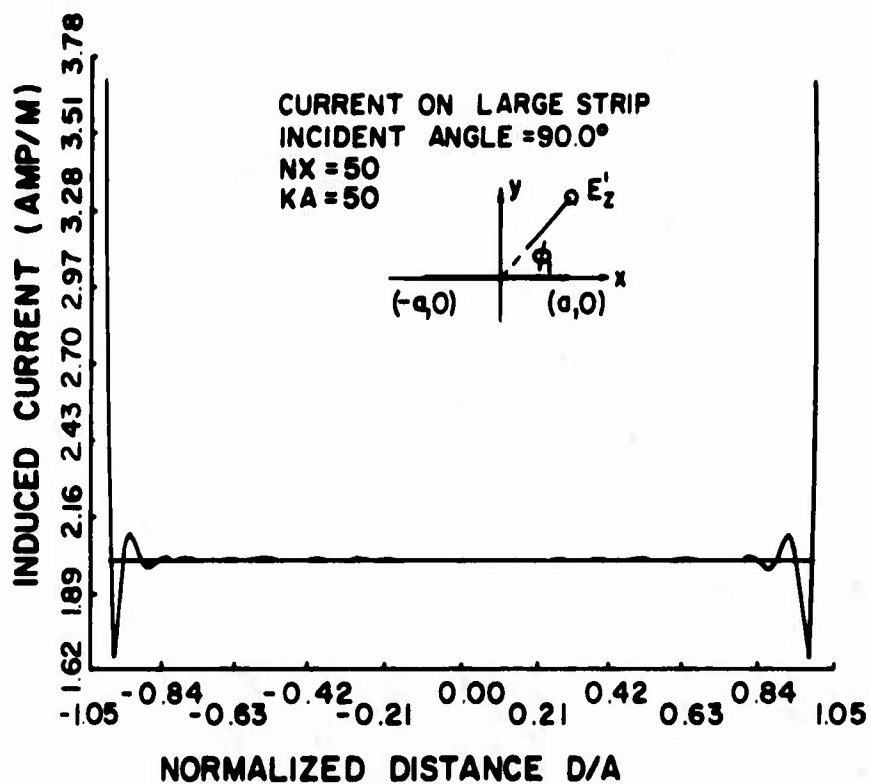
Figure 3.5. Moment method (applied in the spectral domain) solution of the magnitude of the induced surface current density distribution normalized to $1/Z_o$ on the strip of ka = 50. (15.92 λ wide), ϕ_i = 90°.
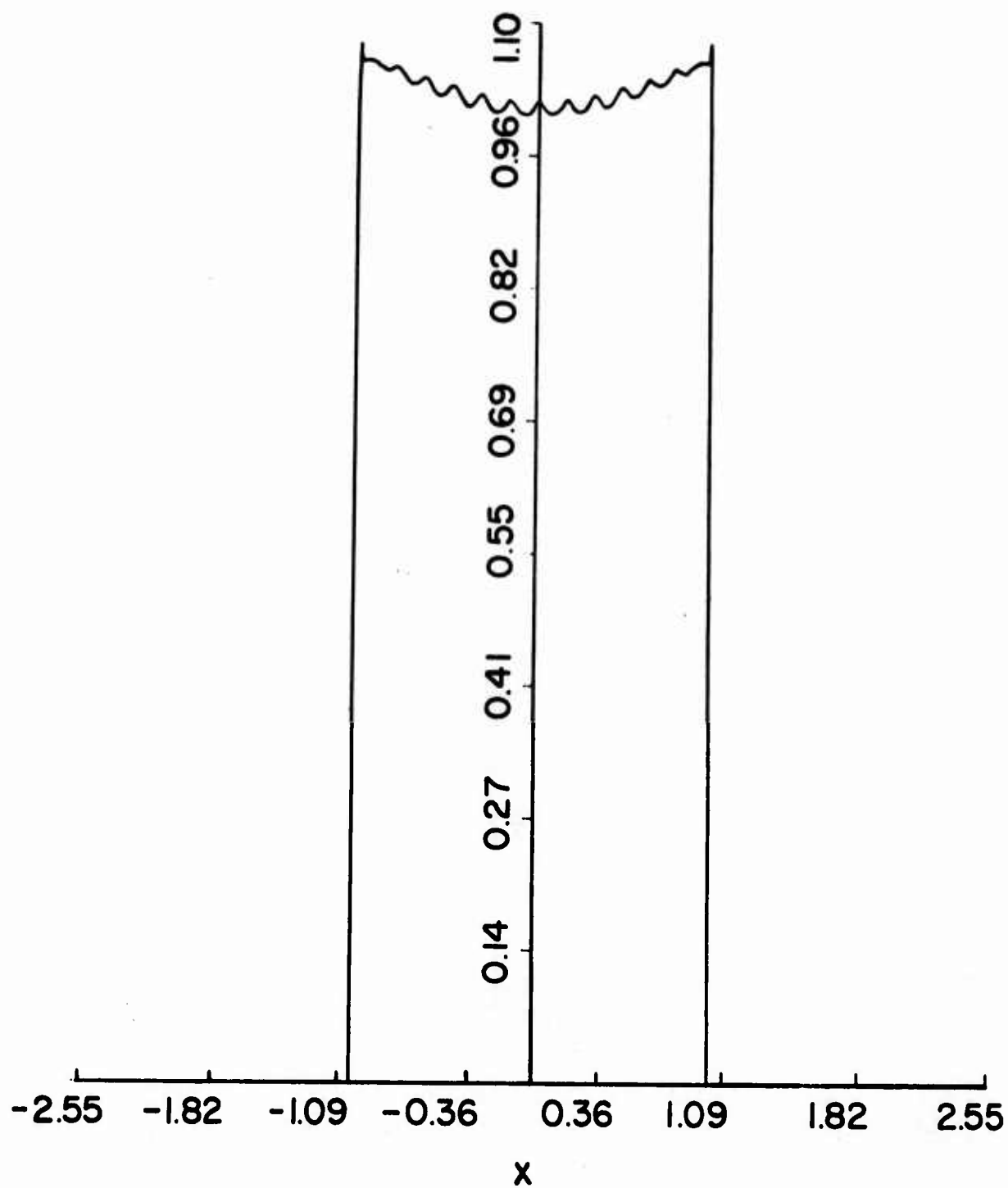
Figure 3.6. Magnitude of the scattered E-field evaluated on the strip of ka = 40., ϕ_0 = 90° (one iteration).
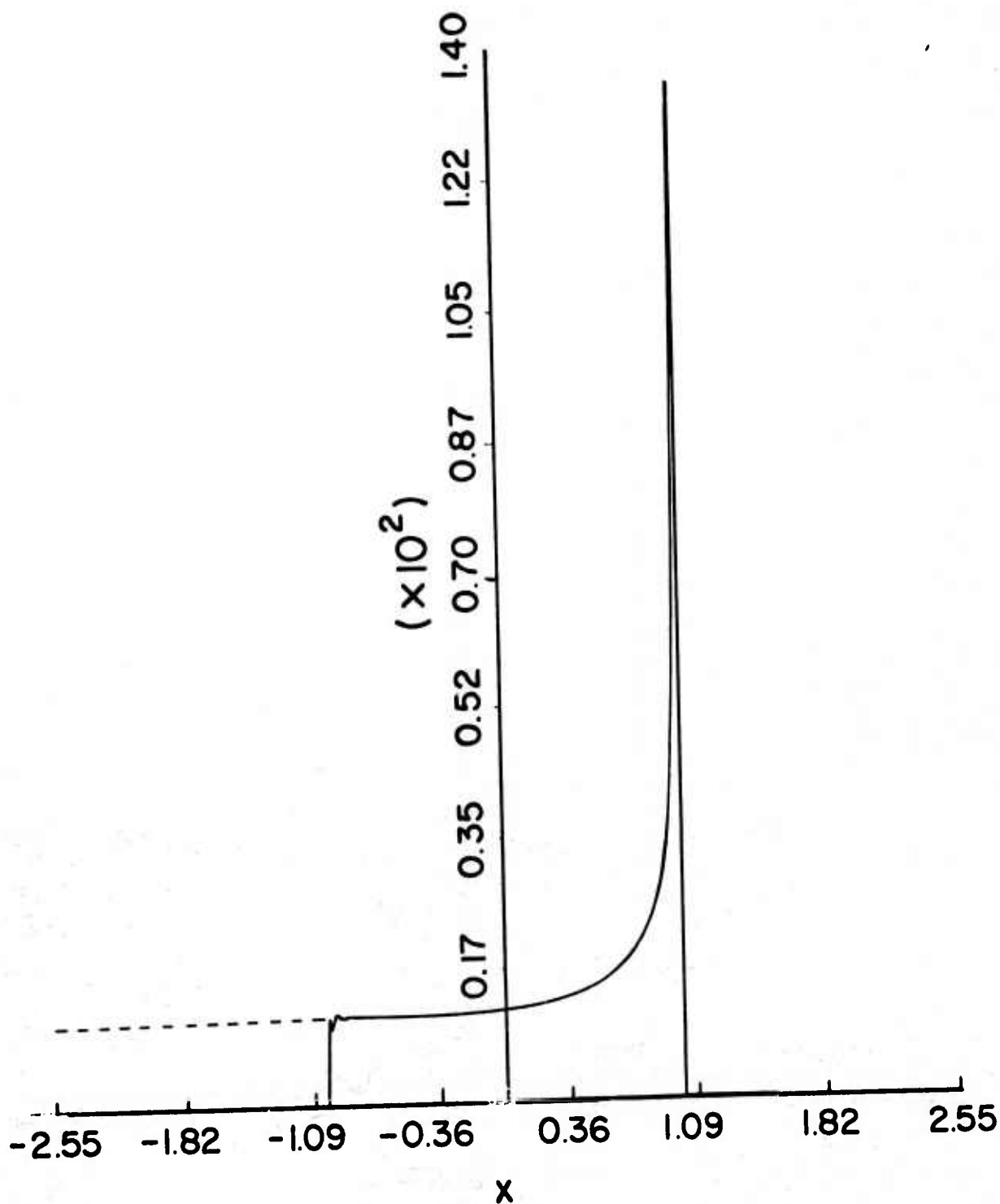
Figure 3.7. Magnitude of the induced surface current density distribution normalized to $(ik_0Z_0)^{-1}$ on the strip of $ka = 40.$, $\phi_0 = 10^o$ (no iteration).
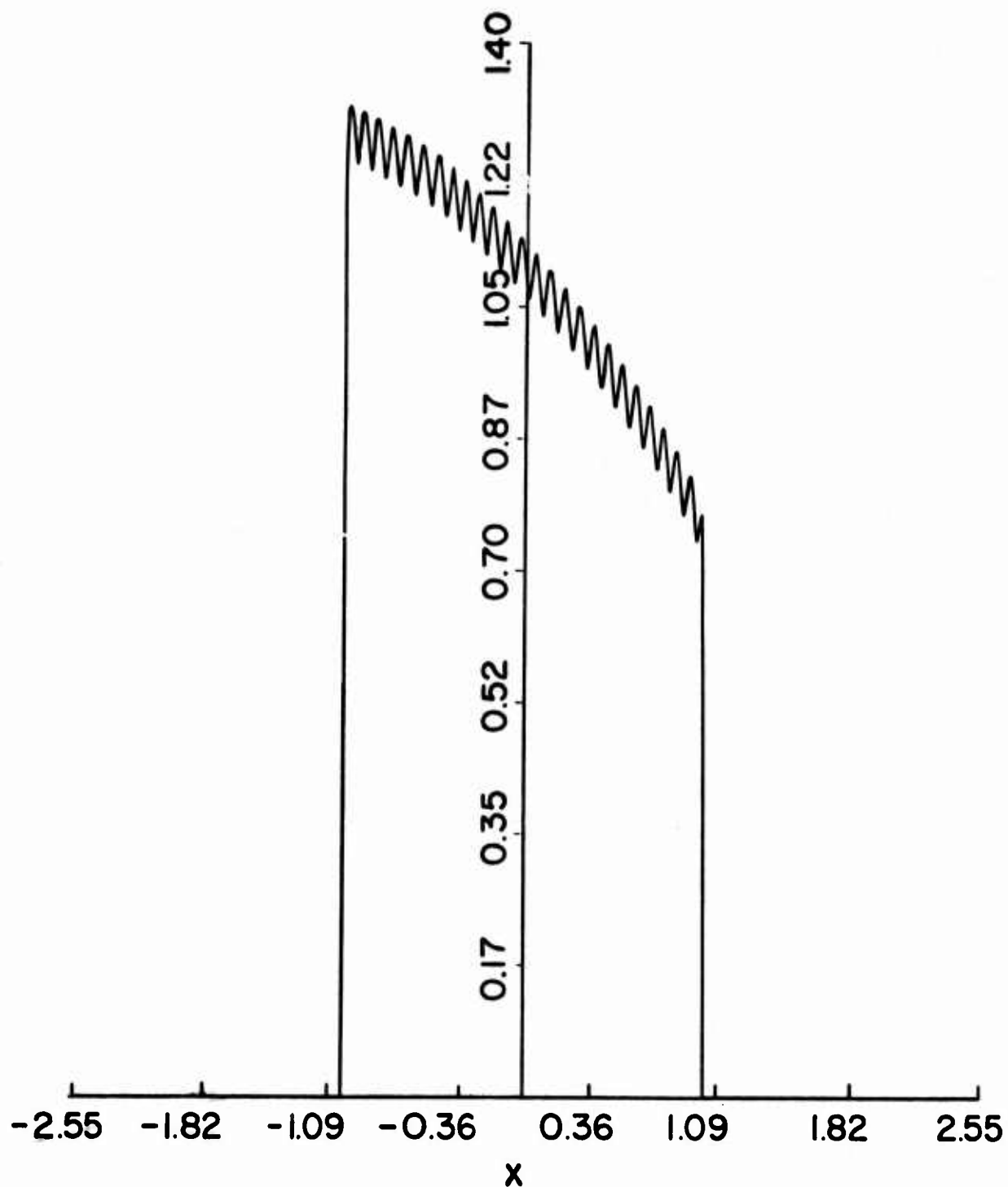
Figure 3.8. Magnitude of the scattered E-field evaluated on the strip of $ka = 40.$, $\phi_0 = 10^o$ (no iteration).
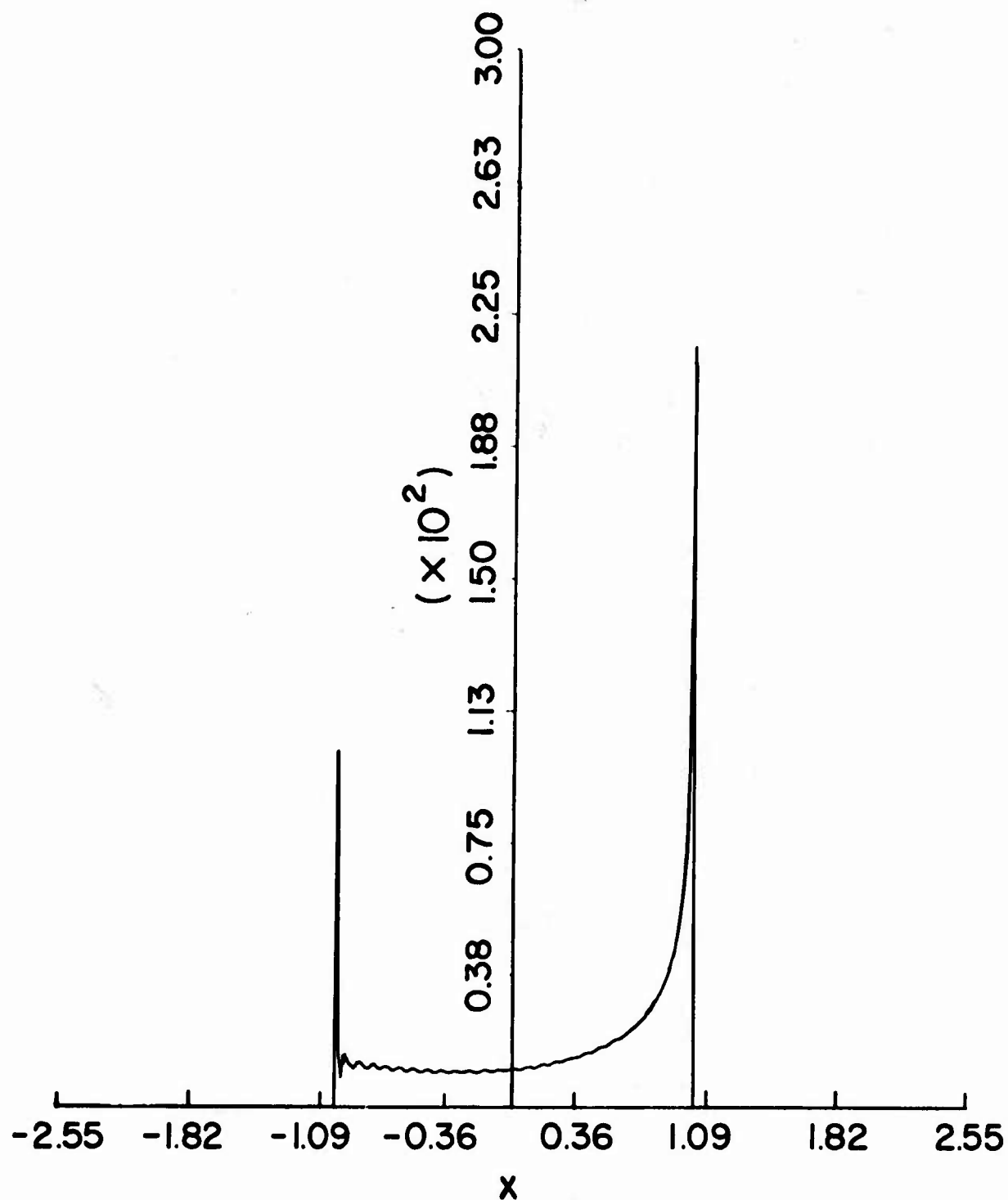
Figure 3.9. Magnitude of the induced surface current density distribution normalized to $(ik_0 Z_0)^{-1}$ on the strip of $ka = 40.$, $\phi_0 = 10^o$ (one iteration).

To see that this is indeed an improved solution, the truncated portion of it is used to calculate the scattered field. It is observed that the satisfaction of the boundary condition has been improved as shown in Figure 3.10.

To verify the convergence of the solution numerically, one more iteration is performed and the result is depicted in Figure 3.11. Note that the shape of the surface current density does not change much which indicates a settling down of the solution has occurred. Also, note that the tail extending outside of the strip has been reduced to an insignificant quantity, which, when truncated, will produce little effect on the scattered field on the surface of the strip.

To further validate the solution, the moment method solution [3] of the same problem with slightly different parameters is shown in Figure 3.12 for a comparison. Again, the agreement is good. However, in terms of computational efficiency, the present method is far superior to the moment-method solution for the accuracy realized.

3.5 Summary

Before closing this chapter, it is worthwhile to recapitulate the main points of the approach discussed. The strip problem has been solved by a combination of the integral equation and asymptotic high-frequency techniques. Formulation of the integral equation in the Fourier transform domain allows one to conveniently obtain the zero-order approximation to the transformed unknown surface current density from the solution of two half-plane problems.
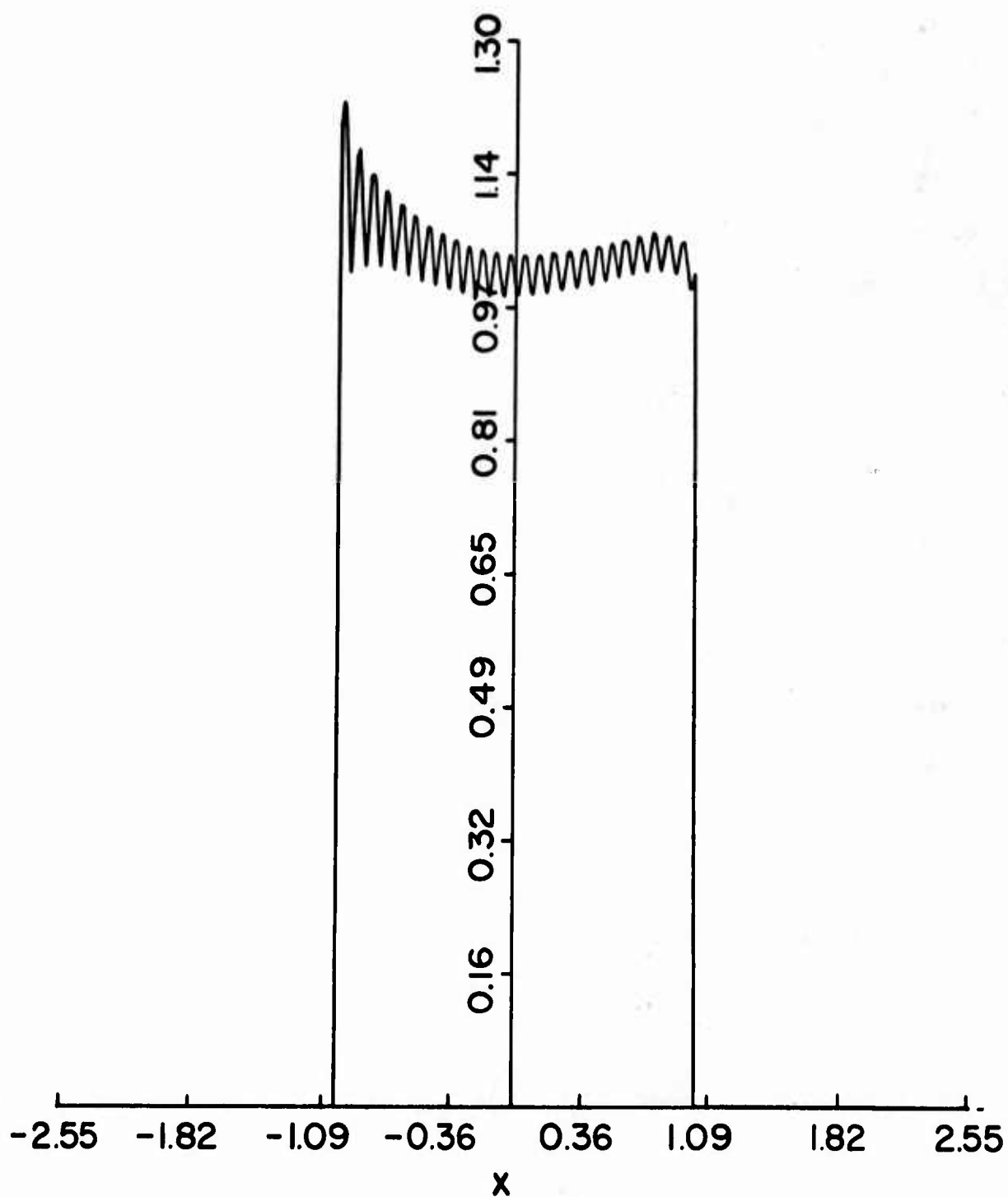
Figure 3.10. Magnitude of the scattered E-field evaluated on the strip of ka = 40., ϕ_0 = 10° (one iteration).
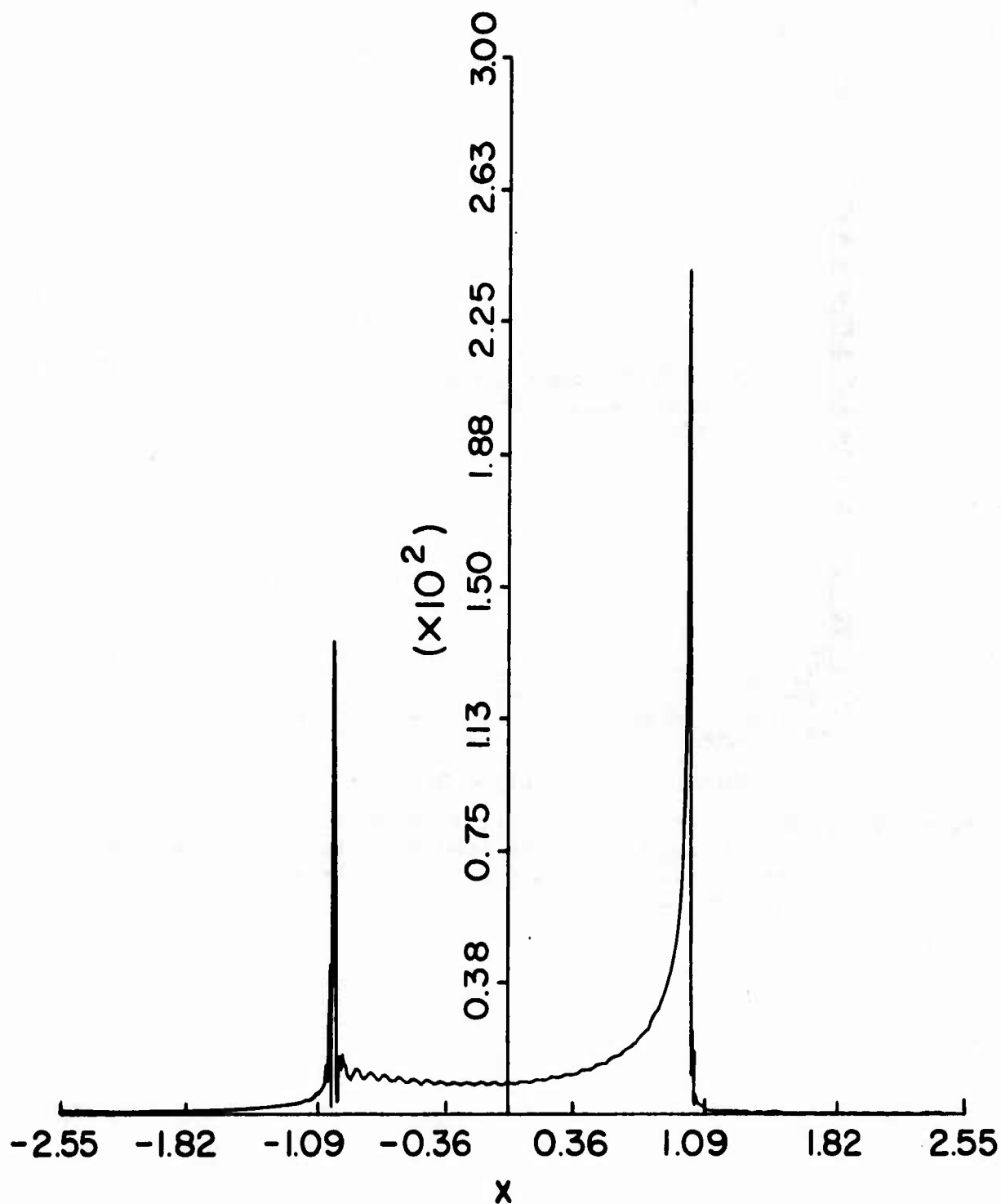
Figure 3.11. Magnitude of the induced surface current density distribution normalized to $(ik_0Z_0)^{-1}$ on the strip of $ka = 40.$, $\phi_0 = 10^{\circ}$ (two iterations).
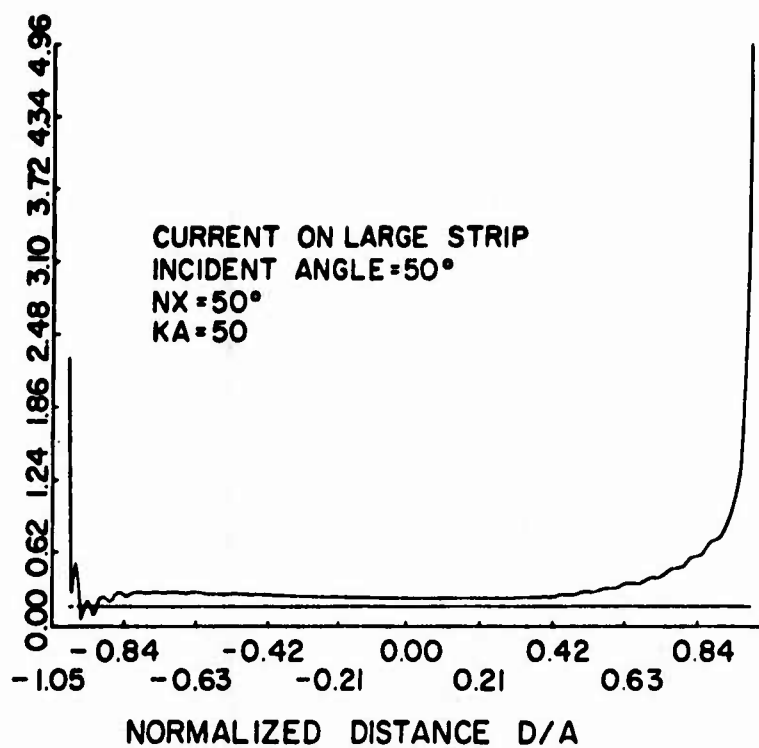
Figure 3.12. Moment method (applied in the spectral domain) solution of the magnitude of the induced surface current density distribution normalized to $1/Z_o$ on the strip of $ka = 50.$, $\phi_o = 5^o$.

Higher-order solutions have been obtained via the iteration steps outlined above and the numerical convergence has been demonstrated. The iteration process generates the proper edge singularities even when they are not present in the original approximation, e.g., physical optics. However, additional iterations are necessary in that case. Validity of the solution has been substantiated by numerically verifying the satisfaction of the boundary condition.

4. DIFFRACTION BY A FINITE THIN PLATE

4.1 Introduction

Having illustrated the usefulness of the hybrid technique for com-
bining the integral equation and GTD techniques relevant to a two-
dimensional scatterer, viz., the strip, we now turn to the more general
three-dimensional problem, a thin rectangular plate illuminated by a
plane wave. This problem was chosen for the following reasons: In
the plate problem, the difficulty in applying GTD to this geometry stems
from the fact that the diffraction coefficient for the corners of the
plate is not known and neglecting the corner effects can cause sub-
stantial errors in the resonance frequency region where the plate size
is of the order of one wavelength squared.

Before we discuss the present approach to solve the plate problem,
we would like to mention two other approaches [14], [4] that are based
on a combination of asymptotic and integral equation techniques. The
one developed by Thiele [14] decomposes a given problem into two parts,
one of which is handled using the GTD method and the other using the
moment method. For the case of a wire antenna on a finite ground plane,
the effect of the edge diffraction from the ground plane is evaluated
using GTD and the result is subsequently used to augment the impedance
matrix of the monopole antenna over an infinite ground plane. Although
the method works rather well when GTD results are accurately known for
the ground plane problem, e.g., a ground plane of circular shape, no
convenient means is available for improving the solution when there are
corners in the plane that contribute substantially to the scattered field.
The latter situation arises when the ground plane is of rectangular shape
and is not large compared to the wavelength, or when the antenna is
mounted close to one or more of the edges.

The second method developed by Burnside [4] tends to rectify the situation alluded to above by solving for surface currents via the moment method in the regions where the GTD solution is not accurate, and by using asymptotic forms for the surface currents in regions where a good approximation for these currents can be employed. However, this method cannot be conveniently applied to either the strip problem with grazing incidence, or to the large plate problem discussed in this thesis. For the strip problem, the GTD solution is quite inaccurate when the incident angle of the illuminating wave is near grazing. For the plate problem, the current does not settle down to known asymptotic form in the center region of the plate until it is at least three to four wavelengths squared. The moment method is incapable of handling the number of unknowns required to accurately solve for the current distribution on plate sizes that are larger than 2λ squared.

In the following sections, we present a new approach using the iteration method developed in Chapter 2 to demonstrate that a successful computation of the induced surface currents on the plate is not only feasible, but also numerically efficient.

4.2 Iteration Method Applied to the Plate Problem

For the sake of simplicity we consider only the case of an x-polarized uniform plane wave which is normally incident on a square thin plate. The geometry of the problem is depicted in Figure 4.1, where the plate is located in the z = 0 plane.

Using classical electromagnetic theory, the following coupled integro-differential equations for the current components J_x and J_y are readily obtained:
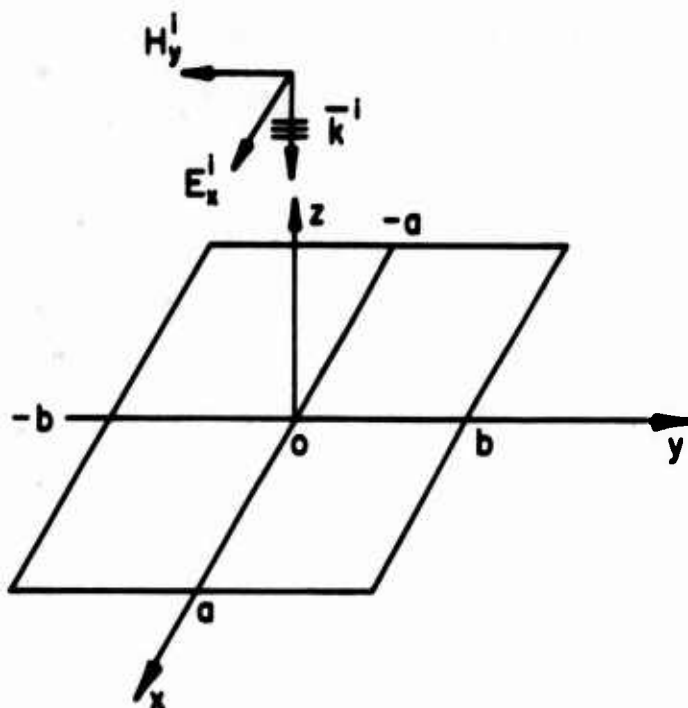
Figure 4.1. Diffraction by a finite rectangular thin plate illuminated by a normally incident plane wave with polarization as shown.
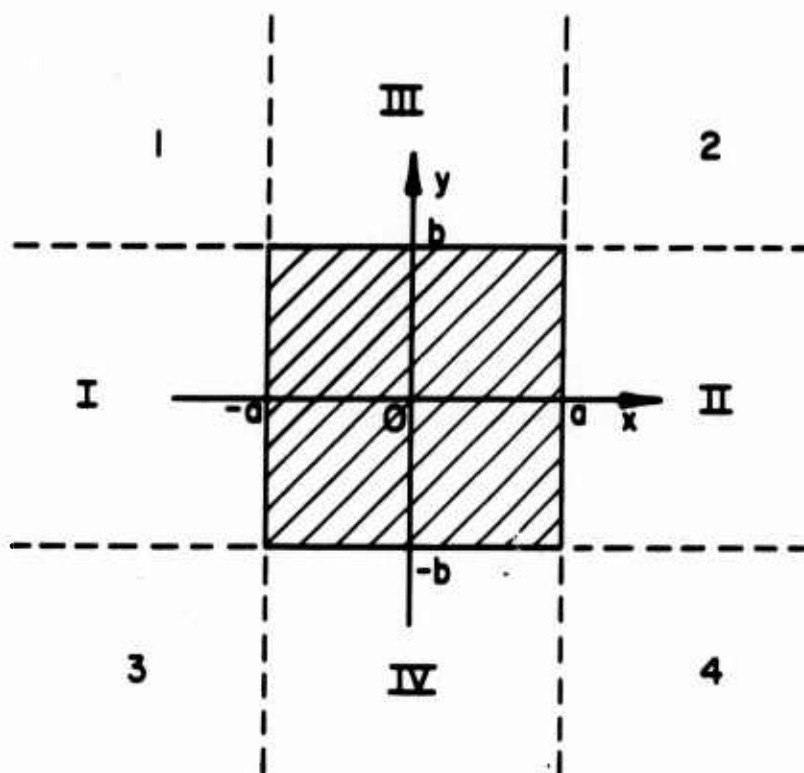
Figure 4.2. Regions in the z = 0 plane in each of which the zero-order approximation of the scattered field is obtained according to Table 4.1.

$$\left(\frac{\partial^2}{\partial x^2} + k^2\right) A_x(x,y) + \frac{\partial^2}{\partial x \partial y} A_y(x,y) = i\omega\epsilon_0 E_x^1(x,y) \tag{4.1a}$$

and

$$\left(\frac{\partial^2}{\partial y^2} + k^2\right) A_y(x,y) + \frac{\partial^2}{\partial x \partial y} A_x(x,y) = 0 \tag{4.1b}$$

where $x \in (-a,a)$, $y \in (-b,b)$, and $z = 0$. A_x and A_y in (4.1a) and (4.1b) are the x- and the y-components of the magnetic vector potential, respectively, containing the unknowns J_x, J_y implicitly.

Since the convolution of the induced surface current density with the free-space Green's function gives the magnetic vector potential, we have the expressions which are valid in the z = 0 plane

$$A_x(x,y) = J_x(x,y) * G(x,y) \tag{4.2a}$$

and

$$A_y(x,y) = J_y(x,y) * G(x,y) \tag{4.2b}$$

where * denotes the convolution operation and the free-space Green's function is given by

$$G(x - x', y - y') = \frac{1}{4\pi} \frac{\exp(ikr)}{r} \tag{4.3}$$

where

$$r = \sqrt{(x - x')^2 + (y - y')^2} , \quad z, z' = 0 \quad .$$

Note that (4.1a), (4.1b) are conventional integro-differential equations which are valid on the plate only. To obtain an extended form of these equations, additional unknown functions $F_x(x,y)$ and $F_y(x,y)$ will be introduced. The domain of these functions is the region complementary to the plate in the $z = 0$ plane. Hence, the extended form of (4.1a), (4.1b) can be written as

$$\left(\frac{\partial^2}{\partial x^2} + k^2\right)A_x(x,y) + \frac{\partial^2}{\partial x \partial y} A_y(x,y) = -i\omega\varepsilon_0\left(-\theta(E_x^i(x,y))\right.$$
$$\left. + \hat{\theta}(F_x(x,y))\right) \tag{4.4a}$$

and

$$\left(\frac{\partial^2}{\partial y^2} + k^2\right)A_y(x,y) + \frac{\partial^2}{\partial x \partial y} A_x(x,y) = -i\omega\varepsilon_0\hat{\theta}(F_y(x,y)) \tag{4.4b}$$

where θ and $\hat{\theta}$ are operators defined in (2.2a) and (2.2b), respectively. Note that (4.4a), (4.4b) are valid for the entire $z = 0$ plane. These equations are now Fourier transformed to obtain

$$(\alpha^2 - k^2)\tilde{J}_x(\alpha,\beta)\tilde{G}(\alpha,\beta) + \alpha\beta\tilde{J}_y(\alpha,\beta)\tilde{G}(\alpha,\beta)$$

$$= \frac{ik_0}{Z_0}\left(\widetilde{-\theta(E_x^i)}(\alpha,\beta) + \widetilde{\hat{\theta}(F_x)}(\alpha,\beta)\right) \tag{4.5a}$$

and

$$(\beta^2 - k^2)\tilde{J}_y(\alpha,\beta)\tilde{G}(\alpha,\beta) + \alpha\beta\tilde{J}_x(\alpha,\beta)\tilde{G}(\alpha,\beta) = \frac{ik_0}{Z_0}\widetilde{\hat{\theta}(F_y)}(\alpha,\beta) \tag{4.5b}$$

where ~ on top indicates the Fourier transform as defined in (3.6a) with transform variables (α, β) corresponding to (x,y), respectively, and $Z_0 = \sqrt{\mu_0/\varepsilon_0}$ is the free-space impedance. In writing (4.5a) and (4.5b), (4.2a) and (4.2b) have been utilized. The Fourier transform of the free-space Green's function, specialized to the $z = 0$ plane as given in (4.3), is

$$\tilde{G}(\alpha,\beta) = \frac{1}{2} \cdot \frac{1}{\sqrt{k_0^2 - \alpha^2 - \beta^2}} \quad . \tag{4.6}$$

Observe that (4.5a), (4.5b) are two algebraic equations in the transform domain as opposed to the two integro-differential equations in (4.4a) and (4.4b). It is a simple step to derive the zero-order solutions of $\tilde{J}_x(\alpha,\beta)$ and $\tilde{J}_y(\alpha,\beta)$ once the estimates of $\widetilde{\hat{\theta}(F_x)}(\alpha,\beta)$ and $\widetilde{\hat{\theta}(F_y)}(\alpha,\beta)$ are available. One merely solves the two coupled algebraic equations for these two unknowns $\tilde{J}_x(\alpha,\beta)$ and $\tilde{J}_y(\alpha,\beta)$. For the present case, $\hat{\theta}(F_y)(x,y)$ is zero due to the particular choice of $\hat{x}$-polarized normal incident plane-wave illumination. With this in mind, the first-order solutions of the transformed surface current density can be expressed as

$$\tilde{J}_x(\alpha,\beta) = \frac{2}{\sqrt{k_0^2 - \alpha^2 - \beta^2}} \left[\frac{\beta^2 - k_0^2}{k_0 Z_0}\right] [-\widetilde{\theta(E_x^1)}(\alpha,\beta) + \widetilde{\hat{\theta}(F_x)}(\alpha,\beta)] \tag{4.7a}$$

and

$$\tilde{J}_y(\alpha,\beta) = \frac{-2}{\sqrt{k_0^2 - \alpha^2 - \beta^2}} \left[\frac{\alpha\beta}{k_0 Z_0}\right] [-\widetilde{\theta(E_x^1)}(\alpha,\beta) + \widetilde{\hat{\theta}(F_x)}(\alpha,\beta)] \quad . \tag{4.7b}$$

$\tilde{J}_x(\alpha,\beta)$ and $\tilde{J}_y(\alpha,\beta)$ are then inverse Fourier-transformed and truncated to obtain the induced surface current densities on the plate.

Next, we estimate the zero-order approximation to $\hat{\theta}(F_x)(x,y)$ using the GTD solutions to four pertinent half-plane problems. The $z = 0$ plane containing the plate has been divided into regions as shown in Figure 4.2 (page 32), where the hatched region is occupied by the plate and the scattered field in this region must be equal to the $-\theta(E^1(x,y))$ to satisfy the boundary condition. The rest of the $z = 0$ plane has been designated by digital numbers and Roman numerals, and the manner in which the scattered fields in these various regions are obtained is concisely tabulated in Table 4.1.

TABLE 4.1

THE ZERO-ORDER APPROXIMATION OF $\hat{\theta}(F_x(x,y))$ IN VARIOUS REGIONS
EXTERNAL TO THE PLATE OBTAINED VIA THE USE OF GTD METHOD

Region	Scattered Field	Remarks
I, II	$E_x(x,z = 0)$	Derived from H-wave strip GTD solution
III, IV	$E_x(y,z = 0)$	Derived from E-wave strip GTD solution
1, 2, 3, 4	0	First estimate

In deriving the zero-order approximation, the *scattered* fields in regions 1, 2, 3 and 4 are neglected although these fields are nonzero in higher-order approximations.

The zero-order approximation to the scattered fields is computed in Regions III and IV, by starting with the E-wave GTD solution for the strip, and truncating it so that it is nonzero only in these regions. In particular,

$$\tilde{F}_{III} = \left\{ -i\sqrt{k}\ \frac{e^{-i\beta b}}{\beta\sqrt{k-\beta}} + i\ \frac{e^{-ib\beta}}{\beta} \right\} \frac{2\ \sin(\alpha a)}{\alpha} \tag{4.8a}$$

and

$$\tilde{F}_{IV} = \left\{ i\sqrt{k}\ \frac{e^{ib\beta}}{\beta\sqrt{\beta+k}} - i\ \frac{e^{ib\beta}}{\beta} \right\} \frac{2\ \sin(\alpha a)}{\alpha} \quad . \tag{4.8b}$$

In Regions I and II, the H-wave GTD solution for a strip is used to obtain $H_y(x, z = 0)$, and then $E_x(x, z = 0)$ is constructed from Maxwell's equations. The resulting solution is again truncated so that it is nonzero only in the appropriate regions. In particular,

$$\tilde{F}_{I} = \left\{ \frac{-i\sqrt{k+\alpha}}{\sqrt{k}}\ \frac{e^{ia\alpha}}{\alpha} + \frac{i\sqrt{k^2-\alpha^2}}{k}\ \frac{e^{ia\alpha}}{\alpha} \right\} \frac{2\ \sin(\beta b)}{\beta} \tag{4.9a}$$

and

$$\tilde{F}_{II} = \left\{ \frac{i\sqrt{k-\alpha}}{\sqrt{k}}\ \frac{e^{-ia\alpha}}{\alpha} - \frac{i\sqrt{k^2-\alpha^2}}{k}\ \frac{e^{-ia\alpha}}{\alpha} \right\} \frac{2\ \sin(\beta b)}{\beta} \tag{4.9b}$$

Having completed the estimation of the zero-order approximation to the scattered field $\hat{\theta}(F_x(x,y))$ external to the plate, we now proceed to solve for the induced surface current on the plate. To this end we return to (4.7a) and (4.7b) and substitute the Fourier transform of $\hat{\theta}(F_x(x,y))$ and compute $\tilde{J}_x$ and $\tilde{J}_y$. The desired induced surface current densities in the space domain are then obtained by inverse Fourier

transformation and truncation. If necessary, the iteration scheme discussed in the previous sections can be followed to obtain higher-order solutions. Convergence of the solution can be checked by performing one more iteration and checking to see whether the solution has "settled down." Validity of the solution can be assured by computing the scattered field on the plate using the solution of the surface current just obtained to see how well the boundary condition is satisfied on the surface of the plate. It should be clear now that all of these steps follow exactly the same line as in the case of the strip problem discussed in Chapter 3.

4.3 Numerical Results and Discussions

The numerical result for the dominant x-component of the surface current density for a one-wavelength squared plate is shown in Figure 4.3a. Note that the surface current density, which goes to zero at the two edges perpendicular to the incident electric intensity vector, tends to grow without bound at the other two edges parallel to the incident electric intensity vector, although no special edge condition has been enforced to derive this behavior. To see that edge behavior better, a 90° rotation of the surface current in Figure 4.3a is shown in Figure 4.3b. It is clearly seen from Figure 4.3b that the cross section of the x-component of the surface current density at $x = 0$ closely resembles the surface current on the strip plotted in Figure 3.3.

Figures 4.4a, 4.4b, and 4.4c exhibit the change in the behavior of the current distribution both in the middle of the plate and at the corners as the plate size is progressively increased.
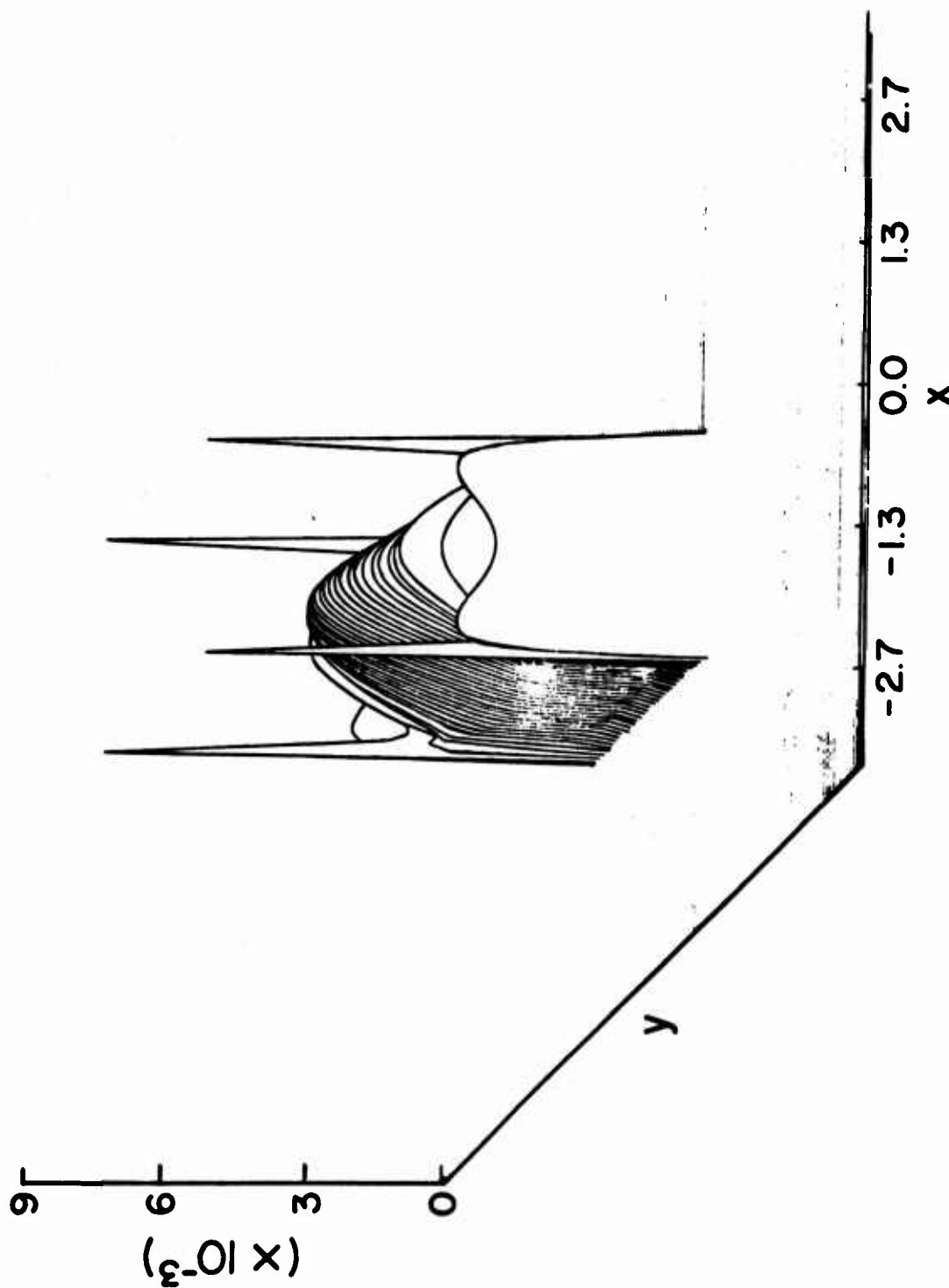
Figure 4.3a. Magnitude of the dominant x-component of the surface current density on a 1λ x 1λ plate (ka = 3.14) with normal incidence; plate region: xε(-1,1), yε(-1,1).
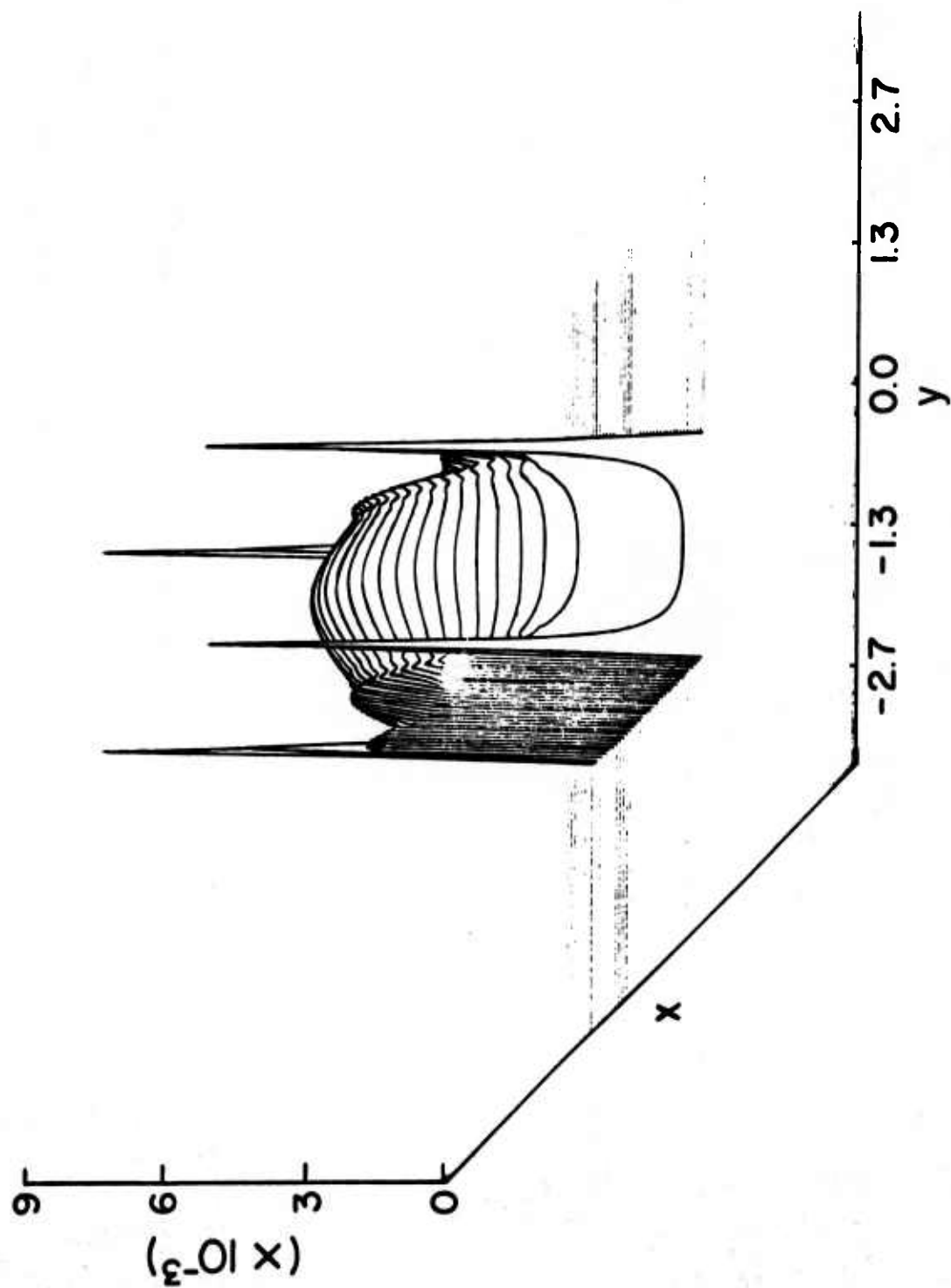
Figure 4.3b. A 90° rotation of the surface current in Figure 4.3a.
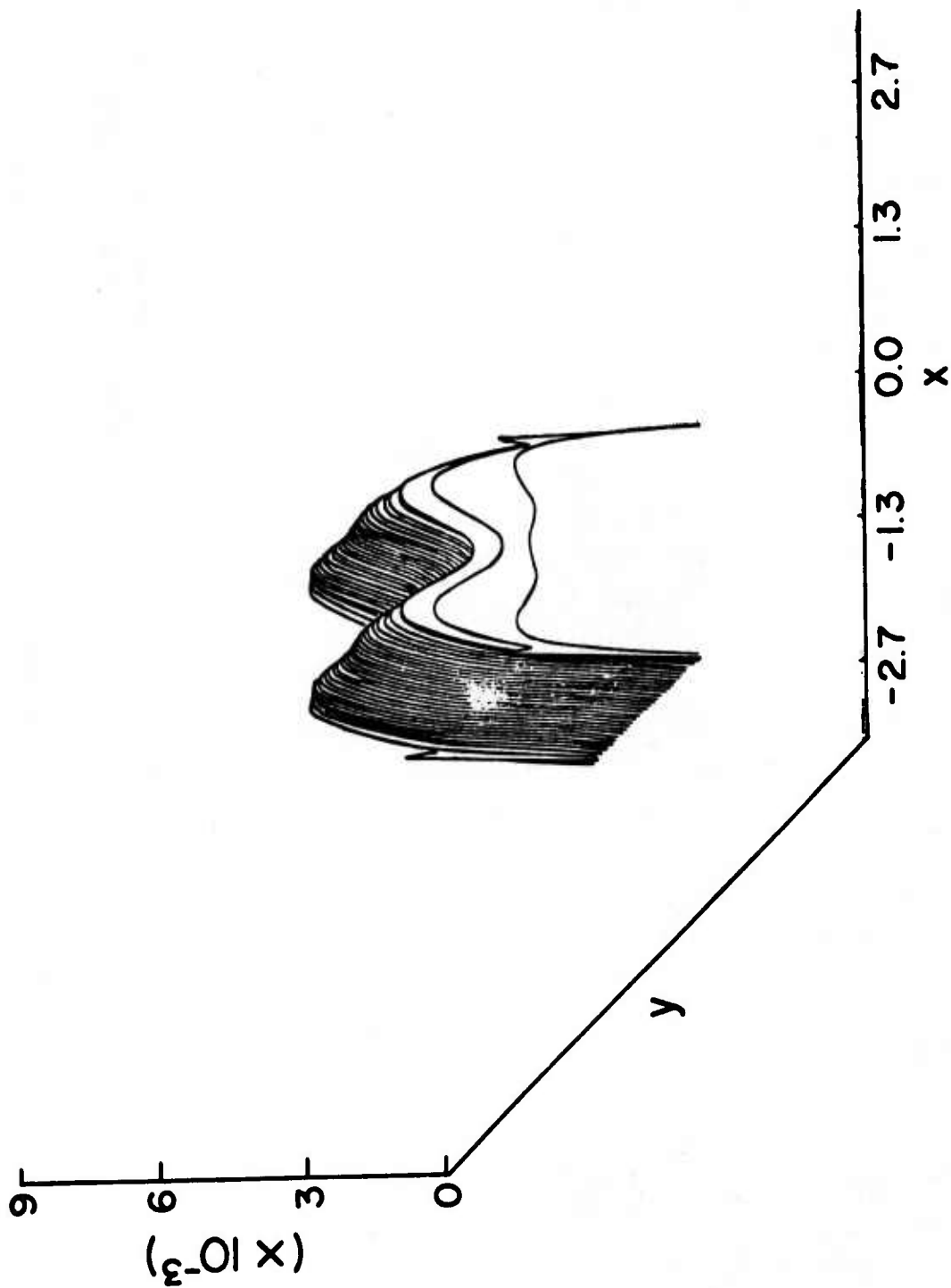
Figure 4.4a. Magnitude of the dominant x-component of the surface current density on a 2λ x 2λ plate (ka = 6.28); plate region: xε(-1,1), yε(-1,1), normal incidence with x-polarization.
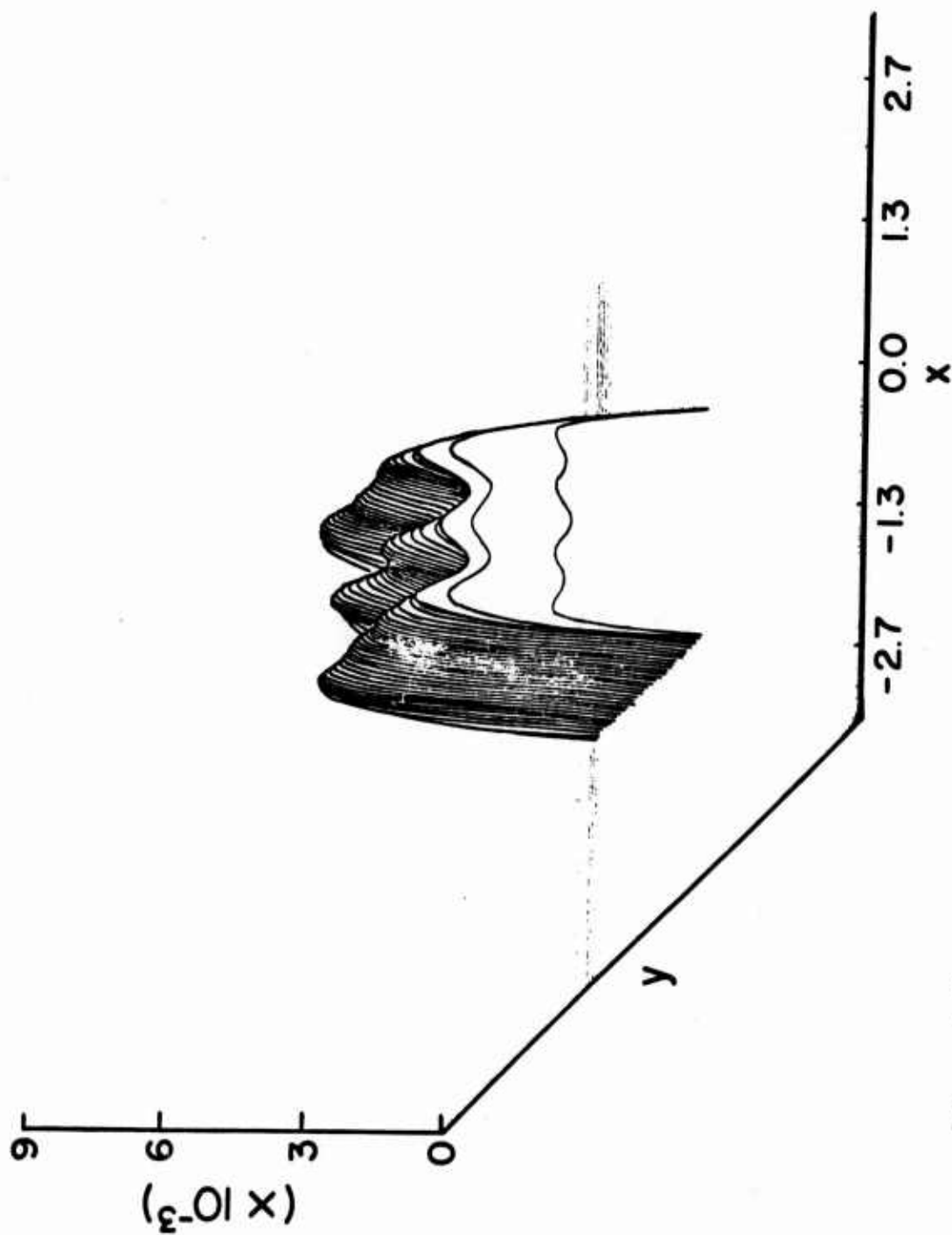
Figure 4.4b. Magnitude of the dominant x-component of the surface current density on a 3λ x 3λ plate (ka = 9.43); plate region: xε(-1,1), yε(-1,1), normal incidence with x-polarization.
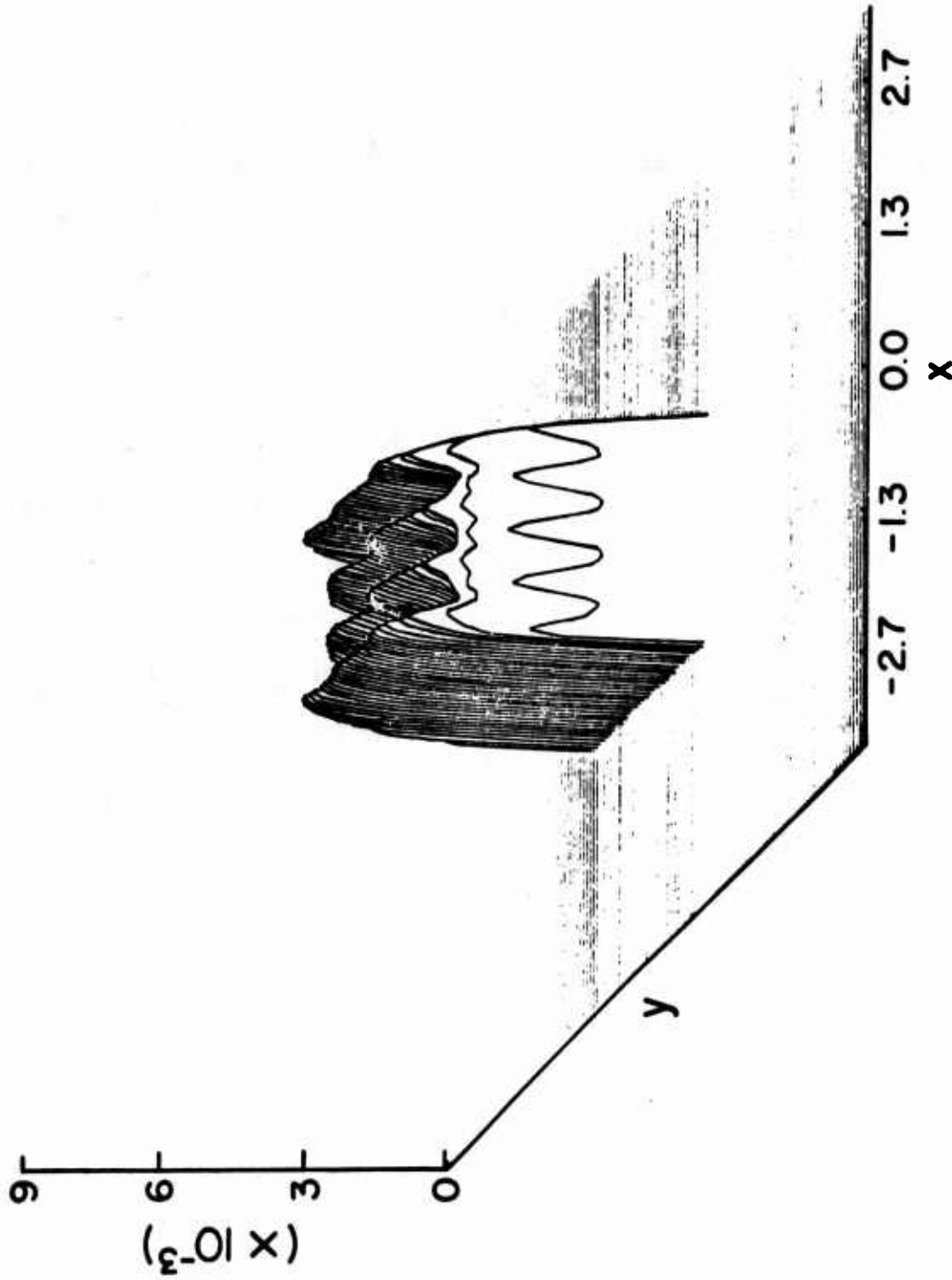
Figure 4.4c. Magnitude of the dominant x-component of the surface current density on a $4\lambda \times 4\lambda$ plate ($ka = 12.6$); plate region: $x\epsilon(-1,1)$, $y\epsilon(-1,1)$, normal incidence with x-polarization.

The corner singularities, which are highly localized, appear to be present only for relatively small sized plates where corner-corner interactions may play a significant role. It has not been possible to verify the correctness of the behavior of the solution at the corners since no reliable analytical or umerical solutions for the corner problem are available at this time.

Figures 4.5a and 4.5b show the cross-polarized component of the surface current density on the plate. This current density goes to zero at the line of symmetry in the middle of the plate and has a tendency to grow without bound at the edges. The results for the one-wavelength squared plate have been checked by moment-method solutions and the agreement is good. For such an electrically small plate, results are available for comparison in the literature [15], [16]. However, for electrically large plates the matrix size becomes prohibitively large when the conventional moment method type of approach is used. In contrast, the accuracy and the convergence of the solution improve even further for a large scatterer. It should also be mentioned that the number of grid points at which the current density of the plate has been evaluated is 2048. Such fine details of the current behavior would also be impractical to obtain using the moment method.
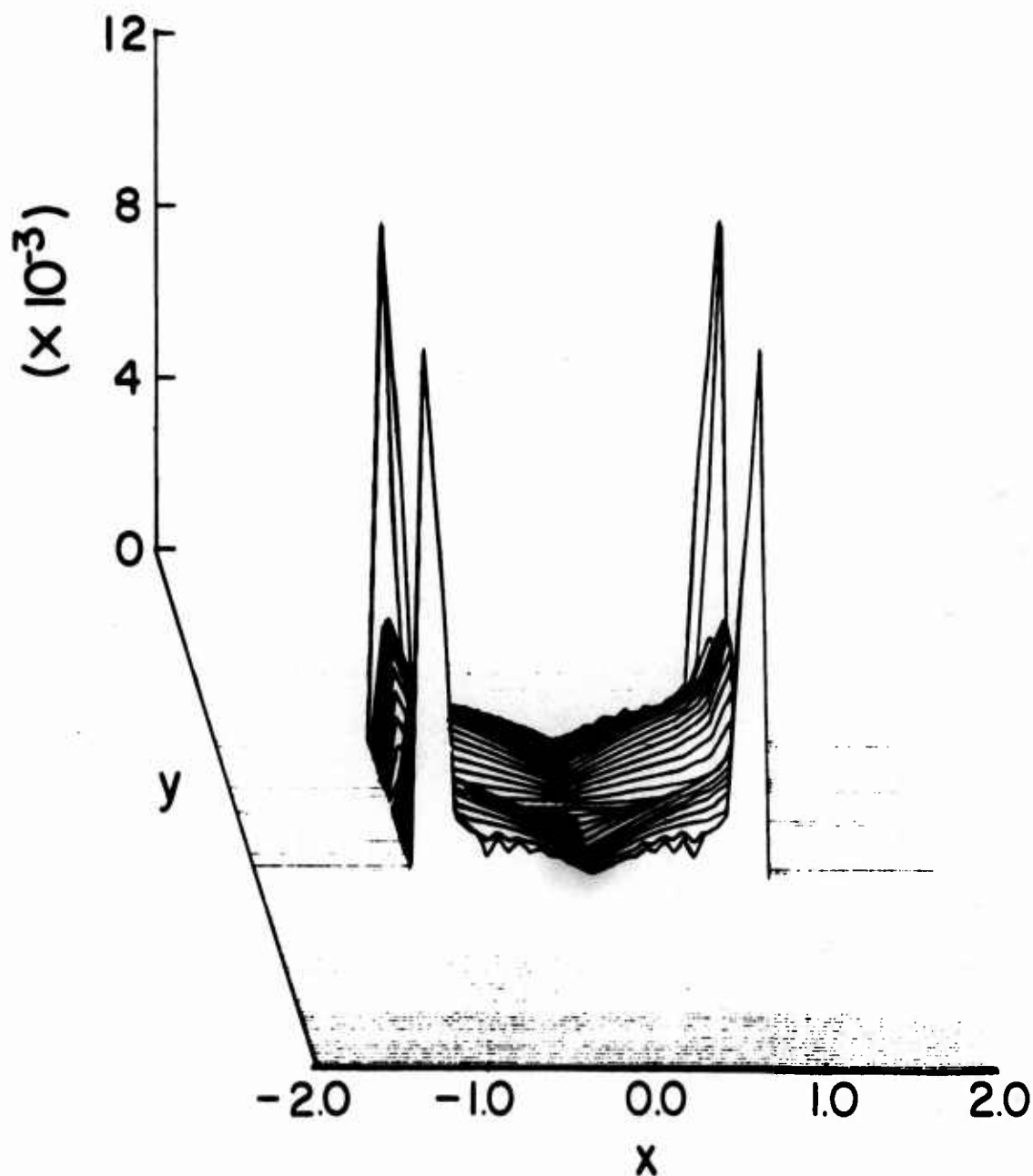
Figure 4.5a. Magnitude of the cross-polarized component of the sur-
face current density on a 1λ x 1λ plate (ka = 3.14);
plate region: xε(-1,1), yε(-1,1), normal incidence with
x-polarization.
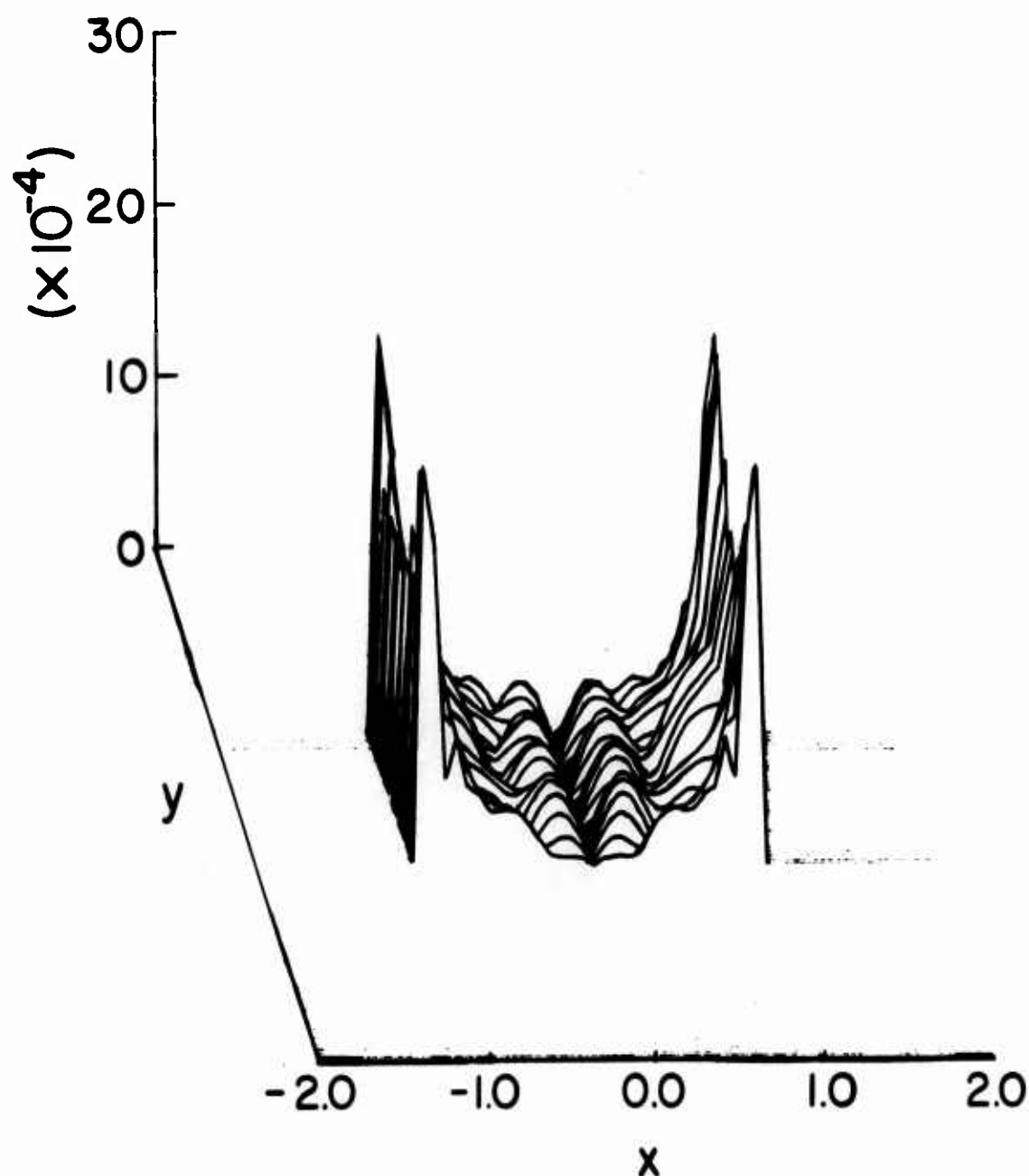
Figure 4.5b. Magnitude of the cross-polarized component of the sur-
face current density on a 3λ x 3λ plate (ka = 9.43);
plate region: $x\epsilon(-1,1)$, $y\epsilon(-1,1)$, normal incidence with
x-polarization.

5. A NEW LOOK AT THE SCATTERING OF A PLANE
WAVE BY A RECTANGULAR CYLINDER

5.1 Introduction

The problem of scattering of electromagnetic waves by a rectangular

cylinder has been investigated by numerous scientific researchers in

the past; yet its flavor has not diminished but quite on the contrary,

it stimulates a strong interest in further pursuing this problem lately

as evidenced by the number of papers appeared in the literature [4], [17],

[18], [19], [20], [21] that deal with this subject.

Due to the two-dimensional nature of the problem, the conventional

moment method [17] can be applied in this case to an electrically large

cylinder when its symmetric properties are also exploited. Therefore,

it provides a convenient validity check for other methods. Indeed,

Burnside *et al.* [4] and Mautz *et al.* [18] have claimed their different

approaches valid only by a comparison of results with the conventional

moment method.

Both of the aforementioned papers made use of the so-called uniform

geometrical theory of diffraction developed by Kouyoumjian *et al.* [8] in

which the classical wedge diffraction coefficient put forth by Keller has

been modified using multiplicative factors in such a manner that one of

these factors goes to zero as the Keller's diffraction coefficient goes

to infinity at one of the shadow or reflection boundaries so that the

product remains finite. The resulting diffraction coefficient is indeed

applicable at all aspect angles. It is conceivable that an additive

term which goes to infinity as the Keller's diffraction coefficient goes

to infinity but with opposite sign will work equally well as does the

multiplicative-factor type of remedy. Indeed, this additive-term type

of remedy has been followed by Lewis *et al.* [22]. Both of these remedies, multiplicative and additive alike, still have room for further development, and it is difficult to judge which one is superior. Furthermore, both of these theories are based on an Ansatz that has no physical justification at all to start with.

In this chapter, we tackle the scattering problem using a completely different technique which is based on a representation of the scattered fields in terms of the spectrum of the induced surface current on the scatterer rather than the rays emanating from it. This spectral domain interpretation of high-frequency diffraction phenomena has been documented in detail in a recent paper by Mittra, Rahmat-Samii and Ko [10]. Ko and Mittra [23] also developed a method based on the spectral domain concept for combining the asymptotic high-frequency technique and the integral equation formulation. The method has been applied successfully to infinitesimally thin scattering objects, e.g., an infinite perfectly conducting strip and a finite perfectly conducting square plate [23]. To further develop the method, we apply it to the perfectly conducting square cylinder.

This particular geometry has been chosen because it serves as a good example for demonstrating that the method can be extended to treat with ease scattering objects with finite thickness and planar surfaces. Moreover, the validity of the method can be easily established by comparing with well-established solutions derived by entirely different approaches available in the literature. We show that starting out with Keller's wedge diffraction coefficient, only one iteration gives a far-field pattern that compares extremely well with that obtained from the moment-method solution for thirty-two unknowns.

To emphasize the simplicity and efficiency of the present approach, it is worth mentioning that the GTD result deviates significantly in those directions which coincide with the orientations of the surfaces of the square cylinder even when multiple-edge interactions are included in a self-consistent manner by introducing eight unknown diffraction coefficients. Only when one further modifies the GTD method with the uniform diffraction coefficient and combines it with the moment method using a total of twenty-four unknowns will the result compare well with the moment-method solution for thirty-two unknowns.

The present approach shows how the Keller's GTD solution can be improved in a straightforward manner based on a physical argument rather than a remedy from an Ansatz. Thus, it gives insight into the mechanism involved in problems of high-frequency scattering from scatterers with planar facets.

5.2 Formulation

The geometry of the electromagnetic scattering problem involving a perfectly conducting infinite rectangular cylinder of cross section 2a x 2b illuminated by a uniform plane wave, whose magnetic intensity vector is oriented parallel to the edges of the cylinder, is depicted in Figure 5.1. For convenience of analysis, an arbitrary incident wave can always be decomposed into two components with respect to the z-axis, namely, TM_z (E-wave) and TE_z (H-wave). In the following discussion we consider the H-wave case only; the E-wave case can be solved in a similar manner by considering $\bar{E}^i = \hat{z}E_0^i$.

In the H-wave case, the incident H-field is given by

$$H_z^i(\rho,\phi) = e^{-ik(x\cos\phi_0 + y\sin\phi_0)} \tag{5.1}$$
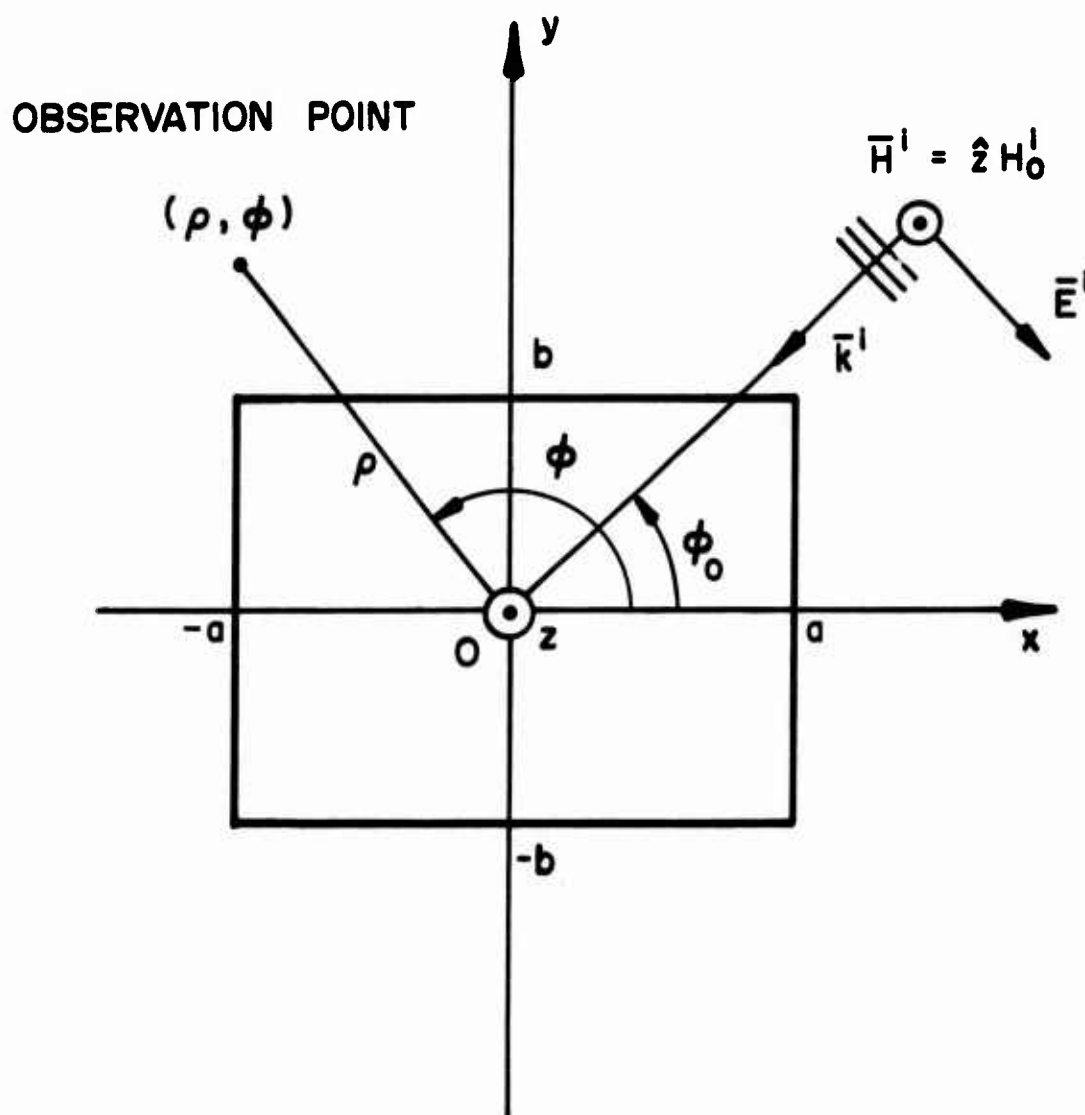
Figure 5.1. Diffraction by a rectangular cylinder illuminated
by an H-polarized plane wave incident at an angle ϕ_0.

where the $e^{-i\omega t}$ time dependence is understood. The geometrical optics reflected field can be derived easily from (5.1) once the geometrical configuration is known. Hence, the geometrical optics part of the total field will not be discussed on further.

We now turn to the diffracted field which results from the sharp edges on the scattering cylinder. As alluded to in Section 5.1, we make use of the Keller wedge diffraction coefficient to find the diffracted fields. To make this discussion as self-contained as possible and to introduce the notations that we have adopted in this chapter, a brief review of the wedge diffraction coefficient is in order.

The geometry of a perfectly conducting wedge immersed in a uniform H-wave in the canonical wedge diffraction problem is shown in Figure 5.2. According to Keller's geometrical theory of diffraction, the diffracted field by the edge of the wedge can be constructed by the following formula:

$$H_z^d \sim H_z^i(\text{at the edge of the wedge}) \ D_h \ \frac{e^{ik\rho}}{\sqrt{\rho}} \ (e^{-i\omega t}) \tag{5.2}$$

where

$$D_h = \frac{e^{i\pi/4}}{\sqrt{2\pi k}} \left[\frac{\frac{1}{n}\sin\frac{\pi}{n}}{\cos\frac{\pi}{n} - \cos\left(\frac{\phi_w - \phi_{0w}}{n}\right)} + \frac{\frac{1}{n}\sin\frac{\pi}{n}}{\cos\frac{\pi}{n} - \cos\left(\frac{\phi_w - \phi_{0w}}{n}\right)} \right] \tag{5.3}$$

and ~ means "asymptotically equal to." In the above formula, $n\pi$ denotes the exterior region while $(2-n)\pi$ denotes the wedge angle. Note that n is not necessarily an integer; in the rectangular cylinder case, it will take on the value 3/2. The subscript w attached to the angle of incidence ϕ_0 and the angle of diffraction ϕ serves as a reminder that these angles are used in the canonical problem and their senses are defined as shown
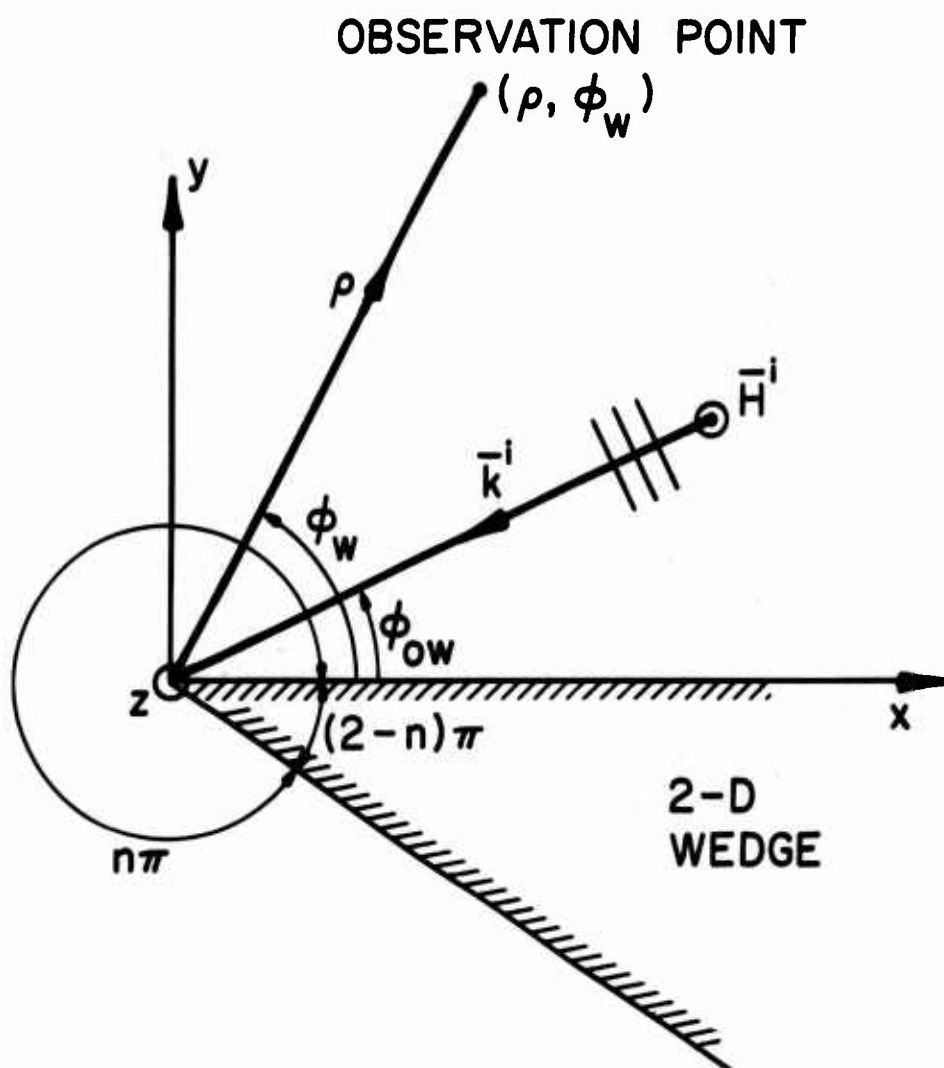
Figure 5.2. Geometry of a perfectly conducting wedge immersed in a uniform H-wave in the canonical wedge diffraction problem.

in Figure 5.2. This fact is worth emphasizing since it is crucial in constructing the diffracted field when several wedges are involved in a scattering problem.

As shown in Figure 5.3, the major contributions to the diffracted field are from wedges 1, 2, and 3 since the three edges of these wedges are being illuminated by the incident field whereas wedge 4 is in the dark and hence it can be ignored in the zeroth-order approximation to the diffracted field. With this in mind, the diffracted far field can be written in a concise fashion as follows:

$$
H_z^d(\rho,\phi) =
\begin{cases}
H_{z1}^d\begin{pmatrix} \phi_w = \phi \\ \phi_{0w} = \phi_0 \end{pmatrix} + H_{z2}^d\begin{pmatrix} \phi_w = \pi - \phi \\ \phi_{0w} = \pi - \phi_0 \end{pmatrix} + H_{z3}^d\begin{pmatrix} \phi_w = \pi/2 - \phi \\ \phi_{0w} = \pi/2 - \phi_0 \end{pmatrix} & , 0 < \phi < \dfrac{\pi}{2} \\[3em]
H_{z1}^d\begin{pmatrix} \phi_w = \phi \\ \phi_{0w} = \phi_0 \end{pmatrix} + H_{z2}^d\begin{pmatrix} \phi_w = \pi - \phi \\ \phi_{0w} = \pi - \phi_0 \end{pmatrix} & , \dfrac{\pi}{2} < \phi < \pi \\[3em]
H_{z1}^d\begin{pmatrix} \phi_w = \phi \\ \phi_{0w} = \phi_0 \end{pmatrix} \hspace{4em} + H_{z3}^d\begin{pmatrix} \phi_w = \pi/2 + (2\pi-\phi) \\ \phi_{0w} = \pi/2 - \phi_0 \end{pmatrix} & , \pi < \phi < \dfrac{3\pi}{2} \\[3em]
H_{z2}^d\begin{pmatrix} \phi_w = 3\pi - \phi \\ \phi_{0w} = \pi - \phi_0 \end{pmatrix} + H_{z3}^d\begin{pmatrix} \phi_w = \pi/2 + (2\pi-\phi) \\ \phi_{0w} = \pi/2 - \phi_0 \end{pmatrix} & , \dfrac{3\pi}{2} < \phi < 2\pi
\end{cases}
$$

$$(5.4)$$
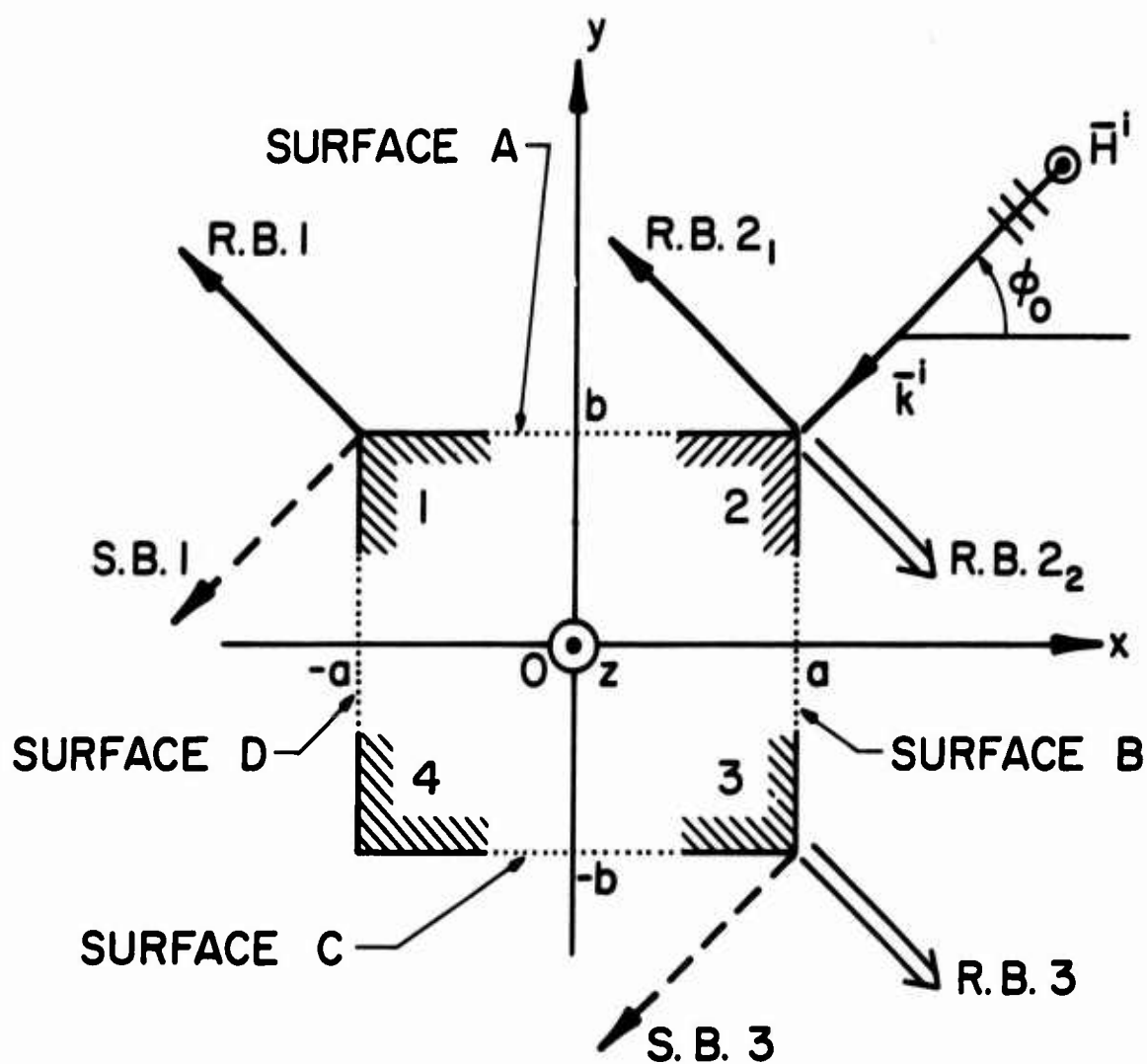
Figure 5.3. For the angle of incidence ϕ_0 as shown, wedges 1, 2, and 3 are illuminated while wedge 4 is in the dark.

where $\phi_0 = \pi/4$. In the above equation, subscripts 1, 2, and 3 on H_z^d designate wedges 1, 2, and 3, respectively. Each of the H_z^d's from the individual wedges is of the form given by (5.2) and (5.3) with proper values for ϕ_w and ϕ_{0w} substituted and proper phase shifts taken care of due to the transfer of the phase center located at the edge of the wedge in each of the individual canonical problems to the common phase center located at the origin of the rectangular coordinate system shown in Figure 5.3.

5.2.1 <u>Pole singularities in the diffraction coefficients</u>

It is well-known that the Keller's diffraction coefficient (5.3) as introduced in the last section will not give the correct value for the diffracted field at certain directions, namely, at the shadow and the reflection boundaries predicted by geometrical optics. One can easily see from (5.3) that the denominator of either one of the two terms in the square brackets vanishes at one of these shadow and reflection boundaries and gives infinite field values at those directions. We know that the field actually remains finite and varies continuously across the shadow and reflection boundaries. Hence, we cannot apply Keller's diffraction coefficient near the shadow and reflection boundaries. It was precisely for this reason that some work had been done in trying to construct a uniform diffraction coefficient. As mentioned earlier in the introduction of this chapter, both multiplicative- and additive-type approaches have been pursued and have shown some success. In the following discussions we show that it is not necessary to use the aforementioned "uniform diffraction coefficient" to solve the rectangular cylinder problem under consideration.

To start, we make direct use of Keller's diffraction coefficient as given in (5.3) and substitute it in (5.2) to find the wedge diffracted field. Observing that the diffraction coefficient contains pole singularities which give nonphysical fields at the shadow and reflection boundaries, we will first subtract out the pole singularities. The reason for subtracting out the pole singularities becomes clear in the next section where these singularities in the diffraction coefficient are shown to correspond exactly to those in the physical optics current that exists on the semi-infinite surface of the wedge in the canonical problem but should not have existed in the rectangular cylinder case since the surfaces of the rectangular cylinder are finite in width. With this in mind, the expressions for the zeroth-order approximation to the diffracted field can be written explicitly as follows: For wedge 1 (see Figure 5.3),

$$H_{z1}^d \sim H_z^i \text{ (at edge of wedge 1) } D_{h1} \frac{e^{ik\rho}}{\sqrt{\rho}} e^{ika\cos\phi} e^{-ikb\sin\phi}$$

$$= e^{-ik(-a\cos\phi_0 + b\sin\phi_0)} \frac{e^{ik\rho}}{\sqrt{\rho}}$$

$$\cdot \frac{e^{i\frac{\pi}{4}}}{\sqrt{2\pi k}} \left[\frac{\frac{2}{3}\sin\frac{2\pi}{3} e^{ika\cos\phi} e^{-ikb\sin\phi}}{\cos\frac{2\pi}{3} - \cos\frac{2}{3}(\phi - \phi_0)} \right.$$

$$- \frac{e^{ik(a\cos(\pi+\phi_0)-b\sin(\pi+\phi_0))}}{\phi - (\pi + \phi_0)}$$

$$+ \frac{\frac{2}{3}\sin\frac{2\pi}{3} e^{ika\cos\phi} e^{-ikb\sin\phi}}{\cos\frac{2\pi}{3} - \cos\frac{2}{3}(\phi + \phi_0)}$$

$$\left. - \frac{e^{ik(a\cos(\pi-\phi_0)-b\sin(\pi-\phi_0))}}{\phi - (\pi - \phi_0)} \right] . \tag{5.5a}$$

where

$$0 \leq \phi_0 \leq \frac{\pi}{2} \text{ and } 0 \leq \phi \leq \frac{3\pi}{2} \quad .$$

Note that the second term in the square brackets is the pole singularity of the first term at the shadow boundary and the fourth term is the pole singularity of the third term at the reflection boundary. For wedge 2 (see Figure 5.3),

$$H_{z2}^d \sim H_z^i \text{ (at edge of wedge 2) } D_{h2} \frac{e^{ik\rho}}{\sqrt{\rho}} e^{-ika\cos\phi} e^{-ikb\sin\phi}$$

$$= e^{-ik(a\cos\phi_0+b\sin\phi_0)} \frac{e^{ik\rho}}{\sqrt{\rho}}$$

$$\cdot \frac{e^{i\frac{\pi}{4}}}{\sqrt{2\pi k}} \left[\frac{\frac{2}{3} \sin \frac{2\pi}{3} e^{-ika\cos\phi} e^{-ikb\sin\phi}}{\cos \frac{2\pi}{3} - \cos \frac{2}{3} [(\pi - \phi) - (\pi - \phi_0)]} \right.$$

$$+ \frac{\frac{2}{3} \sin \frac{2\pi}{3} e^{-ika\cos\phi} e^{-ikb\sin\phi}}{\cos \frac{2\pi}{3} - \cos \frac{2}{3} \begin{cases} (\pi - \phi) + (\pi - \phi_0) & \text{for } 0 \leq \phi \leq \pi \\ (3\pi - \phi) + (\pi - \phi_0) & \text{for } \frac{3\pi}{2} \leq \phi \leq 2\pi \end{cases}}$$

$$+ \frac{e^{-ik(a\cos(\pi-\phi_0)+b\sin(\pi-\phi_0))}}{\phi - (\pi - \phi_0)} \quad \text{for } 0 \leq \phi \leq \pi$$

$$\left. - \frac{e^{-ik(a\cos(2\pi-\phi_0)+b\sin(2\pi-\phi_0))}}{\phi - (2\pi - \phi_0)} \quad \text{for } \frac{3\pi}{2} \leq \phi \leq 2\pi \right] \qquad (5.5b)$$

where

$$0 \leq \phi_0 \leq \frac{\pi}{2} \text{ and } 0 < \phi < \pi \text{ and } \frac{3\pi}{2} < \phi < 2\pi.$$

Note that no singularities are contained in the first term in the given angular domain of ϕ. The third term in the square brackets is the pole singularity of the second term at the reflection boundary for $0 \leq \phi \leq \pi$ and the fourth term is that for $\frac{3\pi}{2} \leq \phi \leq 2\pi$. Also, note that there are no shadow boundaries in this case.

For wedge 3 (see Figure 5.3),

$$H_{z3}^d \sim H_z^i \text{ (at edge of wedge 3) } D_{h3} \frac{e^{ik\rho}}{\sqrt{\rho}} e^{-ikacos\phi} e^{ikbsin\phi}$$

$$= e^{-ik(acos\phi_0 - bsin\phi_0)} \frac{e^{ik\rho}}{\sqrt{\rho}}$$

$$\cdot \frac{e^{i\frac{\pi}{4}}}{\sqrt{2\pi k}} \left[\frac{\frac{2}{3} \sin \frac{2\pi}{3} e^{-ikacos\phi} e^{ikbsin\phi}}{\cos \frac{2\pi}{3} - \cos \frac{2}{3} \begin{cases} (\frac{\pi}{2} - \phi) - (\frac{\pi}{2} - \phi_0) & \text{for } 0 \leq \phi \leq \frac{\pi}{2} \\ [\frac{\pi}{2} + (2\pi - \phi)] - (\frac{\pi}{2} - \phi_0) & \text{for } \pi \leq \phi \leq 2\pi \end{cases}} \right.$$

$$+ \frac{e^{-ik(acos(\pi+\phi_0) - bsin(\pi+\phi_0))}}{\phi - (\pi + \phi_0)} \quad \text{for } \pi \leq \phi \leq 2\pi$$

$$+ \frac{\frac{2}{3} \sin \frac{2\pi}{3} e^{-ikacos\phi} e^{ikbsin\phi}}{\cos \frac{2\pi}{3} - \cos \frac{2}{3} \begin{cases} (\frac{\pi}{2} - \phi) + (\frac{\pi}{2} - \phi_0) & \text{for } 0 \leq \phi \leq \frac{\pi}{2} \\ [\frac{\pi}{2} + (2\pi - \phi)] + (\frac{\pi}{2} - \phi_0) & \text{for } \pi \leq \phi \leq 2\pi \end{cases}}$$

$$\left. + \frac{e^{-ik(acos(2\pi-\phi_0) - bsin(2\pi-\phi_0))}}{\phi - (2\pi - \phi_0)} \quad \text{for } \pi \leq \phi \leq 2\pi \right] \quad (5.5c)$$

where

$$0 \leq \phi_0 \leq \frac{\pi}{2} \text{ and } 0 \leq \phi \leq \frac{\pi}{2} \text{ and } \pi \leq \phi \leq 2\pi \quad .$$

Note that the second term in the square brackets is the pole singularity of the first term at the shadow boundary and the fourth term is that of the third term at the reflection boundary. For future reference, all the pole singularities contained in the diffraction coefficient, which have been discussed in detail above and shown explicitly in (5.5a), (5.5b) and (5.5c), are tabulated in Table 5.1.

5.2.2 Pole singularities in the physical optics currents

It was discussed in the last section how the diffracted far field can be constructed from the diffraction coefficients. In applying these diffraction coefficients, one must recognize the fact that they were derived from solving a canonical problem which involved an infinite perfectly conducting wedge, or more descriptively, two semi-infinite perfectly conducting half planes joining each other at an angle. Therefore, the solution of the canonical problem predicts a physical optics current existing on the illuminated semi-infinite surfaces of the wedge. Since the support of this physical optics current is infinite, it gives rise to infinite fields at certain directions in space. In the following discussions, we show that all the pole singularities contained in the wedge diffraction coefficient are precisely due to these physical optics currents with infinite supports.

To tackle this problem one step at a time, Figure 5.3 has been redrawn in more detail in Figures 5.4a, 5.4b, Figures 5.5a, 5.5b, and Figures 5.6a, 5.6b. These figures exhibit the physical optics currents on the illuminated surfaces of the illuminated wedges of the rectangular cylinder as

TABLE 5.1

POLE SINGULARITIES AT SHADOW AND REFLECTION BOUNDARIES
THAT HAVE BEEN SUBTRACTED FROM THE PERTINENT DIFFRACTION COEFFICIENTS
(S. B.:   SHADOW BOUNDARY, R. B.:   REFLECTION BOUNDARY)

Wedge	Pole at	Pole singularity
1	S. B.	$\dfrac{e^{ik(-a\cos\phi_0 + b\sin\phi_0)}}{\phi - (\pi + \phi_0)}$
1	R. B.	$\dfrac{e^{ik(-a\cos\phi_0 - b\sin\phi_0)}}{\phi - (\pi - \phi_0)}$
2	R. B. 1	$\dfrac{-e^{ika\cos\phi_0}\, e^{-ikb\sin\phi_0}}{\phi - \pi + \phi_0}$
2	R. B. 2	$\dfrac{e^{-ika\cos\phi_0}\, e^{ikb\sin\phi_0}}{\phi - 2\pi + \phi_0}$
3	R. B.	$\dfrac{-e^{-ika\cos\phi_0}\, e^{-ikb\sin\phi_0}}{\phi - 2\pi + \phi_0}$
3	S. B.	$\dfrac{-e^{ika\cos\phi_0}\, e^{-ikb\sin\phi_0}}{\phi - (\pi + \phi_0)}$

Figure 5.4a. Physical optics current $J_{xA1}^{P.O.}$ on the illuminated surface A of wedge 1.
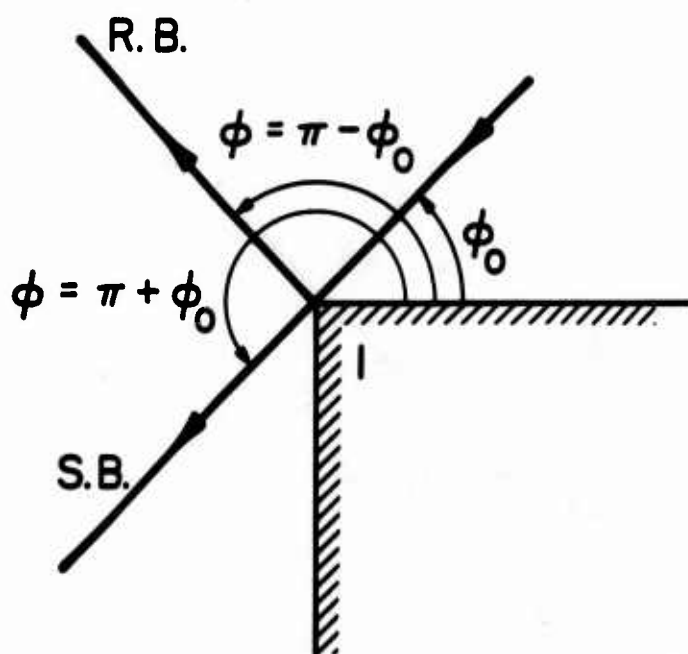
Figure 5.4b. Shadow and reflection boundaries predicted by geometrical optics for wedge 1.
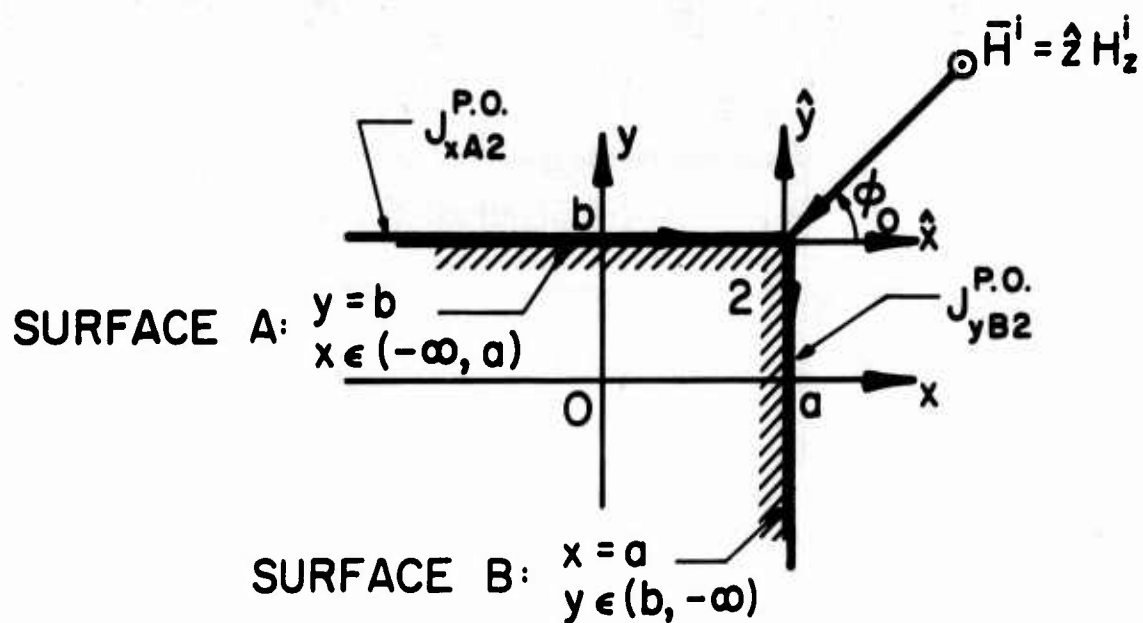
Figure 5.5a. Physical optics currents $J_{xA2}^{P.O.}$ and $J_{yB2}^{P.O.}$ on the illuminated surfaces A and B of wedge 2, respectively.
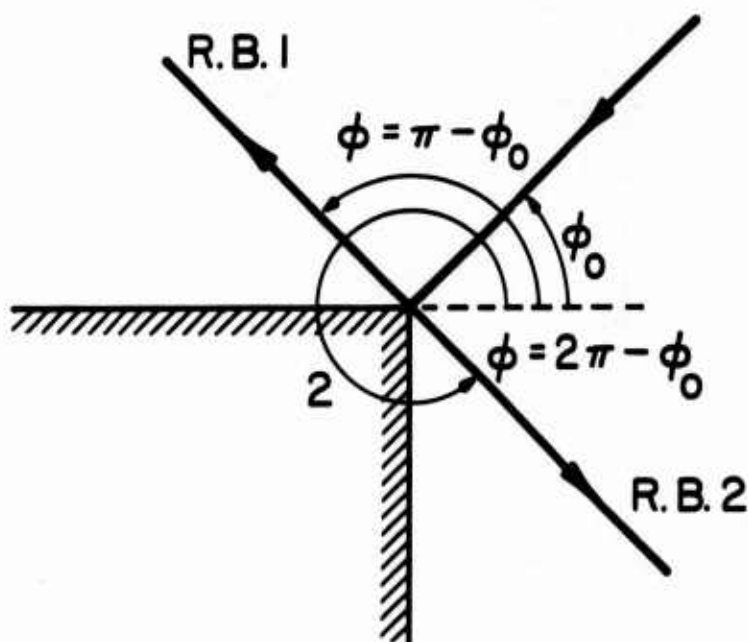
Figure 5.5b. Reflection boundaries predicted by geometrical optics for wedge 2.
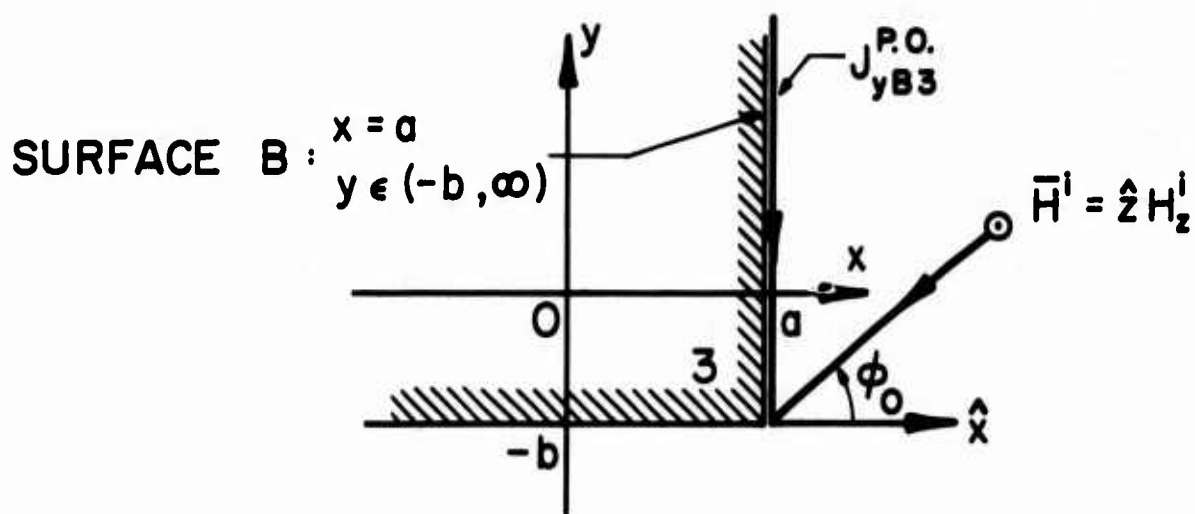
Figure 5.6a. Physical optics current $J_{yB3}^{P.O.}$ on the illuminated surface B of wedge 3.
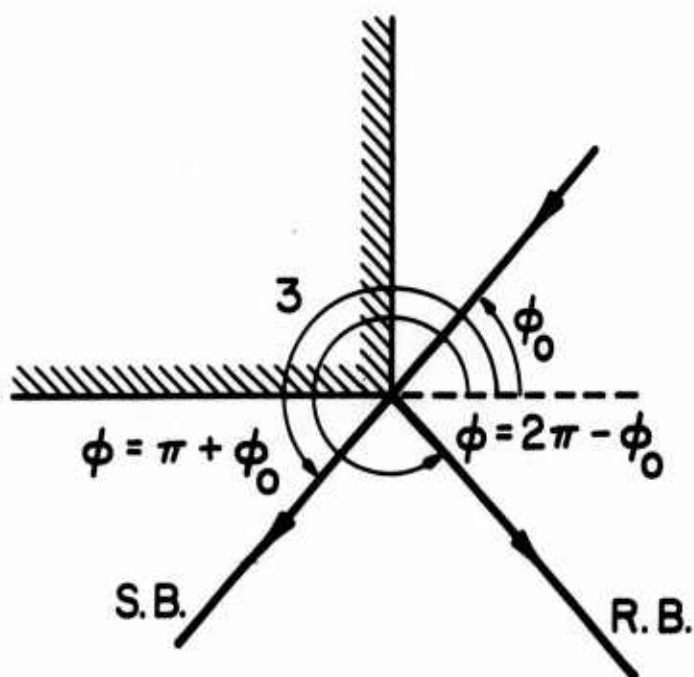
Figure 5.6b. Shadow and reflection boundaries predicted by geometrical optics for wedge 3.

well as the shadow and reflection boundaries created by the illuminating

plane incident wave as predicted by classical geometrical optics.

Referring to Figure 5.4a, the far field $H_{zA1}^{P.0.}$ due to the physical optics

current $J_{xA1}^{P.0.}$ on the semi-infinite surface A of wedge 1 can be obtained

using classical electromagnetic theory. First of all, the subscripts

and superscripts attached to J and H must be understood properly.

The first subscript indicates the vector component of the quantity;

the second subscript designates the surface on which the current exists;

and the third subscript depicts the illuminated wedge under scrutini-

zation. The superscript reveals that the quantity under consideration

is obtained from physical optics. In classical electromagnetic theory,

the far field $H_{zA1}^{P.0.}$ and the surface electric current $J_{xA1}^{P.0.}$ radiating it

in free space are related in the following manner.

$$H_{zA1}^{P.0.} = -ik \frac{e^{ik\rho}}{\sqrt{8\pi k\rho}} e^{i\frac{\pi}{4}} \sin \phi \ \tilde{J}_{xA1}^{P.0.} \tag{5.6}$$

where

$$\tilde{J}_{xA1}^{P.0.} = F\left\{J_{xA1}^{P.0.}\right\}$$

$$= \int_{-\infty}^{\infty} \int_{-a}^{\infty} 2e^{-ik(x\cos\phi_0 + b\sin\phi_0)} \delta(y-b) \ e^{-i\alpha x} e^{-i\beta y} \ dxdy$$

which is the Fourier transform of the surface electric current density

$J_{xA1}^{P.0.}$ obtained by physical optics, i.e., $2\hat{n} \times \bar{H}^i$. The factor of 2 is

present because the original problem, which involved an electric cur-

rent radiating in the presence of a perfectly conducting surface on

which it resides, is equivalent to the problem of twice the electric current radiating in free space. If we ignore all of the effects at infinity, which can be done by introducing an infinitesimal loss in the medium, then the far field due to the physical optics current on surface A of wedge 1 can be expressed as:

$$H_{zA1}^{P.O.} = -ik \frac{e^{ik\rho}e^{i\frac{\pi}{4}}}{\sqrt{8\pi k\rho}} 2 \sin \phi \frac{e^{-ikb\sin\phi_0 - ikb\sin\phi} e^{ia(k\cos\phi_0 + k\cos\phi)}}{i(k\cos\phi_0 + k\cos\phi)} . (5.7)$$

It is very interesting to observe that the denominator in (5.7) vanishes at $\phi = \pi \mp \phi_0$ which are precisely the reflection and shadow boundaries as shown in Figure 5.4b.

Knowing that the field produced by the physical optics current does possess pole singularities at the shadow and reflection boundaries, let us check the singular behavior as ϕ approaches $\pi \mp \phi_0$. To this end, the denominator will be expanded into a Taylor's series in $[\phi - (\pi \mp \phi_0)]$. In this series, only those terms up to the first power of ϕ will be kept while all higher power terms are discarded since their contributions are small compared with the first power term in the series as ϕ approaches infinitely close to $\pi \mp \phi_0$. Putting this in terms of mathematical language, we have

$$H_{zA1}^{P.O.} \underset{\phi \to \phi_p}{\to} -ik \frac{e^{ik\rho}e^{i\frac{\pi}{4}}}{\sqrt{8\pi k\rho}} \left[\frac{2 \sin \phi_p e^{-ikb\sin\phi_0 + ika\cos\phi_0} e^{-ikb\sin\phi_p + ika\cos\phi_p}}{ik\{\cos\phi_0 + \cos\phi_p - \sin\phi_p(\phi - \phi_p) + \ldots\}} \right]$$

$$(5.8)$$

where

$$\phi_p = \pi \mp \phi_0 \quad .$$

Through straightforward algebraic manipulations, we have

$$H_{zA1}^{P.O.} \xrightarrow[\phi \to \pi \mp \phi_0]{} e^{-ikb\sin\phi_0 + ika\cos\phi_0} \frac{e^{ik\rho}}{\sqrt{\rho}}$$

$$\cdot \frac{e^{i\frac{\pi}{4}}}{\sqrt{2\pi k}} \left[\frac{e^{-ikb\sin(\pi\mp\phi_0) + ika\cos(\pi\mp\phi_0)}}{\phi - (\pi \mp \phi_0)} \right] . \tag{5.9}$$

At this point, one may go back to (5.5a) or Table 5.1 to see that these are indeed exactly the pole singularities at the shadow and reflection boundaries of the wedge diffraction coefficient D_{h1}.

Referring to Figure 5.5a and proceeding along similar lines, one can obtain

$$H_{zA2}^{P.O.} = -ik \frac{e^{ik\rho}}{\sqrt{8\pi k\rho}} e^{i\frac{\pi}{4}} \left[2 \sin\phi \; e^{-ikb\sin\phi_0 - ikb\sin\phi} \frac{e^{-ia(k\cos\phi_0 + k\cos\phi)}}{-i(k\cos\phi_0 + k\cos\phi)} \right] \tag{5.10}$$

and

$$H_{zB2}^{P.O.} = -ik \frac{e^{ik\rho}}{\sqrt{8\pi k\rho}} e^{i\frac{\pi}{4}} \left[-2 \cos\phi \; e^{-ika\cos\phi_0 - ika\cos\phi} \frac{e^{-ib(k\sin\phi_0 + k\sin\phi)}}{i(k\sin\phi_0 + k\sin\phi)} \right] . \tag{5.11}$$

Similarly, the singular behavior of $H_{zA2}^{P.O.}$ and $H_{zB2}^{P.O.}$ can be shown to be as follows:

$$H_{zA2}^{P.O.} \xrightarrow[\phi \to \pi \mp \phi_0]{} -e^{-ikb\sin\phi_0 - ika\cos\phi_0} \frac{e^{ik\rho}}{\sqrt{\rho}}$$

$$\cdot \frac{e^{i\frac{\pi}{4}}}{\sqrt{2\pi k}} \left[\frac{e^{-ikb\sin(\pi\mp\phi_0) - ika\cos(\pi\mp\phi_0)}}{\phi - (\pi \mp \phi_0)} \right] \tag{5.12}$$

and

$$H_{zB2}^{P.O.} \xrightarrow[\phi \to \begin{Bmatrix} \pi+\phi_0 \\ 2\pi-\phi_0 \end{Bmatrix}]{} e^{-ika\cos\phi_0 - ikb\sin\phi_0} \frac{e^{ik\rho}}{\sqrt{\rho}}$$

$$\cdot \frac{e^{i\frac{\pi}{4}}}{\sqrt{2\pi k}} \left[\frac{e^{-ika\cos\begin{Bmatrix}\pi+\phi_0\\2\pi-\phi_0\end{Bmatrix} - ikb\sin\begin{Bmatrix}\pi+\phi_0\\2\pi-\phi_0\end{Bmatrix}}}{\phi - \begin{Bmatrix}\pi + \phi_0 \\ 2\pi - \phi_0\end{Bmatrix}} \right] \cdot \qquad (5.13)$$

It is very satisfying to observe that the pole singularity of $H_{zA2}^{P.O.}$ at $\phi = \pi - \phi_0$ is exactly the pole singularity at the reflection boundary off surface A of the diffraction coefficient D_{h2} in (5.5b); and the pole singularity of $H_{zB2}^{P.O.}$ at $\phi = 2\pi - \phi_0$ is exactly the pole singularity at the reflection boundary off surface B of the diffraction coefficient D_{h2} in (5.5b) (see Figure 5.5b). These pole singularities are also listed in Table 5.1. The pole singularity of $H_{zA2}^{P.O.}$ at $\phi = \pi + \phi_0$ cancels the pole singularity of $H_{zB2}^{P.O.}$ at $\phi = \pi + \phi_0$ exactly. It is also interesting to note that the direction $\phi = \pi + \phi_0$ is inside wedge 2.

Finally, referring to Figure 5.6a and proceeding as before, one obtains

$$H_{zB3}^{P.O.} = -ik \frac{e^{ik\rho}}{\sqrt{8\pi k\rho}} e^{i\frac{\pi}{4}} \left[\frac{2\cos\phi \, e^{-ika\cos\phi_0 - ika\cos\phi} \, e^{ib(k\sin\phi_0 + k\sin\phi)}}{i(k\sin\phi_0 + k\sin\phi)} \right]$$

$$(5.14)$$

The singular behavior of $H_{zB3}^{P.O.}$ is studied similarly and the result is shown below.

$$H_{zB3}^{P.O.} \xrightarrow[\phi \to]{\begin{Bmatrix} \pi+\phi_0 \\ 2\pi-\phi_0 \end{Bmatrix}} -e^{-ikacos\phi_0+ikbsin\phi_0} \frac{e^{ik\rho}}{\sqrt{\rho}}$$

$$\cdot \frac{e^{i\frac{\pi}{4}}}{\sqrt{2\pi k}} \left[\frac{e^{-ikacos\begin{Bmatrix} \pi+\phi_0 \\ 2\pi-\phi_0 \end{Bmatrix}+ikbsin\begin{Bmatrix} \pi+\phi_0 \\ 2\pi-\phi_0 \end{Bmatrix}}}{\phi - \begin{Bmatrix} \pi + \phi_0 \\ 2\pi - \phi_0 \end{Bmatrix}} \right] . \tag{5.15}$$

Once again, by referring to Figure 5.6b and (5.5c), one can verify that these pole singularities in $H_{zB3}^{P.O.}$ are indeed those at the shadow and reflection boundaries of the diffraction coefficient D_{h3}.

To recapitulate, the pole singularities contained in the diffraction coefficient at the shadow and reflection boundaries correspond exactly to the pole singularities contained in the physical optics currents with infinite supports. This demonstration explains why we have sub-tracted out the pole singularities in the diffraction coefficient before we applied it to compute the diffracted far field. The main reason is that we are applying these diffraction coefficients to construct the far field diffracted by a finite two-dimensional scatterer where there is, in fact, lack of all these physical optics currents with infinite supports which would have existed on the illuminated surfaces of the semi-infinite wedge in the canonical problem used to identify these wedge diffraction coefficients. After these pole singularities have been subtracted from the diffraction coefficients, the resulting expres-sions for the diffraction coefficients can be used directly in the

construction of the diffracted far field. This procedure has been shown explicitly in (5.5a), (5.5b), and (5.5c).

The superposition of H_{z1}^d, H_{z2}^d, and H_{z3}^d, as done in the manner indicated by (5.4), gives the diffracted far field from the rectangular cylinder. The far-field pattern computed by using $\phi_0 = \frac{\pi}{4}, a = b = 1\lambda$, in (5.4) is depicted in Figure 5.7. This plot shows that there are no sporadic variations near the shadow and reflection boundaries at 225°, 135°, and 315°. This pattern has already been in very good agreement with that obtained by using the moment method, as shown in Figure 5.11. By good agreement, we mean that all the locations of the peaks and nulls are close to the right positions and the levels are more or less on the right track. Except for the obvious discontinuities in the pattern at the angles of 0°, 90°, 180°, and 270°, which correspond to the directions in which the four surfaces of the rectangular cylinder are oriented, it is really remarkable how good a far-field pattern a zeroth-order GTD solution can give! A simple physical interpretation for the existence of these discontinuities can be found; and their elimination is discussed in the following sections.

Before closing this section, it is noteworthy that due to the complete symmetry of the rectangular cylinder, the pole singularities in the wedge diffraction coefficients need not be subtracted out explicitly as done in (5.5a), (5.5b), and (5.5c) before we use them to compute the far field. In other words, the wedge diffraction coefficient as given in its original form shown in (5.3) could have been used directly to compute the far-field pattern; and indeed this is done and the result is plotted in Figure 5.8. It is identical to Figure 5.7. The automatic
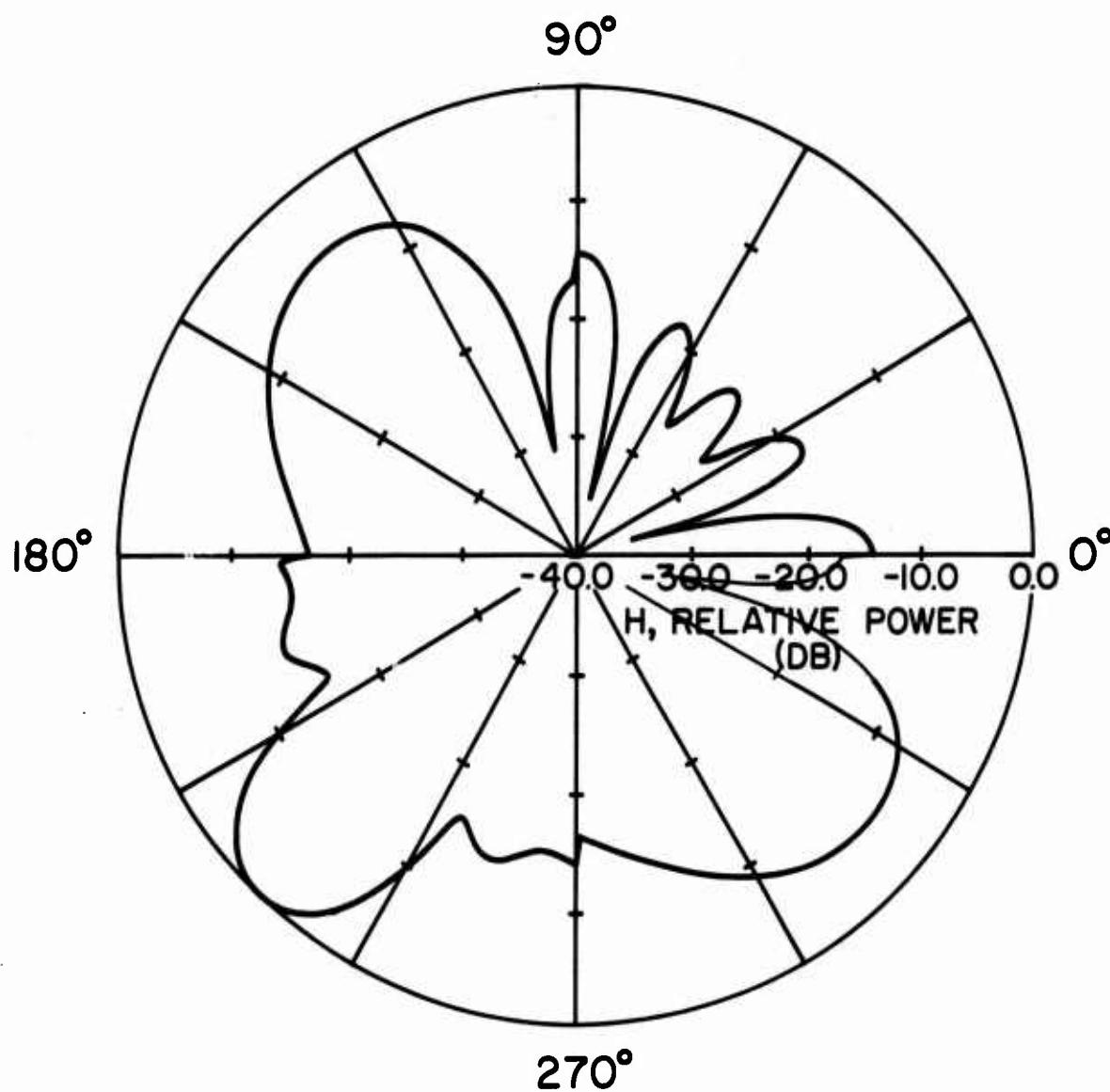
Figure 5.7. Diffracted far-field pattern of the rectangular cylinder obtained by using (5.4); $\phi_0 = \pi/4$, $a = b = 1\lambda$.
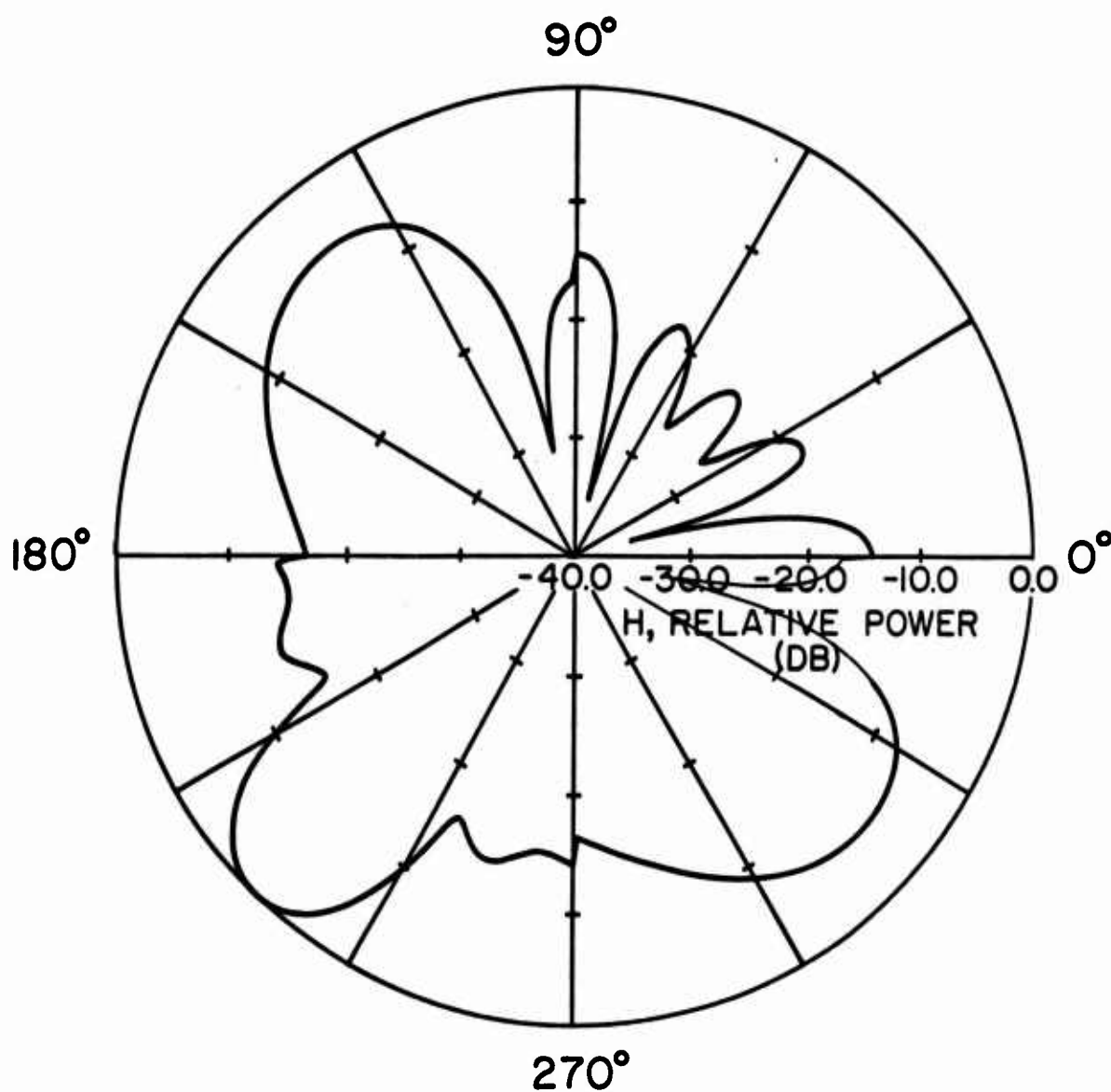
Figure 5.8. GTD diffracted far-field pattern of the rectangular cylinder; $\phi_0 = \pi/4$, $a = b = 1\lambda$.

pole cancellations happened in this completely symmetric case are shown schematically in Figure 5.3 where pole singularities at shadow or reflection boundaries indicated by like arrow pairs annihilate each other. That this is indeed the case can be verified by checking (5.5a), (5.5b), and (5.5c) for the pole singularities enclosed in the square brackets as well as paying attention to the phase factor outside the square brackets. While it is admittedly a happy coincidence that the Keller's diffraction coefficients can be used directly in the rectangular cylinder problem, in more general cases the procedure of subtracting pole singularities explicitly from the diffraction coefficient, as done in (5.5a), (5.5b), and (5.5c), should be followed in order to get meaningful results near the shadow and the reflection boundaries.

5.2.3 Discontinuities in the far-field pattern at $\phi = 0, \frac{\pi}{2}, \pi,$ and $\frac{3\pi}{2}$

In the previous sections the problem of diffraction by a rectangular cylinder was solved by using Keller's wedge diffraction coefficients minus the pole singularities in constructing the diffracted far field. Although the far-field pattern varies smoothly and remains finite across the shadow and reflection boundaries, there are noticeable discontinuities in the pattern at $\phi = 0, \frac{\pi}{2}, \pi,$ and $\frac{3\pi}{2}$. These directions are those in which the surfaces of the rectangular cylinder are oriented. In the next section, a physical interpretation of the existence of these discontinuities is given. Before doing that, these discontinuities are studied and the results are displayed in full detail in this section.

Let us refer to (5.4). The discontinuity in the far field at $\phi = 0$ is

$$H_z^d(\phi = 0) - H_z^d(\phi = 2\pi) \tag{5.16a}$$

$$= \left[H_{z1}^d \begin{pmatrix} \phi_w = 0 \\ \phi_{0w} = \phi_0 \end{pmatrix} + H_{z2}^d \begin{pmatrix} \phi_w = \pi - 0 \\ \phi_{0w} = \pi - \phi_0 \end{pmatrix} + H_{z3}^d \begin{pmatrix} \phi_w = \frac{\pi}{2} - 0 \\ \phi_{0w} = \frac{\pi}{2} - \phi_0 \end{pmatrix} \right]$$

$$- \left[H_{z2}^d \begin{pmatrix} \phi_w = 3\pi - 2\pi \\ \phi_{0w} = \pi - \phi_0 \end{pmatrix} + H_{z3}^d \begin{pmatrix} \phi_w = \frac{\pi}{2} + (2\pi - 2\pi) \\ \phi_{0w} = \frac{\pi}{2} - \phi_0 \end{pmatrix} \right] \tag{5.16b}$$

$$= H_{z1}^d \begin{pmatrix} \phi_w = 0 \\ \phi_{0w} = \phi_0 \end{pmatrix} \tag{5.16c}$$

$$= e^{-ik(-a\cos\phi_0 + b\sin\phi_0)} \frac{e^{ik\rho}}{\sqrt{\rho}}$$

$$\cdot \frac{e^{i\frac{\pi}{4}}}{\sqrt{2\pi k}} \left[\frac{\frac{2}{3} \sin \frac{2\pi}{3} e^{ika}}{\cos \frac{2\pi}{3} - \cos \frac{2\phi_0}{3}} + \frac{\frac{2}{3} \sin \frac{2\pi}{3} e^{ika}}{\cos \frac{2\pi}{3} - \cos(\frac{2}{3} \phi_0)} \right] \tag{5.16d}$$

$$= \frac{e^{i\frac{\pi}{4}}}{\sqrt{2}} \frac{e^{ik\rho}}{\sqrt{\pi k \rho}} \left[e^{-ik(-a\cos\phi_0 + b\sin\phi_0)} \frac{(2)(\frac{2}{3} \sin \frac{2\pi}{3}) e^{ika}}{\cos \frac{2\pi}{3} - \cos \frac{2}{3} \phi_0} \right] . \tag{5.16e}$$

Following the same lines, the discontinuity in the far field at $\phi = \frac{\pi}{2}$ is

$$H_z^d(\phi = \frac{\pi}{2} -) - H_z^d(\phi = \frac{\pi}{2} +) \tag{5.17a}$$

$$= H_{z3}^{d} \begin{pmatrix} \phi_w = 0 \\ \phi_{0w} = \frac{\pi}{2} - \phi_0 \end{pmatrix} \tag{5.17b}$$

$$= \frac{e^{i\frac{\pi}{4}}}{\sqrt{2}} \frac{e^{ik\rho}}{\sqrt{\pi k\rho}} \left[e^{-ik(a\cos\phi_0 - b\sin\phi_0)} \frac{(2)(\frac{2}{3}\sin\frac{2\pi}{3}) e^{ikb}}{\cos\frac{2\pi}{3} - \cos\frac{2}{3}(\frac{\pi}{2} - \phi_0)} \right] . \tag{5.17c}$$

In the above equation,

$$H_z^d(\phi = \frac{\pi}{2} -) = \lim_{\varepsilon \to 0} H_z^d(\phi = \frac{\pi}{2} - \varepsilon) \tag{5.18a}$$

and

$$H_z^d(\phi = \frac{\pi}{2} +) = \lim_{\varepsilon \to 0} H_z^d(\phi = \frac{\pi}{2} + \varepsilon) \tag{5.18b}$$

where $\varepsilon > 0$ is any small positive real number. Similarly, the discontinuity in the far-field pattern at $\phi = \pi$ is

$$H_z^d(\phi = \pi -) - H_z^d(\phi = \pi +) \tag{5.19a}$$

$$= H_{z2}^{d} \begin{pmatrix} \phi_w = 0 \\ \phi_{02} = \pi - \phi_0 \end{pmatrix} - H_{z3}^{d} \begin{pmatrix} \phi_w = \frac{3\pi}{2} \\ \phi_{0w} = \frac{\pi}{2} - \phi_0 \end{pmatrix} \tag{5.19b}$$

$$= e^{-ik(a\cos\phi_0 + b\sin\phi_0)} \frac{e^{ik\rho}}{\sqrt{\rho}} \cdot e^{ika}$$

$$\cdot \frac{e^{i\frac{\pi}{4}}}{\sqrt{2\pi k}} \left[\frac{\frac{2}{3}\sin\frac{2\pi}{3}}{\cos\frac{2\pi}{3} - \cos\frac{2}{3}(\pi - \phi_0)} + \frac{\frac{2}{3}\sin\frac{2}{3}\pi}{\cos\frac{2\pi}{3} - \cos\frac{2}{3}(\pi - \phi_0)} \right]$$

$$- e^{-ik(a\cos\phi_0 - b\sin\phi_0)} \frac{e^{ik\rho}}{\sqrt{\rho}} \cdot e^{ika}$$

$$\cdot \frac{e^{i\frac{\pi}{4}}}{\sqrt{2\pi k}}\left[\frac{\frac{2}{3}\sin\frac{2}{3}\pi}{\cos\frac{2\pi}{3}-\cos\frac{2}{3}(\pi+\phi_0)}+\frac{\frac{2}{3}\sin\frac{2}{3}\pi}{\cos\frac{2\pi}{3}-\cos\frac{2}{3}(2\pi-\phi_0)}\right] \quad . \quad (5.19c)$$

Finally, the discontinuity in the far-field pattern at $\phi = \frac{3\pi}{2}$ is

$$H_z^d(\phi = \frac{3\pi}{2}-) - H_z^d(\phi = \frac{3\pi}{2}+) \qquad (5.20a)$$

$$= H_{z1}^d\left(\begin{matrix}\phi_w = \frac{3\pi}{2}\\ \phi_{0w} = \phi_0\end{matrix}\right) - H_{z2}^d\left(\begin{matrix}\phi_w = \frac{3\pi}{2}\\ \phi_{0w} = \pi - \phi_0\end{matrix}\right) \qquad (5.20b)$$

$$= e^{-ik(-a\cos\phi_0+b\sin\phi_0)} \cdot \frac{e^{ik\rho}}{\sqrt{\rho}} \cdot e^{ikb}$$

$$\cdot \frac{e^{i\frac{\pi}{4}}}{\sqrt{2\pi k}}\left[\frac{\frac{2}{3}\sin\frac{2\pi}{3}}{\cos\frac{2\pi}{3}-\cos\frac{2}{3}(\frac{3\pi}{2}-\phi_0)}+\frac{\frac{2}{3}\sin\frac{2\pi}{3}}{\cos\frac{2\pi}{3}-\cos\frac{2}{3}(\frac{3\pi}{2}+\phi_0)}\right]$$

$$- e^{-ik(a\cos\phi_0+b\sin\phi_0)} \frac{e^{ik\rho}}{\sqrt{\rho}} \cdot e^{ikb}$$

$$\cdot \frac{e^{i\frac{\pi}{4}}}{\sqrt{2\pi k}}\left[\frac{\frac{2}{3}\sin\frac{2\pi}{3}}{\cos\frac{2\pi}{3}-\cos\frac{2}{3}(\frac{\pi}{2}+\phi_0)}+\frac{\frac{2}{3}\sin\frac{2\pi}{3}}{\cos\frac{2\pi}{3}-\cos\frac{2}{3}(\frac{5\pi}{2}-\phi_0)}\right] \quad . \quad (5.20c)$$

To summarize, the discontinuities in the far field at $\phi = 0$, $\frac{\pi}{2}$, π, and $\frac{3\pi}{2}$ have been studied in full detail and the results documented in this section. The fact that the GTD solution of the far field contains discontinuities is well-known. In the next section, the cause of the existence of these discontinuities is investigated and a simple physical interpretation is given which, in turn, provides a clue to their elimination.

5.2.4 <u>Physical interpretation of the existence of the disconti-
nuities in the far-field pattern at $\phi = 0$, $\frac{\pi}{2}$, π, and $\frac{3\pi}{2}$</u>

In the last section, the discontinuities in the far field at

$\phi = 0$, $\frac{\pi}{2}$, π, and $\frac{3\pi}{2}$ have been studied and documented. The fact that

the GTD solution of the far field contains discontinuities is well-

known. The cause of the existence of these discontinuities is investi-

gated and a simple physical interpretation is given which, in turn,

provides a clue to their elimination.

Note that in (5.4), the far field H_z^d is constructed by using

H_{z1}^d, H_{z2}^d, and H_{z3}^d, each of which has its own angular domain of defini-

tion. More explicitly, H_{z1}^d is defined on the angular range $0 \leq \phi \leq \frac{3\pi}{2}$

(see Figure 5.9a); outside of this angular range, H_{z2}^d is simply assumed

to be zero. Likewise, H_{z2}^d is defined on $0 \leq \phi \leq \pi$ and $\frac{3\pi}{2} \leq \phi \leq 2\pi$

(see Figure 5.9b); and H_{z3}^d is on $0 \leq \phi \leq \frac{\pi}{2}$ and $\pi \leq \phi \leq 2\pi$ (see Figure

5.9c). It would have been a valid assumption in the canonical problem

since fields would have existed only in the exterior region of the wedge.

In the rectangular cylinder problem, it should be realized that the

fields do not terminate abruptly at the geometrical planes represented

by dashed lines in Figures 5.9a, 5.9b, and 5.9c. These dashed planes would

have been occupied by the semi-infinite wedge surfaces in the canonical prob-

lems. Physically, the fields should be continuous across these dashed planes

in space. Therefore, in constructing the far field as shown in (5.4),

we have effectively created a discontinuity at each of these dashed

planes. The presence of these discontinuities is solely artificial

because they are created by our abrupt truncation of the fields to

the regions in space corresponding to the exterior regions of the wedges
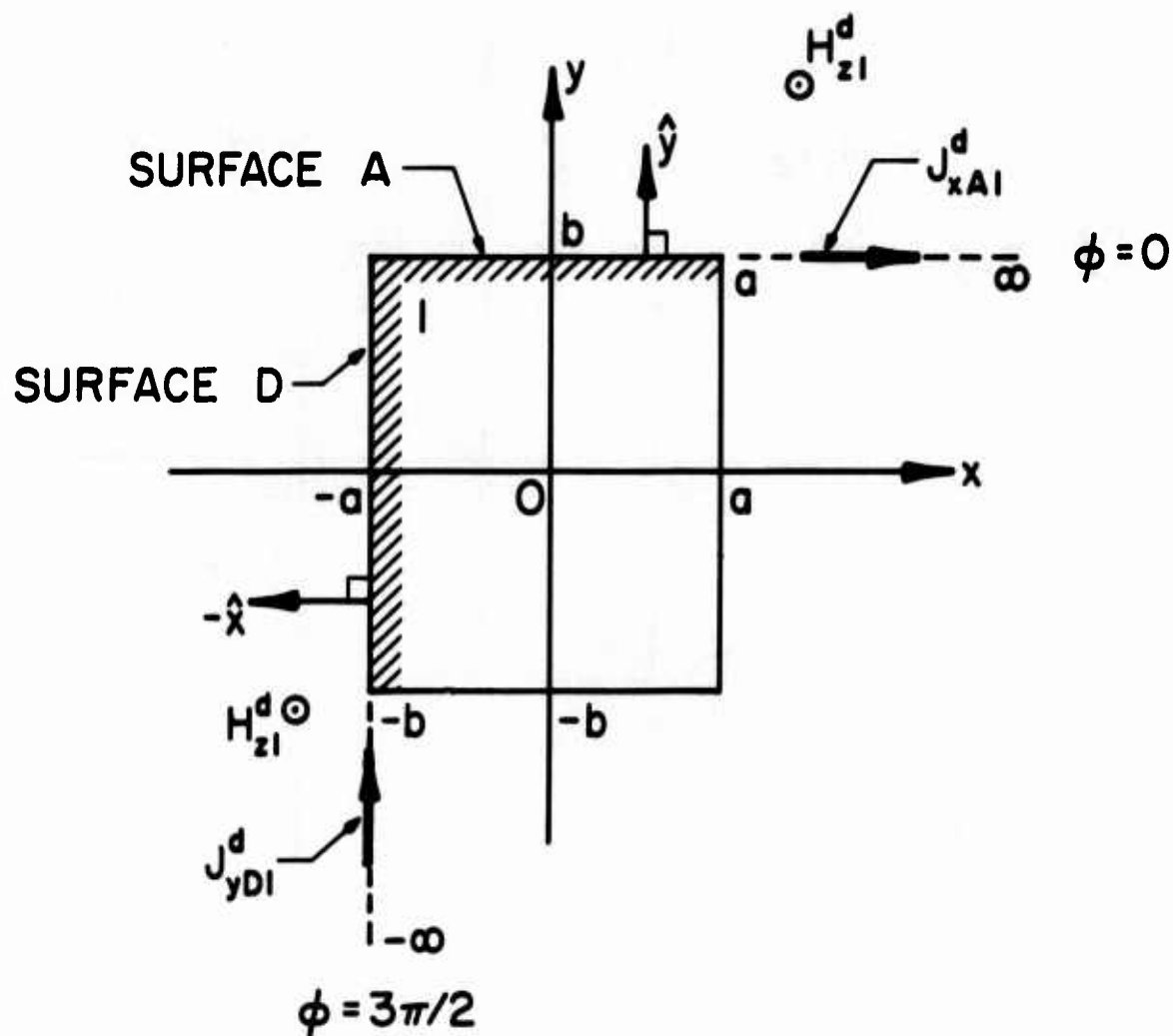
Figure 5.9a. J^d_{yD1}, J^d_{xA1} contribute to the discontinuities in the far field at $\phi = \frac{3\pi}{2}$, $\phi = 0$, respectively.
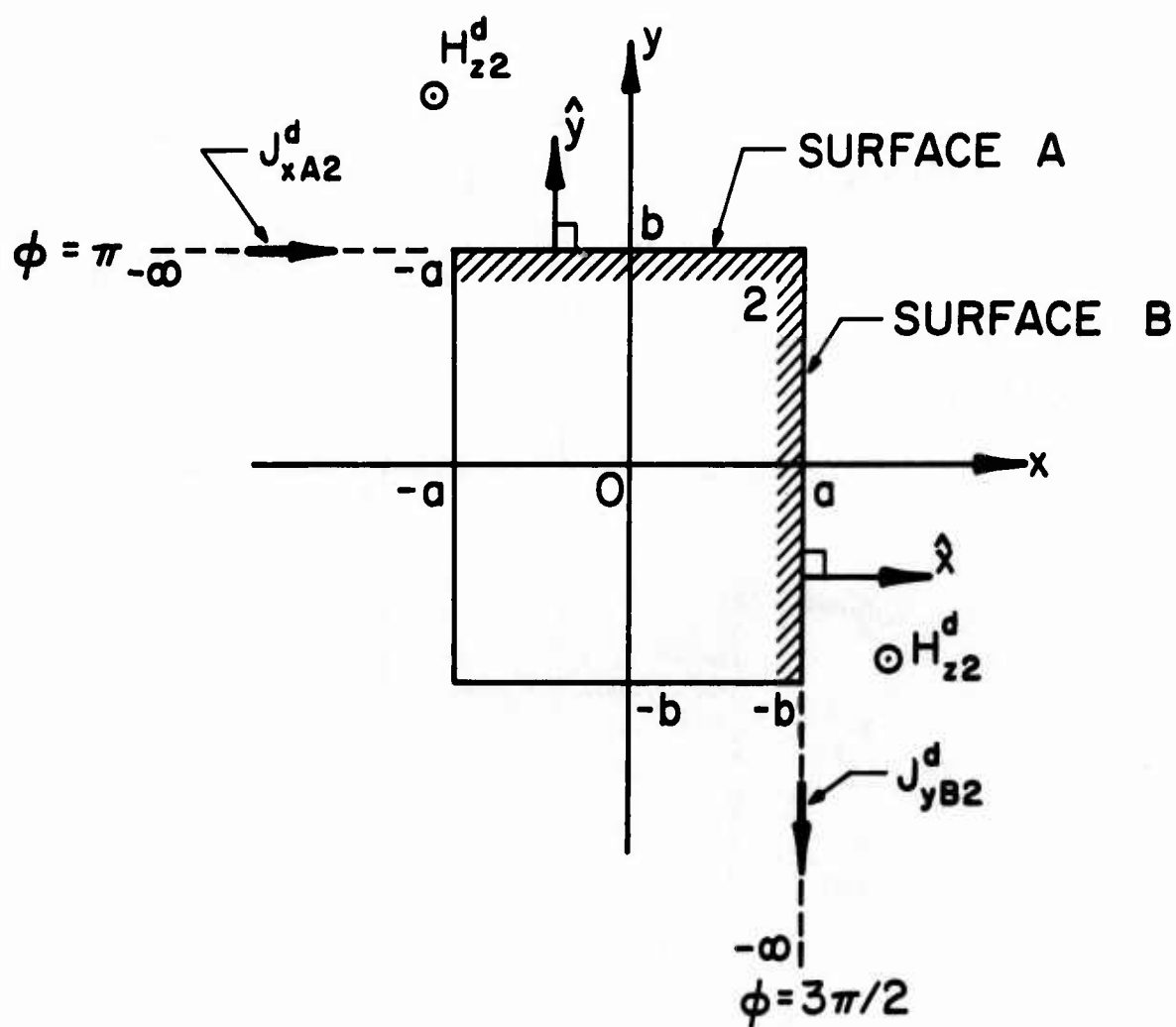
Figure 5.9b. J_{yB2}^d, J_{xA2}^d contribute to the discontinuities in the far field at $\phi = \frac{3\pi}{2}$, $\phi = \pi$, respectively.
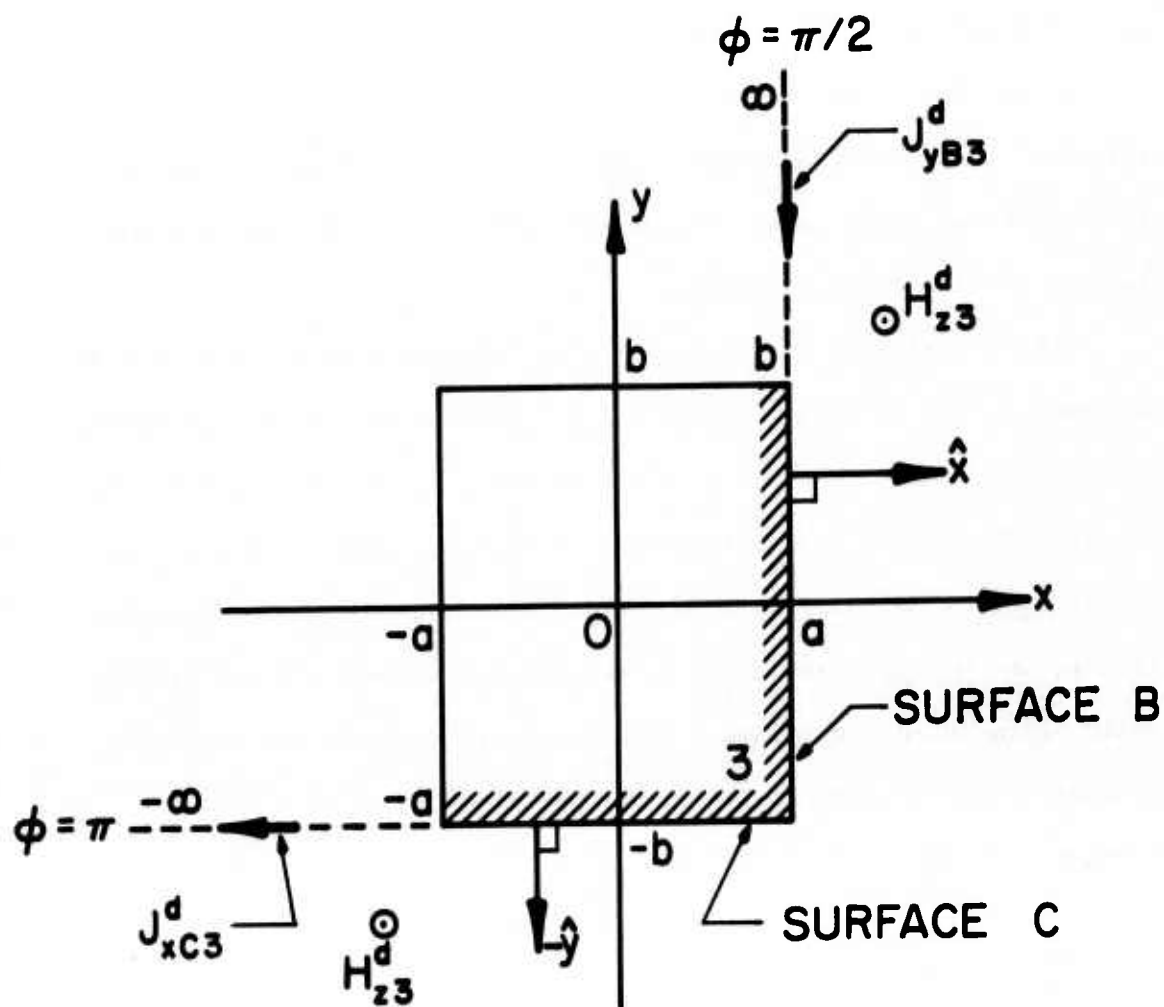
Figure 5.9c. J^d_{xC3}, J^d_{yB3} contribute to the discontinuities in the far field at $\phi = \pi$, $\phi = \frac{\pi}{2}$, respectively.

used in the canonical problems. Now that the cause of the existence of

the discontinuities in the far-field pattern at $\phi = 0$, $\frac{\pi}{2}$, π, and $\frac{3\pi}{2}$

has been found, we proceed to give them a physical interpretation which

in turn provides a clue to their elimination.

In the following discussion, a typical case is studied and the

solution to this case is derived in a step-by-step fashion. While

the results of other cases will be exhibited, their derivations are

left to the interested reader.

The typical case as shown in Figure 5.9a is studied. Let us con-

centrate on the extension of surface A. This extension is represented

by a dashed line from $x = a$ to $x = \infty$ at $y = b$ in the direction $\phi = 0$.

On one side of this plane, there exists H_{z1}^d as shown in Figure 5.9a,

on the other side there is zero field. By classical electromagnetic

theory, we conclude that there is an electric surface current density

existing in the dashed plane. Such a current radiates in free space

to support this discontinuity in the H-field. In compact mathematical

language, we write

$$\bar{J}_{A1}^d = \hat{n} \times \bar{H}_1^d$$

$$= \hat{y} \times \hat{z} H_{z1}^d$$

$$= \hat{x} H_{z1}^d$$

$$= \hat{x} J_{xA1}^d \tag{5.21}$$

where $\hat{n}$ is the unit normal vector to the surface A, the subscript A

refers to the extension of surface A, the subscript 1 designates the

wedge under consideration, the superscript d means diffraction, and the rest should be self-explanatory. Note that a factor of 2 is not present in (5.21) because this J_{xA1}^d is simply the discontinuity in free space of the H-field and there is no backing of perfect conductor in this situation.

Referring to (5.5a) and keeping in mind that the original diffraction coefficient is perfectly valid in the direction $\phi = 0$, which implies that the procedure of subtracting the pole singularities need not concern us here, we can write

$$J_{xA1}^d = H_{z1}^d (\phi = 0)$$

$$= f_1(\phi = 0) \cdot \frac{e^{ik\rho}}{\sqrt{\rho}} \delta(y - b) , \quad \rho \approx x \in (a, \infty) \quad (5.22a)$$

where

$$f_1(\phi = 0) = e^{-ik(-a\cos\phi_0 + b\sin\phi_0)}$$

$$\cdot \frac{e^{i\frac{\pi}{4}}}{\sqrt{2\pi k}} \left[\frac{\frac{2}{3} \sin\frac{2\pi}{3} e^{ika}}{\cos\frac{2\pi}{3} - \cos\frac{2}{3}\phi_0} + \frac{\frac{2}{3} \sin\frac{2\pi}{3} e^{ika}}{\cos\frac{2\pi}{3} - \cos\frac{2}{3}\phi_0} \right] \cdot \quad (5.22b)$$

Note that in the above equation, an approximation of ρ by x has been made and a constant value zero for the variable ϕ has been assumed. The far-field expression as given in (5.5a) can be legitimately used to compute the H-field on the dashed plane because any observation points in that plane will be at least at a distance of $2a = 2\lambda$ away from the edge of wedge 1.

The H-field generated by J_{xA1}^d is

$$\bar{H}_{A1}^{dEx} = -ik \frac{e^{ik\rho}}{\sqrt{8\pi k\rho}} e^{i\frac{\pi}{4}} [-\hat{z}(-\sin \phi \tilde{J}_{xA1}^d)] \qquad (5.23)$$

where the superscript Ex stands for "excess" to remind the reader that this field has been created artificially by abruptly truncating the diffracted fields, therefore, it should not have existed; hence, the word "excess." $\tilde{J}_{xA1}^d$ in (5.23) is given by

$$\tilde{J}_{xA1}^d = F\{J_{xA1}^d\}$$

$$= f_1(\phi = 0) \int_{-\infty}^{\infty} \int_a^{\infty} \frac{e^{ikx}}{\sqrt{x}} \delta(y - b) e^{-i\alpha x} e^{-i\beta y} dxdy$$

$$= f_1(\phi = 0) e^{-i\beta b} \int_a^{\infty} \frac{e^{ix(k-\alpha)}}{\sqrt{x}} dx \qquad . \qquad (5.24)$$

By letting $x(k - \alpha) = \frac{\pi}{2} t^2$, the integral with respect to x can be transformed into an integral with respect to t which may be identified with the well-tabulated Fresnel integrals, i.e.,

$$\int_a^{\infty} \frac{e^{ix(k-\alpha)}}{\sqrt{x}} dx$$

$$= \frac{\sqrt{2\pi}}{\sqrt{k - \alpha}} \int_{\sqrt{\frac{2a}{\pi}(k-\alpha)}}^{\infty} e^{i\frac{\pi}{2}t^2} dt \qquad (5.25a)$$

$$= \frac{\sqrt{2\pi}}{\sqrt{k-\alpha}} \left[\int_0^\infty e^{i\frac{\pi}{2}t^2} dt - \int_0^{\sqrt{\frac{2a}{\pi}(k-\alpha)}} e^{i\frac{\pi}{2}t^2} dt \right] \qquad (5.25b)$$

$$= \frac{\sqrt{2\pi}}{\sqrt{k}\sqrt{1-\cos\phi}} \left[\frac{e^{i\frac{\pi}{4}}}{\sqrt{2}} - \left\{ C\left(\sqrt{\frac{2ak}{\pi}(1-\cos\phi)}\right) + iS\left(\sqrt{\frac{2ak}{\pi}(1-\cos\phi)}\right) \right\} \right] \qquad (5.25c)$$

In writing (5.25), we have explicitly used the relation $\alpha = k\cos\phi$ and the definitions of the Fresnel integrals, i.e.,

$$C(\xi) = \int_0^\xi \cos\left(\frac{\pi}{2}t^2\right) dt \qquad (5.26a)$$

and

$$S(\xi) = \int_0^\xi \sin\left(\frac{\pi}{2}t^2\right) dt \quad . \qquad (5.26b)$$

A knowledgeable reader could raise a question here concerning the validity of the upper limit of the integral in (5.25a). However, one need not be concerned with limits at this point of the derivation; instead, one should merely view this as a formal transformation so that the original integral can be manipulated into a form in which the limit can be readily studied. The validity of this transformation will also be substantiated by numerical computations in the next section.

Substituting (5.25c) in (5.24) and the resulting expression for $\tilde{J}^d_{xA1}$ back into (5.23), we have

$$\bar{H}_{A1}^{dEx} = -ik \frac{e^{ik\rho}}{\sqrt{8\pi k\rho}} e^{i\frac{\pi}{4}} \left[-2 \left(-\sin\phi f_1(\phi = 0) e^{-ikb\sin\phi} \right. \right.$$

$$\left. \left. \cdot \frac{\sqrt{2\pi}}{\sqrt{k}\sqrt{1-\cos\phi}} \left[\frac{e^{i\frac{\pi}{4}}}{\sqrt{2}} - \left\{ C\left(\sqrt{\frac{2ak}{\pi}(1-\cos\phi)} \right) + iS\left(\sqrt{\frac{2ak}{\pi}(1-\cos\phi)} \right) \right\} \right] \right) \right] \tag{5.27}$$

where $f_1(\phi = 0)$ is given in (5.22b).

Now we have the expression for the field generated by J_{xA1}^d as shown in (5.27). The next step is to examine the discontinuity introduced at $\phi = 0$ by $\bar{H}_{A1}^{dEx}$. To this end, all we need to pay attention to is the following limit:

$$\lim_{\phi \to \binom{0}{2\pi}} \frac{\sin\phi}{\sqrt{1-\cos\phi}} = \lim_{\phi \to \binom{0}{2\pi}} \frac{2\sin\frac{\phi}{2}\cos\frac{\phi}{2}}{\sqrt{2}\sin\frac{\phi}{2}} = \left\{ \begin{matrix} \sqrt{2} \\ -\sqrt{2} \end{matrix} \right\} \quad . \tag{5.28}$$

Using (5.28) and (5.27), the discontinuity introduced at $\phi = 0$ by $\bar{H}_{A1}^{dEx}$ is found to be

$$\bar{H}_{A1}^{dEx}(\phi = 0) - \bar{H}_{A1}^{dEx}(\phi = 2\pi)$$

$$= -ik \frac{e^{ik\rho}}{\sqrt{8\pi k\rho}} e^{i\frac{\pi}{4}} \left[-2 \left(-[\sqrt{2} - (-\sqrt{2})] f_1(\phi = 0) \cdot \sqrt{\frac{2\pi}{k}} \frac{e^{i\frac{\pi}{4}}}{\sqrt{2}} \right) \right]$$

$$= 2 \frac{e^{i\frac{\pi}{4}}}{\sqrt{2}} \frac{e^{ik\rho}}{\sqrt{\pi k\rho}} \left[e^{-ik(-a\cos\phi_0 + b\sin\phi_0)} \frac{(2)(\frac{2}{3}\sin\frac{2\pi}{3})e^{ika}}{\cos\frac{2\pi}{3} - \cos\frac{2}{3}\phi_0} \right] \quad . \tag{5.29}$$

It is indeed enlightening to see that this discontinuity is exactly the discontinuity given in (5.16e). The study of the typical case is now completed. For the cases depicted in Figures 5.9a, 5.9b, and 5.9c, we simply list the results as follows:

The H-field generated by J_{yD1}^d in Figure 5.9a is

$$\bar{H}_{D1}^{dEx} = -ik \frac{e^{ik\rho}}{\sqrt{8\pi k\rho}} e^{i\frac{\pi}{4}} \left[-2 \cos \phi \ f_1(\phi = \frac{3\pi}{2}) \ e^{ikacos\phi} \right.$$

$$\left. \cdot \frac{\sqrt{2\pi}}{\sqrt{k}\sqrt{1 + \sin \phi}} \left[\frac{e^{i\frac{\pi}{4}}}{\sqrt{2}} - \left\{ C\left(\sqrt{\frac{2bk}{\pi}}(1 + \sin \phi) \right) + iS\left(\sqrt{\frac{2kb}{\pi}}(1 + \sin \phi) \right) \right\} \right] \right]$$

$$(5.30a)$$

where

$$f_1(\phi = \frac{3\pi}{2}) = e^{-ik(-acos\phi_0 + bsin\phi_0)} \cdot e^{ikb}$$

$$\cdot \frac{e^{i\frac{\pi}{4}}}{\sqrt{2\pi k}} \left[\frac{\frac{2}{3} \sin \frac{2\pi}{3}}{\cos \frac{2\pi}{3} - \cos \frac{2}{3}(\frac{3\pi}{2} - \phi_0)} + \frac{\frac{2}{3} \sin \frac{2\pi}{3}}{\cos \frac{2\pi}{3} - \cos \frac{2}{3}(\frac{3\pi}{2} + \phi_0)} \right] \cdot$$

$$(5.30b)$$

The H-field generated by J_{xA2}^d in Figure 5.9b is

$$\bar{H}_{A2}^{dEx} = -ik \frac{e^{ik\rho}}{\sqrt{8\pi k\rho}} e^{i\frac{\pi}{4}} \left[-2\left(-\sin \phi \ f_2(\phi = \pi) \ e^{-ikbsin\phi} \right. \right.$$

$$\left. \left. \cdot \frac{\sqrt{2\pi}}{\sqrt{k}\sqrt{1 + \cos \phi}} \left[\frac{e^{i\frac{\pi}{4}}}{\sqrt{2}} - \left\{ C\left(\sqrt{\frac{2ak}{\pi}}(1 + \cos \phi) \right) + iS\left(\sqrt{\frac{2ak}{\pi}}(1 + \cos \phi) \right) \right\} \right] \right) \right]$$

$$(5.31a)$$

where

$$f_2(\phi = \pi) = e^{-ik(a\cos\phi_0 + b\sin\phi_0)} \cdot e^{ika}$$

$$\cdot \frac{e^{i\frac{\pi}{4}}}{\sqrt{2\pi k}} \left[\frac{\frac{2}{3}\sin\frac{2\pi}{3}}{\cos\frac{2\pi}{3} - \cos\frac{2}{3}(\pi - \phi_0)} + \frac{\frac{2}{3}\sin\frac{2}{3}\pi}{\cos\frac{2\pi}{3} - \cos\frac{2}{3}(\pi - \phi_0)} \right] \quad .(5.31b)$$

The H-field generated by J_{yB2}^d in Figure 5.9b is

$$\bar{H}_{B2}^{dEx} = -ik \frac{e^{ik\rho}}{\sqrt{8\pi k\rho}} \frac{e^{i\frac{\pi}{4}}}{} \left[-2 \cos\phi \; f_2(\phi = \frac{3\pi}{2}) \; e^{-ika\cos\phi} \right.$$

$$\left. \cdot \frac{\sqrt{2\pi}}{\sqrt{k}\sqrt{1 + \sin\phi}} \left[\frac{e^{i\frac{\pi}{4}}}{\sqrt{2}} - \left\{ C\left(\sqrt{\frac{2bk}{\pi}(1 + \sin\phi)} \right) + iS\left(\sqrt{\frac{2bk}{\pi}(1 + \sin\phi)} \right) \right\} \right] \right]$$
$$(5.32a)$$

where

$$f_2(\phi = \frac{3\pi}{2}) = -e^{-ik(a\cos\phi_0 + b\sin\phi_0)} \cdot e^{ikb} \cdot \frac{e^{i\frac{\pi}{4}}}{\sqrt{2\pi k}}$$

$$\cdot \left[\frac{\frac{2}{3}\sin\frac{2}{3}\pi}{\cos\frac{2\pi}{3} - \cos\frac{2}{3}[(3\pi - \frac{3\pi}{2}) - (\pi - \phi_0)]} \right.$$

$$\left. + \frac{\frac{2}{3}\sin\frac{2\pi}{3}}{\cos\frac{2\pi}{3} - \cos\frac{2}{3}[(3\pi - \frac{3\pi}{2}) + (\pi - \phi_0)]} \right] . \qquad (5.32b)$$

The H-field generated by J_{yB3}^d in Figure 5.9c is

$$\bar{H}_{B3}^{dEx} = -ik \frac{e^{ik\rho}}{\sqrt{8\pi k\rho}} e^{i\frac{\pi}{4}} \left[-\hat{z} \cos \phi \, f_3(\phi = \frac{\pi}{2}) \, e^{-ikacos\phi} \cdot \frac{\sqrt{2\pi}}{\sqrt{k}\sqrt{1 - \sin \phi}} \right.$$

$$\left. \cdot \left[\frac{e^{i\frac{\pi}{4}}}{\sqrt{2}} - \left\{ C\left(\sqrt{\frac{2bk}{\pi}}(1 - \sin \phi) \right) + iS\left(\sqrt{\frac{2bk}{\pi}}(1 - \sin \phi) \right) \right\} \right] \right] \qquad (5.33a)$$

where

$$f_3(\phi = \frac{\pi}{2}) = -e^{-ik(acos\phi_0 - bsin\phi_0)} \cdot e^{ikb} \cdot \frac{e^{i\frac{\pi}{4}}}{\sqrt{2\pi k}}$$

$$\cdot \left[\frac{\frac{2}{3} \sin \frac{2}{3}\pi}{\cos \frac{2\pi}{3} - \cos \frac{2}{3}(\frac{\pi}{2} - \phi_0)} + \frac{\frac{2}{3} \sin \frac{2\pi}{3}}{\cos \frac{2\pi}{3} - \cos \frac{2}{3}(\frac{\pi}{2} - \phi_0)} \right] \qquad (5.33b)$$

The H-field generated by J_{xC3}^d in Figure 5.9c is

$$\bar{H}_{C3}^{dEx} = -ik \frac{e^{ik\rho}}{\sqrt{8\pi k\rho}} e^{i\frac{\pi}{4}} \left[\hat{z} \sin \phi \, f_3(\phi = \pi) \, e^{ikbsin\phi} \cdot \frac{\sqrt{2\pi}}{\sqrt{k}\sqrt{1 + \cos \phi}} \right.$$

$$\left. \cdot \left[\frac{e^{i\frac{\pi}{4}}}{\sqrt{2}} - \left\{ C\left(\sqrt{\frac{2ak}{\pi}}(1 + \cos \phi) \right) + iS\left(\sqrt{\frac{2ak}{\pi}}(1 + \cos \phi) \right) \right\} \right] \right] \qquad (5.34a)$$

where

$$f_3(\phi = \pi) = -e^{-ik(acos\phi_0 - bsin\phi_0)} \cdot e^{ika} \cdot \frac{e^{i\frac{\pi}{4}}}{\sqrt{2\pi k}}$$

$$\cdot \left[\frac{\frac{2}{3} \sin \frac{2\pi}{3}}{\cos \frac{2\pi}{3} - \cos \frac{2}{3}(\pi + \phi_0)} + \frac{\frac{2}{3} \sin \frac{2\pi}{3}}{\cos \frac{2\pi}{3} - \cos \frac{2}{3}(2\pi - \phi_0)} \right] \qquad (5.34b)$$

To examine the discontinuity introduced at $\phi = \frac{\pi}{2}$ by $\bar{H}_{B3}^{dEx}$, we use (5.33) to obtain

$$\bar{H}_{B3}^{dEx}\left(\phi = \frac{\pi}{2}-\right) - \bar{H}_{B3}^{dEx}\left(\phi = \frac{\pi}{2}+\right) = -ik\frac{e^{ik\rho}\,e^{i\frac{\pi}{4}}}{\sqrt{8\pi k\rho}}$$

$$\cdot\left[-\hat{z}\{(\sqrt{1 + \sin\frac{\pi}{2}})-(-\sqrt{1 + \sin\frac{\pi}{2}})\}\cdot f_3(\phi = \frac{\pi}{2})\cdot\frac{\sqrt{2\pi}}{\sqrt{k}}\cdot\frac{e^{i\frac{\pi}{4}}}{\sqrt{2}}\right]$$

$$= 2\frac{e^{ik\rho}\,e^{i\frac{\pi}{4}}}{\sqrt{2}\sqrt{\pi k\rho}}\left[e^{-ik(a\cos\phi_0 - b\sin\phi_0)}\frac{(2)(\frac{2}{3}\sin\frac{2\pi}{3})\,e^{ikb}}{\cos\frac{2\pi}{3} - \cos\frac{2}{3}(\frac{\pi}{2} - \phi_0)}\right].(5.35)$$

Again, this discontinuity is identical to that given in (5.17c).

To examine the discontinuity at $\phi = \pi$, we use both $\bar{H}_{A2}^{dEx}$ and $\bar{H}_{C3}^{dEx}$ given by (5.31) and (5.34), respectively, since both J_{xA2}^d and J_{xC3}^d contribute to the discontinuity. Hence, the discontinuity at $\phi = \pi$ is

$$\left[\bar{H}_{A2}^{dEx}(\phi = \pi-) - \bar{H}_{A2}^{dEx}(\phi = \pi+)\right] + \left[\bar{H}_{C3}^{dEx}(\phi = \pi-) - \bar{H}_{C3}^{dEx}(\phi = \pi+)\right]$$

$$= -ik\frac{e^{ik\rho}\,e^{i\frac{\pi}{4}}}{\sqrt{8\pi k\rho}}\left[2\{(\sqrt{2}\sin\frac{\pi}{2})-(-\sqrt{2}\sin\frac{\pi}{2})\}\,f_2(\phi = \pi)\cdot\frac{\sqrt{2\pi}}{\sqrt{k}}\cdot\frac{e^{i\frac{\pi}{4}}}{\sqrt{2}}\right]$$

$$- ik\frac{e^{ik\rho}\,e^{i\frac{\pi}{4}}}{\sqrt{8\pi k\rho}}\left[2\{(\sqrt{2}\sin\frac{\pi}{2})-(-\sqrt{2}\sin\frac{\pi}{2})\}\,f_3(\phi = \pi)\cdot\frac{\sqrt{2\pi}}{\sqrt{k}}\cdot\frac{e^{i\frac{\pi}{4}}}{\sqrt{2}}\right]$$

$$= \frac{e^{ik\rho}\,e^{i\frac{\pi}{4}}}{\sqrt{\pi k\rho}}\left[2\frac{1}{\sqrt{2}}\cdot e^{-ik(a\cos\phi_0 + b\sin\phi_0)}\cdot e^{ika}\cdot 2\cdot\frac{\frac{2}{3}\sin\frac{2\pi}{3}}{\cos\frac{2\pi}{3} - \cos\frac{2}{3}(\pi - \phi_0)}\right]$$

$$+ \frac{e^{ik\rho}}{\sqrt{\pi k\rho}} \left[2\, \frac{e^{i\frac{\pi}{4}}}{\sqrt{2}} \cdot (-1)\, e^{-ik(a\cos\phi_0 - b\sin\phi_0)}\, e^{ika} \right.$$

$$\left. \cdot \left\{ \frac{\frac{2}{3}\sin\frac{2\pi}{3}}{\cos\frac{2\pi}{3} - \cos\frac{2}{3}(\pi + \phi_0)} + \frac{\frac{2}{3}\sin\frac{2\pi}{3}}{\cos\frac{2\pi}{3} - \cos\frac{2}{3}(2\pi - \phi_0)} \right\} \right] \qquad (5.36)$$

which is identical to the discontinuity in (5.19c).

Finally, to examine the discontinuity at $\phi = \frac{3\pi}{2}$ due to both J_{yD1}^d and J_{yB2}^d, we use $\bar{H}_{D1}^{dEx}$ and $\bar{H}_{B2}^{dEx}$ given in (5.30) and (5.32), respectively, to get

$$\left[\bar{H}_{D1}^{dEx}\left(\frac{3\pi}{2}-\right) - \bar{H}_{D1}^{dEx}\left(\frac{3\pi}{2}+\right) \right] + \left[\bar{H}_{B2}^{dEx}\left(\frac{3\pi}{2}-\right) - \bar{H}_{B2}^{dEx}\left(\frac{3\pi}{2}+\right) \right]$$

$$= -ik\, \frac{e^{ik\rho}}{\sqrt{8\pi k\rho}}\, e^{i\frac{\pi}{4}} \left[-2\{(-\sqrt{2}) - (\sqrt{2})\} \cdot f_1\left(\phi = \frac{3\pi}{2}\right) \cdot \frac{\sqrt{2\pi}}{\sqrt{k}} \cdot \frac{e^{i\frac{\pi}{4}}}{\sqrt{2}} \right]$$

$$- ik\, \frac{e^{ik\rho}}{\sqrt{8\pi k\rho}}\, e^{i\frac{\pi}{4}} \left[-2\{(-\sqrt{2}) - (\sqrt{2})\} \cdot f_2\left(\phi = \frac{3\pi}{2}\right) \cdot \frac{\sqrt{2\pi}}{\sqrt{k}} \cdot \frac{e^{i\frac{\pi}{4}}}{\sqrt{2}} \right]$$

$$= \frac{e^{ik\rho}}{\sqrt{\pi k\rho}} \left[2\, \frac{e^{i\frac{\pi}{4}}}{\sqrt{2}} \cdot e^{-ik(-a\cos\phi_0 + b\sin\phi_0)}\, e^{ikb} \right.$$

$$\left. \cdot \left[\frac{\frac{2}{3}\sin\frac{2\pi}{3}}{\cos\frac{2\pi}{3} - \cos\frac{2}{3}(\frac{3\pi}{2} - \phi_0)} + \frac{\frac{2}{3}\sin\frac{2\pi}{3}}{\cos\frac{2\pi}{3} - \cos\frac{2}{3}(\frac{3\pi}{2} + \phi_0)} \right] \right]$$

$$+ \frac{e^{ik\rho}\, e^{i\frac{\pi}{4}}}{\sqrt{\pi k\rho}} \left[2\, \frac{1}{\sqrt{2}} \cdot (-1) \cdot e^{-ik(a\cos\phi_0 + b\sin\phi_0)}\, e^{ikb} \right.$$

$$\cdot \left[\frac{\frac{2}{3} \sin \frac{2\pi}{3}}{\cos \frac{2\pi}{3} - \cos \frac{2}{3}(\frac{\pi}{2} + \phi_0)} + \frac{\frac{2}{3} \sin \frac{2\pi}{3}}{\cos \frac{2\pi}{3} - \cos \frac{2}{3}(\frac{5\pi}{2} - \phi_0)} \right] \right] \tag{5.37}$$

which is identical to the discontinuity in (5.20c).

Before closing this section, it is worthwhile to recapitulate the main points discussed. The discontinuities at $\phi = 0$, $\frac{\pi}{2}$, π, and $\frac{3\pi}{2}$ in the far-field pattern obtained by the GTD technique have been shown to be caused by the abrupt truncation of the diffracted field which is effectively equivalent to artificially introducing sheets of electric surface current in free space. When these current sheets radiate strongly in the directions $\phi = 0$, $\frac{\pi}{2}$, π, and $\frac{3\pi}{2}$, they produce discontinuities corresponding exactly to those in the GTD far-field pattern. This discovery provides us a clue to further improve the GTD far-field pattern. One simply subtracts out all these artificially created "excess" fields from the GTD far-field pattern to get rid of these discontinuities. The improved GTD far-field pattern is discussed in the next section along with some comparisons with the conventional moment method solution and results obtained by a GTD-moment method hybrid technique [4] and a self-consistent method [24].

5.3 Improved Far-Field Pattern and Comparison with Results Obtained by Other Approaches

In the last section, Keller's wedge diffraction coefficient was used to construct the far field scattered by a rectangular cylinder. It was shown that when the pole singularities contained in the physical optics current with infinite support on the semi-infinite wedge surface

were subtracted from the wedge diffraction coefficient, the far field remained finite and varied smoothly across the geometrical optics shadow and reflection boundaries. Other than the noticeable discontinuities in the directions in which the surfaces of the rectangular cylinder are oriented, that far-field pattern was in fair agreement with the conventional moment method solution.

Then it was found that these discontinuities were caused by abrupt truncations of the diffracted field to the regions in space which correspond to the exterior regions in the wedge canonical problems. These abrupt truncations were demonstrated to be effectively equivalent to artificial introductions of semi-infinite electric surface current sheets in free space. An in-depth study of these current sheets consequently showed that they radiated strongly and introduced identical discontinuities in those directions corresponding to the discontinuities in the GTD far field. This discovery provides a clue which leads to further improvement of the GTD far-field pattern.

The elimination of these discontinuities can be achieved by subtracting $\bar{H}_{A1}^{dEx}$, $\bar{H}_{D1}^{dEx}$, $\bar{H}_{A2}^{dEx}$, $\bar{H}_{B2}^{dEx}$, $\bar{H}_{B3}^{dEx}$, and $\bar{H}_{C3}^{dEx}$, given in (5.27), (5.30), (5.31), (5.32), (5.33), and (5.34), correspondingly, from the GTD H_z^d given in (5.4). The improved GTD far-field pattern so obtained is displayed in Figure 5.10. It is very interesting to observe that not only the discontinuities at $\phi = 0$, $\frac{\pi}{2}$, π, and $\frac{3\pi}{2}$ disappear completely, but also that nulls, which were not present in the GTD far-field pattern in Figure 5.7, are showing up in the neighborhood of $\phi = \pi$ and $\phi = \frac{3\pi}{2}$. The disappearance of the discontinuities is to be expected since these discontinuities have been examined carefully in the last section
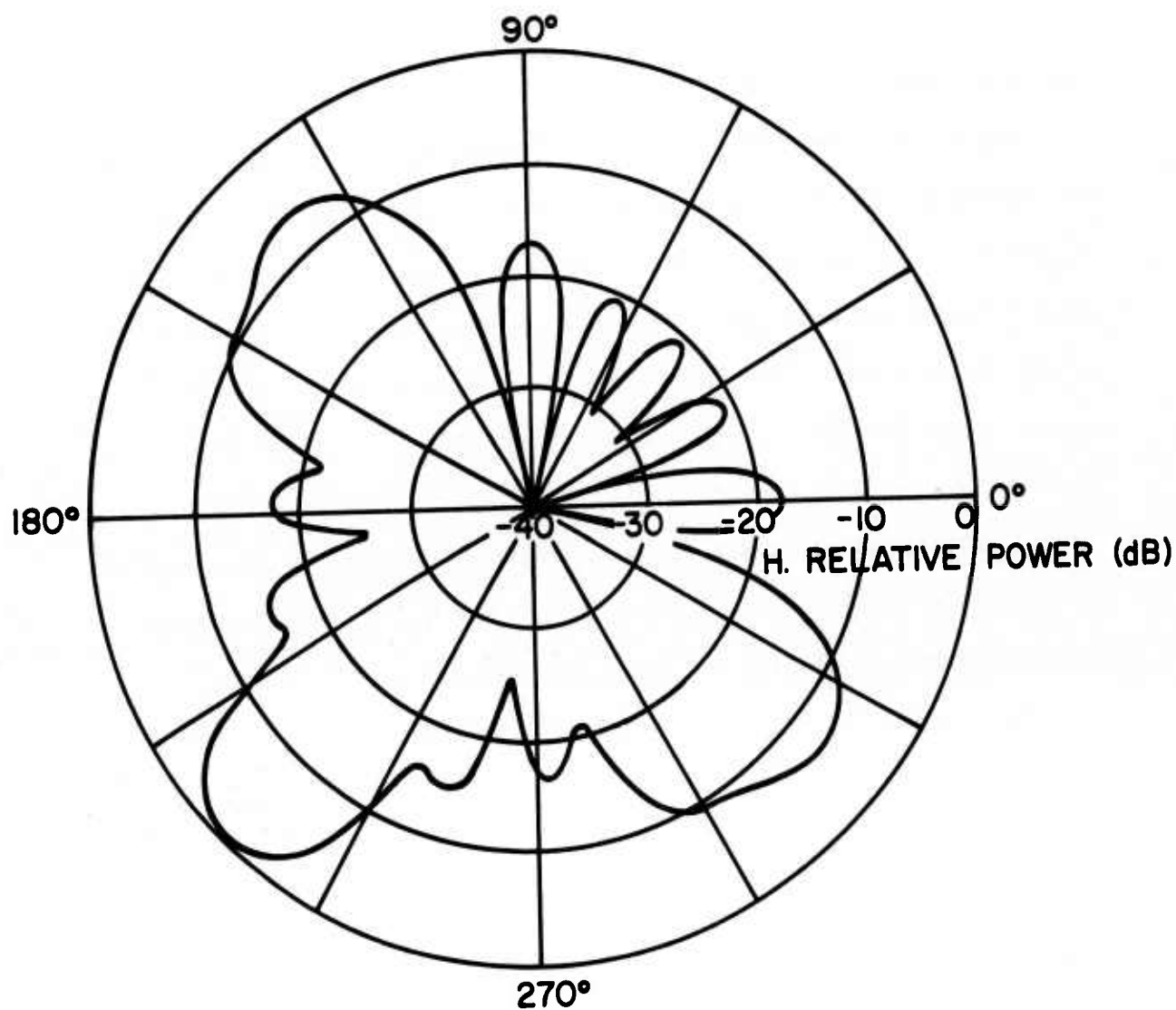
Figure 5.10.   Improved scattered far-field pattern of the rectangular
cylinder; $\phi_0 = \pi/4$, $a = b = 1\lambda$.

(see (5.29), (5.35), (5.36), and (5.37)) and were shown to be identical to those in the GTD far-field pattern in Figure 5.7.

Finally, results obtained by using (a) conventional moment method [17] with 32 unknowns, (b) hybrid moment method and GTD technique by Burnside *et al.* [4] with 24 unknowns, and (c) self-consistent method [24] with 8 unknowns are exhibited in Figure 5.11. If one pays attention to the insertion in Figure 5.11 showing the geometry of their problem, one will realize that their incident field is from a direction exactly opposite to the one used in this study, hence, their far-field pattern is opposite to that in Figure 5.10. Note that in Figure 5.11, the solution obtained by the self-consistent method, which apparently includes *all* higher-order multiple-edge interactions in its formulation, still has the discontinuities at $\phi = 0$, 90°, 180°, and 270°. While the conventional moment method solution and the moment method-GTD hybrid solution deviate only slightly in the backscattering direction, the present method solution as shown in Figure 5.10 is in good agreement with them.
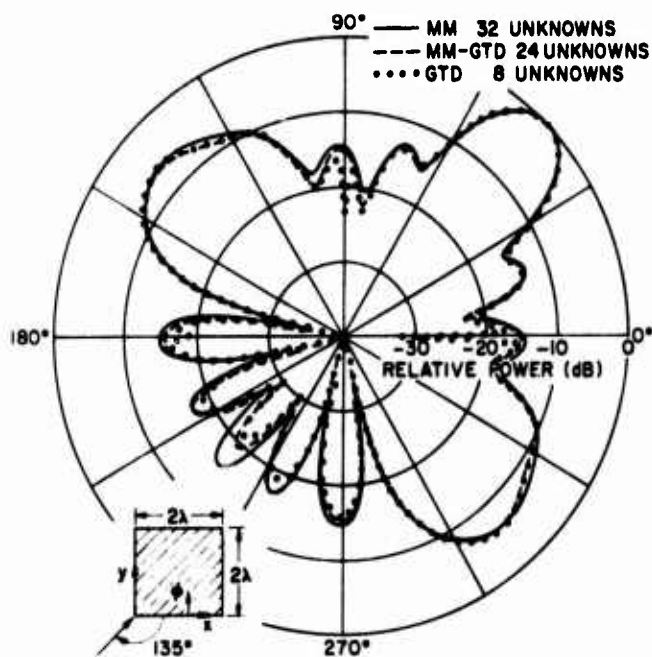
Figure 5.11. Scattered far-field patterns obtained
by other approaches.

5.4 Accuracy Check

In the previous sections, a method has been discussed for obtaining an improved scattered far-field pattern of a perfectly conducting rectangular cylinder illuminated by a plane wave whose magnetic intensity vector is parallel to the axis of the cylinder. The resulting improved scattered far-field pattern has been compared with results obtained by other approaches in the literature. In particular, results obtained by using (a) conventional moment method [17] with 32 unknowns; (b) hybrid moment method and GTD technique by Burnside *et al.* [4] with 24 unknowns, and (c) self-consistent method [24] with 8 unknowns have been used for comparisons.

Out of these three different approaches, only the conventional moment method has *consistently* taken into account in its formulation the boundary condition, requiring the tangential components of the total electric field be vanished on the surface of the rectangular cylinder. In Burnside's hybrid moment method and GTD technique, the boundary condition is not enforced on the entire surface of the scattering object, as in the case of the conventional moment method. Instead, point matching is applied at the midpoint of each of the pulse current segments located near the diffracting edges of the wedges of the rectangular cylinder, and at some arbitrary points in the GTD regions of the surface of the rectangular cylinder in order to obtain an equal number of equations as the involved unknowns including the current samples and the diffraction constants. The final result is somewhat dependent on the locations of the arbitrarily chosen additional matching points in the GTD region on the surface of the scatterer. Therefore, it takes a judicious choice

of the locations of the aforementioned matching points and quite often, in
such a situation, more matching points than unknowns are needed such
that some averaging schemes can be applied to obtain meaningful results.
In the self-consistent method, no considerations are given to the satis-
faction of the boundary condition.

Although the comparisons of the scattered far-field pattern with
those obtained by the aforementioned methods are very favorable, indicating
the solutions are in good agreement with the true solution, an independent
accuracy check must be applied to further validate the approximate solu-
tion, especially when there are no available results in the literature
to compared with. Such an accuracy check is often needed but is not
readily available in the high-frequency asymptotic techniques.

In this section, we present a method which allows us to calculate
the tangential components of the scattered electric field on the surface
of the scatterer using the approximate scattered far-field pattern. The
accuracy of the solution can then be checked simply by observing whether
these tangential components of the scattered electric field on the sur-
face of the scatterer are equal to the negative of the tangential components
of the incident electric field on the surface of the scatterer. If the
outcome of such an observation is favorable, then the solution is good;
otherwise, further improvement is needed.

5.4.1 Method of computation

In classical electromagnetic theory, it is well-known that the
scattered magnetic far field is related to the Fourier transform of
the scattered electric field on an aperture in a relatively simple manner.
Consider the aperture shown in Figure 5.12. This aperture is a plane
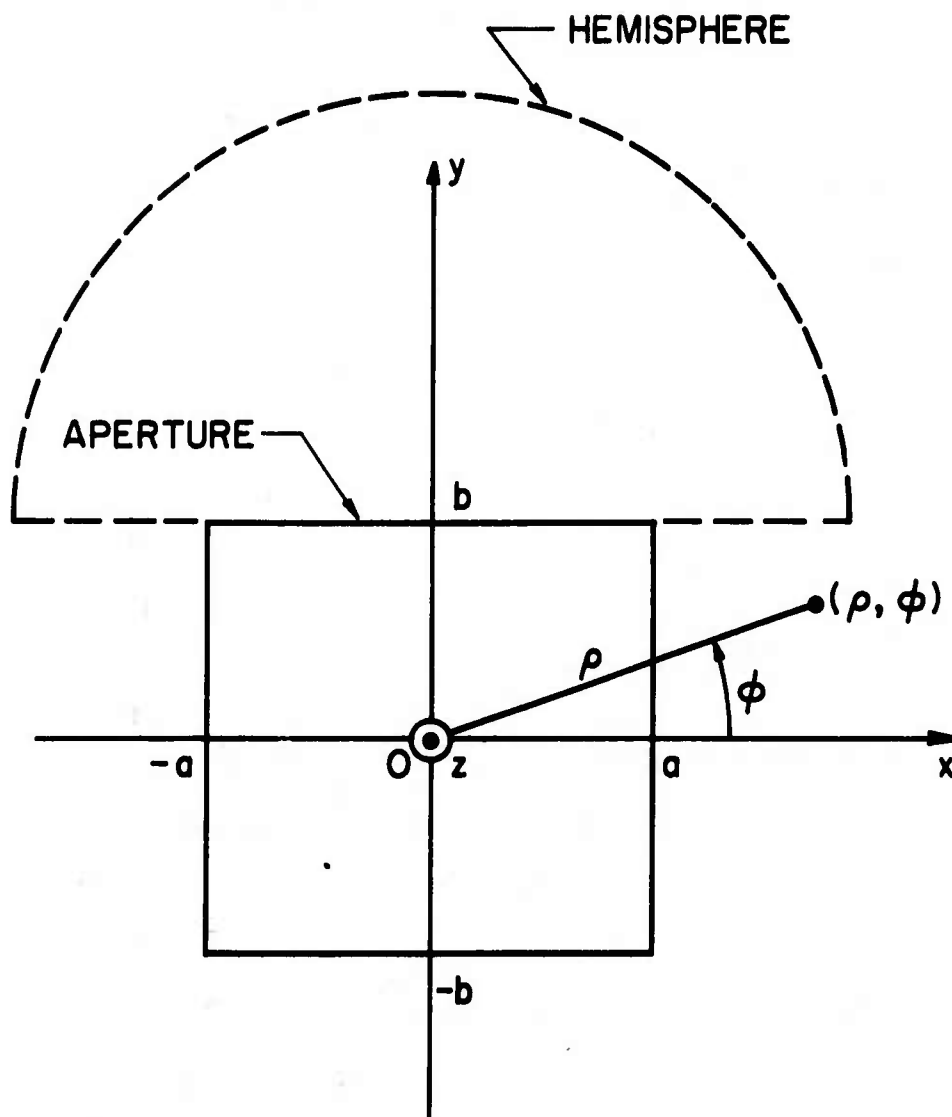
Figure 5.12. Scattered far-field pattern in the hemisphere is used to obtain the scattered E-field on the aperture.

at y = b, containing the surface of the rectangular cylinder as its central portion. The scattered far-field pattern enclosed in the hemisphere corresponding to this aperture as shown in Figure 5.12 is used to compute the Fourier transform of the scattered electric field on the aperture. In particular, for the H-wave case considered in this chapter, the Fourier transform of the tangential component of the scattered electric aperture field can be written as

$$\tilde{E}^s_{xAP}(\phi)$$

$$= \frac{Z_0}{ik} \cdot \frac{1}{2g(\rho)} \cdot T^H(\phi) \cdot \exp(-ikb \sin \phi) \tag{5.38}$$

where

$$g(\rho) = \frac{e^{ik\rho + i\frac{\pi}{4}}}{\sqrt{8\pi k\rho}}$$

Z_0 is the free space characteristic impedance

$T^H(\phi)$ is that portion of the scattered magnetic far field pattern enclosed in the proper hemisphere corresponding to the aperture under consideration, and

ρ and ϕ are the polar coordinates.

The phase factor in (5.38) is to assure that the aperture at y = b, but not at y = 0, is under consideration. The tangential scattered electric aperture field in the space domain can be obtained readily by an inverse Fourier transform, viz.,

$$E^s_{xAP}(x, y = b) = F^{-1}[\tilde{E}^s_{xAP}(\phi(\alpha))] \quad . \tag{5.39}$$

The tangential scattered electric aperture field in (5.39) is truncated to the surface of the scatterer, i.e., $x \in [-a,a]$ and an observation can be made to judge whether the tangential scattered electrical field on the surface of the rectangular cylinder is indeed equal to the tangential incident electric field.

The hemisphere shown in Figure 5.12 is for the aperture at $y = b$. Similar hemispheres and apertures corresponding to the other surfaces of the rectangular cylinder can be established and the tangential components of the scattered electric field on these surfaces can be computed in a similar fashion.

5.4.2 Results and comments

In the previous sections, an improved scattered magnetic far-field pattern has been obtained (see Figure 5.10). The accuracy of that pattern can be verified by computing the tangential component of the scattered electric field on the surface of the rectangular cylinder using the method outlined in Subsection 5.4.1. The resulting tangential component of the scattered electric field on the surface: $x \in [-a,a]$, $y = b$, is shown in Figures 5.13a and 5.13b. These curves were obtained by using that portion of the improved pattern (Figure 5.10) enclosed in the hemisphere schematically indicated in Figure 5.12, and by using the one-dimensional FFT for the inverse Fourier transform operation.

The magnitude of the tangential scattered E-field shown in Figure 5.13a oscillates around the constant value 266.58, which is the magnitude of the tangential component of the incident E-field. More precisely, for normalized H-wave incidence, $|H^1| = 1, |E^1| = 377$, and the incident angle $\phi_0 = 45^o$, therefore, the magnitude of the tangential component of
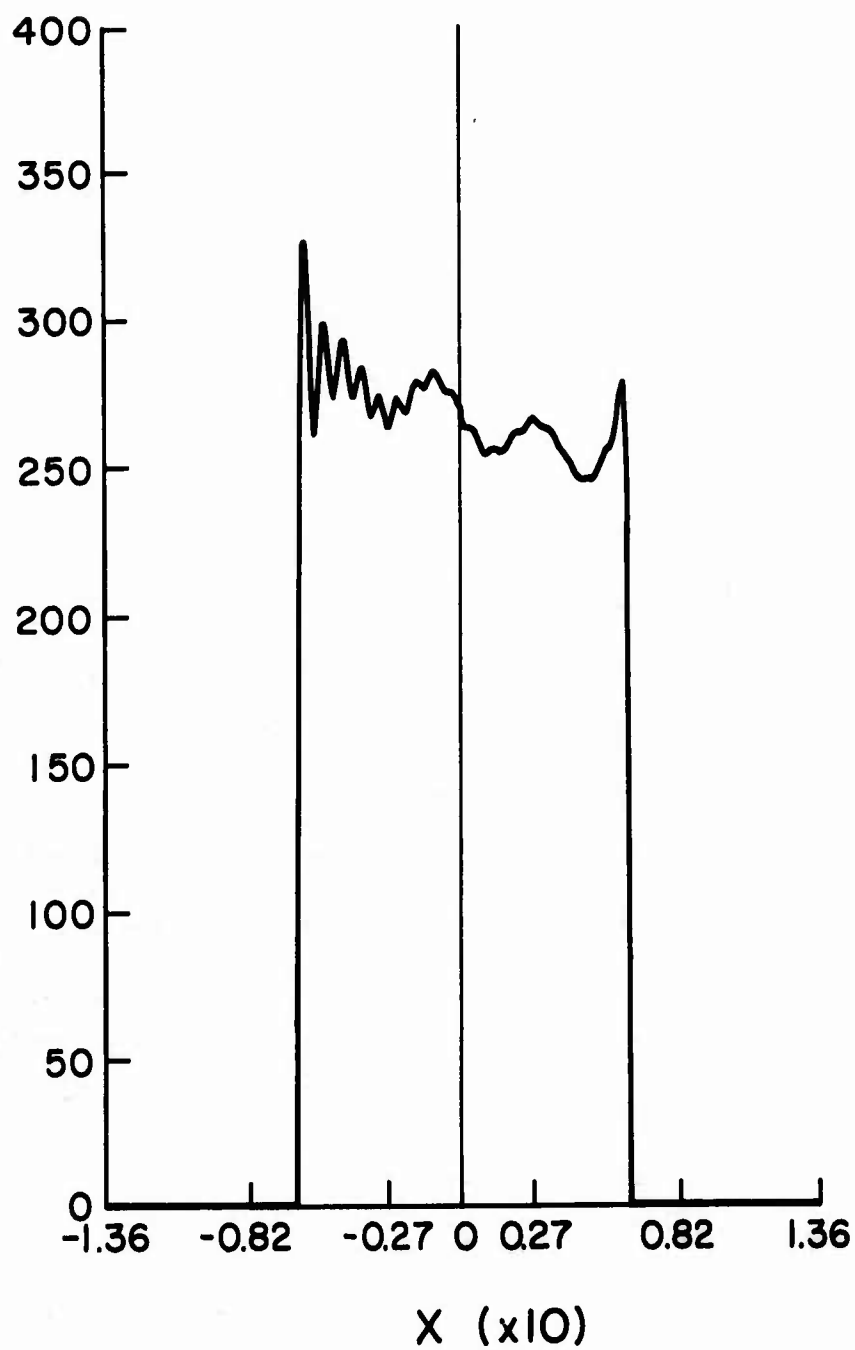
Figure 5.13a. Magnitude of the scattered E-field on the aperture
shown in Figure 5.12, truncated to the surface of
the rectangular cylinder.
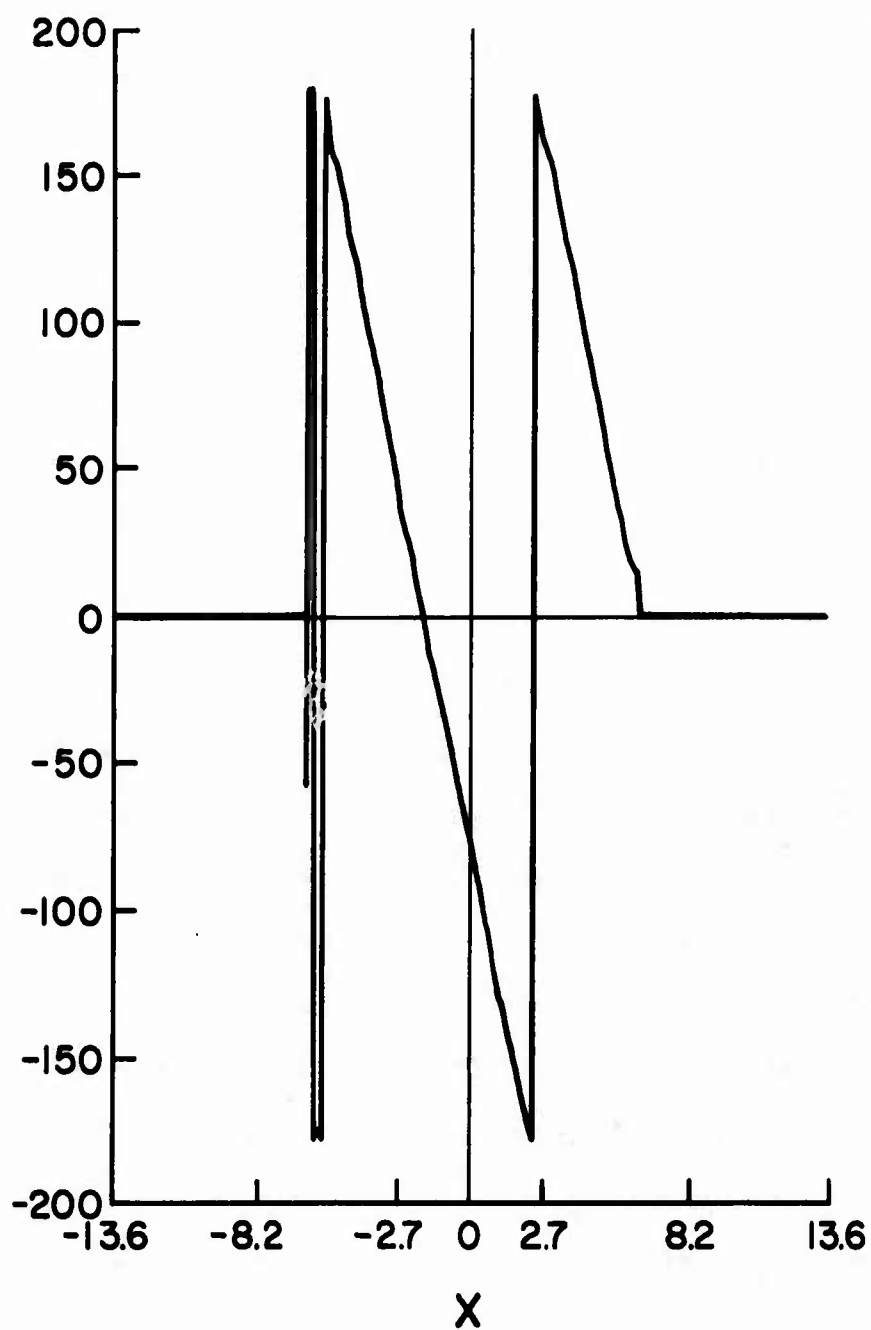
Figure 5.13b. Phase of the scattered E-field on the aperture shown in Figure 5.12, truncated to the surface of the rectangular cylinder.

the incident E-field is $|E^1 \cos 45^o| = 266.58$. The phase of the tangential

scattered E-field shown in Figure 5.13b is varying linearly across the

surface of the rectangular cylinder and can be readily verified to be of

a phase difference of π or 180° from the phase of the tangential incident

E-field on the surface. Similar behaviors of the tangential scattered

E-field on other surfaces of the rectangular cylinder can be obtained

and are not repeated here. These observations confirm that the improved

far-field pattern obtained in the last section is indeed a very good

approximation to the true scattered field. Of course, the comparisons

with results obtained by other approaches as done in the previous section

not only further validate the approximate solution, but also demonstrate

the effectiveness of the accuracy checking method developed in this

section.

5.5 Summary

In this chapter, the scattered far-field pattern of a perfectly

conducting rectangular cylinder illuminated by a plane H-wave has been

obtained by a zeroth-order GTD approximation and the result improved by

a straightforwardly physical interpretation of the existence of the

discontinuities in the zeroth-order GTD far-field pattern.

The improved scattered far-field pattern has been compared with

results obtained by other different approaches and the similarities and

differences between these results have been discussed. Generally speaking

the improved pattern obtained by the present approach is in good agreement

with the conventional moment-method solution with 32 unknowns.

An accuracy checking method has also been presented so that an in-

dependent check on the satisfaction of the boundary condition on the

surface of the rectangular cylinder can be performed. The results of such an accuracy check are quite favorable, which demonstrates that the improved far-field pattern obtained by the present approach is indeed a close approximation to the true solution. The merit of such an independent accuracy checking scheme is that the approximate solution obtained can be validated without making comparisons with other methods. This accuracy check is much desired especially when there are new results obtained and no available information in the literature that can be trustworthy to compare with.

6. A SYNTHETIC-APERTURE-DISTRIBUTION APPROACH TO THE HIGH-FREQUENCY ELECTROMAGNETIC SCATTERING OF OBSTACLES WITH CONVEXLY CURVED SURFACE

6.1 Introduction

In the previous chapters, we have discussed new approaches for solving the high-frequency electromagnetic scattering problems involving obstacles with planar surfaces and sharp edges. For all of these problems, the zeroth-order approximation to the scattered far-field can be constructed from Keller's wedge-diffraction coefficient (including the edge-diffraction coefficient as a special case) in a relatively simple manner. The improvement of the zeroth-order solution can be achieved in a systematic way, as demonstrated in the previous chapters, where the infinite perfectly conducting thin strip, the finite perfectly conducting rectangular thin plate, and the perfectly conducting rectangular cylinder have been used as illustrative examples.

In reality, most of the scattering objects possess a smoothly curved surface instead of planar facets and sharp edges. A circular perfectly conducting cylinder is the simplest geometry of this category of smooth-surfaced obstacles. The scattering by a circular cylinder is among the few electromagnetic scattering problems that can be solved by the method of separation of variables in partial differential equations. From a mathematician's point of view, the scattering by a circular cylinder is solved when the scattered field is expressed in terms of an infinite series of eigenfunction expansion involving transcendental functions. However, such an eigenfunction solution usually converges slowly and many terms in the infinite series expansion must be included before a "settled-down" solution can be obtained. For high-frequency

scattering, the obstacle is normally large in terms of wavelengths. When it comes to numerical computations, such an eigenfunction expansion is no more than a mathematical elegance but is totally useless in practicality.

For many decades, scientific-minded people have stared at this exact solution which is expressed in such an elegant manner and yet so formidable to get numerical results out of it. Before the advent of the latest generation of large computer systems, many of the former graduate students have spent a good deal of their time working on research projects involving numerical evaluations of the exact solutions with the aid of desk calculators. The introduction of the first large computer system was expected to release them of these tedious calculations. However, they soon found out that the evaluation of the exact eigenfunction expansion solutions on the computer was extremely time-consuming. Furthermore, they discovered that the problem of numerical instabilities would occur when increasingly higher-order terms were included successively in the computation. Therefore, in high-frequency scattering where the higher-order terms must be included in the series to obtain a convergent solution, the numerical evaluation of the exact solution is still hopeless.

Even before their disenchantment with the large scale computer systems, people were so frustrated by the numerical evaluation of the exact solution that they started deriving asymptotic formulas for both high-frequency and low-frequency approximations to the exact solution. Most of the high-frequency asymptotic formulas may be obtained either directly, e.g., by the Luneburg-Kline method [25], or by asymptotic

evaluations of contour-integral representations of the exact solution. Saddle-point integration and the stationary-phase method are most often used to obtain an asymptotic series if the integral representation of the exact solution is the starting point of the derivation.

For high-frequency scattering, in most of the cases, the first term of the asymptotic-series expansion gives an extremely good approximation to the exact solution. However, for the case in which the first term does not give a good approximation to the exact solution, including the next higher-order term in the asymptotic series may or may not be able to improve the approximate solution. This is a well-known property of the asymptotic series, because in most situations, the asymptotic series is a divergent instead of a convergent series.

To date, a method for systematically improving the asymptotic solution is still the most desirable. In spite of all the efforts that have been concentrated on this solution in the two decades since Keller's first conception of the diffraction coefficient approach, no systematic way exists to improve the high-frequency-asymptotic solution when necessary. Many theories, which are improved versions of the original Keller's geometrical theory of diffraction (GTD) [26] have been proposed, among these theories are the uniform theory of diffraction (UTD) [8], the uniform asymptotic theory (UAT) [9], and the spectral theory of diffraction (STD) [10]. Nevertheless, the computational efficiency of these theories when applied to practical situations still remains to be seen.

Two of the state-of-the-art methods for solving the high-frequency scattering problems involving perfectly conducting convex cylindrical

structures have been presented, one has been published in the literature [4], while the other has been presented at the USNC/URSI 1975 annual meeting [5]. The first method uses a combination of the geometrical theory of diffraction and the moment method to solve a circular cylinder scattering problem, wherein the cylindrical surface is divided into three regions, namely, the physical optics region in the well-illuminated side, the GTD region in the deep shadow, and the pulse region in the transition region between the lit and the dark sides. The surface current is first obtained, then the far-field can presumably (Burnside *et al*. did not show the far-field pattern) be obtained by a numerical double-integration of the surface current. There are three weaknesses in Burnside's method:

(1) The composite surface current computed by using different techniques in different regions on the cylindrical surface as indicated above is not smoothly connected at the boundaries of each region. These discontinuities are clearly shown in Figure 6.20;

(2) The far-field pattern must be computed by a numerical double-integration of the surface current. Such a computation may be time consuming; and

(3) Furthermore, the discontinuities at the high end in the surface current (see Figure 6.20) may introduce extraneous high-level sidelobes in the far-field pattern (see Section 6.4 for a demonstration).

The second method used an N-sided polygon to model the circular cylinder. Wang and Richmond's analysis is based on the self-consistent geometrical theory of diffraction [24]. Two cylindrical waves with unknown amplitudes are assumed to travel in opposite directions

(traverse to the axis of the cylinder) on each facet of the polygon.
The boundary conditions for the corners are applied to set up a matrix
equation for 2N unknowns (the amplitudes associated with the traveling
cylindrical waves). Crout's method is used to solve the matrix equation.
After the amplitudes for the traveling waves have been determined,
the far field is obtained by the self-consistent method. There are
three weaknesses in Wang and Richmond's method:

(1) Sharp edges are introduced artificially in modeling the smooth
circular cylindrical surface by a polygonal cylinder. In other
words, the nature of the problem has been changed substantially;

(2) In order to accurately model an electrically large circular cylinder,
it is conceivable that N, the number of polygonal facets used,
must be large; otherwise, the problem of a polygonal instead of a
circular cylinder is being solved. Hence, the number of unknowns,
2N, in the matrix equation can be large and the computation be-
comes, again, time consuming; and

(3) In addition, the self-consistent method, as pointed out in the
last chapter, may not be able to get rid of the extraneous vari-
ations in the far-field pattern in the directions coincident with
the orientations of the individual facets of the modeling poly-
gonal cylinder.

It is also well-known in the high-frequency scattering that asymp-
totic evaluation of the integral representation of the scattered field
results in an infinite series whose terms can be interpreted as highly
attenuated, surface-mode, traveling-waves around the surface of the
obstacle. The diffraction coefficients and attenuation constants in

the Keller's geometrical theory of diffraction for smoothly curved surfaces can be identified from the terms in the series. Such traveling waves propagate around the obstacle at a slightly slower speed than that of light in free space, and continuously shed energy in directions tangential to the surface as they travel along; hence, they are highly attenuated. These waves are known as "creeping waves." It was once of great hope that the creeping-wave contributions would complete the picture of the geometrical-optics solution of scattering problems by providing a means of calculating the diffracted field in the deep-shadow region. Conceptually, the creeping wave theory is attractive; but, actually, due to the high-attenuation property of the creeping waves, those waves that "crept" around the obstacle more than once contribute little to the total diffracted field. Therefore, if the first-order creeping wave failed to improve the geometrical-optics solution to a certain extent, including higher-order creeping waves seldom improves the solution further. Besides, creeping waves are too complicated to compute, hence, are not suited for programming on computers.

All of the above discussions point to the fact that a conceptually simple, computationally efficient method of solving high-frequency electromagnetic scattering problems involving curved-surface scatterers is still much desired.

In this chapter, we introduce a new approach to the high-frequency electromagnetic scattering of obstacles with a convexly curved surface. The idea is to transfer information characterizing the curved surface onto a planar aperture where maneuvers for improving the geometrical-optics solution are carried out. In conventional strategies, maneuvers

110

for improvement are carried out either directly on the surface current
or directly on the far field. The introduction of a planar aperture in
the present approach is a marked difference from all of the conventional
methods. A salient feature of the method is that the far field is
obtained by Fourier transforming the aperture-field distribution; hence,
it can handle problems involving an n-dimensional obstaclc by an
(n - 1)-dimensional fast Fourier transform (FFT), where n = 2,3.
Therefore, the unwieldy three-dimensional FFT is circumvented, hence,
the method is numerically efficient. Another important feature of the
method is that the aperture-field distribution is slowly varying, i.e.,
not rapidly oscillatory, in *magnitude* and in *phase*. Hence, maneuvers
for improvement can be achieved in a relatively straightforward manner.
Moreover, the method is conceptually simpler than other conventional
methods in the literature, because maneuvers for improvement are car-
ried out on a plane rather than on a curved surface.

The best way to explain the method is to apply it to solve the
scattering problem of a plane wave by a perfectly conducting circular
cylinder, because the principle involved can be illustrated without
the unnecessary complexities.

To make this chapter as self-contained as possible, we briefly
derive the exact solution in Section 6.2 and the geometrical-optics
solution in Section 6.3. Synthesizing the approximate aperture-field
distribution is demonstrated in Section 6.4. Computation of surface
current is carried out in Section 6.5. An accuracy check of the ap-
proximate solution is discussed in Section 6.6. A summary for the
chapter can be found in Section 6.7.

6.2 Exact Solution

In this section, we briefly discuss the exact solution to the problem of scattering of a plane wave by a perfectly conducting circular cylinder. The geometry of the problem is shown in Figure 6.1. A perfectly conducting circular cylinder located at the origin of the coordinate system is illuminated by a uniform plane wave whose electric intensity vector is parallel to the axis of the cylinder.

Using the method of separation of variables [27], the scattered field can be written as

$$E_z^s(\rho,\phi) = \sum_{n=-\infty}^{\infty} (i)^n a_n H_n^{(1)}(k\rho) \, e^{in\phi} \tag{6.1}$$

where $H_n^{(1)}(k\rho)$ is the Hankel function of the first kind, and the a_n's are unknown coefficients. The time convention $e^{-i\omega t}$ is understood. To determine the a_n's, we evaluate (6.1) at $\rho = a$, the radius of the cylinder, i.e., at the surface of the cylinder and then apply the boundary condition. To do this, we first expand the incident electric field into a series, namely,

$$E_z^i(\rho,\phi) = \sum_{n=-\infty}^{\infty} (i)^n J_n(k\rho) \, e^{in\phi} \tag{6.2}$$

where $J_n(k\rho)$ is the Bessel function of the first kind. The boundary condition requires that the total tangential electric field vanish on the surface of a perfectly conducting obstacle. Therefore,

$$E_z^s(a,\phi) + E_z^i(a,\phi) = 0 \quad . \tag{6.3}$$
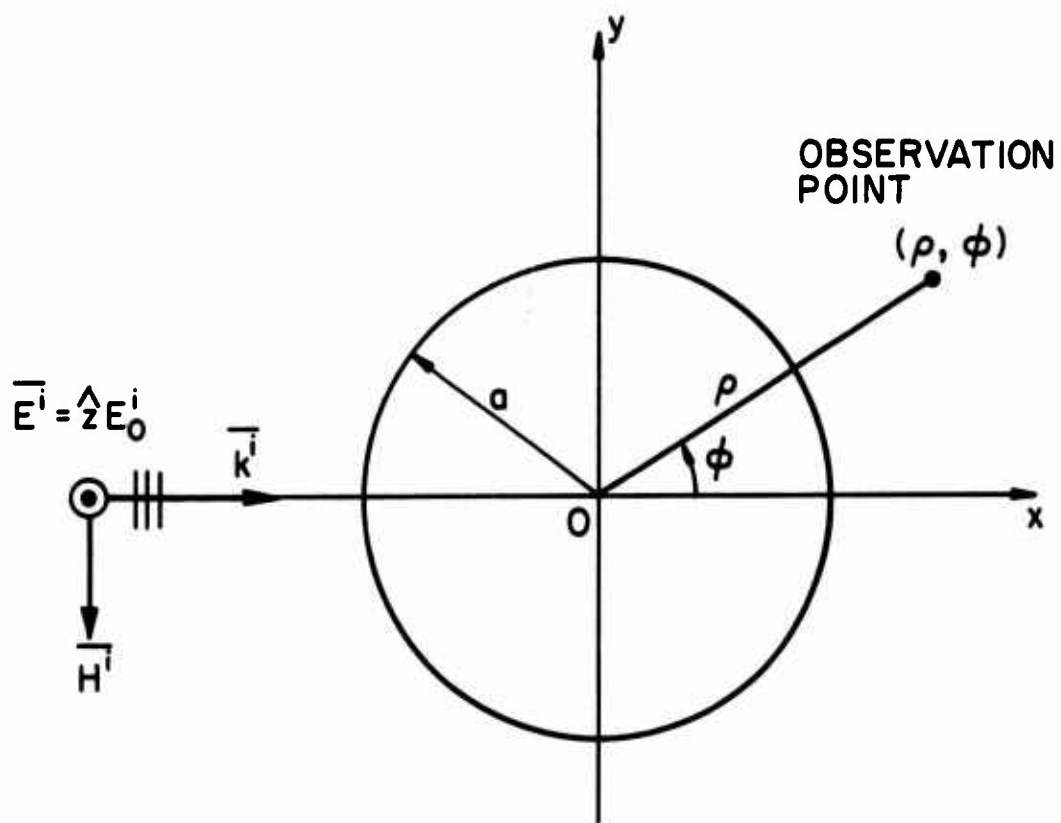
Figure 6.1. Diffraction by a circular cylinder illuminated by an E-wave incident along the x-axis.

Using (6.1) and (6.2) in (6.3), we obtain

$$a_n = \frac{-J_n(ka)}{H_n^{(1)}(ka)} \quad . \tag{6.4}$$

Substituting (6.4) in (6.1), we have

$$E_z^s(\rho,\phi) = -\sum_{n=-\infty}^{\infty} (i)^n \frac{J_n(ka)}{H_n^{(1)}(ka)} H_n^{(1)}(k\rho) \, e^{in\phi} \quad . \tag{6.5}$$

The far-field pattern of the scattered field is of interest. At large distances from the cylinder, we can use the asymptotic formula for $H_n^{(1)}$, namely,

$$H_n^{(1)}(k\rho) \xrightarrow[k\rho\to\infty]{} \sqrt{\frac{2}{i\pi k\rho}} \, i^{-n} \, e^{ik\rho} \tag{6.6}$$

and (6.5) becomes

$$E_z^s(\rho,\phi) \xrightarrow[k\rho\to\infty]{} \sqrt{\frac{2}{\pi k\rho}} \, e^{ik\rho} \, e^{i\frac{\pi}{4}} \, i \sum_{n=-\infty}^{\infty} \frac{J_n(ka)}{H_n^{(1)}(ka)} \, e^{in\phi} \quad . \tag{6.7}$$

The magnitude of the ratio of the scattered field to the incident field is therefore

$$\frac{\left| E_z^s \right|}{\left| E_z^i \right|} = \sqrt{\frac{2}{\pi k\rho}} \left| \sum_{n=-\infty}^{\infty} \frac{J_n(ka)}{H_n^{(1)}(ka)} \, e^{in\phi} \right| \quad . \tag{6.8}$$

This is the scattered far-field pattern. For ka = 1, 5, 10, and 6π, the far-field patterns are shown in Figures 6.2a, 6.2b, 6.2c, and 6.2d.
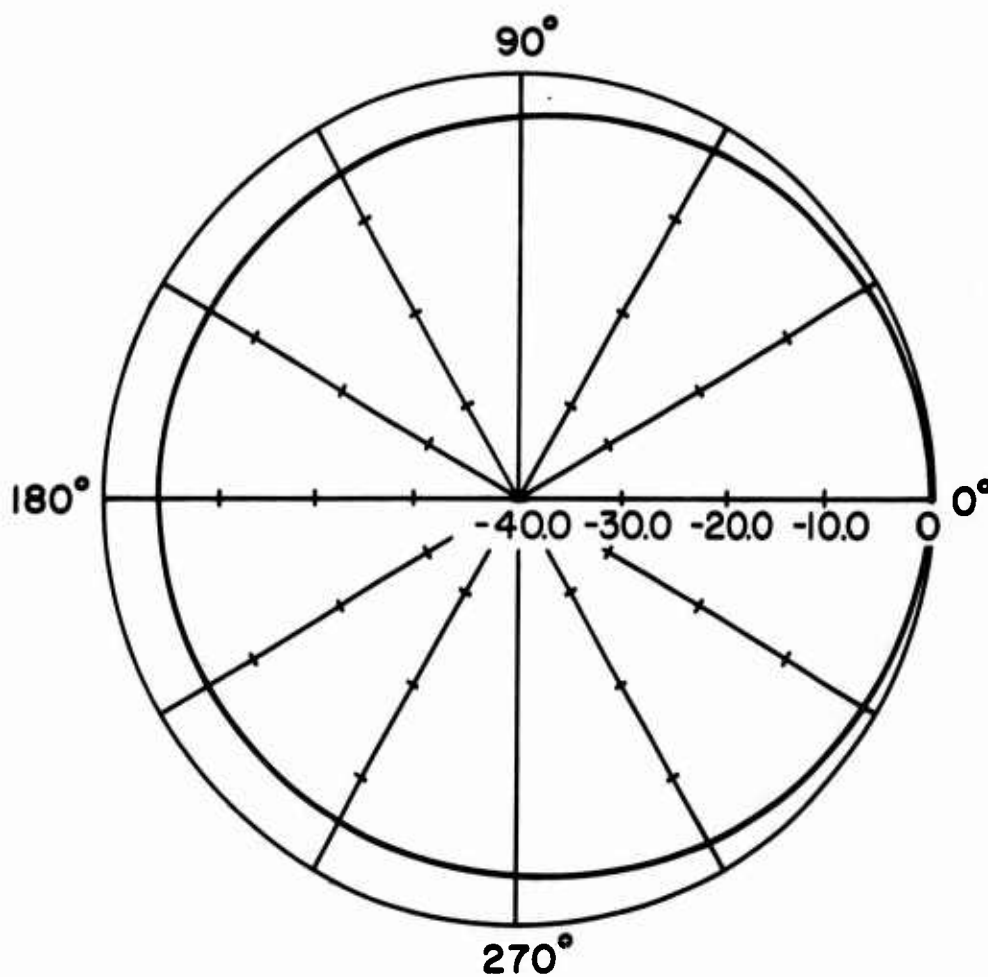
Figure 6.2a.   Exact scattered far-field pattern in dB of a circular
cylinder with ka = 1.
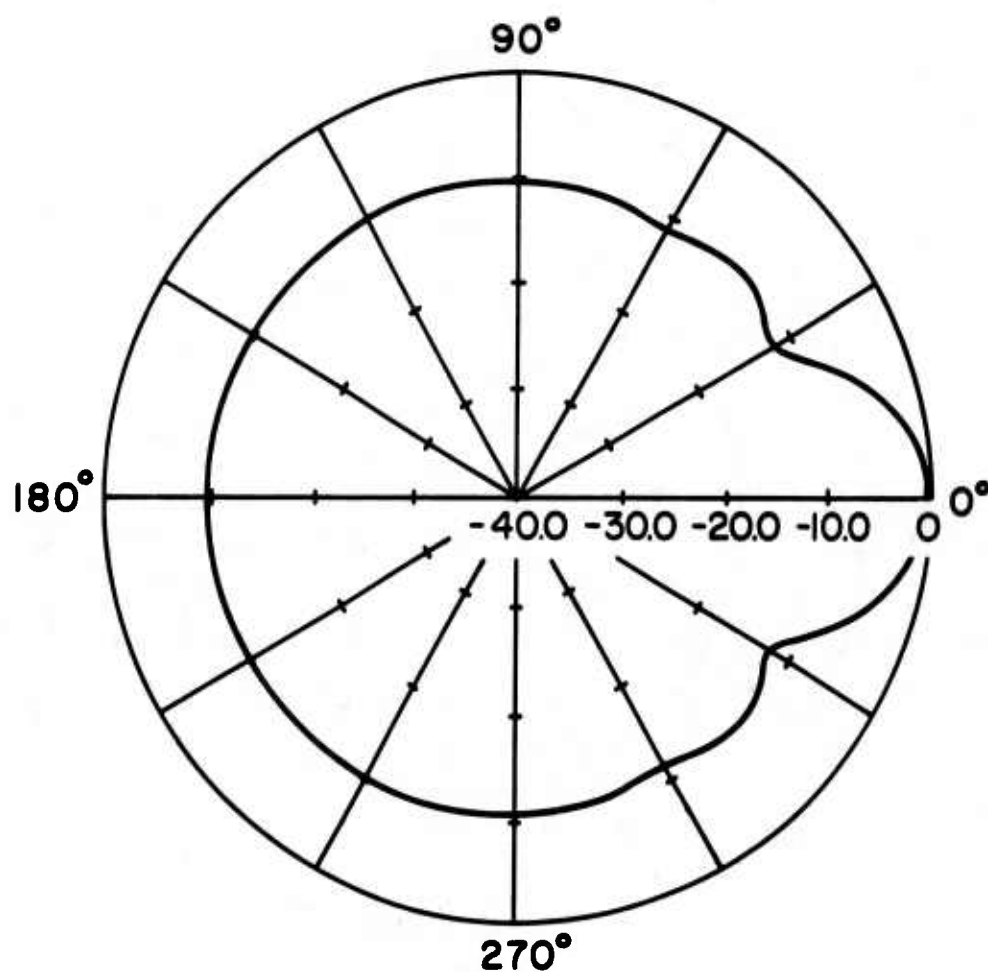
Figure 6.2b. Exact scattered far-field pattern in dB of a circular cylinder with ka = 5.
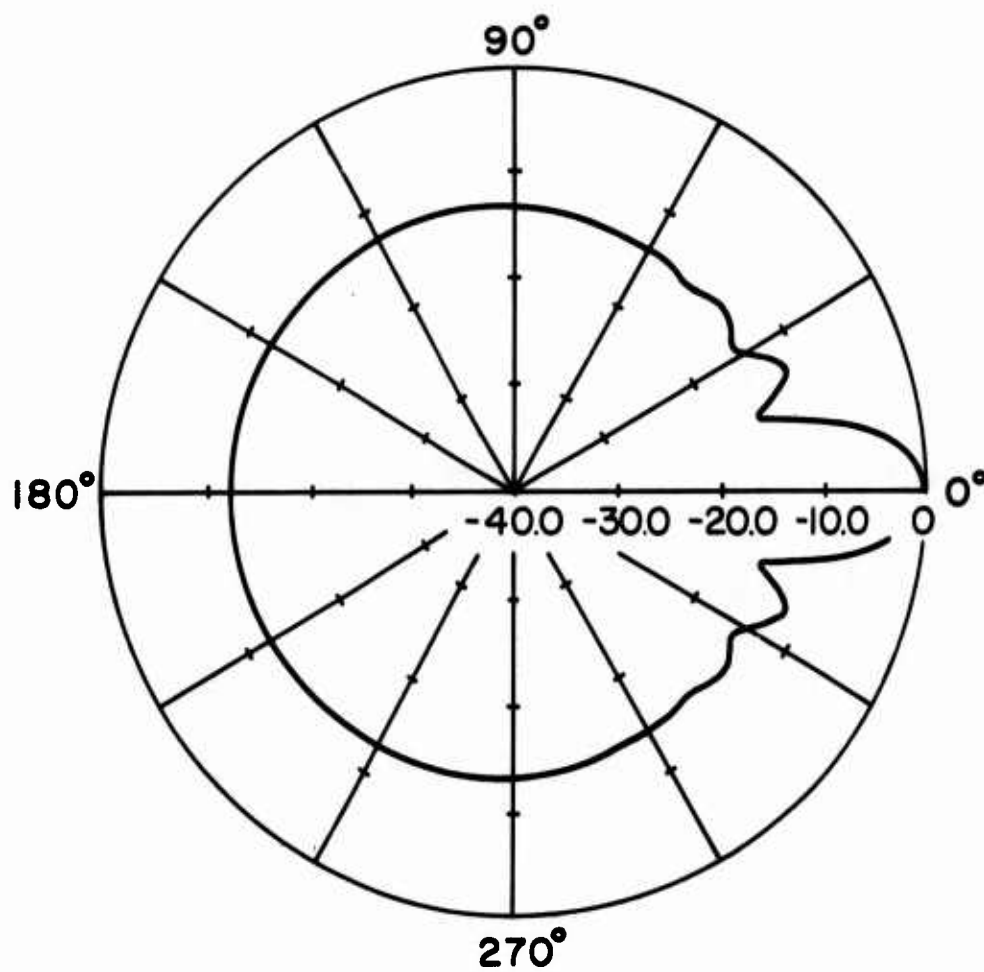
Figure 6.2c. Exact scattered far-field pattern in dB of a circular cylinder with ka = 10.
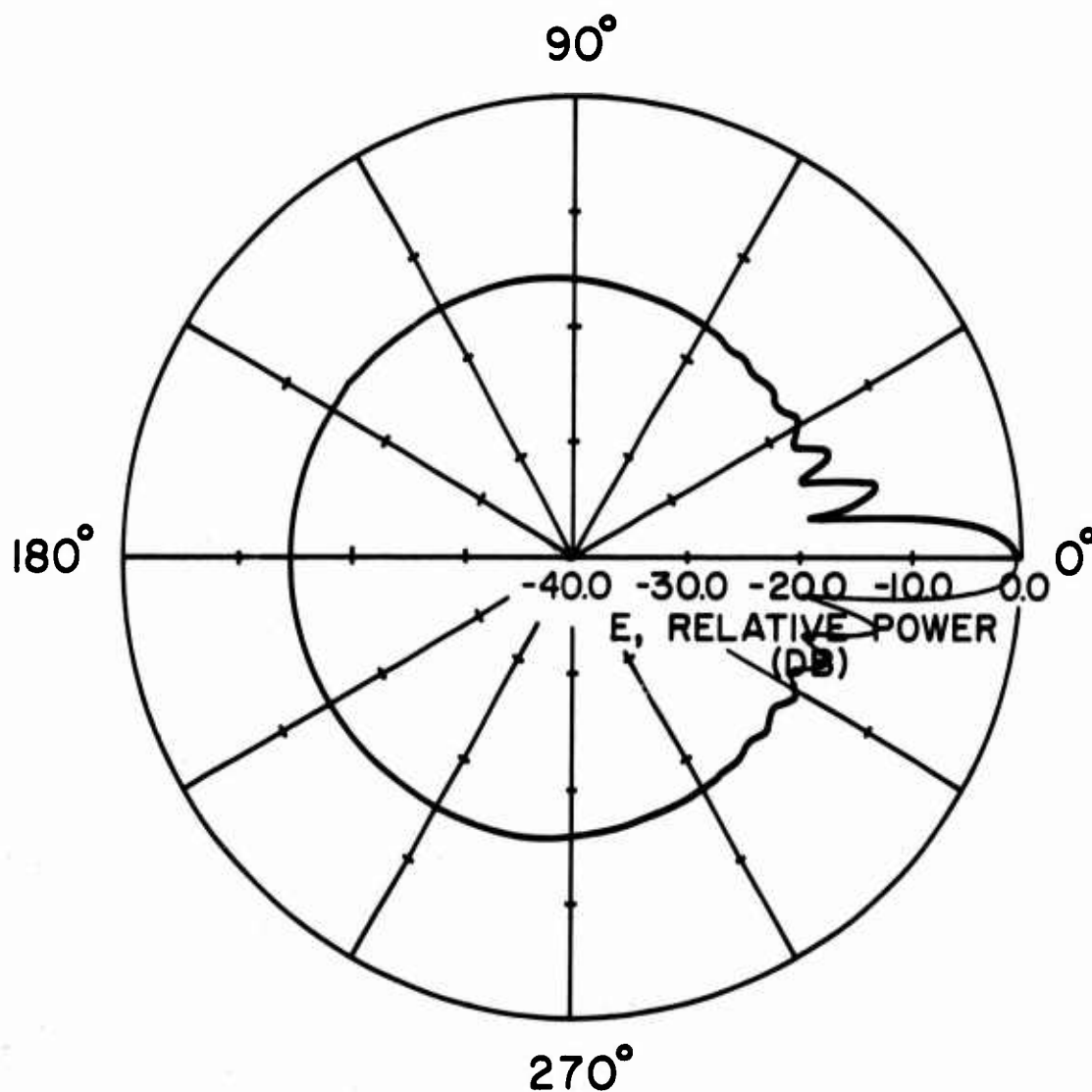
Figure 6.2d.   Exact scattered far-field pattern in dB of a circular
cylinder with ka = 6π.

Experience shows that the number of terms one should take in (6.8) to compute the far-field pattern is of the order of ka, which means that the convergence of the series is extremely slow for an electrically large cylinder and the computation becomes time-consuming. For high-frequency scattering, one must resort to approximation solutions to obtain meaningful numerical results.

The surface current on the cylinder is also of interest. It can be obtained from Maxwell's equations, i.e.,

$$J_z = H_\phi \Big|_{\rho=a} = \frac{1}{-i\omega\mu} \frac{\partial E_z}{\partial \rho}\Big|_{\rho=a} \tag{6.9}$$

where $E_z = E_z^i + E_z^s$. Using (6.2) and (6.5), and simplifying the result by the Wronskian of Bessel's equation, we obtain

$$J_z(\phi) = \frac{2}{\pi ka Z_0} \sum_{n=-\infty}^{\infty} \frac{i^n e^{in\phi}}{H_n^{(1)}(ka)} \tag{6.10}$$

where Z_0 is the free-space characteristic impedance. The surface current for the case of $a = 3\lambda$ is shown in Figures 6.3a and 6.3b.

6.3 Geometrical Optics Solution

6.3.1 Fields of a ray

A point source radiating in all directions is indicated in Figure 6.4. The energy between a set of such rays is assumed to remain constant. Four of these rays, as shown in Figure 6.5, constitute a tube of rays. The energy passing through the cross-sectional areas A_1 and A_2 must be a constant under the assumption of no fringing. A linear relation
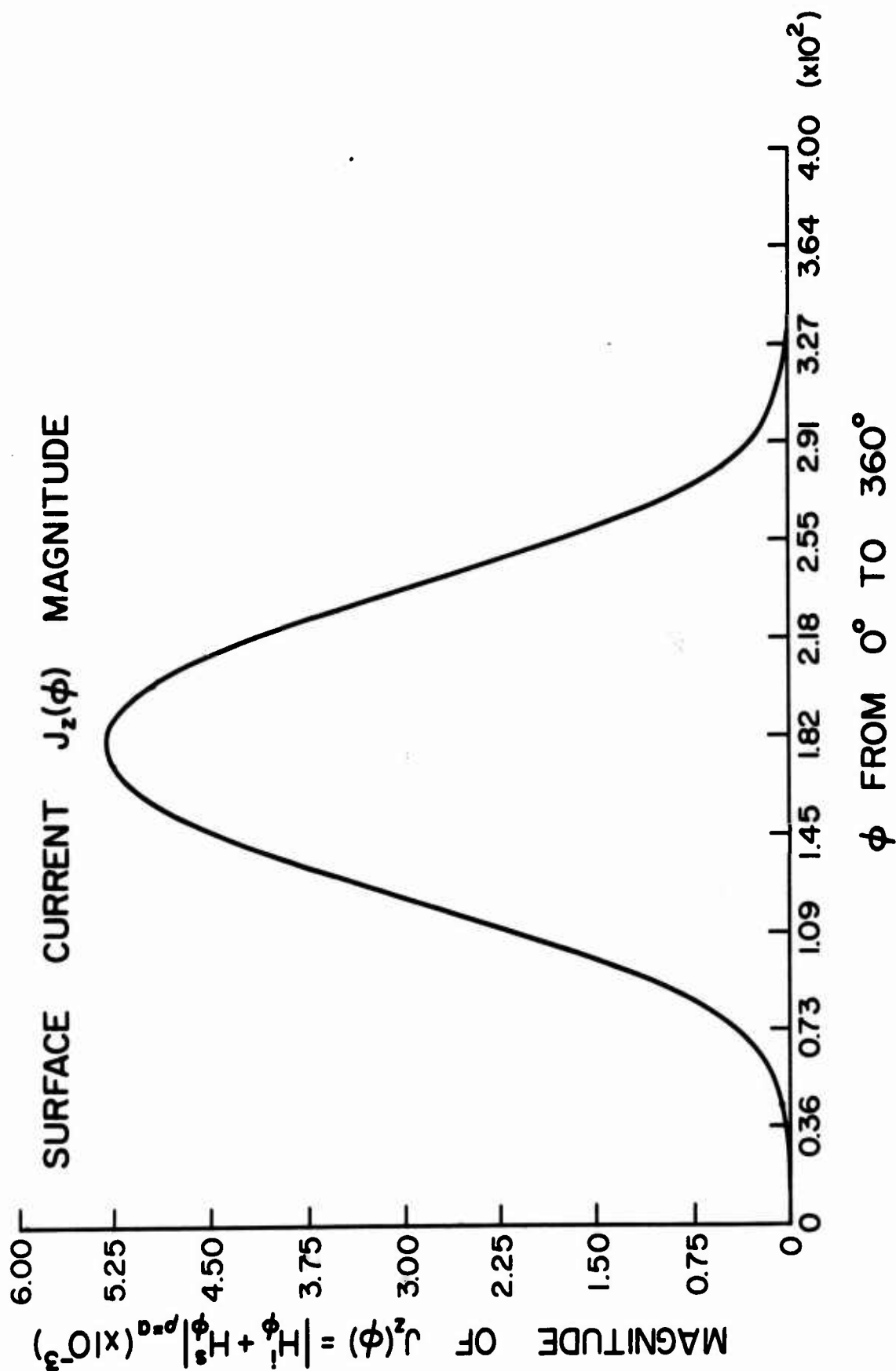
Figure 6.3a. Magnitude of the total induced surface current on a circular cylinder with radius $a = 3\lambda$.
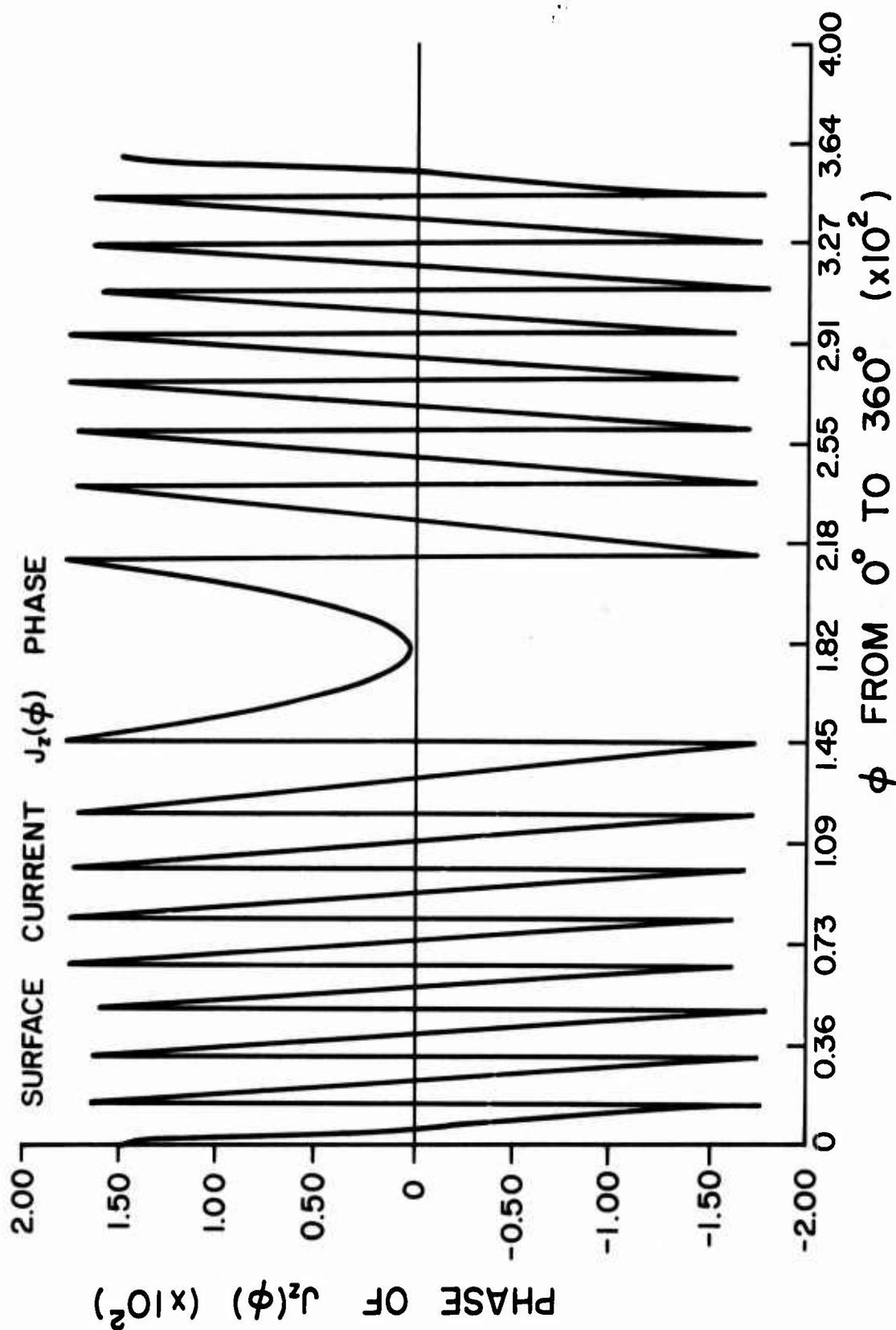
Figure 6.3b. Phase of the total induced surface current on a circular cylinder with radius a = 3λ.
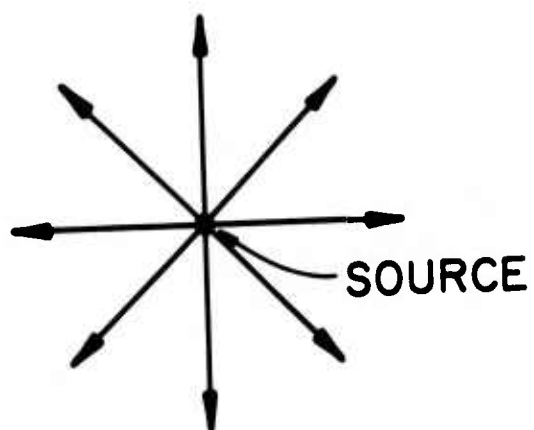
Figure 6.4. Rays of a point source.
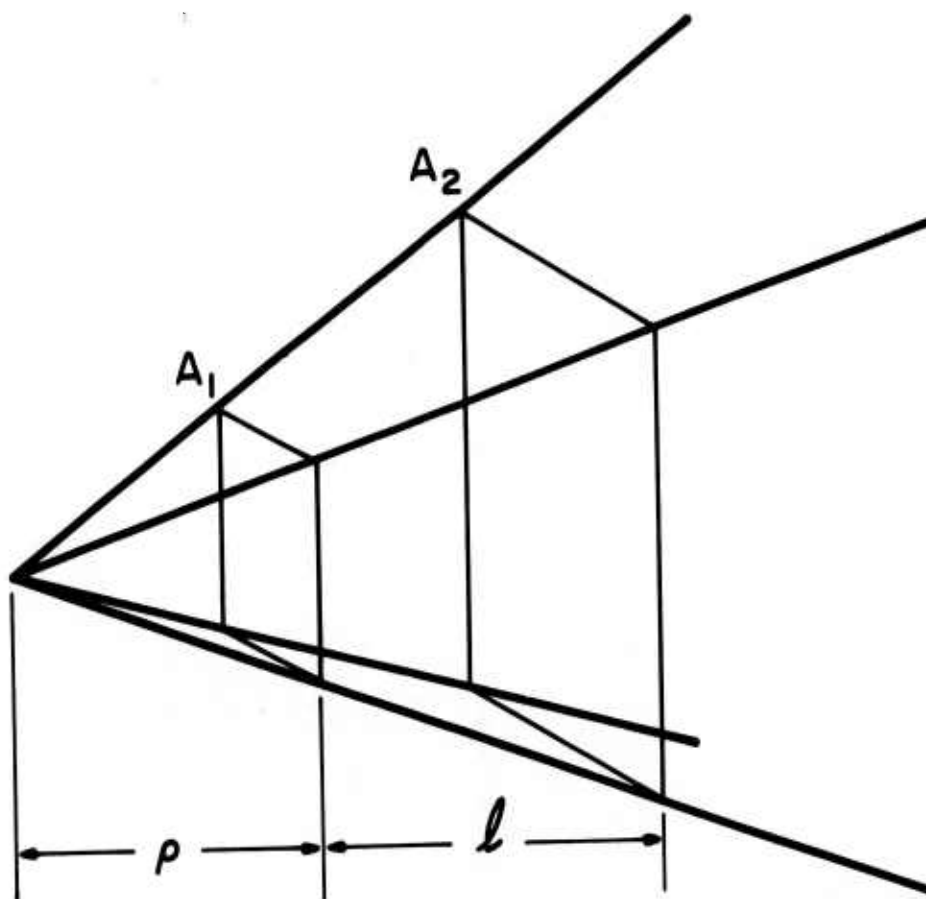
Figure 6.5. Tube of rays from a point source.

exists between the length of a side and its position ρ or $(\rho + \ell)$

shown in Figure 6.5. Thus, the ratio of the areas is

$$\frac{A_1}{A_2} = \frac{\rho^2}{(\rho + \ell)^2} \quad .$$ (6.11)

A field quantity at the position $(\rho + \ell)$ may be written in terms
of its value at the position ρ. The field quantity considered here is
a scalar. A vector field can be resolved into two component fields,
one polarized in and the other normal to the plane of incidence, and
each component field treated as a scalar field. It should be empha-
sized that this is exactly the physical scattering process that occurs
at a boundary between two different media. The field quantity is then

$$U_2 = U_1 \sqrt{\frac{A_1}{A_2}} = U_1 \frac{\rho}{\rho + \ell}$$ (6.12)

where U represents the scalar E- or H-field.

One may also consider a more general case involving an astigmatic
ray tube shown in Figure 6.6. In this case, the scalar field quantity
is given by

$$U_2 = U_1 \sqrt{\frac{\rho_1 \rho_2}{(\rho_1 + \ell)(\rho_2 + \ell)}} \quad .$$ (6.13)

The electrical phase of the ray tube is given by the spatial phase
delay factor $e^{ik\ell}$, when the time convention $e^{-i\omega t}$ is understood. This,
of course, assumes that the phase reference position coincides with
the amplitude reference. Now one may write an expression for the fields
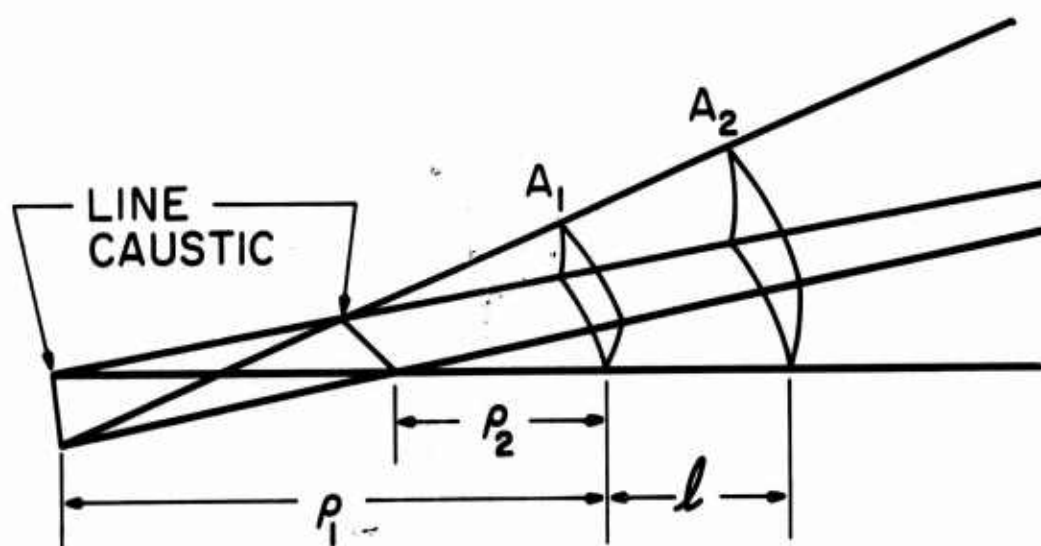
Figure 6.6. Astigmatic ray tube.

of this astigmatic tube of rays in the form

$$U_2 = U_1 e^{i\phi_1} \sqrt{\frac{\rho_1 \rho_2}{(\rho_1 + \ell)(\rho_2 + \ell)}} \, e^{ik\ell} \quad . \tag{6.14}$$

There are other phase changes that must be carefully preserved. Observe that the quantity under the radical becomes negative as ℓ becomes less than $-\rho_2$. This introduces a phase jump of -90° or $-\frac{\pi}{2}$ radians. This point is called a caustic. The fields at the caustic point cannot be determined by geometrical optics but the correct fields can be found on either side of the caustic. If ℓ becomes less than ρ_1, then the phase shift of 180° or π radians occurs.

The general geometrical optics expression for the field may be written in the form

$$U(\ell) = U_0 e^{i\phi_0} F(\ell) \, e^{ik\ell} \tag{6.15}$$

where U_0 is a reference amplitude at $\ell = 0$;

ϕ_0 is the reference phase at $\ell = 0$;

$$F(\ell) = \sqrt{\frac{\rho_1 \rho_2}{(\rho_1 + \ell)(\rho_2 + \ell)}}$$ is the spatial attenuation factor;

and $e^{ik\ell}$ is the spatial phase delay factor. In other words,

$$U(\ell) = [\text{reference field}] \begin{bmatrix} \text{spatial attenuation} \\ \text{factor} \end{bmatrix} \begin{bmatrix} \text{spatial phase} \\ \text{delay factor} \end{bmatrix} \quad . \tag{6.16}$$

6.3.2 Reflection at a curved surface boundary separating two different media

In this section we discuss a simple technique for obtaining the reflected field from a curved surface which is a boundary between two different media. The cylindrical or two-dimensional geometry is considered simply to avoid any unnecessary complexities. Other surfaces can be treated in the same manner.

The source is a line source as shown in Figures 6.7a and 6.7b. A plane wave is obtained simply by allowing ℓ_0 to go to infinity. The reflected rays now appear to be coming from a virtual source located a distance ρ_1 inside the surface. All factors in (6.16) should be written in terms of distance from the element of the surface as illustrated by ℓ_0, ℓ_1. The quantity r_c is the radius of curvature of the surface.

Now we proceed to determine the reflected fields. From (6.15), the reflected field is obtained and takes the form

$$U_r = RU_0 \sqrt{\frac{\rho_1}{\rho_1 + \rho_1}} \, e^{ik\ell_1} \tag{6.17}$$

where R is the reflection coefficient and U_0 is the reference field at the surface.

The only remaining task is to evaluate ρ_1 in (6.17). From trigonometry, the angle ξ_1 (see Figure 6.7a) is expressed as follows:

$$\xi_1 = \pi - \alpha - (\pi - \theta_0)$$

$$= \theta_0 - \alpha \quad . \tag{6.18}$$

Similarly,
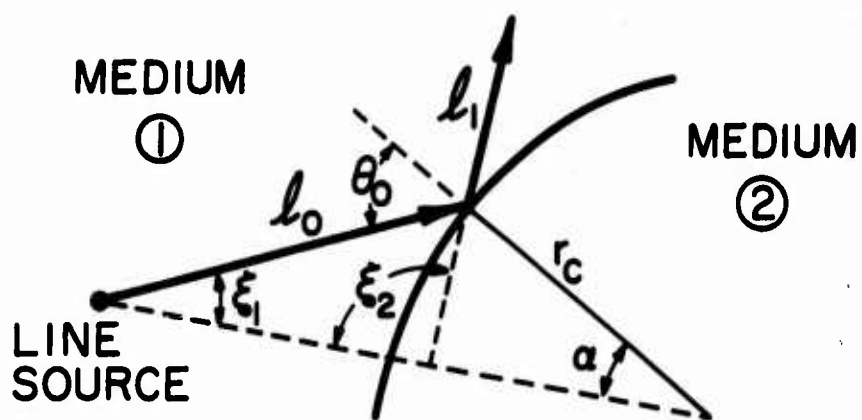
Figure 6.7a. Coordinate system.
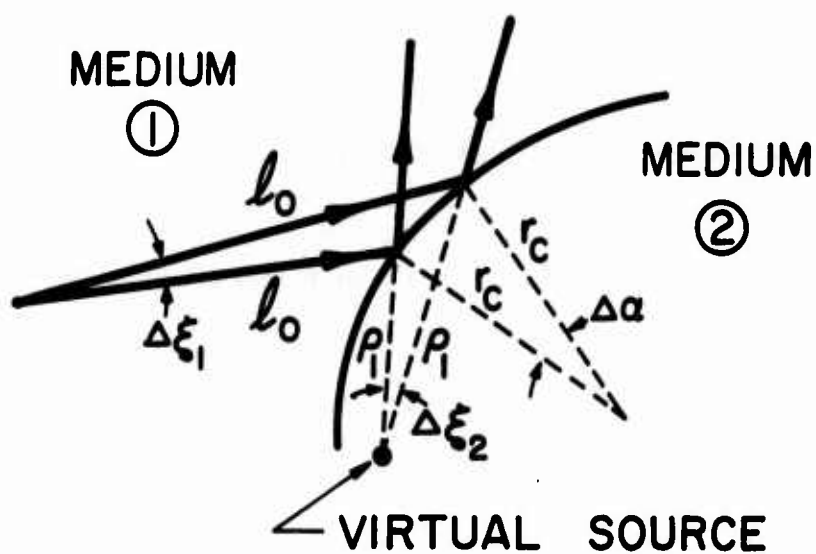
Figure 6.7b. Reflection from a curved surface.

$$\xi_2 = \theta_0 + \alpha \quad . \tag{6.19}$$

The element of arc-length is equal to $r_c(\Delta\alpha)$ (see Figure 6.7b) and it is also equal to $(\Delta\xi_1) \ell_0/\cos \theta_0$. Therefore,

$$r_c(\Delta\alpha) = \frac{(\Delta\xi_1) \ell_0}{\cos \theta_0} = \frac{(\Delta\theta_0 - \Delta\alpha) \ell_0}{\cos \theta_0} \tag{6.20}$$

where the last equality is obtained by means of (6.18) and Δ denotes the differential in the usual sense. By the same token,

$$r_c(\Delta\alpha) = \frac{(\Delta\xi_2) \rho_1}{\cos \theta_0} = \frac{(\Delta\theta_0 + \Delta\alpha) \rho_1}{\cos \theta_0} \tag{6.21}$$

where the last equality is obtained with the aid of (6.19). Eliminating $\Delta\alpha$ from (6.20) and (6.21) yields

$$\frac{1}{\rho_1} = \frac{1}{\ell_0} + \frac{2}{r_c \cos \theta_0} \quad . \tag{6.22}$$

Substituting (6.22) in (6.17) completes the solution for the reflected field from the curved surface.

Thus, the expression for the field reflected by a two-dimensional curved surface has been obtained in a relatively simple manner. The validity of this expression has been checked by comparing solutions of this type with exact solutions for spheres and cylinders [28]. For further discussions on the subject of electromagnetic reflection from a perfectly conducting surface, the interested reader is referred to the literature [29].

6.3.3 Scattering of a plane wave by a circular cylinder

In this section we apply the general formulas derived in the last section for reflection at an arbitrarily convexly-curved boundary-surface to the special case of a circular cylinder. The geometry of the scattering problem is shown in Figure 6.8. A plane wave polarized parallel to the axis of the circular cylinder located at the origin of the coordinate system is incident from the negative x-direction, viz.,

$$\bar{E}^i(\rho,\phi) = \hat{z}e^{ik\rho\cos\phi} \tag{6.23}$$

where the time convention $e^{-i\omega t}$ is understood.

To obtain the geometrical optics reflected field, we use (6.17). Since this is a perfectly conducting circular cylinder, the reflection coefficient, R, is -1. The reference field, U_0, is the incident field at the point of reflection, $\bar{P}_r$, on the circular cylinder. From (6.23),

$$U_0 = E_z^i(\rho = a, \phi = \xi)$$

$$= e^{ika\cos\xi} \quad . \tag{6.24}$$

The spatial attenuation factor is determined when the caustic position, ρ_1, is known. To find ρ_1, we use (6.22). For plane wave incidence, $\ell_0 \to \infty$. The radius of curvature in this case is simply a constant, i.e., the radius of the circular cylinder, a. Hence, the caustic position is given by

$$\rho_1 = \frac{a \cos \theta_0}{2} \quad . \tag{6.25}$$

$\overline{r}$: POINT OF OBSERVATION
$\overline{P}_r$: POINT OF REFLECTION
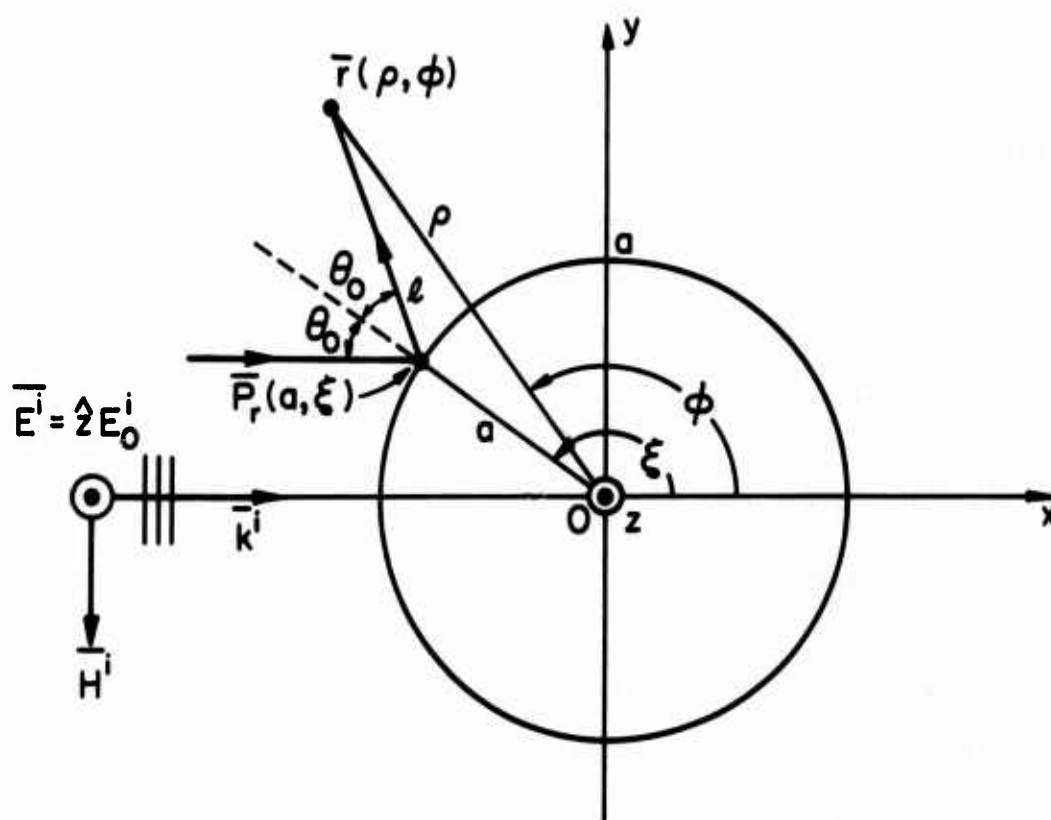
Figure 6.8. Geometry of the scattering problem of a circular cylinder.

Note that the angle of reflection, θ_0, in (6.25) is a function of ϕ, i.e., it depends on the location of the point of reflection on the cylindrical surface. The quantity ℓ_1 in (6.17) is the distance between the point of reflection, $\bar{P}_r(a,\xi)$, and the point of observation, $\bar{r}(\rho,\phi)$. This distance is denoted by ℓ in Figure 6.8. To obtain an expression for the scattered field at an observation point, $\bar{r}(\rho,\phi)$, we must first find a relation between the parameters (θ_0, ℓ, ξ) and the coordinates (ρ, ϕ). However, there is no simple relation that can be found to express θ_0, ℓ, and ξ explicitly in terms of ρ and ϕ. Therefore, in practice, one has to resort to numerical methods. There are basically two routes that one can follow, namely, either searching for the point of reflection when a point of observation is given, or interpolating for the field when a point of reflection is chosen.

Nevertheless, a simple closed-form expression can be found for the far field $(\rho \to \infty)$. In particular, we use the following approximations when $\rho \gg a > \lambda$:

$$\rho \simeq \ell \qquad\qquad \text{in the amplitude} \qquad\qquad (6.26a)$$

$$\rho \simeq \ell + a \cos \theta_0 \qquad\qquad \text{in the phase} \qquad\qquad (6.26b)$$

$$\theta_0 \simeq \left| \frac{\pi - \phi}{2} \right| \qquad\qquad \text{for } 0 \le \phi \le 2\pi \qquad\qquad (6.26c)$$

and

$$\xi \simeq \frac{\pi + \phi}{2} \qquad\qquad \text{for } 0 \le \phi \le 2\pi \quad . \qquad\qquad (6.26d)$$

Using (6.24), (6.25), and (6.26) in (6.17), and after some algebraic manipulations, we obtain

$$\bar{E}^{s}_{G.O.}(\rho,\phi) = -\hat{z}\sqrt{\frac{a}{2\rho}} \sin\frac{\phi}{2} \, e^{ik\rho} \, e^{-ik2a\sin\frac{\phi}{2}} \qquad (6.27)$$

where

$$0 \leq \phi \leq 2\pi$$

$$\rho \gg a > \lambda$$

and the time convention $e^{-i\omega t}$ is understood. The scattered far-field pattern obtained from (6.27) for the case of $a = 3\lambda$ is shown in Figure 6.9. For further discussions on the geometrical optics reflected fields, the interested reader is referred to the literature [30].

6.4   Synthesizing the Approximate Aperture Field Distribution

In the last section we discussed the geometrical optics solution to the problem of scattering of a plane wave by a perfectly conducting circular cylinder. The geometrical optics scattered far-field pattern is in excellent agreement with the exact (eigenfunction series expansion) solution in the hemisphere containing the lit surface of the circular cylinder. However, the geometrical optics solution fails completely in the forward-scattering direction because it predicts a zero field instead of the maximum of the main beam in that direction. This result does not come as a surprise since in a geometrical optics solution only the illuminated portion of the surface of an obstacle is taken into account, whereas the shadowed portion of the surface of the obstacle is completely ignored in the solution. As a matter of fact, the shadowed side of the scatterer could have been of any arbitrary shape and the
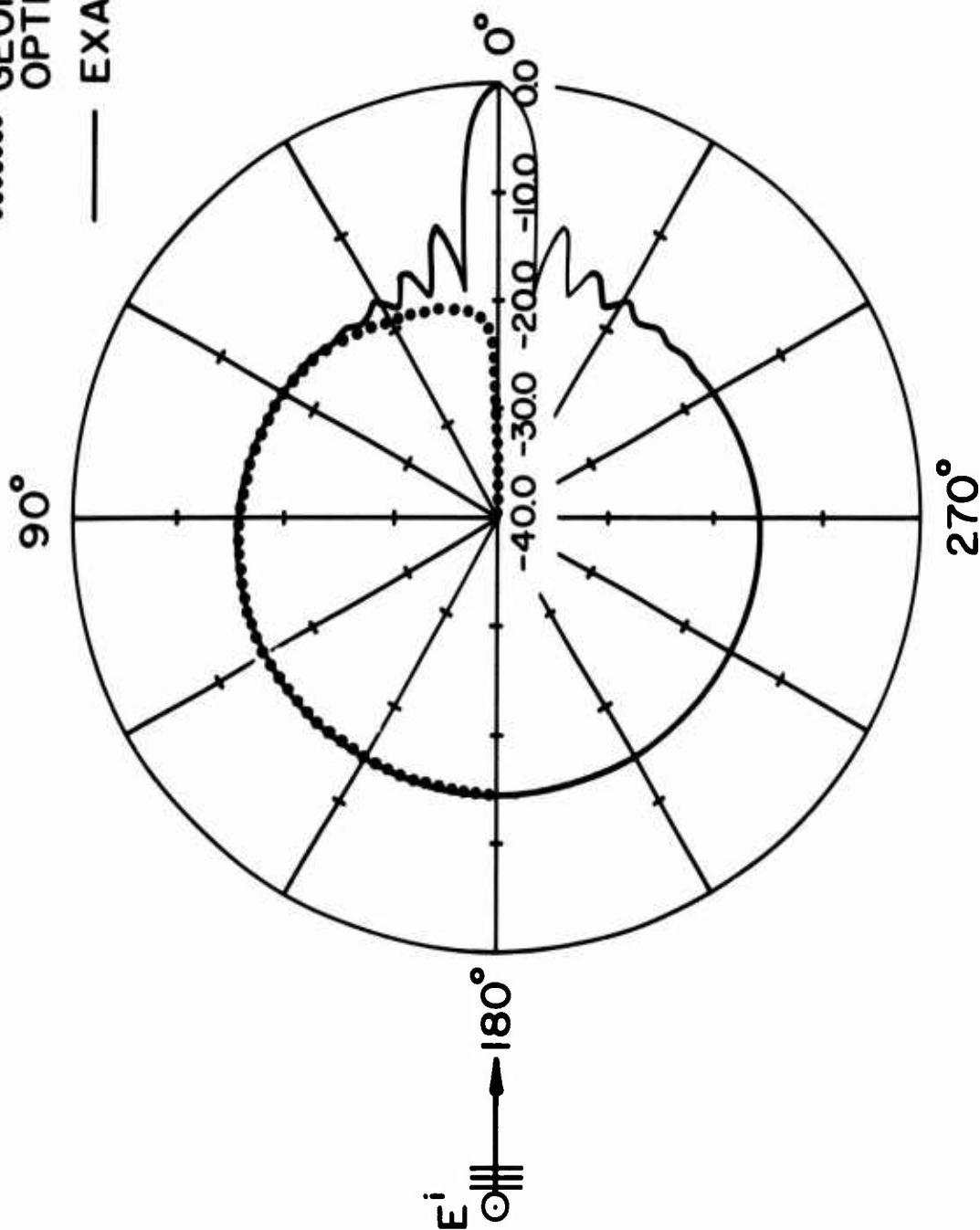
Figure 6.9. Geometrical optics scattered far-field pattern in dB of a circular cylinder with radius a = 3λ.

geometrical optics solution would have still predicted the same scattered
far-field pattern as long as the illuminated portion of the surface
were cylindrical.

In spite of the serious discrepancy in the forward-scattering di-
rection, the geometrical optics far-field solution is, nonetheless, in
good agreement with the exact solution for a wide range of angles ex-
tending from the lit hemisphere deep into the dark hemisphere. Only
within a narrow range of angles in the immediate neighborhood of the
forward-scattering direction does the geometrical optics far-field start
to deviate from the exact far-field pattern. This observation leads to
the conclusion that the geometrical optics solution is a very good ap-
proximation to the exact solution except in the neighborhood of the
forward-scattering direction.

It is our conjecture here that the main beam in the forward-
scattering direction may be obtained from an aperture-field distribution.
If an infinite, planar aperture cutting the entire space into two half-
spaces is erected on the far-side of the cylinder when we view it from
the source side, we may stop all the geometrical optics rays at this
aperture and calculate the aperture-field distribution. For observa-
tion points beyond this aperture, we simply use Huygens' principle to
find the fields. Theoretically, this procedure of stopping the rays
at the aperture and then letting the aperture-field propagate beyond
it should not be different from the original ray fields which propagate
continuously undisturbed. Hence, we should obtain nothing more than
the original geometrical optics far-field pattern. However, if the
aperture is in juxtaposition with the cylinder, then that portion of

the aperture field in the vicinity of the cylinder must be completely different from the ray fields. As a matter of fact, the geometrical optics ray fields are no longer meaningful in that region. Consequently, an option is opened here for modifying the aperture-field distribution so that an improved far-field pattern can be obtained. Methods of synthesizing the aperture-field distribution are discussed in the following subsections.

The format of presentation of the methods is as follows. In each of the subsections, a method of synthesizing the   rture-field distribution is illustrated and the resulting far-field pattern displayed. Each subsection is concluded by a discussion of the method and a hint for a better synthesis. These methods for synthesizing the aperture-field distribution are arranged in the order of increasing degree of sophistication and accuracy. The first two methods presented below give totally unsatisfactory far-field patterns; however, they serve as good examples to indicate some of the pitfalls that one may run into, hence, their inclusion here is well justified.

6.4.1 Method I

All scientific progress starts from observations. It is no exception in the development of this method. The exact scattered electric aperture field in the shadow region cast by the geometrical-optics rays is depicted in Figure 6.10. Note that the width of this shadow is simply the diameter of the circular cylinder. In this particular example, the radius of the circular cylinder is thrice the wavelength of the incident plane wave which is polarized in the z-direction and has
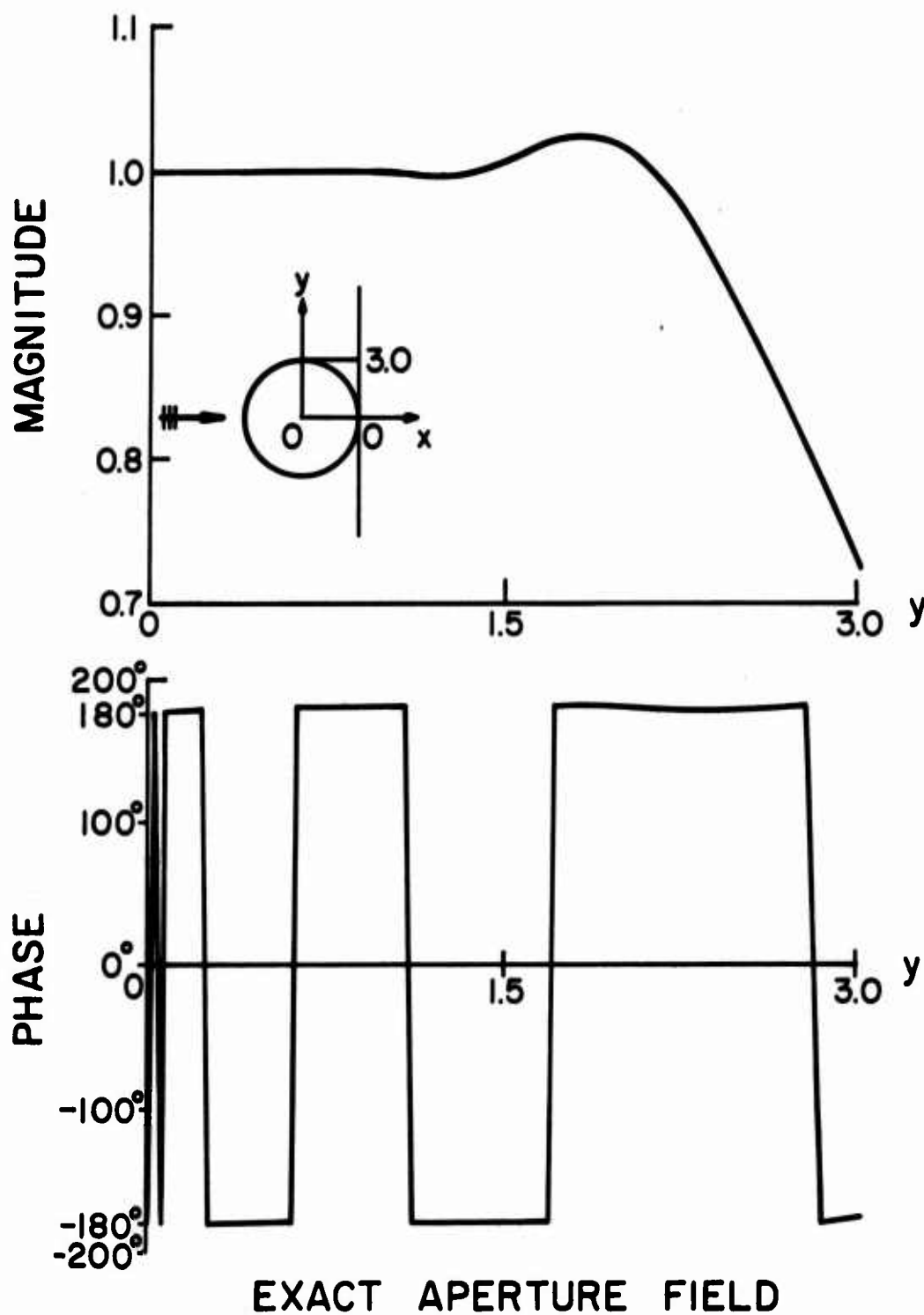
Figure 6.10. Exact scattered electric aperture-field in the geometrical optics shadow region.

a magnitude of 1. Due to symmetry, only half of the shadow-region scat-
tered aperture-field is plotted.

The magnitude curve has a constant value 1 at the center of the
shadow and hardly varies until it is about two wavelengths away from the
center, at which point the magnitude starts to decrease. The overshoot
in the magnitude curve is highly exaggerated because the scale runs from
0.7 to 1.1 only. The value of the magnitude of the exact scattered
aperture field at the edge of the geometrical-optics shadow is approx-
imately 0.73. Note that the phase variation throughout the entire
shadow region is nothing more than attributing a negative sign to the
magnitude. This fact does not come as a surprise, because, in the
deep-shadow region, the total electric field should be zero; hence, the
scattered E-field in that region should be just the negative of the
incident E-field.

Having observed this fact about the scattered electric aperture
field, a first attempt to improve the geometrical-optics far-field is
naturally to assume an aperture distribution which is the negative of the
incident E-field in the geometrical-optics shadow region and is zero
outside this shadow region. Alternatively, the scattered electric
aperture field outside the shadow region could have been assumed the
value of the geometrical-optics scattered E-field. However, the process
of stopping the geometrical-optics rays at the aperture and then letting
them radiate again to generate the far-field is not much different from
the far-field obtained directly from the geometrical-optics rays prop-
agating to the far-field zone undisturbed. The only significant dif-
ference is an additional contribution generated by the shadow-region
aperture-field to the far-field. The scattered far-field pattern is

obtained by superimposing the geometrical-optics far-field and the additional far-field computed by Fourier transforming the assumed scattered aperture E-field in the shadow region.

The far-field pattern obtained by this method is shown as a dotted curve in Figure 6.11. Recall that the Fourier transform of the rectangular pulse aperture distribution results in a sin x/x, or the sinc function, type of far-field pattern. Therefore, the main beam in the forward-scattering direction shows up. A comparison of Figure 6.2, Figure 6.9, and Figure 6.11 manifests the remarkable improvement in the geometrical-optics far-field pattern by the additional far-field generated by the deep-shadow aperture-distribution which is precisely what was ignored in the geometrical-optics solution. The deep nulls in the neighborhood of the forward-scattering direction are due to the phase interferences between the geometrical-optics solution and the Fourier transform of the aperture-distribution. Moreover, the relatively pronounced oscillations in the far-field pattern are caused by the discontinuities in the aperture-field distribution. In the next subsection we discuss another method of synthesizing the aperture-field distribution so that the extraneous oscillations can be suppressed.

6.4.2 Method II

The method discussed in the last subsection substantially improved the geometrical-optics solution of the scattered far-field pattern. However, extraneous oscillations occurred in the far-field pattern and further improvement is necessary. It is well-known in the field of antenna design that a tapered aperture field produces a low side-lobe radiation-pattern. Therefore, the second attempt to improve the geometric-optics solution is to synthesize a smoothly tapered aperture-distribution of the scattered E-field. To this end, consider a
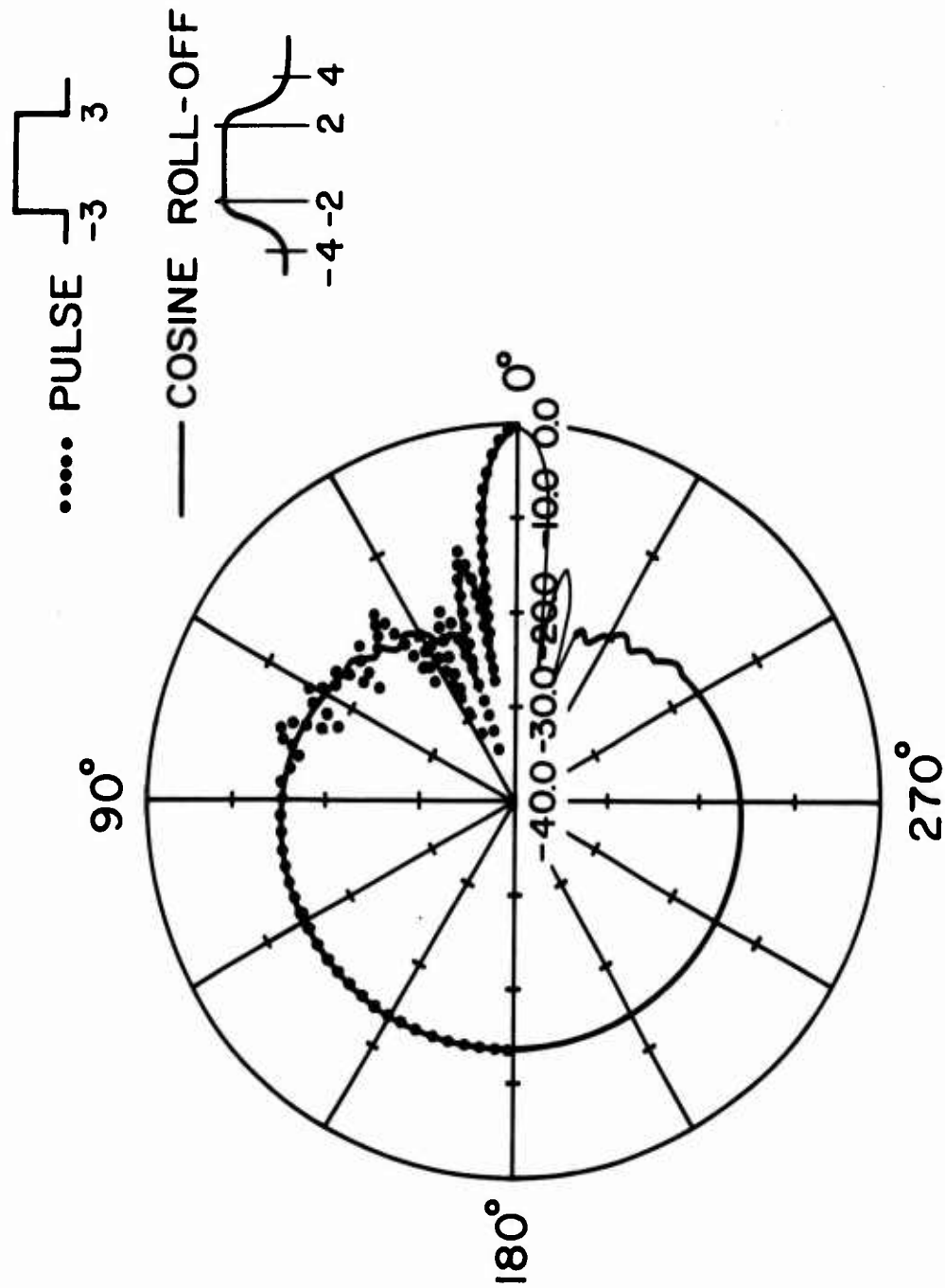
Figure 6.11. Scattered far-field patterns in dB of a circular cylinder with radius a = 3λ obtained by Methods I and II.

sinusoidal roll-off function of the form

$$f(y) = -\frac{1}{2} + \frac{1}{2} \cos \frac{A - y}{A - B} \pi \qquad (6.28)$$

where A and B are parameters. Note that the attractive property of such a sinusoidal roll-off function is that it serves as a very good interpolating curve between the constant values -1 and zero. Not only the values, but also the slopes of the function being interpolated are matched at the two end points of the interpolation interval designated by [A,B]. In a sense, such a curve possesses the properties of a spline.

The parameters A and B are chosen to correspond to the width of the penumbra-region, or better-known as the "transition-region" on the aperture. To date, no reliable techniques are available in the literature to determine the width of the transition-region to a considerable degree of accuracy. In the literature, it has always been assumed that the transition-region is located symmetrically about the boundary of the geometrical shadow. However, such an assumption is not very accurate because from the exact aperture-field distribution, the transition-region is observed to be *asymmetric* about the boundary of the geometrical-optics shadow and it extends much farther into the illuminated region than the dark region. This point is discussed further in the next subsection.

Nevertheless, it is educational to compute the far-field using the aperture-field distribution synthesized from the tapering sinusoidal roll-off functions in the penumbra-region and the negative of the incident field in the deep-shadow region. In this example, the radius of the cylinder is 3λ; the closest approximation to the width of the transition region is 1λ on either side of the boundary of the

geometrical-optics shadow, which means that a 2λ-transition region is assumed.

The far-field pattern obtained by this method is shown as a solid curve in Figure 6.11. As expected, the extraneous oscillations present in the far-field pattern obtained by Method I are suppressed. However, there are still quite an amount of discrepancies from the exact solution. The reason for these discrepancies can be traced to the ignorance of the phase information in the course of solution. So far, the phase has been assumed to take on the value π in the entire aperture-field distribution. Actually, this is not the case in the transition region. The phase information must be included in the process of solution; otherwise, the far-field pattern cannot be improved further by simply manipulating the magnitude. In the next subsection we discuss another method of synthesizing the aperture distribution so that both the magnitude and phase variations are taken into account in the process of solution; hence, further improvements on the far-field pattern can be achieved.

6.4.3 Method III

In the last two subsections, methods of synthesizing the scattered electric aperture-field distribution in the geometrical-optics deep-shadow region and the transition or the penumbra region have been discussed. Although the manipulations for magnitude only do give a substantial improvement over the geometrical-optics far field, the failure to account for the phase variation in the transition region prevents us from further improving the far-field pattern. Recognizing the importance of the phase-variation, we reexamine the basic principles

underlying the synthesis of the aperture distribution. It is found
that if the procedures in the following paragraph are followed to
synthesize the aperture distribution, the proper phase information can
be included in the solution.

As alluded to earlier in Subsection 6.4.1 when we discussed Method
I, the scattered electric aperture field in the well-illuminated region
may alternatively be approximated by the geometrical-optics scattered
far-field evaluated on the aperture. In other words, we stop the geo-
metrical-optics rays at the aperture and establish an aperture-distri-
bution which is nothing more than the equivalent sources in the Huygens'
principle. When this aperture-distribution reradiates, the far-field
beyond the aperture can be recovered as if the rays propagated directly
to the far-zone undisturbed. Then, the original geometrical-optics
far-field pattern should be recovered intact.

However, if the negative of the incident field is assumed in the
deep-shadow region, the main beam of the scattered far-field pattern is
regained as shown in the previous two subsections. As before, for the
extraneous oscillations in the far-field pattern to disappear, the
magnitude of the aperture distribution must not contain any sharp cor-
ners or discontinuities. With this in mind, curve-fitting techniques
may be employed in the transition-region to smoothly join the assumed
approximate aperture-distributions in the well-illuminated region and
the deep-shadow region.

The simplest interpolating curve that fulfills the aforementioned
requirement for suppressing extraneous oscillations is the cubic spline
of the form

$$f(y) = c_1 + c_2 y + c_3 y^2 + c_4 y^3 \quad . \tag{6.29}$$

The derivative of $f(y)$ is

$$f'(y) = 0 + c_2 + 2c_3 y + 3c_4 y^2 \quad . \tag{6.30}$$

The coefficients c_1, c_2, c_3 and c_4 can be completely determined if the values and the slopes of the interpolating cubic polynomial are known at the end points of the interpolation interval. The interpolation interval in the present example for a circular cylinder with radius 3λ is roughly from $y = 2\lambda$ to $y = 6\lambda$, which is obtained by observation of the width of the transition region in the exact aperture-field distribution. The values and slopes of the magnitudes and phases of the geometrical-optics scattered aperture-field at the illuminated end and the negative of the incident electric field at the dark end of the transition region can be computed numerically. Then the coefficients c_1, c_2, c_3 and c_4 can be obtained by solving the following matrix equation:

$$\begin{bmatrix} 1 & 2\lambda & (2\lambda)^2 & (2\lambda)^3 \\ 0 & 1 & 2(2\lambda) & 3(2\lambda)^2 \\ 1 & 6\lambda & (6\lambda)^2 & (6\lambda)^3 \\ 0 & 1 & 2(6\lambda) & 3(6\lambda)^2 \end{bmatrix} \begin{bmatrix} c_1 \\ c_2 \\ c_3 \\ c_4 \end{bmatrix} = \begin{bmatrix} f(2\lambda) \\ f'(2\lambda) \\ f(6\lambda) \\ f'(6\lambda) \end{bmatrix} \tag{6.31}$$

where

$f(2\lambda)$ is the value of the magnitude or phase of the negative in-
cident field at $y = 2\lambda$,

$f'(2\lambda)$ is the slope of the magnitude or phase of the negative
of the incident field at $y = 2\lambda$,

$f(6\lambda)$ is the value of the magnitude or phase of the geometrical-

optics field at $y = 6\lambda$,

$f'(6\lambda)$ is the slope of the magnitude or phase of the geometrical-

optics field at $y = 6\lambda$,

and

λ is the incident wavelength.

Thus, two sets of coefficients, one for the magnitude, and the other

for the phase, are obtained from (6.31) by first substituting the mag-

nitude entries into the right-hand-side column-vector, and then doing

the same thing for the phase entries.

The magnitude and phase curves are chosen to be interpolated be-

cause they are slowly varying smooth curves. The curve fitting cannot

be applied to the real- and imaginary-part curves of the same complex

quantity because they are highly oscillatory curves.

To summarize, an aperture-field distribution has been synthesized

with the negative of the incident electric field in the deep-shadow

region, the geometrical-optics scattered field in the well-illuminated

region, and the cubic-spline interpolations (applied to the magnitude-

and phase-curves) in the transition-region. The synthesis is sche-

matically shown in Figure 6.12.

The scattered far-field pattern is computed in two steps: (1) For

the forward-scattering hemisphere, the far-field pattern is obtained by

Fourier transforming the synthesized aperture distribution via the well-

known relationship between the far-zone field and the aperture field.

(2) For the back-scattering hemisphere, the far-field pattern is simply

obtained from the geometrical-optics solution. The Fourier transform

can be performed efficiently by a one-dimensional fast Fourier trans-

form (FFT).
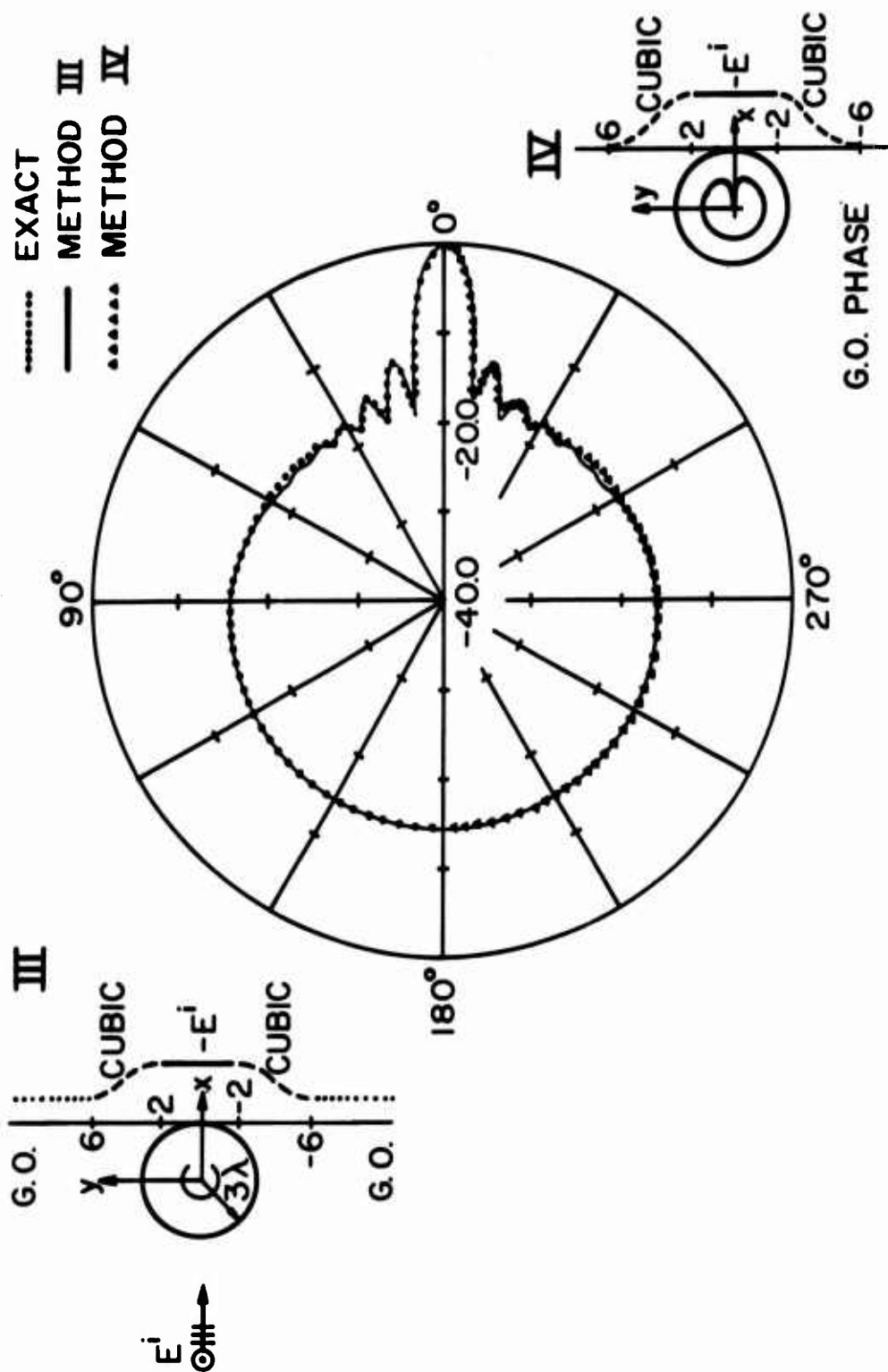
Figure 6.12. Scattered far-field patterns in dB of a circular cylinder with radius a = 3λ obtained by Methods III and IV.

However, attention must be called to the fact that the FFT result is forced to zero at 90° and 270° because the aperture must be truncated to a finite width (even as large as 90λ, thirty times the radius of the cylinder) in order to apply the FFT. Nevertheless, the FFT result is extremely good in the forward-scattering direction. As mentioned in the previous section, the geometrical-optics far-field is well-defined and is accurate for a wide range of observation angles extending from the lit side into the dark side. It is found that the FFT result and the geometrical-optics far-field overlap for a relatively wide range of angles (about 20 degrees) in the neighborhood of 70° and 290°, hence, the two far-field patterns can be joined smoothly at 70° and 290° without any discernible discontinuities.

The far-field pattern obtained in the above manner is shown in Figure 6.12. Except for the slight differences in the directions around 50° and 310°, the pattern is in excellent agreement with the exact solution, which demonstrates that the inclusion of the phase information in the transition region is crucial in obtaining an accurate approximation to the exact solution. Due to the slow variation of the magnitude and phase of the aperture-field distribution, the phase information is adequately obtained by a relatively straightforward cubic-spline interpolation. In the next subsection, we discussed another method of synthesizing the aperture-distribution so that the computation of the aperture field can be reduced substantially while the accuracy in the far-field pattern is still preserved.

6.4.4 Method IV

In the last subsection, an aperture-field distribution has been synthesized with the negative of the incident electric field in the deep-shadow region, the geometrical-optics scattered field in the well-illuminated region, and the cubic-spline interpolations (applied to the magnitude- and phase-curves) in the transition region. The scattered far-field pattern obtained by that method was in good agreement with the exact solution.

However, a reevaluation of the synthesis in Method III reveals that the computation of the geometrical-optics scattered field on the aperture is redundant. Recall that in Method I or Method II, the aperture-field distribution in the well-illuminated region was assumed to be zero, and the far-field pattern in the forward-scattering hemisphere was obtained by the superposition of the geometrical-optics far-field and the far-field radiated by the assumed aperture-field distribution in the geometrical shadow region. The superposition of the two far-fields in such a manner is equivalent to an alternative approach that was mentioned in Subsection 6.4.3, i.e., the Huygens' equivalent sources for the geometrical-optics far-field are created on the well-illuminated portion of the aperture, and combined with the assumed aperture-field distribution on the complementing nonilluminated portion of the aperture to obtain a complete scattered electric aperture-field distribution which, when reradiated into the forward-scattering hemisphere, produces the scattered far-field pattern in that hemisphere.

Theoretically, these two different approaches for obtaining the scattered far-field in the forward-scattering hemisphere give the same

result. From a computational standpoint, however, the approach using
the geometrical-optics scattered field directly in the far-zone for
superposition is more efficient than the other approach. The reason for
its superiority is two-fold: First, computational time can be reduced
substantially because the aperture-field distribution in the illuminated
portion of the aperture need not be computed but is simply set equal to
zero; and second, the fast Fourier transform can be applied to its full
capacity, meaning no inaccuracies near 90° and 270°, because the aperture-
field distribution is completely confined to that portion of the aperture
which includes the deep-shadow plus the transition-region only. To
further emphasize the advantage of eliminating the calculations of the
aperture-field in the illuminated region, we discuss the labor involved
in setting up an aperture-field distribution in the next paragraph.

In order to obtain a facsimile of the Fourier transform of the in-
finite aperture-distribution using the fast Fourier transform (FFT),
the aperture must be truncated at points beyond which the aperture-field
has decreased to a negligible quantity; which means that the illuminated
portion of the aperture is typically as large as fifteen times the geo-
metrical-optics shadow on the aperture. As mentioned earlier in Section
6.3 where the geometrical-optics solution was briefly derived, there
is no simple relation that can be found to explicitly express in terms
of the polar coordinates (ρ,ϕ) the parameters θ_0, ℓ, and ξ, in the geo-
metrical-optics scattered-field expression. The far-field approximation
$(\rho \rightarrow \infty)$ cannot be directly employed to accurately calculate the geo-
metrical-optics aperture-field distribution because the aperture-plane
is in juxtaposition with the cylinder; hence, for a considerably large
portion of the aperture, the far-field approximation, e.g., (6.27), is

still too crude. Therefore, in practice, one has to resort to numerical

methods. There are basically two routes that one can follow, namely,

either searching for the point of reflection when a point of observation

on the aperture is given, or interpolating for the field when a point

of reflection is chosen. While the accuracies of the numerical results

obtained by these two different approaches are comparable, the latter is

more straightforward in computer programming and more efficient compu-

tation-wise. But in either case, the geometrical-optics scattered

aperture-field has to be computed.

In this subsection, we discuss a synthesizing method which is, in

part, similar to Methods I and II, i.e., the calculations of the aperture-

field in the illuminated region are eliminated. However, the major

difference is the inclusion of the phase information in the transition-

region in the present synthesis. As in all of the previously discussed

methods, the scattered electric aperture-field distribution in the deep-

shadow region is assumed to be the negative of the incident field. The

field distribution in the well-illuminated portion of the aperture is set

equal to zero. In the transition-region, curve-fitting techniques are

employed to smoothly join the assumed approximate aperture-distributions

in the well-illuminated and the deep-shadow regions. A cubic spline is

obtained (for the magnitude of the aperture-field) by simply substituting

$f(6\lambda) = 0.0$ and $f'(6\lambda) = 0.0$ into the right-hand-side of the column-

vector in (6.31) and solving the resulting matrix-equation for the un-

known coefficients. The interpolated curve is the gradually tapered

magnitude curve of the aperture-field distribution. It seems the phase

curve, at the first look, cannot be obtained as straightforwardly as the

magnitude curve, because the assumed aperture-field at the illuminated
end of the transition-region is zero and the value and slope of the
phase curve are unknown. However, the value and slope of the phase of
the geometrical-optics scattered field at the illuminated end of the
transition region can be used in (6.31) for obtaining the phase-informa-
tion in the transition region. This point is discussed further in the
next paragraph.

In particular, the aperture-field being synthesized is the difference
of two aperture-field distributions, namely, the aperture-field synthe-
sized by Method III and the geometrical-optics aperture-field, i.e.,

$$E_{AP}^{IV} e^{i\phi_{AP}^{IV}} = E_{AP}^{III} e^{i\phi_{AP}^{III}} - E_{AP}^{G.O.} e^{i\phi_{AP}^{G.O.}} \tag{6.32}$$

where E is the magnitude and ϕ is the phase of the complex quantity.
Superscripts IV, III, and G.O. stand for Method IV, Method III, and
geometrical optics, correspondingly. Subscript AP stands for aperture.
Note that

$$\phi_{AP}^{III}(6\lambda) = \phi_{AP}^{G.O.}(6\lambda) \tag{6.33a}$$

and

$$E_{AP}^{III}(6\lambda) = E_{AP}^{G.O.}(6\lambda) \tag{6.33b}$$

which are direct consequences of the synthesis in Method III. Therefore,
at $y = 6\lambda$, we have

$$E_{AP}^{IV} \, e^{i\phi_{AP}^{IV}} = (E_{AP}^{III} - E_{AP}^{G.O.}) \, e^{i\phi_{AP}^{G.O.}} \tag{6.34a}$$

$$= 0e^{i\phi_{AP}^{G.O.}} \,. \tag{6.34b}$$

This confirms the remarks made in the last paragraph that the magnitude is zero and the phase is the geometrical-optics phase at the illuminated end of the transition region.

Thus, an interpolation by a cubic spline for the phase in the transition region gives an identical phase variation as in Method III. Note, however, that the phase curve need be computed only in the deep-shadow and the transition region where the magnitude of the aperture distribution is nonzero. In the well-illuminated region of the aperture, the phase variation becomes irrelevant because the magnitude of the aperture distribution is zero.

As mentioned previously, the illuminated portion of the aperture is typically as large as fifteen times the geometrical-optics shadow region in order to obtain a facsimile of the Fourier transform of the infinite aperture distribution using the fast Fourier transform. There-fore, in setting up the aperture distribution for the Fourier-transform operation, the present method is computationally more efficient than Method III. In addition, the fast Fourier transform can be applied to its full capacity, meaning no inaccuracies near 90° and 270°, because the aperture-field distribution is completely confined to that portion of the aperture which includes the deep-shadow plus the transition re-gion only. This renders it unnecessary to join the two far-field patterns at 70° and 290° as in Method III.

To summarize, an aperture-field distribution has been synthesized
with the negative of the incident electric field in the deep-shadow
region, the zero field in the well-illuminated region, and the cubic-
spline interpolations (one of which is between the magnitude of the
incident field and zero-field for the magnitude-variation, and the other
is between the phase of the incident field and the phase of the geometrical-
optics field for the phase-variation) in the transition region. The
synthesis is schematically shown in Figure 6.12.

The scattered far-field pattern is computed in two steps:
(1) For the forward-scattering hemisphere, the far-field pattern is ob-
tained by Fourier transforming the synthesized aperture distribution
via the well-known relationship between the far-zone field and the aper-
ture field. The Fourier transformed result is then superposed on the
geometrical-optics far field to obtain   the scattered far-field pattern
in that hemisphere. (2) For the back-scattering hemisphere, the far-
field pattern is simply obtained from the geometrical-optics solution.
Note that the geometrical optics far field is used throughout the en-
tire range of observation angles (0 to 360°) because in the synthesis
of the aperture-field distribution, the geometrical-optics aperture
field has not been taken into account (see (6.32)); hence, in step (1)
above, a direct superposition of the far fields is necessary to obtain
the scattered far-field pattern in the forward-scattering hemisphere.

The far-field pattern obtained in the above manner is shown in
Figure 6.12. Observe that the positions of the maxima and minima are
in good agreement with the exact solution. However, the oscillations
are not as pronounced and there are slight discrepancies (about ±1 dB)
in the levels of the maxima and minima in comparison with the exact

solution. Nevertheless, the far-field pattern of this method is in better agreement with the exact pattern in the directions around 50° and 310° than the far-field pattern of Method III. Generally speaking, the overall far-field pattern is in reasonably good agreement with the exact solution.

The slight discrepancies in the far-field pattern are due to the failure to take into account the shadowed portion of the cylindrical surface in the solution process. As a matter of fact, the shadowed portion of the obstacle can be of an arbitrary shape, but as long as the illuminated portion of the obstacle is circularly cylindrical, the far-field pattern obtained using the present method (or any one of the methods discussed so far) will be the same as that of the circular cylinder. In the next subsection, we discuss the use of Galerkin's method applied in the spectral domain to further improve the scattered far-field pattern by taking into account the information characterizing the shadowed portion of the obstacle, e.g., the radius of curvature of the shadowed surface, in the process of solution.

6.4.5 Method V

In the last subsection, we presented a method of synthesizing the aperture-field distribution so that the redundant computations of the aperture-field in the well-illuminated portion of the apertu e were completely eliminated while the accuracy in the far-field pattern was still preserved to an extent that the overall far-field pattern was in reasonably good agreement with the exact solution. The slight discrepancies in the far-field pattern were due to the failure to take into account the shadowed portion of the surface of the obstacle in the

process of solution. In this subsection, we discuss a method of synthe-
sizing the aperture-field distribution taking into account the informa-
tion characterizing the shadowed portion of the obstacle in the process
of solution so that further improvement of the scattered far-field pattern
can be achieved.

As alluded to in Section 6.1, the Introduction of this chapter,
a marked difference between the present approach and all of the con-
ventional methods available in the literature is the introduction of an
infinite planar aperture in juxtaposition with the obstacle. The scat-
tered far-field pattern in the forward-scattering hemisphere is obtained
by a Fourier transformation of the scattered field distributions on this
aperture. Therefore, operations for improving the scattered far-field
pattern can be performed on the scattered aperture-field distribution,
in contrast to the conventional approaches in which they are done either
directly on the induced surface current or directly on the scattered
far field. The advantage of concentrating our efforts on improving
the aperture-field distribution is two-fold. Firstly, the magnitude
and the phase of the aperture-field distribution are smoothly, non-
oscillatorily varying functions of positions in the plane of the aper-
ture; hence, improvement can be achieved in a relatively straightforward
manner. Secondly, the operations for improvement are performed on a
planar surface rather than on a curved surface as in the case of at-
tempting to directly improve the surface current on the obstacle in a
conventional approach, hence, the present method is conceptually simpler.
An improved scattered far-field pattern in the forward scattering hemi-
sphere of an n-dimensional obstacle can be obtained by Fourier trans-
forming an improved (n - 1)-dimensional scattered aperture-field

distribution, where n = 2,3. This is a salient feature of the method
which manifest itself to be numerically efficient by the circumvention
of the unwieldy three-dimensional fast Fourier transform (FFT). These
important points have been demonstrated in the previously discussed
methods of synthesizing the aperture-field distribution.

Because of the nonoscillatory nature of the magnitude and the phase
variations of the scattered aperture-field distribution, a very close
approximation to the exact aperture-field distribution was obtained by
Method III in which a simple cubic-spline interpolation-scheme was used
in the transition region to join the negative of the incident field
in the deep-shadow region smoothly to the geometrical optics scattered
field in the well-illuminated region. Again, a similar interpolation-
scheme was employed in the synthesis of the aperture-field distribution
in Method IV in which the *difference* of the aperture-field distribution
of Method III and the geometrical-optics scattered aperture-field was
closely approximated by joining the negative of the incident field in
the deep-shadow region smoothly to the zero "difference-field" in the
well-illuminated region. However, the magnitude and the phase varia-
tions in the transition region are slightly different from the inter-
polating cubic polynomials. Although the approximations made by these
cubic polynomials are very close to the true variations of the magni-
tude and the phase of the aperture-field distribution, these slight de-
viations manifest themselves in the resulting scattered far-field pat-
terns shown in Figure 6.12.

.he idea to further improve the scattered far-field pattern, or
equivalently, the synthesis of the aperture-field distribution of
Method IV, is to expand the aforementioned slight *deviations* of the

aperture-field distributions in the transition region into a series of
known basis functions with unknown coefficients. The unknown coef-
ficients can be determined by enforcing the boundary conditions on
the shadowed portion of the cylindrical surface of the obstacle. This
particular portion of the surface of the obstacle is chosen because it
has the strongest effect on the variations of the aperture-field dis-
tribution in the transition region. In a sense, this is an application
of the Galerkin's method in the spectral domain to solve for the un-
known *deviations* of the first-order synthesis of the scattered aperture-
field distribution from the true variations of the scattered aperture-
field distribution to obtain an improved second-order synthesis. Note,
however, that the unknown quantities are the *deviations* from, but not
the true variations themselves. Since the first-order synthesis of
Method IV is already a reasonably good approximation to the true solution,
only a refinement of the synthesis is necessary; and the Galerkin's
method applied in the spectral domain is well-suited for this purpose.

A word of caution is in order in regard of the choice of basis
functions in the Galerkin's method. Rectangular pulses are not recom-
mended for the basis because they introduce abrupt discontinuities into
the aperture-field distribution and give rise to the extraneous oscil-
lations in the scattered far-field pattern. This point has been demon-
strated in Method II of Subsection 6.4.2. Therefore, only smoothly
varying and gradually tapering off functions are suited for the use
as basis. With this in mind, a Gaussian pulse, as shown in Figure 6.13,
is used as the basis function, i.e.,

$$f_n(x_\ell) = \exp(-a^2 x_\ell^2) \tag{6.35}$$
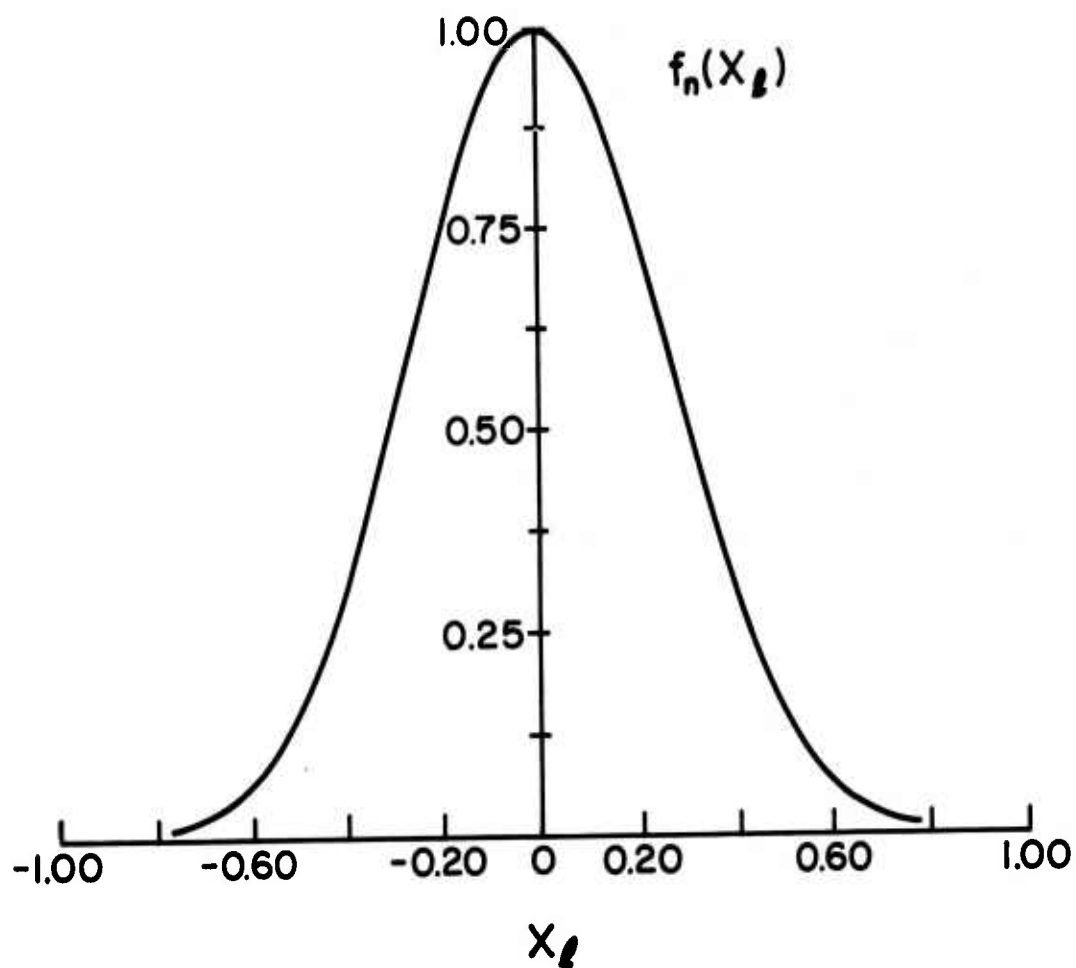
Figure 6.13. A Gaussian pulse.

where a = 2.75 and x_ℓ is a local coordinate. This particular choice of
the spread of the Gaussian pulse, 1/a, is to assure that the Gaussian
pulse decreases to 1 percent of its peak value at x_ℓ = 0.78, and it
decreases to approximately 1/e of its peak value at the crossover point
of two adjacent Gaussian pulses, which means that the gaps between ad-
jacent Gaussian pulses are filled up properly and the interferences
with Gaussian pulses beyond the adjacent ones are practically eliminated.
Thus, a superposition of these basis functions results in a smoothly
varying curve, which is precisely what is wanted in the refinement of
the aperture-field distribution.

In applying the Galerkin's method in the spectral domain, the
Fourier transform of the basis function is needed. For the particular
choice of a Gaussian pulse in (6.35) as a basis function, its Fourier
transform is simply another Gaussian function, namely,

$$\tilde{f}_n(\alpha_\ell) = F\{f_n(x_\ell)\}$$

$$= \frac{\sqrt{\pi}}{a} \exp\left(\frac{-\alpha_\ell^2}{4a^2}\right) \tag{6.36}$$

which is shown in Figure 6.14. In the above equation, α_ℓ is the Fourier
transform variable corresponding to the spatial variable x_ℓ.

The testing function in the Galerkin's method is the same as the
basis function. The locations of the basis functions on the aperture
and the testing functions on the surface of the obstacle are schematically
shown in Figure 6.15. Observe that the basis functions are situated
within the transition region in addition to the cubic-spline interpolation
of Method IV. The testing functions are arranged in the manner shown
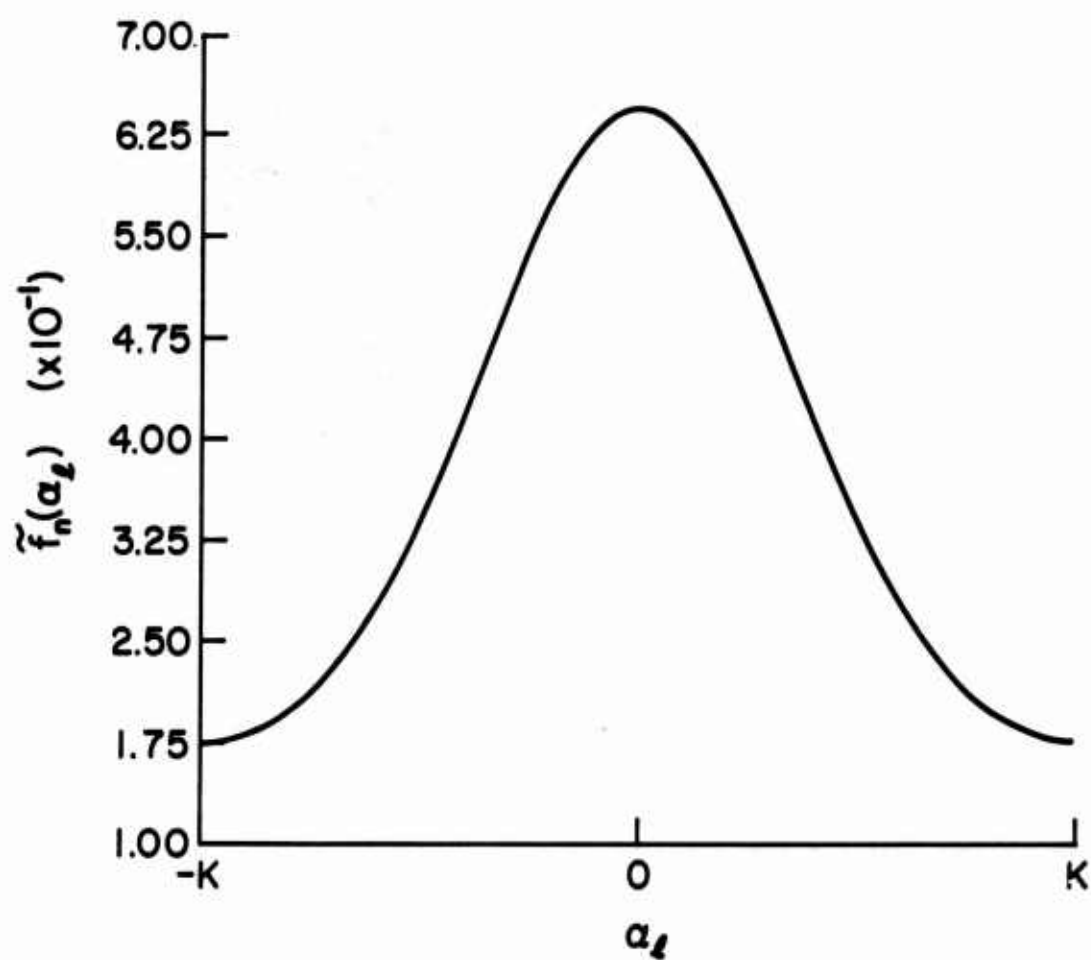
Figure 6.14.   Fourier transform of the Gaussian pulse in Figure 6.13.
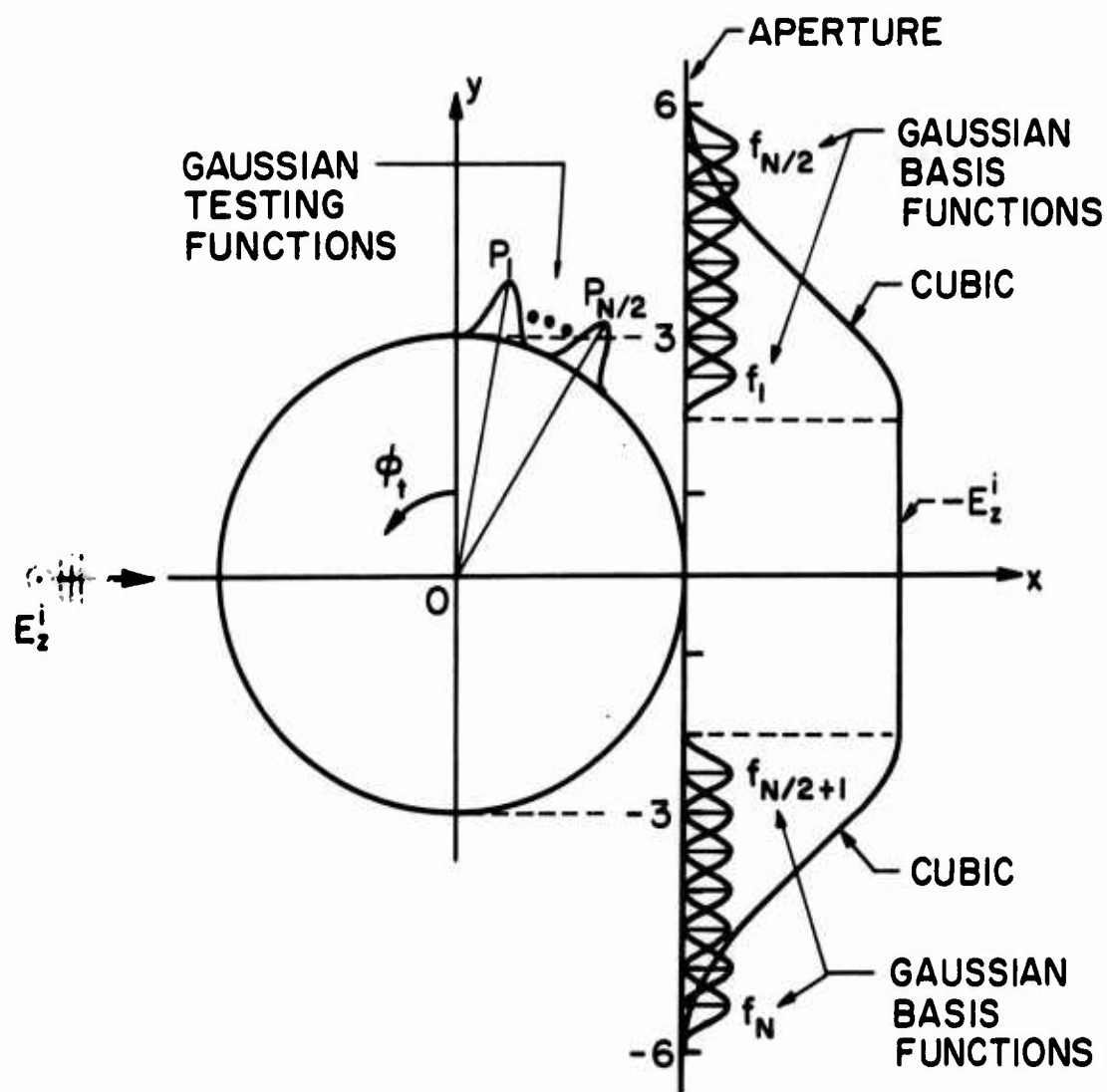
Figure 6.15. Locations of the basis functions on the aperture and the testing functions on the surface of the obstacle.

in Figure 6.15 because that particular portion of the surface of the
obstacle has the strongest effect on the variations of the aperture-
field distribution in the transition region. Due to the symmetry of the
problem, N basis functions, $f_1, f_2, \ldots, f_N$, are used but only N/2 un-
known coefficients need be solved, hence N/2 testing functions,
$P_1, P_2, \ldots, P_{N/2}$.

The aperture-field being synthesized is

$$\bar{E}_{AP}^{V} = \bar{E}_{AP}^{IV} + \sum_{n=1}^{N/2} c_n (f_n + f_{(N/2+n)}) \qquad (6.37)$$

where $\bar{E}_{AP}^{IV}$ is the difference aperture-field distribution of Method IV
(see (6.32)), and the deviations of $\bar{E}_{AP}^{IV}$ from the true variations are
approximated by the series in basis function of the form given in (6.35),
or specifically,

$$f_n(y) = \exp[-a^2 (y - y_{0n})^2] , \quad n = 1, 2, \ldots, N \qquad (6.38)$$

where y_{0n} is the position at which the peak of the nth basis function
is located (see Figure 6.15). The unknown coefficients c_n's are to be
determined by the Galerkin's method in the spectral domain.

Consider the aperture for the hemisphere of a testing function P_m
as shown in Figure 6.16. The portion of the aperture underneath the
Gaussian pulse is embedded in the obstacle. The width of this embedded
portion of the aperture is determined by the particular choice of the
spread of the Gaussian in (6.35) so that it is subtended by an angle
of 30° as shown in Figure 6.16. The scattered E-field on this embedded
portion of the aperture must be the negative of the incident E-field,

Figure 6.16. Aperture for the hemisphere of a testing function P_m.

$-E_m^i$, to satisfied the extended boundary condition [31]. The scattered E-field outside of this portion of the aperture is unknown and is designated by F_m as shown in Figure 6.16. Therefore, the scattered E-field on this aperture can be written as

$$E_{mAP}^s = -E_m^i + F_m \qquad (6.39)$$

where the subscript m signifies the aperture corresponding to the mth testing function, P_m. The Fourier transform of (6.39) reads

$$\tilde{E}_{mAP}^s = -\tilde{E}_m^i + \tilde{F}_m \qquad (6.40)$$

where ~ on top indicates the Fourier transform of the corresponding term in (6.39).

Now we take the inner product of the Fourier transform of P_m, $\tilde{P}_m$, with (6.40), which results in the following equation:

$$\langle \tilde{P}_m, \tilde{E}_{mAP}^s \rangle = -\langle \tilde{P}_m, \tilde{E}_m^i \rangle + \langle \tilde{P}_m, \tilde{F}_m \rangle \qquad (6.41)$$

where the angle brackets indicate an inner product of two complex functions of β, e.g., $A(\beta)$ and $B(\beta)$, defined as

$$\langle A, B \rangle = \int_{-\infty}^{\infty} A^*(\beta) B(\beta) \, d\beta \qquad (6.42)$$

where the asterisk denotes complex conjugate. By Parseval's theorem the second term in the right-hand-side member of (6.41) can be written as

$$\langle \tilde{P}_m, \tilde{F}_m \rangle = 2\pi \langle P_m, F_m \rangle \equiv 0 \qquad (6.43)$$

because P_m and F_m are defined in complementary domains on the aperture for the hemisphere of P_m (see Figure 6.16). Therefore, (6.41) becomes

$$<\tilde{P}_m, \tilde{E}^S_{mAP}> = -<\tilde{P}_m, \tilde{E}^1_m> \quad .$$ (6.44)

The Fourier transform of the aperture E-field, $\tilde{E}^S_{mAP}$, is related to the *far-field pattern in the hemisphere of* $P_m, T_m(\phi_\ell)$, by the following relation:

$$\tilde{E}^S_{mAP} = \frac{2}{k \sin \phi_\ell} T_m(\phi_\ell)$$ (6.45)

where $\phi_\ell = \phi - \phi_t$, ϕ_ℓ being the local polar coordinate, ϕ the central polar coordinate, and ϕ_t the polar coordinate of the location of P_m, all of which are shown in Figure 6.16. $T_m(\phi_\ell)$ is obtained by truncating the complete scattered far-field pattern, $T^V(\phi_\ell)$, to the hemisphere of P_m. $T^V(\phi)$ is given by

$$T^V(\phi) = T^{IV}(\phi) + \sum_{n=1}^{N/2} c_n (T^f_n(\phi) + T^f_{N/2+n}(\phi))$$ (6.46)

where $T^{IV}(\phi)$ is the scattered far-field pattern of Method IV; and $T^f_n(\phi)$ is the scattered far-field pattern of the nth basis function, f_n, in Figure 6.15. More specifically, $T^f_n(\phi)$ is expressed in terms of the Fourier transform of the nth basis function, $\tilde{f}_n$, in the following manner:

$$T^f_n(\phi) = \frac{-k}{2} e^{-ikA\cos\phi} \tilde{f}_n(\phi) \cos \phi$$

$$0 \le \phi \le 90^o \text{ and } 270^o \le \phi \le 360^o$$ (6.47)

in which A is the radius of the cylinder, and $\tilde{f}_n(\phi)$ is obtained from (6.36) using the shifting relation between Fourier pairs; hence,

$$\tilde{f}_n(\phi) = \frac{\sqrt{\pi}}{a} \exp\left(\frac{-k^2 \sin^2 \phi}{4a^2}\right) \cdot e^{-iky_{0n}\sin\phi} \quad , \quad n = 1, 2, \ldots, N \qquad (6.48)$$

where y_{0n} is the position at which the peak of the nth basis function, f_n, is located (see Figure 6.15).

Using (6.48), (6.47), (6.46), and (6.45) in (6.44), an equation of N/2 unknowns, $c_1, c_2, \ldots, c_{N/2}$, is obtained. Repeating the above procedure with different locations of the testing function on the surface of the obstacle results in a system of N/2 linear equations of N/2 unknowns, which is then solved by standard matrix-inversion techniques.

The matrix elements are generated by the inner products of (6.44) in a straightforward manner. The inner product on the left-hand-side of (6.44) simply becomes a linear superposition of the inner products of $\tilde{P}_m$ with the individual far-field patterns. This can be seen from (6.45) and (6.46). Since the invisible spectra of the far-field patterns are highly attenuated and they hardly contribute to the inner products, therefore, they can be ignored in the computation of the inner products. Hence, the formula for computing the inner product of $\tilde{P}_m$ and T is

$$<\tilde{P}_m, T>$$

$$= \sum_{\phi_{\ell i}=0}^{\phi_{\ell i}=\pi} e^{ik\sin\phi_{\ell i}A\cos 15^{\circ}} \frac{\sqrt{\pi}}{a} \exp\left(\frac{-k^2 \cos^2 \phi_{\ell i}}{4a^2}\right) 2T(\phi_{\ell i}) \, \Delta\phi_{\ell i} \qquad (6.49)$$

where T stands for T^{IV} or T_n^f. Using Parseval's theorem, the left-hand-side

of (6.44) can be written as

$$-<\tilde{P}_m,\tilde{E}_m^1> = -2\pi<P_m,E_m^1> \quad . \tag{6.50}$$

Since P_m is assumed nonzero only on the embedded portion of the aperture for the hemisphere of P_m, (Figure 6.16), the formula for computing the inner product in (6.50) is

$$<P_m,E_m^1>$$

$$= \sum_{x_{\ell i}=-A\sin 15^O}^{x_{\ell i}=A\sin 15^O} \exp(-a^2 x_{\ell i}^2 + ikx_{\ell i}\cos \phi_t - ikA \cos 15^O \sin \phi_t)\Delta x_{\ell i}. \tag{6.51}$$

After the unknown coefficients, $c_1, c_2, \ldots, c_{N/2}$, have been determined by the Galerkin's method, we can substitute them into (6.37) to obtain the improved synthesis of the "difference" scattered aperture-field distribution, $\bar{E}_{AP}^V$, and then proceed as in Method IV to compute the far-field. Alternatively, the coefficients, $c_1, c_2, \ldots, c_{N/2}$, can be substituted into (6.46) to directly obtain the improved far-field pattern, $T^V(\phi)$. The far-field pattern obtained by this method with $N/2 = 7$ and $\phi_t = -15^O$ to -45° at 5° increments is shown in Figures 6.17a and 6.17b and is in excellent agreement with the exact far-field pattern.
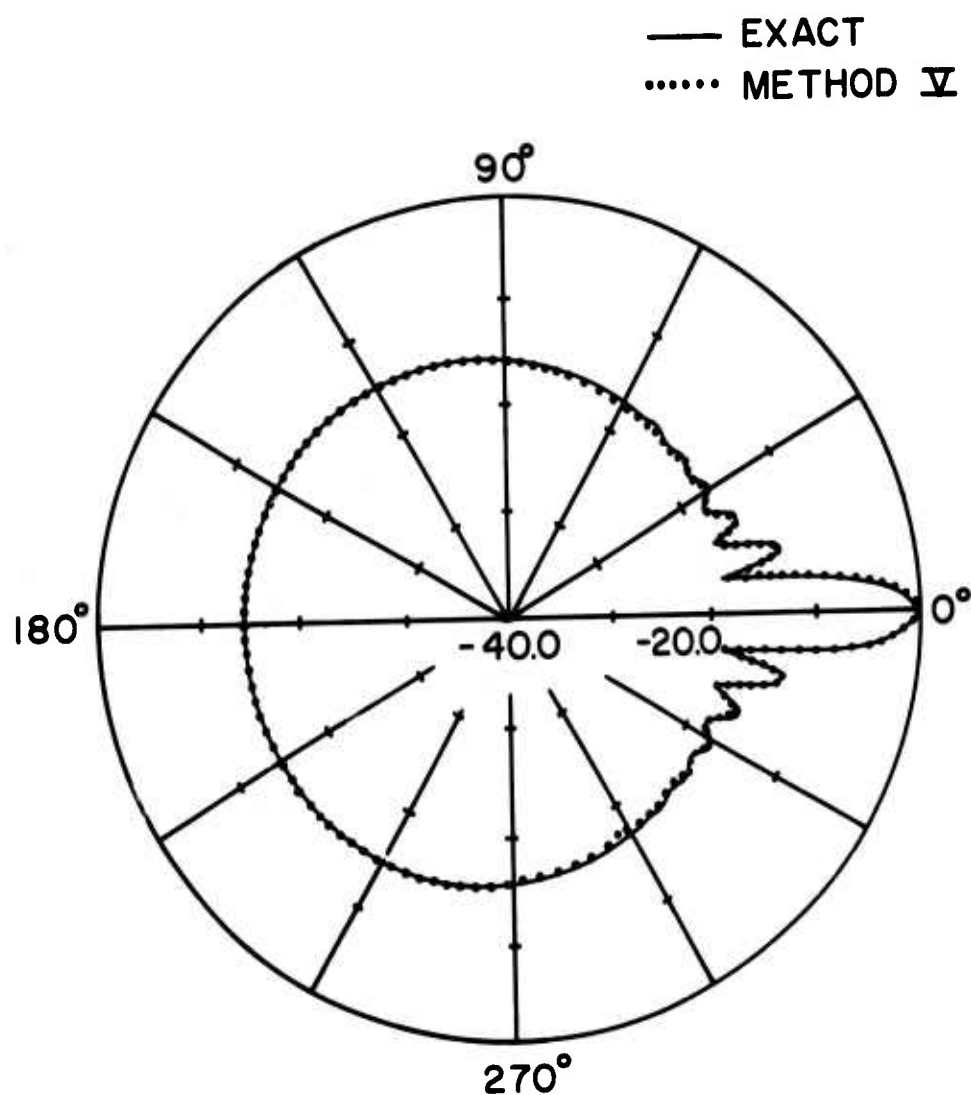
Figure 6.17a. Scattered far-field pattern in dB of a circular cylinder with radius a = 3λ obtained by Method V.
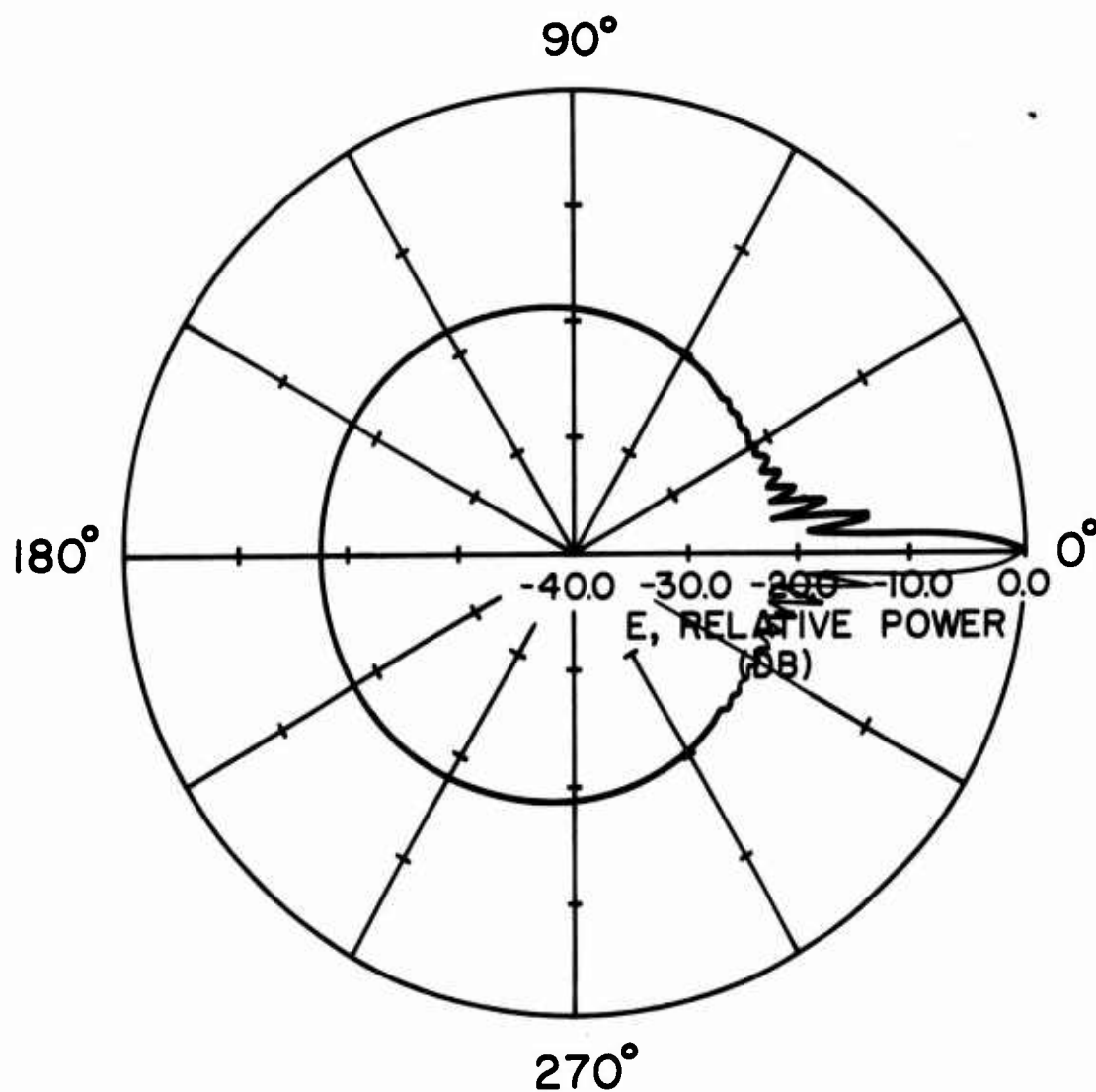
Figure 6.17b. Scattered far-field pattern in dB of a circular cylinder
with radius a = 6λ obtained by Method V.

6.5 Computation of Induced Surface Current

In electromagnetic wave scattering, two quantities are of vital importance, one is the scattered far-field pattern, from which the bi-static radar-cross-section (RCS) can be determined, and the other is the induced surface current on the scatterer, from which information can be extracted to aid in the design of the mounting of antennas and sensor booms on a practical scattering obstacle, e.g., a satellite. A detailed discussion of the computation of the scattered far-field pattern by systematically synthesizing the aperture-field distribution has been presented in the last section. An excellent approximation to the exact scattered far-field pattern has been obtained in a relatively straight-forward manner by the introduction of an aperture on which the improvement operations were performed. Such an accurate scattered far-field pattern motivates us to develop a feasible technique for the computation of the induced surface current on the obstacle to a reasonable degree of accuracy.

In the conventional approaches in the literature, the calculation of the scattered far-field pattern from an induced surface current may be formidable because of the numerical multiple-integration involved; on the other hand, the evaluation of the induced surface current directly from an approximate scattered far-field pattern may not be feasible because such a far-field pattern is not accurate enough. The development of the present approach provides a means to evade such a dilemma so that the induced surface current can be evaluated with ease when the approximate scattered far-field pattern has been improved. This method of computation of the induced surface current is made

possible by the extremely close approximation of the true scattered far-field pattern obtainable by the method of synthetic aperture distribution discussed in the last section. The detailed development of the method for computing the induced surface current is presented in the next subsection.

6.5.1 Method of computation

Suppose the induced surface current at a point Q on the surface of the obstacle as shown in Figure 6.18 is to be evaluated. The polar coordinates of the point Q are simply (A, ϕ_t), A being the radius of the circular cylinder and ϕ_t the angular displacement from the y-axis with positive reference direction counterclockwise. An infinite aperture with Q as the point of tangency to the cylinder is established for the hemisphere of Q as shown schematically in Figure 6.18. A local rectangular coordinate system (x_ℓ, y_ℓ) and the accompanying local polar coordinate system (ρ_ℓ, ϕ_ℓ) are set up for the aperture. The idea is to use that portion of the scattered far-field pattern contained in the hemisphere of point Q to obtain the scattered H-field on the aperture. The scattered H-field at point Q is subsequently combined with the incident H-field at point Q to obtain the total surface current at point Q. For other points on the surface of the obstacle, the induced surface currents can be obtained in the same manner by using their corresponding hemispheres and apertures.

The relation between the scattered far-field pattern and the Fourier transform of the scattered magnetic aperture field, $\tilde{H}^s$, is readily obtained as

$$\tilde{H}^s(\phi_\ell) = \frac{-2}{kZ_0} T(\phi_\ell) \exp(-ikA \sin \phi_\ell) \tag{6.52}$$
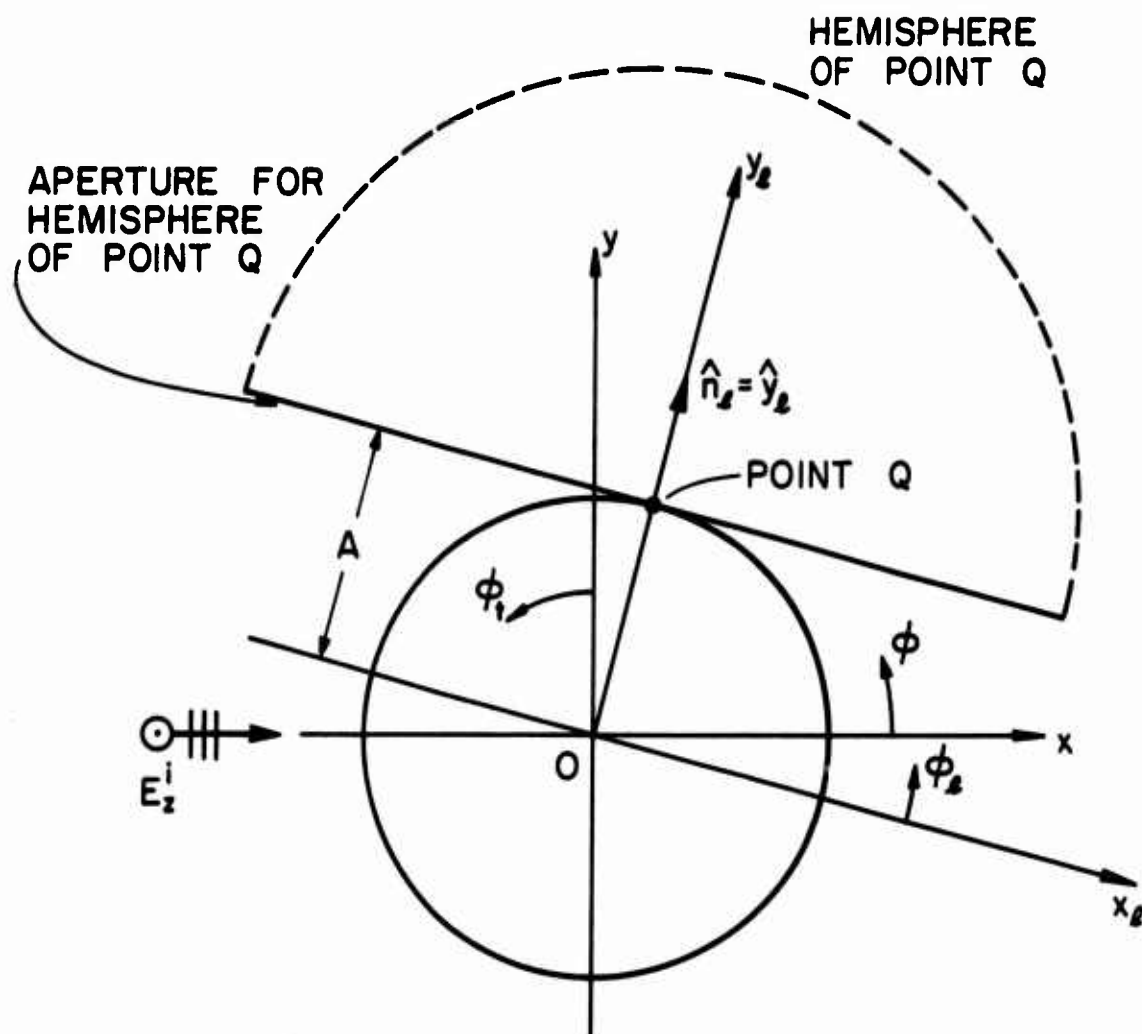
Figure 6.18. Aperture for hemisphere of point Q at which the induced surface current is evaluated.

where $T(\phi_\ell)$ is the scattered far-field pattern in the proper hemisphere, Z_0 is the free space characteristic impedance, and $\phi_\ell = \phi - \phi_t$ is the local polar coordinate. The phase factor in (6.52) is to assure that the aperture at $y_\ell = A$ but not at $y_\ell = 0$ is considered. The scattered magnetic aperture field, H^S, is obtained by an inverse Fourier transform of $\tilde{H}^S$ in (6.52), i.e.,

$$H^S(x_\ell) = F^{-1}\{\tilde{H}^S(\phi_\ell(\alpha))\} \quad . \tag{6.53}$$

However, only the value of the magnetic scattered field at $x_\ell = 0$ is of interest. Therefore, ignoring the negligible contributions from the invisible range of the far-field pattern, $H^S(x_\ell = 0)$ can be expressed as an integral of the following form:

$$H^S(x_\ell = 0) = \frac{-1}{\pi Z_0} \int_{\phi_\ell=0}^{\phi_\ell=\pi} T(\phi_\ell) \sin \phi_\ell \, d\phi_\ell \quad . \tag{6.54}$$

The numerical evaluation of $H^S(x_\ell = 0)$ is expedited by the following procedure: the interval of integration from 0 to π, $[0,\pi]$, is divided into 36 subintervals, each of which is of length $\pi/36$. Throughout the entire subinterval, the sinusoid, $\sin \phi_\ell$, can be assumed to have the constant value at the midpoint of the subinterval. Thus, (6.54) can be written as

$$H^S(x_\ell = 0) = \sum_{i=1}^{36} \sin(\phi_{\ell i}) \int_{\phi_{\ell j}=\phi_{\ell i}-\frac{\pi}{72}}^{\phi_{\ell j}=\phi_{\ell i}+\frac{\pi}{72}} T(\phi_{\ell j}) \frac{\pi}{180} \tag{6.55}$$

where $\phi_{\ell i}$ is the midpoint of the ith subinterval. If the scattered far-field pattern $T(\phi_\ell)$ is calculated at an increment of 1°, the index $j = 1,2, \ldots, 5$.

Note that the above procedure expedites the numerical evaluation of $H^s(x_\ell = 0)$ without sacrificing the fine detail of the scattered far-field pattern. This point is worth-emphasizing because the accuracy of the scattered far-field pattern obtained in the last section should be preserved as much as possible. Further degradation of the scattered far-field pattern may give intolerable numerical results.

The incident H-field at the point Q is given by

$$H_y^i = \frac{-1}{Z_0} e^{ikA\cos\phi} \quad . \tag{6.56}$$

Combining (6.55) with (6.56), and using the relation between the total surface current, $\bar{J}$, and the total H-field at the surface, i.e.,

$$\bar{J} = \hat{n} \times \bar{H}$$

$$= \hat{n} \times (\bar{H}^i + \bar{H}^s) \tag{6.57}$$

the total surface current at the point $Q(x_\ell = 0, y_\ell = A)$ is obtained. This completes the development of the method of computation of the induced surface current.

6.5.2 Results and comments

The magnitude and the phase of the total surface current on a perfectly conducting circular cylinder with radius $= 3\lambda$ are displayed in Figure 6.19. The exact eigenfunction solution of the total surface current is also shown in the figure for comparison. It is seen that the
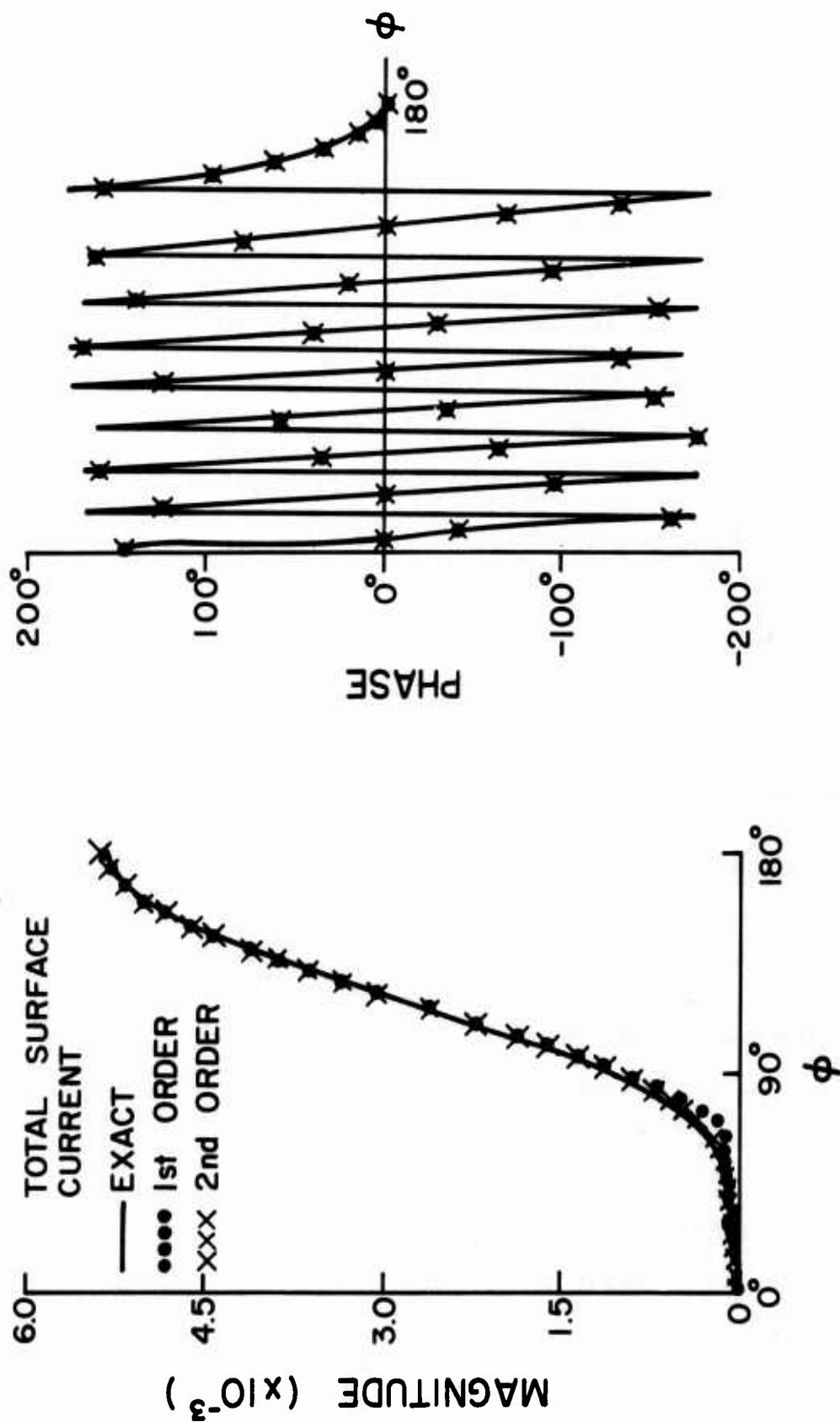
Figure 6.19. Total surface current on a perfectly conducting circular cylinder with radius a = 3λ.

solution of this study deviates slightly from the exact solution in

the neighborhood of 80°. However, the small deviation occurs at the

low end of the current curve, therefore, it is tolerable for practical

purposes. The rest of the curve is in remarkable agreement with the

exact solution.

Before closing this section, it is worthwhile to contrast the

present approach with the one developed by Burnside *et al.* [4]. Their

method uses a combination of the geometrical theory of diffraction and

the moment method to solve a circular cylinder scattering problem,

wherein the cylindrical surface is divided into three regions, namely,

the physical optics region in the well-illuminated side, the GTD region

in the deep shadow, and the pulse region in the transition region be-

tween the lit and the dark sides. It is a typical example of the con-

ventional approaches of attempting to directly improve the surface cur-

rent. However, one finds that the composite surface current computed

by using different techniques in different regions on the cylindrical

surface as indicated above is not smoothly connected at the bound-

aries of each region. These discontinuities are clearly shown in

Figure 6.20, which is Figure 4 in [4] reproduced here for comparison.

Furthermore, the discontinuities at the high end in the surface cur-

rent may introduce extraneous high-level sidelobes in the far-field

pattern. In addition, the surface current of Burnside's method de-

viates from the exact solution in both the high and the low ends of

the current curve. Moreover, the pulse region in Burnside's method

is typically one half of the circumference of the circular cylinder;

therefore, many current samples are needed for an electrically large
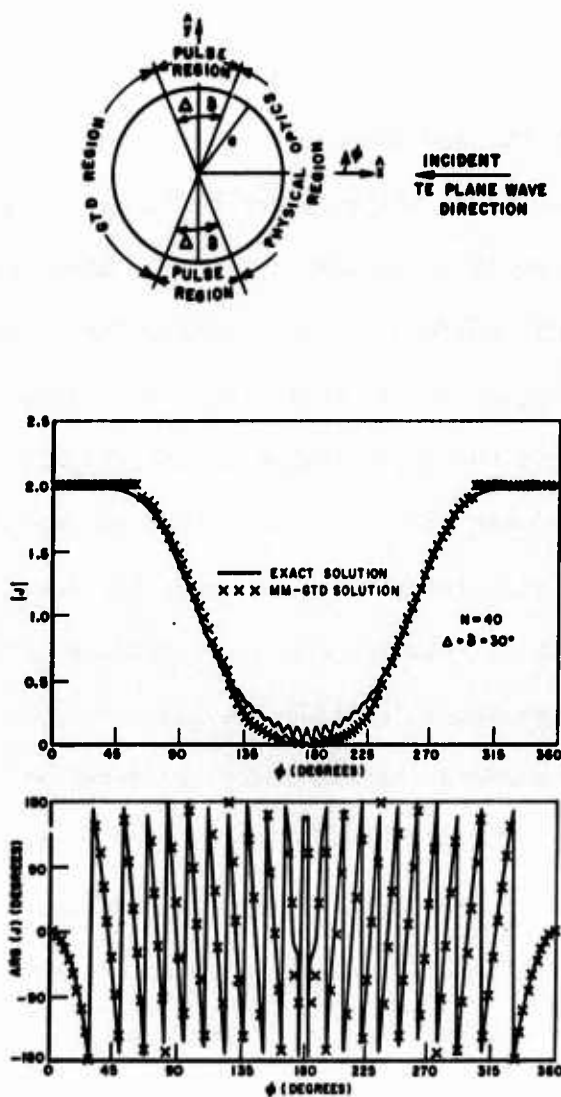
Figure 6.20. Burnside's MM-GTD solution for the induced surface current on a circular cylinder with radius a = 4λ.

cylinder, especially in the case of an E-wave incidence where the surface current starts to deviate from the physical optics current much faster than it does in the H-wave case.

In Burnside's approach, the far-field pattern must be computed by a numerical double integration of the surface current. Such a computation may be very time consuming. In contrast, we have presented a conceptually simple, computationally efficient method to obtain both the scattered far-field pattern and the induced surface current, which are in remarkably good agreement with the true solution.

6.6 Accuracy Check

In the previous sections, methods have been discussed for obtaining scattered far-field patterns and induced surface currents. The results have been compared with the available exact solution so that the accuracies of the approximate solutions were verified. However, in many practical situations, the exact solution is impossible to obtain, and quite often, the solutions arrived at by other approaches may not be accurate enough to compare with. Of course, experimental results provide a good evidence to validate the computed results. Nonetheless, experiments are expensive to set up and also can be time-consuming. Moreover, special techniques and ingenuities may be required to extract the needed information from the experimental data, viz., the measurable quantities. In addition, many environmental factors may inflict adverse effects on the measurable quantities and affect the results of the experiment. Therefore, an economical means of validating a computed solution is very much desired.

In the previous chapters, the approximate solutions of the scattered far-field patterns or induced surface currents were validated by a self-checking procedure, i.e., the tangential components of the scattered E-fields on the surface of the scatterers were computed and compared with the tangential components of the incident E-fields to check if the boundary conditions were satisfied. For scatterers with planar facets, the accuracy checking method developed in the previous sections is feasible. On the other hand, for scatterers with smoothly varying surface, or more precisely, surface with continuously varying curvatures, the accuracy checking method developed in the previous chapter becomes inefficient because a large number of points on the surface of the scatterer need be checked and each application of the method yields relevant information at a single point, viz., the point of tangency of an aperture and the obstacle. In order to provide a more efficient means of checking the accuracy of the approximate solutions, the self-checking procedure of the previous chapters need be modified to apply to the curved surface scatterers.

The idea is to use the concept of the extended boundary condition [31] instead of the ordinary boundary condition. Very briefly, the extended boundary condition requires that the total electric field be vanished in the region enclosed by the surface of the scatterer. This concept allows a portion of the aperture be embedded in the obstacle as illustrated in Figure 6.16. Thus, the accuracy check of the approximate solution can be done in the Galerkin's sense, which means that (6.44) is employed as a criterion for validating the approximate solution. The detailed discussion of the computations of the inner products in (6.44) has been presented in Subsection 6.4.5 where Method V was

developed; hence, to save repetition, the analysis is omitted in this section. The only important point need be emphasized is that the approximate scattered far-field pattern, $T(\phi)$, whose accuracy is being examined, is to be used to compute $\tilde{E}^s_{mAP}$ in the inner product of the left-hand-side member of (6.44).

This accuracy checking procedure has been applied to the approximate far-field patterns obtained by Method IV of Subsection 6.4.4 for the cases of $A = 3\lambda$ and $A = 6\lambda$, with the testing Gaussian pulse located at $\phi_t = -15^o$, -30°, and -45°. Results of these accuracy checks are tabulated in Tables 6.1 and 6.2.

Observe that the dominant parts of the entries in the second and the third columns of these tables are identical to two significant digits. The differences of the entries in the second and the third columns are shown in the fourth columns of these tables. The maximal deviation is about ±5 percent from the expected zero value, which shows that the results of the accuracy checks are quite satisfactory; hence, the scattered far-field patterns of Method IV can be concluded to be quite accurate without comparisons with the exact solutions. Of course, in the case of $A = 3\lambda$, the exact scattered far field has also been computed and a comparison with the approximate solution of Method IV not only further confirms the validity of the approximate solution, but also indicates that the accuracy check procedure is effective. For the scattered far-field pattern obtained by Method V, the self-checking procedure has already been built into that method as part of the solution process; hence, a separate accuracy check is repetitive.

TABLE 6.1

ACCURACY CHECK RESULTS FOR THE A = 3λ CASE

ϕ_t	$\langle \tilde{P}_m, \tilde{E}^s_{mAP} \rangle$	$-\langle \tilde{P}_m, \tilde{E}^1_m \rangle$	$\langle \tilde{P}_m, \tilde{E}^s_{mAP} \rangle + \langle \tilde{P}_m, \tilde{E}^1_m \rangle$
-15°	0.0004793 + i1.1452	$-$ 0.000003465 + i1.19533	0.0004828 $-$ i0.0501185
-30°	1.46487 $-$ i0.42989	1.44525 $-$ i0.48077	0.0196276 + i0.050886
-45°	$-$ 2.05293 $-$ i0.59244	$-$ 2.016778 $-$ i0.64182	$-$ 0.036151 + i0.04938

TABLE 6.2

ACCURACY CHECK RESULTS FOR THE A = 6λ CASE

ϕ_t	$\langle \tilde{P}_m, \tilde{E}^s_{mAP} \rangle$	$-\langle \tilde{P}_m, \tilde{E}^1_m \rangle$	$\langle \tilde{P}_m, \tilde{E}^s_{mAP} \rangle + \langle \tilde{P}_m, \tilde{E}^1_m \rangle$
-15°	1.18760 + i0.02917	1.19917 $-$ i0.00001	$-$ 0.01565 + i0.029184
-30°	$-$ 1.20338 + i0.943703	$-$ 1.21897 + i0.911953	0.015594 + i0.03175
-45°	$-$ 1.72229 $-$ i1.24086	$-$ 1.72114 $-$ i1.21891	$-$ 0.0011549 $-$ i0.0219545

6.7 Summary

In this chapter, a synthetic-aperture-distribution approach to the high-frequency electromagnetic scattering of obstacles with convexly curved surface has been presented. The idea was to transfer information characterizing the curved surface onto a planar aperture where operations for improving the geometrical-optics solution were carried out. The introduction of a planar aperture in the present approach is a marked difference from all of the conventional methods. A salient feature of the method is that the far field is obtained by Fourier transforming the aperture-field distribution; hence, it can handle problems involving an n-dimensional obstacle by an (n - 1)-dimensional fast Fourier transform (FFT), where n = 2,3. Therefore, the unwieldy three-dimensional FFT is circumvented; hence, the method is numerically efficient. Another important feature of the method is that the aperture-field distribution is slowly varying, i.e., not rapidly oscillatory, in *magnitude* and in *phase*. Hence, operations for improvement can be achieved in a relatively straightforward manner. Moreover, the method is conceptually simpler than other conventional methods in the literature, because operations for improvement are carried out on a plane rather than on a curved surface.

The method has been applied to solve the scattering problem of a plane wave by a perfectly conducting circular cylinder. The underlying principles involved have been illustrated by a detailed discussion on the syntheses of the approximate aperture-field distribution.

The Galerkin's method applied in the spectral domain not only results in a self-checking synthesis of Method V, as described in Subsection 6.4.5,

but also provides a convenient accuracy check of the approximate solution obtained by other methods.

The remarkable agreement between the scattered far-field obtainable by the method with the true solution makes it possible to devise a means of obtaining the induced surface current on the obstacle directly from the knowledge of the scattered far field. The computed surface current is in reasonable agreement with the true solution.

Considering the efforts involved in the formulations of the solutions and the computations of numerical results in conventional methods, the present approach indeed manifests itself as a conceptually simple, computationally efficient method for solving high-frequency electromagnetic scattering problems of curved-surface scatterers.

7. CONCLUDING REMARKS

A new approach for combining the integral equation and high frequency asymptotic techniques has been demonstrated with four illustrative examples--diffraction by a strip, a thin plate, a rectangular cylinder, and a circular cylinder. The basic idea is to start with the asymptotic high-frequency solution leading to the zero-order approximation of the scattered far field, and to use the latter in the Fourier-transformed version of the extended form of the integral equation to derive an improved result for the induced surface current density and the scattered far field. By formulating the problem in the spectral domain, the spatial domain integral equation becomes an algebraic equation, which can be recast in an iteration scheme suitable for manipulations on the computer. A salient feature of the method is that the accuracy of the solution for the surface current density and the scattered far field can be conveniently checked by verifying whether the scattered field, which is also computed in the process of generating the solution, indeed satisfies the boundary condition at the surface of the scatterer. Therefore, this approach not only provides a way for systematically improving the GTD solution using the self-consistent, integral equation formulations, but also provides a convenient validity check of the ray optics solution. Furthermore, the method of solution yields both the induced surface current density and the far field--an important feature which is not present in conventional asymptotic high-frequency methods.

The convergence of the iterative scheme in Chapter 2 has not been proven rigorously but has been demonstrated by numerical verification

only. Note, however, that the iteration procedure can always be followed, after a few iterations, by an application of the Galerkin's method in the transform domain. The iterated solutions, being close to the true solution, provide a very convenient choice for the basis set that may include some other functions as well. In fact, for curved surface structures, such as the circular cylinder in Chapter 6, the Galerkin's method has been found to be the more desirable one to follow.

We would like to mention two other approaches [14], [4] that are based on a combination of asymptotic and integral equation techniques. The one developed by Thiele [14] decomposes a given problem into two parts, one of which is handled using the GTD method and the other using the moment method. For the case of a wire antenna on a finite ground plane, the effect of the edge diffraction from the ground plane is evaluated using GTD and the result is subsequently used to augment the impedance matrix of the monopole antenna over an infinite ground plane. Although the method works rather well when GTD results are accurately known for the ground plane problem, e.g., a ground plane of circular shape, no convenient method is available for improving the solution when there are corners in the plane that contribute substantially to the scattered field. The latter situation arises when the ground plane is rectangular shaped and is not large compared with the wavelength, or when the antenna is mounted close to one or more of the edges.

The second method developed by Burnside [4] tends to rectify the situation alluded to above by solving for surface currents via the moment method in the regions where the GTD solution is not accurate, and by using asymptotic forms for the surface currents in regions where a

good approximation for these currents can be employed. However, this method cannot be conveniently applied to either the strip problem with grazing incidence, or to the large plate problem discussed in this thesis. For the strip problem, the GTD solution is quite inaccurate when the incident angle of the illuminating wave is near grazing. For the plate problem, the current does not settle down to known asymptotic form in the center region of the plate until it is at least three to four wavelengths squared. The moment method is incapable of handling the number of unknowns required to accurately solve for the current distribution on plate sizes that are larger than 2λ squared. To demonstrate that the present method is equally well applicable to the same type of practical structures which have been solved by the hybrid technique developed by Burnside [4], the geometries, including a rectangular cylinder, possessing multiple sharp edges and a circular cylinder having a smooth curved surface, have been investigated. Both the relative accuracy and the efficiency of the transform method have been found to be very favorable. The detailed description of this work has been presented in Chapters 5 and 6.

One other method developed by Bojarski [32] should be mentioned for completeness since he also uses the transform technique to convert the integral equation into an algebraic form. However, he uses a three-dimensional Fourier transform which again becomes unwieldy, both in terms of computer storage and time. In contrast, the present method employs (n - 1)-dimensional transforms even for an n-dimensional curved surface, where n = 2,3, as shown in Chapter 6, thus achieving a saving in the storage requirement by approximately two orders of magnitude

and a corresponding saving in CPU and I/O times as well. One other point with respect to Bojarski's work is that no advantageous use is made of the available analytic form of the GTD solution for the far field in the visible and invisible ranges, which, in many cases, forms an excellent starting point of the iteration procedure.

In conclusion, a conceptually simple, computationally efficient method for solving high-frequency electromagnetic scattering problems has been illustrated. The method has devised ways and means to systematically improve the far field as well as the induced surface current. It has been shown by examples that the method is applicable to scatterers with multiple edges as well as those with smooth curved surface. The computational efficiency of the method has been demonstrated. Both the far field and the surface current are obtainable in the process of solution. Furthermore, accuracy check is a built-in feature of the method.

It was the purpose of this study to demonstrate that a new approach to the high-frequency scattering is feasible. However, to develop the method further, it will be desirable to investigate its applications to more practical problems. The pioneering work done and documented herein is hoped to stimulate strong interests in future research activities along similar lines based on the present approach. The ultimate goal of the approach as well as any other approaches is to solve scattering problems involving arbitrarily shaped obstacles. Therefore, the next stage of development of the method should be an extension of it to cope with elliptical cylinders, spheres, and ellipsoids. All of these scatterers are of fundamental interests in high-frequency scattering. The fact

that the present approach uses two-dimensional FFT even for three-dimensional scatterers should make it feasible in obtaining reasonable results for these scatterers, which, in turn, can considerably augment the scope of future research.

REFERENCES

[1] R. F. Harrington, *Field Computation by Moment Methods*. New York: Macmillan, 1968.

[2] R. Mittra, Ed., *Computer Techniques for Electromagnetics*. Oxford: Pergamon Press, 1973.

[3] R. Mittra and T. S. Li, "A spectral domain approach to the numerical solution of electromagnetic scattering problems," *AEÜ*, vol. 29, pp. 217-222, 1975.

[4] W. D. Burnside, C. L. Yu and R. J. Marhefka, "A technique to combine the geometrical theory of diffraction and the moment method," *IEEE Trans. Antennas Propagat.*, vol. AP-23, pp. 551-558, July 1975.

[5] N. N. Wang and J. H. Richmond, "User-oriented GTD computer program for convex cylinders with arbitrary cross section." A paper presented at the USNC/URSI Annual Meeting at Boulder, Colorado, October 1975.

[6] E. O. Brigham, *The Fast Fourier Transform*. New Jersey: Prentice Hall, 1974.

[7] A. J. Poggio and E. K. Miller, "Integral equation solutions for three dimensional scattering problems," in [2], Chapter 4, 1973.

[8] R. G. Kouyoumjian and P. H. Pathak, "A uniform geometrical theory of diffraction for an edge in a perfectly-conducting surface," *Proc. IEEE*, vol. 62, pp. 1448-1461, November 1974.

[9] S. W. Lee and G. A. Deschamps, "A uniform asymptotic theory of electromagnetic diffraction by a curved wedge," *IEEE Trans. Antennas Propagat.*, vol. AP-24, pp. 25-34, January 1976.

[10] R. Mittra, Y. Rahmat-Samii and W. L. Ko, "Spectral theory of diffraction," *Appl. Phys.*, 1976 (in press).

[11] Y. Rahmat-Samii and R. Mittra, "Comparison of four high-frequency diffraction techniques based on analytical and numerical studies," to appear.

[12] A. W. Maue, "Formulation of general diffraction problems through an integral equation," *Zeltschrift für Physik*, vol. 126, pp. 601-618, 1949.

[13] R. Mittra and S. W. Lee, *Analytical Techniques in the Theory of Guided Waves*. New York: Macmillan, p. 81, 1971.

[14] G. A. Thiele and T. H. Newhouse, "A hybrid technique for combining moment methods with the geometrical theory of diffraction," *IEEE Trans. Antennas Propagat.*, vol. AP-23, pp. 62-69, January 1975.

[15] Y. Rahmat-Samii and R. Mittra, "Integral equation solution and RCS computation of a thin rectangular plate," IEEE Trans. Antennas Propagat., vol. AP-22, pp. 608-610, July 1974.

[16] J. L. Lin, W. L. Curtis and M. C. Vincent, "On the field distribution of an aperture," IEEE Trans. Antennas Propagat., vol. AP-22, pp. 467-471, May 1974.

[17] K. K. Mei and J. G. Van Bladel, "Scattering by perfectly-conducting rectangular cylinders," IEEE Trans. Antennas Propagat., vol. AP-11, pp. 185-192, March 1963. Also see corrections.

[18] J. R. Mautz and R. F. Harrington, "Radiation and scattering from large polygonal cylinders, transverse electric fields," Scientific Report No. 7, AFCRL-TR-75-0343, Department of Electrical and Computer Engineering, Syracuse University, Syracuse, New York, June 1975.

[19] M. F. Iskander and M. A. K. Hamid, "Scattering by a regular polygonal conducting cylinder," to appear.

[20] R. G. Kouyoumjian and N. Wang, "Diffraction by a perfectly conducting rectangular cylinder which is illuminated by an array of line sources," Report 3001-7, Electro-Science Laboratory, Department of Electrical Engineering, Ohio State University, Columbus, Ohio, prepared under Grant NGR 36-008-144 for NASA, August 1973.

[21] J. H. Richmond, "An integral-equation solution for TE radiation and scattering from conducting cylinders," Research Report, Electro-Science Laboratory, Ohio State University, Columbus, Ohio, April 1973.

[22] R. M. Lewis, D. S. Ahluwalia and J. Boersma, "Uniform asymptotic theory of diffraction by a plane screen," SIAM J. Appl. Math., vol. 16, pp. 783-807, 1968.

[23] W. L. Ko and R. Mittra, "A new approach based on a combination of integral equation and asymptotic techniques for solving electro-magnetic scattering problems," IEEE Trans. Antennas Propagat., vol. AP-24, November 1976 (in press).

[24] J. S. Yu and R. C. Rudduck, "On higher-order diffraction concepts applied to a conducting strip," IEEE Trans. Antennas Propagat., vol. AP-15, pp. 662-668, September 1967.

[25] J. B. Keller, R. M. Lewis and B. D. Seckler, "Asymptotic solution of some diffraction problems," Comm. Pure Appl. Math., vol. 9, pp. 207-265, 1956.

[26] J. B. Keller, "Geometrical theory of diffraction," J. Opt. Soc. Amer., vol. 52, pp. 116-130, 1962.

[27] R. F. Harrington, Time Harmonic Electromagnetic Fields. New York: McGraw-Hill, 1961.

[28] R. G. Kouyoumjian, L. Peters, Jr., and D. T. Thomas, "A modified geometrical optics method for scattering by dielectric bodies," _IEEE Trans. Antennas Propagat._, vol. AP-11, pp. 690-703, November 1963.

[29] S. W. Lee, "Electromagnetic reflection from a conducting surface: Geometrical optics solution," _IEEE Trans. Antennas Propagat._, vol. AP-23, pp. 184-191, March 1975.

[30] J. J. Bowman, T. B. A. Senior and P. L. E. Uslenghi, "Electromagnetic and acoustic scattering by simple shapes," Final Report AFCRL-70-0047, p. 100, January 15, 1970.

[31] P. C. Waterman, "Matrix formulation of electromagnetic scattering," _Proc. IEEE_, vol. 53, pp. 805-812, August 1965.

[32] N. N. Bojarski, "K-space formulation of the electromagnetic scattering problem," Technical Report AFAL-TR-71-75, March 1971.

APPENDIX A

UNDERSTANDING AND APPLYING THE FAST FOURIER TRANSFORM

This appendix is written to serve as a tutorial presentation of the Cooley-Tukey Fast Fourier Transform for rapid computation of the Discrete Fourier Transform of a function represented by a discrete set of data points.

The Fourier transform of a function $f(t)$ may be defined by

$$F(\omega) = \mathcal{F}\{f(t)\} = \int_{-\infty}^{\infty} f(t) \, e^{-j\omega t} \, dt \quad . \tag{A.1}$$

Both $F(\omega)$ and $f(t)$ are complex functions of real variables.

Suppose that $f(t)$ is not available analytically, but instead is expressed as a sequence of samples, $f(nT)$. If these samples are taken to be the sequence produced by sampling $f(t)$ with a Dirac delta function sampler, we may write

$$f*(t) = \sum_{n=-\infty}^{\infty} f(nT) \, \delta(t - nT) \tag{A.2}$$

where the asterisk implied a sampled function.

The equation (A.2) has a Fourier transform

$$F*(\omega) = \sum_{n=-\infty}^{\infty} f(nT) \, e^{-j\omega nT} \quad . \tag{A.3}$$

If $f(nT) = 0$ for $n < 0$, (A.3) reduces to the familiar z-transform

$$F(z) = \sum_{n=0}^{\infty} f(nT) \, z^{-n} \quad . \tag{A.4}$$

Observation of (A.3) shows that the Fourier transform of any train of impulses is periodic in ω with a period $2\pi/T$.

A.1 The Discrete Fourier Transform

Suppose that $f(t)$ is represented by a finite number of samples, say N, such that the samples are $f(nT)$, $0 < n < N - 1$. Further, let the spectral function $F(\omega)$ be represented by $F(k\Omega)$, $0 < k < N - 1$. The variables T and Ω represent the spacing of samples in time and frequency, respectively. Then in (A.2) and (A.3) there are only a finite number of samples and we can write

$$f*(t) = \sum_{n=0}^{N-1} f(nT)\delta(t - nT) \tag{A.5}$$

and

$$F*(k\Omega) = \sum_{n=0}^{N-1} f(nT)\, e^{-j\Omega Tkn} \quad . \tag{A.6}$$

The equation (A.6) represents a discretizing of the integral transform (A.1) in both time and frequency. Thus, the expression (A.6) can be readily computed. From (A.6) we drop the asterisk notation and define the Discrete Fourier Transform (DFT) of $f(t)$ as

$$F(k\Omega) = \sum_{n=0}^{N-1} f(nT)\, e^{-j\Omega Tnk} \tag{A.7a}$$

where

$$\Omega = \frac{2\pi}{NT} \quad . \tag{A.7b}$$

We may show that for this choice of Ω, there are only N distinct values
of $F(k\Omega)$ which can be computed.

Consider an arbitrary integer k. This integer can be expressed
as

$$k = rN + k_0$$

where

$$k_0 = k \text{ modulo } N$$

and

$$r = (k - k_0)/N \quad .$$

We can thus write

$$F(k\Omega) = \sum_{n=0}^{N-1} f(nT)\, e^{-j\Omega Tn(rN+k_0)}$$

$$= \sum_{n=0}^{N-1} f(nT)\, e^{-j\Omega Tnk_0}\, e^{-j\Omega TNnr} \quad .$$

Now

$$\Omega TN = 2\pi \text{ from (A.7b), so } e^{-j\Omega TNnr} = 1$$

and

$$F(k\Omega) = \sum_{n=0}^{N-1} f(nT)\, e^{-j\Omega Tnk_0} \quad .$$

So for $k > N - 1$, $F(k\Omega)$ reduced to $F[(k \bmod N)\Omega]$. That is to say that $F(k\Omega)$ is periodic in k with period N.

A.2 Properties of the DFT

The DFT can be shown to be frequency selective. Suppose $f(nT) = e^{jq\Omega nT}$ where we have let $\omega = q\Omega$ be a multiple of Ω. (It is not necessary that q be an integer.) Then

$$F(k\Omega) = \sum_{n=0}^{N-1} e^{j(q-k)n\Omega T} \tag{A.8a}$$

$$= \frac{1 - e^{j(q-k)N\Omega T}}{1 - e^{j(q-k)\Omega T}} \ . \tag{A.8b}$$

Consider (A.8) for integral q. If $k = q \bmod N$, $e^{j(q-k)N\Omega T} = e^{j(q-k)\Omega T} = 1$, and (A.8b) is seen to be a 0/0 form. However, it is clearly seen from (A.8a) that $F(k\Omega) = N$ in this case. For $k \neq q \bmod N$, the exponential in the numerator of (A.8b) still has a value of 1, but the exponential in the denominator does not, so $F(k\Omega) = 0$.

$$F(k\Omega) = \begin{cases} N & k = q \bmod N \\ 0 & k \neq q \bmod N \end{cases} \ . \tag{A.9}$$

If q is not an integer, we may deduce from (A.8b) that $F(k\Omega) \neq 0$ for all k. Thus, from (A.9) we see that the DFT is frequency selective for frequency which is an integral multiple of Ω;--a property which corresponds closely to the frequency selectivity of the continuous Fourier transform.

The DFT is a linear operator directly from the definition of (A.7). This may be expressed by the statement

$$DFT\{af(nT) + bg(nT)\} = aDFT\{f(nT)\} + bDFT\{g(nT)\} \ . \tag{A.10}$$

An inverse DFT exists which will map a DFT back into its generating sequence. This inverse is expressed by

$$f(\ell T) = \frac{1}{N} \sum_{k=0}^{N-1} F(k\Omega) \ e^{+j\Omega T\ell k} \quad . \tag{A.11}$$

This differs from (A.7) in the $\frac{1}{N}$ scale factor and the sign of the rotation of the exponential.

We may show (A.11) to be valid by substituting (A.7) for $F(k\Omega)$.

$$f(\ell T) = \frac{1}{N} \sum_{k=0}^{N-1} \sum_{n=0}^{N-1} f(nT) \ e^{-j\Omega Tnk} \ e^{+j\Omega T\ell k}$$

$$= \frac{1}{N} \sum_{n=0}^{N-1} f(nT) \sum_{k=0}^{N-1} e^{j\Omega T(\ell-n)k} \quad .$$

Now

$$\sum_{k=0}^{N-1} e^{j\Omega T(\ell-n)k} = \begin{cases} N & n = \ell \bmod N \\ 0 & n \neq \ell \bmod N \end{cases}$$

so

$$f(\ell T) = \frac{1}{N} \ f[(\ell \bmod N)T]N$$

$$= f[(\ell \bmod N)T] \quad .$$

We observe that the inverse transform reproduces the original function with a periodic extension of period N.

A.3   Fast Fourier Transform Algorithms

The DFT of a function can be calculated through a direct application of (A.7). The compute time required for this calculation would be proportional to N^2 if all N frequency points were extracted.

The Cooley-Tukey algorithm uses the presence of redundant calculations in (A.7) and of factorable multiplications in order to reduce the compute time of the computation. For N, which is a power of two, the computation is proportional to $N \log_2 N$. This provides substantial time savings. For example, if $N = 1024$, $N^2 = 1,048,576$, while $N \log_2 N = 10,240$, or just under one percent of N^2.

In describing the Cooley-Tukey algorithm, for notational simplicity, we define

$$W = e^{-j\Omega T} = e^{-j(2\pi/N)} \quad . \tag{A.12}$$

This definition requires that we not neglect the dependence of W on N. For instance, when we transform a sequence with N/2 points W would be replaced by W^2.

Consider a set of N samples f_k, where N is divisible by 2. Let us decompose the sequence into a sequence of even numbered samples and a sequence of odd numbered samples:

$$
\begin{aligned}
g_\ell &= f_{2\ell} \\
&\qquad\qquad \ell = 0,1,2, \ldots, N/2 - 1 \quad . \\
h_\ell &= f_{2\ell+1}
\end{aligned}
\tag{A.13}
$$

The DFT's of these sequences may be written as

$$G_k = \sum_{\ell=0}^{N/2-1} g_\ell (W^2)^{\ell k}$$

$$H_k = \sum_{\ell=0}^{N/2-1} h_\ell (W^2)^{\ell k} \quad . \tag{A.14}$$

We can also write the DFT of the entire sequence as

$$F_k = \sum_{n=0}^{N} f_n W^{nk}$$

$$= \sum_{\ell=0}^{N/2-1} (g_\ell W^{2\ell k} + h_\ell W^{(2\ell+1)k})$$

$$= \sum_{\ell=0}^{N/2-1} g_\ell (W^2)^{\ell k} + W^k \sum_{\ell=0}^{N/2-1} h_\ell (W^2)^{\ell k}$$

$$= G_k + W^k H_k \quad . \tag{A.15}$$

Hence, the DFT of the sequence can be written as a combination of the DFT's of two shorter sequences. Thus, through separating the sequences the computation time of (A.15) can be reduced to something proportional to $N + (N/2)^2$. Further, since G and H have a period N/2, only half of the N points is needed to reproduce F.

If N/2 is also divisible by 2, each of G and H can be reduced to the DFT of two shorter sequences. This procedure, termed decimation in time, can be continued until the sequence is reduced to subsequences of two points. These subsequences can be DFT'ed, and from these DFT's

the DFT of the total sequence can be constructed. The computation time
in this case can be derived to be proportional to $N \log_2 N$.

In the case that N is not divisible by two but is factorable, the
above procedure may be repeated for other divisions than two. The number
of points involved in the largest DFT subsequence will be the largest
prime factor of N. The decimation in "time" algorithm may be used in
exactly the same fashion for the inverse transform by changing the sign
of the exponent in the definition of W.

A similar algorithm termed decimation in frequency has been derived
by Sande, Cooley, Stockham and others. This algorithm calculates even
and odd subscripted points in the frequency domain from half sequences
in the time domain. The computational efficiency of this method is
equivalent to that of the decimation in time method.

This procedure can be employed in an N-dimensional Fourier trans-
form. The algorithms, being equivalent, will not be discussed here.

A.4 Employing FFT Subroutines

There are five FFT routines available through the IBM Common Computer
User Group Library. The routines are written in USASI Basic Fortran
and hence may be used with most third generation Fortran processors.
The routines are designed such that they take maximum advantage of data
form for the problem at hand. Substantial time penalties will result
from using a program general beyond the requirements of a given problem.
Table A.1 lists the routines and their functional characteristics.
The user is referred to IBM documentation for the details of using these
routines.

TABLE A.1

FFT SUBROUTINES

FOURI	One dimensional Power of two data points
FOURG	General one dimensional
FOURZ	Multidimensional Power of two data points in all dimensions
FOURT	General multidimensional
FOR2D	Multidimensional Power of two data points Data stored on direct access file